



UNIVERSIDAD AUTÓNOMA DE MADRID

Departamento de Física de la Materia Condensada

---

---

# Orbital Selective Spin-Fluctuations physics in iron-based superconductors

---

---

*Tesis doctoral presentada por*

**Raquel Fernández Martín**

Programa de doctorado de Física de la Materia Condensada,  
Nanociencia y Biofísica

*Directora*

**Belén Valenzuela Requena**

*Codirectora*

**Laura Fanfarillo**

*Tutor*

**Amadeo López Vázquez de Parga**

Madrid, Mayo de 2021

*A todos aquellos que  
creyeron que era posible.*

# Agradecimientos

Esta tesis ha sido lo más parecido a una montaña rusa. Todos estos años me han hecho aprender a mirar la vida de una manera muy distinta a la que tenía antes de comenzar. Desde el primer momento, el camino que seguí no fue exactamente de rosas, pero gracias a muchas personas pude continuar andando.

En primer lugar me gustaría agradecer a Belén, mi directora de tesis, el haberme dado la oportunidad de trabajar junto a ella. Gracias por haber creído en mí, por apoyarme en todos estos años. Gracias por estar a mi lado hasta el final. Tú no sólo me has enseñado física, sino que de ti he aprendido muchos aspectos personales que me acompañarán durante mi futuro camino. También quiero agradecer a Laura, por haber accedido a ser mi codirectora de tesis. Sin tu inestimable ayuda esta tesis no sería lo que es ahora. Gracias por todos tus valiosos consejos. Por último quiero agradecer a Amadeo por ser mi tutor durante este tiempo.

Durante mi paso por el ICMM conocí a investigadoras e investigadores brillantes que me han brindado su ayuda siempre que ha sido necesaria. En particular quiero agradecer a María José y a Leni, con las que no sólo he compartido momentos profesionales sino que también me han ofrecido la oportunidad de disfrutar y contribuir al arte de la divulgación. Voy a echar mucho de menos al fantasma Cooper, con el que tantos momentos hemos compartido. También agradezco haber aprendido de personas como Alberto, Yago, Pablo, Pilar, Paco y Rafa. Por último agradezco el poder haber colaborado con Belén, Laura, Lara y María José durante estos años.

En el lado más personal, el ICMM ha hecho que conociese a personas extraordinarias que me han alegrado cada día de trabajo. Gracias a mis compañeras de despacho Sandra y Ana por haberme aguantado y haber cerrado la ventana del despacho en repetidas ocasiones para salvar la vida del ordenador. Gracias a las “amiguitas de la segunda planta” María Jesús y María por esas conversaciones y esos momentos de risas inolvidables. Gracias a Alfonso, gran actor, por sacarme una sonrisa incluso en los momentos más duros, y por ayudarme con la huerta, la cual permanecerá existiendo por mucho tiempo gracias a la inolvidable Marisa. Muchas gracias Marisa por haber cuidado (y seguir cuidando) de todas mis plantas y por estar haciendo la más difícil de las tesis. Gracias también a Álvaro, Fernando, César y a Vicente, Óscar y Dani que aunque no estuvieseis en la planta adecuada también vuestra presencia ha sido imprescindible en todos estos años. Sin todos vosotros nada hubiera sido igual.

No puedo olvidarme de la “gente del IMDEA” a los que conocí como primera familia al entrar en el ICMM. Gracias a Jose, Francesca, Ángel, Luca, “el Vene”, Nacho y Vincenzo por acogerme y cuidarme en mis primeros años de tesis. Las comidas en psicología y los karaokes ya no son lo mismo.

Quiero agradecer también a toda la gente que me ha acompañado durante este camino. A mis compañeros del máster: Medrano, Jose cordobés, Javi, Pablo murciano y el

---

otro Pablo, pero en particular quiero agradecer a Edu Zaragoza y a “el canario” por haber estado siempre presentes y por haberme enseñado la gran canción del “maná-maná”. Gracias también a mis amigos de la carrera: Huertis, Barbudis, Heredia, Acero, Jota, Beirán, Vicente, Diego, David, Ibai... con los que espero seguir teniendo la mítica cena de Navidad.

Fuera del ámbito profesional no puedo olvidarme a gente con la que he compartido momentos prácticamente durante toda mi vida. Muchas gracias a Cris, Julia, Vals, Carlos, Álvaro, Fer, Luis, Solache, Rubén, Javi, Esther, Marcos, Cosín, Lillo... Por muy lejos que estemos cada uno, sin vuestra amistad y vuestro apoyo tampoco hubiese sido posible. Espero con ansias poder coger la A-2 en septiembre. También querría agradecer a mis amigas del cole: Raquel, Cuca, Teresa, Espe, Bea e Irene a las que conozco desde que tenía 3 años! Gracias por estar ahí desde hace tanto tiempo.

Gracias a mi familia. A Tomás, excelente investigador, por haberme aconsejado desde el principio de mi doctorado. Tu gran pasión por la ciencia hace que cualquier persona pueda maravillarse por ella. Gracias también a mis tíos y primas. Y no puedo olvidarme de mis abuelos, aunque muchos ya no estén, han sido y seguirán siendo una pieza fundamental en mi vida. Pero sobre todo esta tesis no hubiese sido posible sin mis padres. Gracias a vosotros soy todo lo que soy. No se cómo expresaros mi más profundo agradecimiento por haberme dado todo y enseñado tanto en la vida. Gracias por aguantarme incluso en ocasiones en las que era totalmente inaguantable. Gracias por vuestro amor incondicional. Espero ser capaz algún día de poder devolveros aunque sea una mínima parte de todas las cosas maravillosas que he recibido de vosotros.

Y por último quiero agradecer a ti, Edu, todos estos años. Gracias por tu cariño, tu paciencia, tus consejos, tus explicaciones físicas y no físicas. Gracias por entenderme, por animarme, por apoyarme. Gracias por todas las aventuras vividas y las que nos quedan por vivir. Este camino lo empezamos juntos y lo hemos terminado juntos. Gracias por haberme ayudado tanto todo este tiempo. Sin ti, nada hubiese sido posible.

# Publications

This work is based on the following papers:

1. “*Anisotropy of the dc conductivity due to orbital-selective spin fluctuations in the nematic phase of iron superconductors*”  
R. Fernández-Martín, L. Fanfarillo, L. Benfatto, B. Valenzuela.  
[Phys. Rev. B 99, 155117 \(2019\)](#); arXiv e-Print: [1804.07293 \[cond-mat\]](#)
2. “*Magnetic excitations in the Orbital Selective Spin-Fluctuations model for iron-based superconductors*”  
R. Fernández-Martín, M.J. Calderón, L. Benfatto, L. Fanfarillo, B. Valenzuela.  
Invited paper for a special Issue “Fluctuations and Highly Non-linear Phenomena in Superfluids and Superconductors IIF” in Condensed Matter edited by MDPI.  
In preparation.
3. “*xy-nematicity from orbital selective spin-fluctuations in a five-pockets model for iron-pnictides*”  
R. Fernández-Martín, L. Benfatto, L. Fanfarillo, B. Valenzuela.  
In preparation.

# Contents

<b>Introduction</b>	<b>1</b>
<b>Introducción</b>	<b>7</b>
<b>1. Iron-based Superconductors</b>	<b>13</b>
1.1. Materials and Structure . . . . .	13
1.2. Phase Diagram and tuning parameters . . . . .	14
1.3. Electronic Structure . . . . .	15
1.4. Instabilities and ordered phases . . . . .	17
1.5. Modeling iron-based superconductors within a spin-driven scenario . . . . .	20
1.5.1. Multiband models . . . . .	21
1.5.2. Multiorbital Hubbard models . . . . .	24
1.5.3. Orbital selective nature of the spin excitations . . . . .	26
<b>2. Orbital Selective Spin Fluctuation (OSSF) Model</b>	<b>29</b>
2.1. Spin-nematic model in the band-basis . . . . .	29
2.2. Spin-nematic scenario driven by orbital selective spin-fluctuations . . . . .	33
2.2.1. Model Hamiltonian . . . . .	33
2.2.2. Effective action for orbital selective spin excitations . . . . .	36
2.2.3. Role of the orbital nesting in the OSSF model . . . . .	37
2.3. Self-energy corrections from interband spin-fluctuations . . . . .	40
2.3.1. Self-energy effects due to spin-fluctuation in a multiband model . . . . .	40
2.3.2. Self-energy effects in the OSSF model . . . . .	42
<b>3. Magnetic excitations and superconductivity in the OSSF model</b>	<b>47</b>
3.1. Introduction . . . . .	47
3.2. Magnetic excitations and superconductivity in the multiorbital Hubbard model . . . . .	48
3.3. Magnetic excitations in the OSSF model: RPA analysis . . . . .	50
3.4. Superconductivity mediated by the OSSF . . . . .	54
3.4.1. Superconducting vertex: RPA analysis . . . . .	54
3.4.2. Superconducting gaps . . . . .	55
3.5. Conclusion Chapter 3 . . . . .	60
<b>4. Anisotropy of the dc conductivity in the nematic phase</b>	<b>63</b>
4.1. Introduction . . . . .	63
4.2. Conductivity in the OSSF model: a quantum field theory approach . . . . .	64
4.2.1. Current-current correlation function . . . . .	65

4.2.2. Dc conductivity . . . . .	67
4.3. 122 and FeSe dc conductivity within the OSSF model . . . . .	68
4.3.1. Analytical estimate of the dc-conductivity anisotropy . . . . .	69
4.3.2. Numerical estimate of the dc-conductivity anisotropy . . . . .	72
4.4. Discussion and comparison with experiments . . . . .	78
4.5. Conclusion Chapter 4 . . . . .	79
<b>5. OSSF within a five-pockets model</b>	<b>81</b>
5.1. Introduction . . . . .	81
5.2. Model Hamiltonian . . . . .	82
5.2.1. Kinetic Hamiltonian . . . . .	82
5.2.2. Interacting Hamiltonian . . . . .	83
5.3. Effective action for the five-pocket spin-nematic model . . . . .	84
5.3.1. Perfect circular nested Fermi surfaces . . . . .	86
5.3.2. Effect of the ellipticity in the model . . . . .	88
5.4. Orbital selectivity in the $\Gamma$ -XY <i>vs</i> MXY pocket model . . . . .	91
5.4.1. $\Gamma$ -XY model . . . . .	91
5.4.2. MXY model . . . . .	92
5.4.3. $\Gamma$ -XY model <i>vs</i> MXY model . . . . .	93
5.5. Conclusion Chapter 5 . . . . .	95
<b>6. Conclusions</b>	<b>99</b>
<b>Conclusiones</b>	<b>103</b>
<b>Appendices</b>	<b>107</b>
<b>A. Spin-driven nematic transition as spontaneous <math>Z_2</math>-symmetry breaking</b>	<b>109</b>
<b>B. Kinetic model for IBS</b>	<b>113</b>
B.1. Symmetry adapted low-energy model for the four-pocket model . . . . .	113
B.2. Perfect circular nested and elliptical Fermi surfaces . . . . .	115
B.3. Model parameters for the kinetic Hamiltonian . . . . .	116
<b>C. Appendix Chapter 3</b>	<b>117</b>
C.1. Magnetic excitations in the OSSF model: RPA analysis . . . . .	117
C.1.1. Computation of the spin susceptibility . . . . .	117
C.1.2. Four pocket model susceptibilities . . . . .	119
C.2. Superconductivity mediated by OSSF . . . . .	119
C.2.1. Computation of the RPA pairing vertex . . . . .	119

C.2.2. Orbital-dependent superconducting order parameters . . . . .	121
C.2.3. Band parameters to reproduced the multiorbital model . . . . .	121
<b>D. Appendix Chapter 4</b>	<b>123</b>
D.1. Computation of the dc conductivity from the optical conductivity in the OSSF model . . . . .	123
D.1.1. Current-current correlation function . . . . .	123
D.1.2. Dc conductivity . . . . .	125
D.2. Analytical computation of the anisotropy of the dc conductivity for the 122 and FeSe . . . . .	127
D.2.1. Perfect nested circular Fermi surfaces . . . . .	127
D.2.2. Anisotropy of the dc conductivity . . . . .	128
D.3. Model parameters for FeSe and 122 systems . . . . .	131
<b>E. Appendix Chapter 5</b>	<b>133</b>
E.1. Estimation of the quadratic and quartic terms of the effective action for the five-pocket model . . . . .	133
E.1.1. Perfect circular nested and elliptical Fermi surfaces . . . . .	133
E.1.2. Evaluation of the sum over frequency and momenta . . . . .	134
E.2. Magnetic and nematic couplings and order parameters: eigenvalues and eigenvectors of the quartic term of the effective action . . . . .	136
E.2.1. Three and four-pockets models . . . . .	136
E.2.2. Five pockets model . . . . .	137
E.3. Parameters for the quantitative analysis for the $\Gamma$ -XY and MXY models . .	139
<b>Bibliography</b>	<b>141</b>



# Introduction

*“Why haven’t we theoretical physicists solved this problem yet?  
The only reason that we cannot do this problem of superconductivity  
is that we haven’t got enough imagination.”*

R. P. FEYNMAN

There is no temperature below absolute zero. Out of curiosity, researchers have tried to reach this lower limit and this, in turn, has led to the discovery of new physical phenomena, and it has widened our understanding of the structure of the matter that surrounds us. This curiosity led Heike Kamerlingh Onnes and his student Gille Holst to cool down mercury with the aid of liquid helium in 1911. As the temperature reached a critical value  $T_c$  of  $4.2K$ , the electrical resistance of mercury dropped to zero [1]. They had discovered superconductivity. In 1933 Walther Meissner and Robert Ochsenfeld showed that a superconductor is more than just a perfect conductor. They observed that, except from a thin region near the surface, these materials expelled the magnetic flux from their interior, i.e., they are perfect diamagnets. This effect is the so-called Meissner effect [2]. Perfect diamagnetism and perfect conductivity are the two hallmarks of a superconductor.

Since its discovery, most of the brightest physicists tried, unsuccessfully, to develop a microscopic theory of superconductivity [3]. But it was not until 1957 when John Bardeen, Leon N. Cooper and John Robert Schrieffer developed a revolutionary theory of superconductivity, the BCS theory [4, 5]. This theory postulated that phonons, the quantum excitations of the crystal lattice, mediate an attractive interaction between the electrons, leading to the formation of bound pairs of electrons, the so-called Cooper pairs. These pairs condense in a coherent macroscopic quantum state, the superconducting state, of pairs with opposite momenta and spins.

In the early years, superconductivity was mostly discovered in metals and alloys that could be well described by the BCS theory. Nevertheless, the discovery of heavy fermions superconductors in the 70’s [6], challenged the theoretical understanding of the phenomenon as in these materials superconductivity cannot be explained within a BCS framework. We refer to those superconductors for which BCS theory does not work as unconventional, in contrast to conventional superconductors for which the attraction is mediated by phonons. Despite the findings of these new superconductors critical temperatures were still extremely low, and liquid helium was needed to reach them. The discovery of materials that could superconduct at higher temperatures, providing much wider applications, was the dream of researchers.

In 1986 J. G. Bednorz and K. A. Müller reported for the first time the observation of superconductivity in a cuprate-based ceramic. The compound contained lanthanum, copper, and oxygen and doped with barium presented a superconducting transition at a critical temperature slightly above  $30K$  [7]. This discovery triggered an intense research and it was soon found that replacing the lanthanum with yttrium raised the critical temperature up to  $T_c = 93K$  [8]. This temperature jump was extremely significant, since it finally allowed researchers to use liquid nitrogen as a refrigerant instead of liquid helium. The high temperature superconductors (HTSC) era had just started. In a few years, many

copper-based superconducting materials were discovered giving rise to the first class of HTSC, the cuprates. But the history of superconductivity does not end here. In 2008 another breakthrough happened when a new class of HTSC was discovered, the iron-based superconductors (IBS) [9–11]. H. Hosono and his group announced the discovery of superconductivity in fluorine-doped  $LaO_{1-x}F_xFeAs$ , at  $T_c = 26K$  [12], which was later found to superconduct at  $T_c = 43K$  under pressure [13].

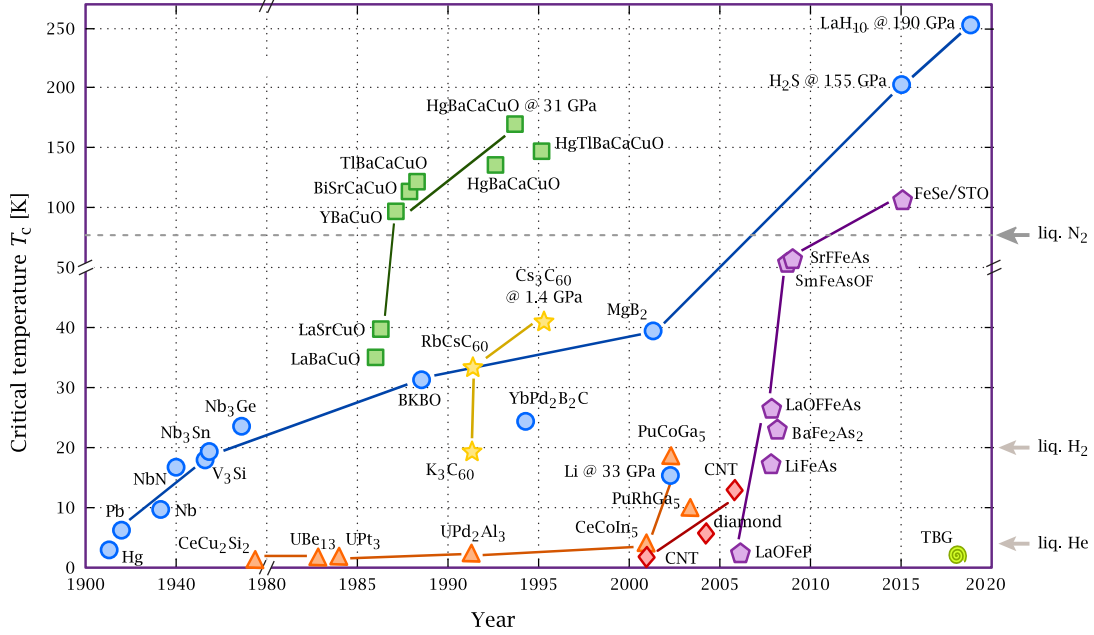


**Figure 1:** Timeline of the discovery of superconducting materials. Colors represent different classes of materials: BCS superconductors in blue circles, heavy fermions in orange triangles, cuprates in green squares, fullerene- $C_{60}$  in yellow stars, carbon-allotrope in red diamond, iron-based in violet pentagon, and twisted bilayer graphene in light green spiral. Partly based on [14].

The two main families of HTSC, cuprates and iron-based, are unconventional superconductors in which the pairing mechanism is still nowadays under debate. It is notable that in most of IBS and cuprates superconductivity emerges at the frontier of an antiferromagnetic phase [15]. This observation indicates a close interplay between magnetism and unconventional superconductivity, and suggests that spin fluctuations may play an important role in the formation of the Cooper pairs. The hope to find a consensus about the pairing mechanism in IBS, and then to apply this knowledge to cuprates, is intriguing. However, thirteen years of intense research following the IBS discovery has led to the understanding that the physics of IBS is far richer than originally thought, and characterized by a number of highly non-trivial properties which have no analogs in cuprates [15]. This Thesis focuses on the study of IBS. In this theoretical work we analyze the role of spin-fluctuation in the IBS physics and try to understand whether the spin fluctuations represent the key to explain the complex phenomenology of IBS.

IBS materials, in contrast to cuprates, are characterized by multi-orbital physics, as theoretically predicted by *ab initio* calculations and confirmed by experiments [16–21]. The phase diagram of these materials exhibits a range of different phases including the magnetic phase and the superconducting one [9–11, 22]. An intriguing nematic phase just above the magnetic one is also present in the phase diagram of many IBS. The nematic

instability is characterized by a structural transition and a marked electronic anisotropy, much larger than the one expected by the structural transition itself. The origin of the nematic phase is one of the most controversial topics in this field [23]. It is also puzzling that, although most of IBS present similar crystal structures, their phenomenology can be extremely different, as the case of FeSe [24] in which a nematic order develops without an antiferromagnetic order nearby.

A theoretical proposal able to explain the complex phenomenology of IBS within a common framework is one of the most challenging issues in the field of HTSC. Within this Thesis we focus on theoretical analysis based on a itinerant spin-driven scenario. In that respect, there are two main approaches that can be used based on multiband or multiorbital description of the low-energy electronic bands [25].

Low-energy multiband models offer an appealing and simple framework to explain the origin and interplay of the different orders. Within this modeling both magnetism and superconductivity are explained in terms of Fermi-surface instabilities due to the exchange of spin-fluctuations between different Fermi surface sheets. At the same time, spin-fluctuation are also at the origin of the nematic phase. Nematicity is interpreted as a precursor effect of magnetism that originates from the  $x/y$  anisotropy of spin-fluctuations realized when the long-range magnetic order is not yet established. Although very successful in explaining the emergence and interplay of several orders, low-energy multiband models have a main limitation. They do not include the information about the orbital composition of the bands and thus they cannot be used to study phenomena involving orbital physics.

Multiorbital models, instead, start from a description of the electronic bands in the orbital basis and thus are able to capture the multiorbital physics of IBS. Random phase approximation (RPA) calculations have been proven to be suitable to quantitatively study magnetism and superconductivity. However, the analysis of nematicity, i.e. a fluctuation-driven phenomenon, cannot be performed via the standard RPA method and required the inclusion of fluctuations beyond RPA in the multiorbital description. Implementation of this procedure is possible, however it is quite complex given the number of orbitals involved and does not lead to a unambiguous definition of nematicity.

The absence of orbital information within band-based approaches, the lack of connection between multiband and multiorbital modelings, and, in particular, the difficulties to analyze the spin-driven nematicity within multiorbital models leave several important open questions. The development of a theoretical frame in which the simplicity of multiband models merges with the orbital information contained in multiorbital descriptions is necessary to unveil the spin-orbital interplay in IBS and provide a deeper understanding of the IBS physics. The analysis of such a theoretical description is one of the aims of this dissertation.

In this Thesis, we focus on the analysis of the Orbital Selective Spin-Fluctuation (OSSF) model. This is a minimal low-energy model for IBS that operates in the band basis, but fully incorporates the orbital composition and symmetries of the low-energy excitations. This description, originally proposed in [26, 27], unveiled a precise orbital dependence of the spin-fluctuations. The description in terms of orbital-selective spin-fluctuations retains the simplicity of the band-basis modeling, but fully account for the orbital degree of freedom. As within a multiband description, the emergence of the ordered phases can be explained analyzing the spin interaction and its fluctuations at various orders; within this model, however, the spin-fluctuations are also orbital-selective and this

has profound consequences. This approach provides a common framework that account for the spin-orbital interplay and explain the origin and interplay of different phases of IBS.

Throughout this Thesis, we compare the physics of the OSSF model with the descriptions obtained within multiband and multiorbital models to highlight the advantages of a theoretical analysis based on the OSSF description. The low energy description provided by the OSSF model allow us to calculate in an feasible way response functions that we can compare to experimental results. Analytical results are available in certain limits; this makes the results obtained easily readable and physically understandable and provides further insight in the IBS phenomenology. Moreover the model can be easily adapted to analyze the phenomenology of different IBS families.

This Thesis counts six chapters. The first two contains a summary of experimental and theoretical results obtained for IBS in the literature. The rest of the Thesis contains the original work performed during the Ph.D program.

In Chapter 1 we provide a brief overview on IBS, highlighting experimental and theoretical aspects that have served as motivations for this work. We first summarize IBS phenomenology and discuss their electronic properties emphasizing the multiorbital character of these systems. We then introduce the theoretical approaches used to described the low-energy physics of IBS within a spin-driven scenario: multiband and multiorbital models. We show how an effective low-energy model including the orbital degrees of freedom is needed in order to reproduce the complex phenomenology of iron-based materials and provide a unified picture for different members of the iron-based family. In Chapter 2 we review the main steps of the derivation of the OSSF model and we compare it to the low-energy multiband model to show how the inclusion of the orbital degree of freedom qualitatively affects the results of the analysis. We also discuss how the spin-nematic order parameter defined within the OSSF model is unambiguously defined and has a clear physical interpretation, in contrast with the multi-component spin-nematic order parameter defined within a multiorbital analysis.

The following chapters contains the original work performed during this Thesis. The main scope of this work is to understand the phase diagram of different families of IBS within a common framework given by the OSSF model.

We start by analyzing, in Chapter 3, the magnetic excitation and the spin-mediated superconductivity of the OSSF within a RPA analysis. First, we compute explicitly the orbital-dependent magnetic spin susceptibility for a typical IBS Fermi surface. Then, assuming the spin fluctuations mediating superconductivity, we analyse the pairing vertex and the gap functions. We compare our results with analogous RPA analysis of multiorbital models and show how the orbital selectivity, encoded in the OSSF model, simplifies substantially the analysis, allowing for analytical treatments, while retaining all the main features of both spin-excitations and gap functions computed using multiorbital models.

In Chapter 4 we analyze the anisotropy of the electronic properties of IBS in the nematic phase. In particular, we compute analytically and numerically the dc conductivity anisotropy in the nematic phase using realistic parameters to reproduce different IBS families. We want to address two main questions: First, how the anisotropy of the orbital selective spin-fluctuations, at the origin of nematicity, affects the dc resistivity? Second, can we reconcile in a single theoretical framework the strong material-dependence anisotropy of the dc resistivity found experimentally in the various IBS family? By explicitly

computing the current response function for the OSSF model, we show that due to the spin-orbital interplay encoded in our description, the anisotropy of the orbital-selective spin-fluctuations affects in an anisotropic way both the velocity and the scattering rate of the carriers. This result qualitatively differs from the one obtained within spin-driven multiband models in which only the scattering rate of the carriers is renormalized. We then analyze the outcomes of our calculations for different families of IBS. This analysis helps us to clarify the different degrees of freedom affecting the result and allows us to reconcile the experimental observations reported in different families of IBS within a single description.

The OSSF model has been derived within a four-pocket model representative for IBS. However, a complete analysis of IBS requires to consider a five-pocket model. This extra pocket differs among compounds and depends on doping or applied pressure. In Chapter 5 we extend the analysis of the OSSF model to the case of Fermi surfaces made by five-pockets. Generalizing what previously done for a four-pocket model, we derive the effective action in terms of the spin degree of freedom and define the OSSF model for the five-pockets case. We discuss the new physics emerging from this generalization by comparing the results of this model with the ones obtained within a three/four-pockets.

In the final Chapter of this Thesis, Chapter 6, we give our conclusions and provide an outlook of the possible avenues of research that one could follow building up on this thesis.

# Introducción

*“ ¿Por qué los físicos teóricos aún no hemos resuelto este problema?  
La única razón por la que no podemos resolver este problema de la  
superconductividad es porque no tenemos suficiente imaginación. ”*

R. P. FEYNMAN

No existe temperatura por debajo del cero absoluto. La curiosidad por alcanzar temperaturas cercanas a este límite nos ha permitido descubrir nuevos fenómenos físicos, así como ampliar nuestra comprensión de la estructura de la materia que nos rodea. Esta curiosidad fue la que llevó a Heike Kamerlingh Onnes junto con su estudiante Gille Holst a enfriar mercurio con helio líquido en 1911. Cuando la temperatura alcanzaba un valor crítico de  $T_c = 4,2K$ , la resistencia eléctrica del mercurio se hacía exactamente cero [1]. Acababan de descubrir el fenómeno de la superconductividad. En 1933 Walther Meissner y Robert Ochsenfeld demostraron que un superconductor es mucho más que un conductor perfecto. Vieron que dichos materiales excluían el campo magnético de su interior, salvo de una pequeña región cercana a la superficie, es decir, son materiales diamagnéticos perfectos. Este efecto es conocido como el efecto Meissner [2]. Diamagnetismo perfecto y conductividad perfecta son las dos principales características de un superconductor.

Desde su descubrimiento, muchos de los físicos más brillantes intentaron, sin éxito, desarrollar una teoría microscópica de la superconductividad [3]. Pero no fue hasta 1957 cuando John Bardeen, Leon N. Cooper y John Robert Schrieffer desarrollaron una teoría revolucionaria de la superconductividad, la teoría BCS [4, 5]. Esta teoría propone que los fonones, excitaciones cuánticas de una red cristalina, son los mediadores de una interacción atractiva entre los electrones que da lugar a la formación de pares de electrones ligados, los pares de Cooper. Estos pares condensan en un estado cuántico coherente macroscópico, el estado superconductor, de pares con momento y espín opuestos.

En los primeros años, la superconductividad fue descubierta sobre todo en metales y aleaciones los cuales se entendían bajo el marco de la teoría BCS. Sin embargo, el descubrimiento en los años 70 de los fermiones pesados [6], desafió la comprensión teórica de la superconductividad ya que estos materiales no podían ser explicados con la teoría BCS. Nos referimos a los materiales superconductores que no pueden ser explicados con la teoría BCS como no convencionales, a diferencia de los superconductores convencionales cuya atracción está mediada por fonones. A pesar del descubrimiento de estos nuevos superconductores, sus temperaturas críticas eran aún extremadamente bajas y el helio líquido era necesario para poder enfriarlos. El descubrimiento de materiales que pudieran ser superconductores a temperaturas más altas, proporcionando muchas más aplicaciones, era el sueño de muchos investigadores.

En 1986 J. G. Bednorz y K. A. Müller observaron por primera vez superconductividad en una cerámica a base de cuprato. El compuesto contenía lantano, cobre y oxígeno, y dopado con bario presentaba una temperatura crítica de la transición superconductora por encima de  $30K$  [7]. Este descubrimiento desencadenó una intensa investigación y no se tardó en descubrir que reemplazando el lantano por itrio la temperatura crítica se elevaba hasta  $T_c = 93K$  [8]. Este salto en temperatura fue extremadamente significativo,

ya que finalmente permitió a los investigadores usar nitrógeno líquido como refrigerante en vez de helio líquido. La era de los superconductores de alta temperatura (HTSC) acababa de empezar. En pocos años, muchos más materiales superconductores basados en cobre fueron descubiertos, dando lugar a la primera clase de HTSC, los cupratos. Pero la historia de la superconductividad no acaba ahí. En 2008 ocurrió otro gran avance, cuando una nueva clase de HTSC fueron descubiertos, los superconductores basados en hierro (IBS) [9–11]. H. Hosono y su grupo anunció el descubrimiento de superconductividad en  $LaO_{1-x}F_xFeAs$  dopado con flúor, a  $T_c = 26K$  [12], el cual se encontró más tarde que también era superconductor bajo presión a  $T_c = 43K$  [13].

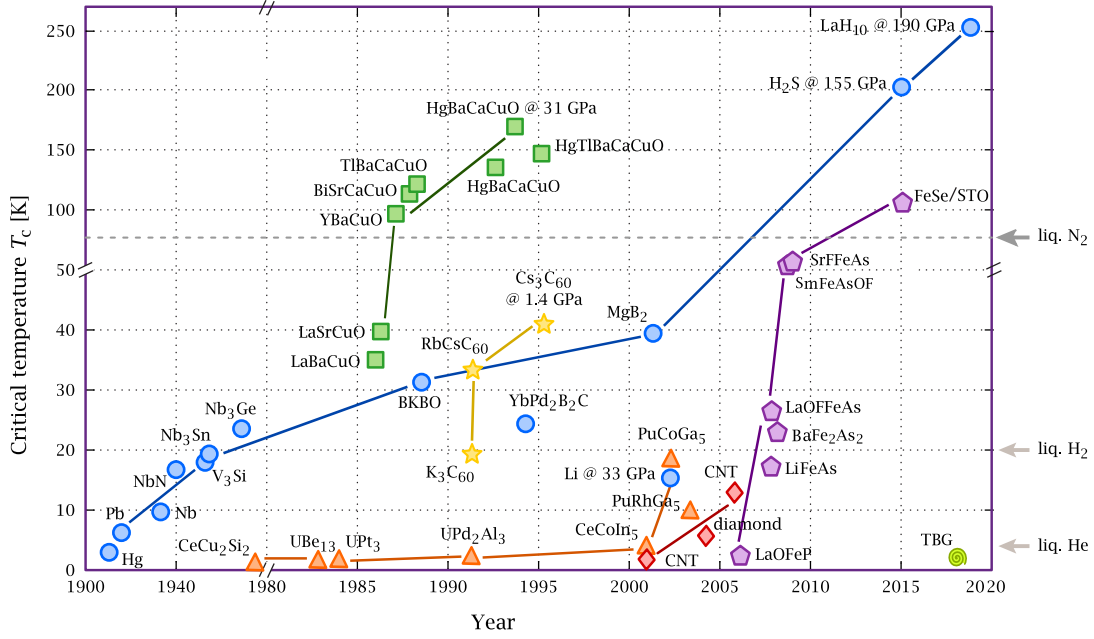


**Figura 2:** Cronología del descubrimiento de los materiales superconductores. Los colores representan diferentes clases de materiales: superconductores BCS en círculos azules, fermiones pesados en triángulos naranjas, cupratos en cuadrados verdes, fullereno- $C_{60}$  en estrellas amarillas, alótropos del carbono en diamantes rojos, superconductores basados en hierro en pentágonos violetas y el grafeno bicapa girado con la espiral verde clara. Figura parcialmente basada en [14].

Las dos familias de HTSC, los cupratos y los materiales basados en hierro, son superconductores no convencionales en los que el mecanismo de la superconductividad aún está en debate. Es curioso que en la mayoría de IBS y cupratos, la superconductividad emerge en la frontera de una fase antiferromagnética [15]. Esto podría indicar una estrecha relación entre el magnetismo y la superconductividad no convencional, sugiriendo que las fluctuaciones de espín podrían jugar un papel importante en la formación de los pares de Cooper. La esperanza de encontrar un consenso sobre el mecanismo de la superconductividad en los IBS, y luego aplicar este conocimiento a los cupratos, es intrigante. Sin embargo, trece años de intensa investigación desde el descubrimiento de los IBS ha llevado a comprender que la física de los IBS es mucho más rica de lo que se pensaba originalmente, y está caracterizada por un gran número de propiedades altamente no triviales que no tienen analogía con los cupratos. En esta Tesis nos centramos en el estudio de los IBS. En este trabajo teórico, analizamos el papel de las fluctuaciones de espín en la física de los IBS e



intentamos entender si las fluctuaciones de espín representan la llave para poder explicar la compleja fenomenología de los IBS.

Los superconductores basados en hierro, al contrario que los cupratos, están caracterizados por física multiorbital, como fue predicho teóricamente por cálculos *ab initio* y confirmado más tarde por experimentos [16–21]. El diagrama de fases de estos materiales exhibe un gran rango de fases diferentes entre las que se incluye la fase magnética y la superconductora [9–11, 22]. Una fase nemática intrigante aparece justo por encima de la fase magnética en la mayoría de los diagramas de fases los IBS. La inestabilidad nemática está caracterizada por una transición estructural y una notable anisotropía electrónica, mucho mayor que la esperada de la transición estructural. El origen de la fase nemática es uno de los temas más polémicos en este campo [23]. También es desconcertante que, aunque la mayoría de los IBS presentan estructuras cristalinas similares, su fenomenología puede ser extremadamente diferente, como el caso del FeSe [24] en el que se desarrolla un orden nemático sin un orden antiferromagnético cerca.

Uno de los mayores retos en el campo de los HTSC es encontrar un modelo teórico que sea capaz de explicar la compleja fenomenología de los IBS dentro de un marco común. Esta Tesis se centra en un análisis teórico basado en un escenario itinerante impulsado por espines. En ese sentido, hay dos enfoques principales que se basan en una descripción multibanda o multiorbital de las bandas electrónicas a baja energía [25].

Los modelos multibanda de baja energía ofrecen un marco atractivo y sencillo para explicar el origen y la interacción de los distintos órdenes. En este modelo tanto el magnetismo como la superconductividad son explicadas en términos de las inestabilidades en la superficie de Fermi que son debidas al intercambio de fluctuaciones de espín entre diferentes partes de la superficie de Fermi. Al mismo tiempo, las fluctuaciones de espín son también el origen de la fase nemática. La nematicidad es interpretada como un precursor del magnetismo que se origina a partir de la anisotropía en  $x/y$  de las fluctuaciones de espín que se obtiene cuando aún no se ha establecido el orden magnético de largo alcance. Aunque los modelos multibanda de baja energía son exitosos en explicar el surgimiento y la interacción entre varios órdenes, tienen una limitación principal. No incluyen la información sobre la composición orbital de las bandas y por lo tanto no pueden usarse para estudiar fenómenos relacionados con la física orbital.

Los modelos multiorbitales, en cambio, empiezan desde una descripción de las bandas electrónicas en la base orbital y por ello son capaces de capturar la física multiorbital de los IBS. Se ha demostrado que los cálculos de Aproximación de Fase Aleatoria (RPA) son adecuados para estudiar cuantitativamente el magnetismo y la superconductividad. Sin embargo, el análisis de la nematicidad, que es un fenómeno impulsado por espines, no puede ser realizado mediante el método estándar de RPA y requiere tener en cuenta fluctuaciones más allá de RPA en la descripción multiorbital. La implementación de este procedimiento es posible, pero es bastante complejo dado el gran número de orbitales involucrados y no conduce a una definición inequívoca de la nematicidad.

La ausencia de información orbital con los modelos basados en las bandas, la falta de conexión entre dichos modelos y los multiorbitales, y en particular, la dificultad para analizar la nematicidad impulsada por espín en los modelos multiorbitales dejan varias preguntas abiertas. El desarrollo de un marco teórico en el que la simplicidad de los modelos multibandas se una junto con la información orbital contenida en la descripción multiorbital es necesario para desvelar la relación entre el espín y el orbital en los IBS y proporcionar



una comprensión más profunda de la física de los IBS. El análisis de dicha descripción teórica es uno de los principales objetivos de esta tesis.

En esta Tesis nos centramos en el análisis del modelo de Fluctuaciones de Espín con Selección Orbital (OSSF). Este es un modelo mínimo de baja energía para los IBS que opera en la base de las bandas pero que incorpora completamente la composición orbital y las simetrías de las excitaciones de baja energía. Esta descripción, originalmente propuesta en [26, 27], reveló una precisa dependencia orbital de las fluctuaciones de espín. La descripción en términos de fluctuaciones de espín con selección orbital conserva la simplicidad de los modelos basados en las bandas, pero tiene en cuenta el grado de libertad orbital. Al igual que en la descripción multibanda, la aparición de las fases ordenadas puede explicarse analizando la interacción entre espines y sus fluctuaciones en varios órdenes; con este modelo, sin embargo, las fluctuaciones de espín proporcionan además, una selección orbital lo que tiene profundas consecuencias. Esta propuesta ofrece un marco común que tiene en cuenta la relación entre el espín y el orbital y que también puede explicar el origen y la relación de las distintas fases de los IBS.

A lo largo de esta Tesis, comparamos la física del OSSF model con las descripciones obtenidas con los modelos multibanda y multiorbitales para resaltar las ventajas de un análisis teórico basado en el modelo OSSF. La descripción de baja energía dada por el OSSF model nos permite calcular de manera factible funciones respuesta que podemos comparar con los resultados experimentales. También podemos obtener resultados analíticos en ciertos límites que nos proporcionan resultados físicamente comprensibles que se pueden interpretar fácilmente y nos proporcionan una mayor comprensión de la fenomenología de los IBS. Además el modelo se puede adaptar fácilmente para analizar la fenomenología de las diferentes familias de los IBS.

Esta Tesis cuenta con seis capítulos. Los dos primeros contienen un resumen de los resultados experimentales y teóricos obtenidos para los IBS en la literatura. El resto de la Tesis contiene el trabajo original llevado a cabo durante este programa de doctorado.

En el Capítulo 1 damos una visión general de los IBS, resaltando los aspectos experimentales y teóricos que han servido como motivación para este trabajo. Primero resumimos la fenomenología de los IBS y discutimos sus propiedades electrónicas enfatizando el carácter multiorbital de estos sistemas. Luego introducimos los enfoques teóricos usados en la descripción de la física de baja energía de los IBS dentro de un escenario impulsado por el espín: los modelos multibanda y multiorbitales. Mostramos como es necesario un modelo efectivo de baja energía que incluya el grado de libertad orbital para reproducir toda la compleja fenomenología de los materiales basados en hierro y proporcionar una visión unificada de los diferentes miembros de las familias de los IBS. En el Capítulo 2 revisamos los pasos necesarios para la derivación del modelo OSSF y lo comparamos con los modelos de bandas de baja energía para demostrar como la inclusión del grado de libertad orbital afecta cualitativamente al resultado del análisis. También discutimos como el parámetro de orden espín-nemático en el modelo OSSF está definido de manera inequívoca y tiene una interpretación física clara, en comparación con el parámetro de orden espín-nemático definido en el análisis multiorbital.

Los capítulos siguientes contienen el trabajo original llevado a cabo durante esta Tesis. El objetivo principal de este trabajo es entender el diagrama de fases de las diferentes familias de IBS dentro de un mismo marco común dado por el modelo OSSF.

Empezamos analizando, en el Capítulo 3, la excitación magnética y la superconductividad mediada por espines en el modelo OSSF con un análisis RPA. Primero, calculamos explícitamente la dependencia orbital de la susceptibilidad de espín magnética para una superficie de Fermi típica de un IBS. Luego, asumiendo que las fluctuaciones de espín median la superconductividad, analizamos el vértice superconductor y las ecuaciones del gap. Nuestros resultados son comparados con el análisis RPA análogo para un modelo multiorbital y mostramos como la selectividad orbital, codificada en el modelo OSSF, simplifica sustancialmente el análisis permitiendo un tratamiento analítico de éste, al tiempo que conserva todas las características principales de tanto las excitaciones de espín como de las ecuaciones del gap calculadas en un modelo multiorbital.

En el Capítulo 4 analizamos la anisotropía en las propiedades electrónicas de los IBS en la fase nemática. En particular, calculamos analíticamente y numéricamente la anisotropía en la conductividad dc en la fase nemática usando parámetros realistas para reproducir varias familias de los IBS. Con ello queremos abordar dos preguntas principales: Primero, ¿cómo afecta la anisotropía de las fluctuaciones de espín con selección orbital, en el origen de la nematicidad, a la resistividad dc? En segundo lugar, ¿podemos reconciliar en un sólo marco teórico toda la variedad de diferentes anisotropías que se encuentra experimentalmente para los distintos materiales de las diversas familias de IBS? Calculando explícitamente la función respuesta de la corriente en el modelo OSSF podemos demostrar que gracias a la interacción entre el espín y el orbital, codificada en nuestra descripción, la anisotropía de las fluctuaciones de espín con selección orbital afecta de manera anisotrópica tanto a la velocidad como al tasa de dispersión de los electrones. Este resultado difiere cualitativamente del obtenido en un modelo impulsado por el espín multibanda, en el que solo la tasa de dispersión de los electrones se ve renormalizada. A continuación hacemos un análisis profundo de los resultados de nuestros cálculos para las diferentes familias de IBS. Gracias a este análisis podemos clarificar los diferentes grados de libertad que afectan al resultado y nos permite conciliar las observaciones experimentales reportadas en diferentes familias de IBS dentro de un mismo marco teórico.

El modelo OSSF ha estudiado el modelo de cuatro áreas que es representativo de la mayoría de IBS. Sin embargo, para llevar a cabo un análisis completo de los IBS se requiere un modelo de cinco áreas. Esta área extra difiere entre los compuestos y depende del dopaje o de la presión aplicada. En el Capítulo 5 extendemos el análisis del modelo OSSF al caso de una superficie de Fermi con cinco áreas. Generalizando lo que se hizo anteriormente para un modelo de cuatro áreas, derivamos la acción efectiva en términos del grado de libertad del espín y definimos el modelo OSSF para el caso de cinco áreas. Luego discutimos la física nueva que emerge de esta generalización comparando los resultados obtenidos en este modelo con los obtenidos con un modelo de tres o cuatro áreas.

En el capítulo final de esta Tesis, Capítulo 6, exponemos nuestras conclusiones y proporcionamos algunas de las posibles vías de investigación que se podrían seguir a partir de esta Tesis.

# 1

## Iron-based Superconductors

Iron-based superconductors were discovered in 2008 when Hosono and coworkers reported the observation of a superconducting transition below  $T_c = 26K$  in LaOFeAs under F-doping [12]. Since then, several members of the iron-based superconductors (IBS) family have been identified [9, 10]. All IBS present a similar layered structure whose common building block is the Fe-atoms square lattice. *Ab initio* band structure calculations including all the five Fe-*d* orbitals qualitatively reproduce the Fermi Surface experimentally observed, with several hole- and electron-like bands crossing the Fermi level in different parts of the Brillouin zone [16–20].

The multiband character of the electronic structure has been immediately recognized as an unavoidable ingredient of any theoretical description of the unconventional IBS superconductivity. Already in 2008, indeed, it was proposed that pairing could be mediated by the exchange of repulsive spin fluctuations between the hole and electron bands, connected at the Fermi level by the same wave-vector characteristic of the spin modulations of the magnetic phase [19, 20]. However, within this scenario, the Fermi Surface geometry of a system should rule completely its phenomenology; on the contrary, we find a huge variety of phase diagrams associated to materials characterized by similar Fermi Surface. In that respect, it has been recently proposed that the orbital composition of the bands connected by the spin fluctuations could play an essential role and determining which instability is realized at low-temperature [26, 27]. This proposal requires to revise the standard spin-fluctuations low-energy model originally discussed in [28] including the orbital degree of freedom in the low-energy description of both the IBS bands and the spin excitations.

In what follows we provide a brief overview of the IBS phenomenology, we discuss explicitly as the multiband/multiorbital physics is accounted in theoretical approaches based on a spin-fluctuations scenario for IBS and show how the orbital selectivity of the spin-excitations naturally emerges in a description that incorporate the orbital degree of freedom in a low-energy multiband modeling.

### 1.1. Materials and Structure

The crystal structures of all IBS is characterized by the presence of a tetrahedral Fe-pnictides/chalcogen layers in which the iron ions form a planar square lattice, while the pnictogen (P, As) or chalcogen (S, Se, Te) ions are located at the center the squares, alternatively above or below the Fe-planes. Depending on the family, we find the tetra-

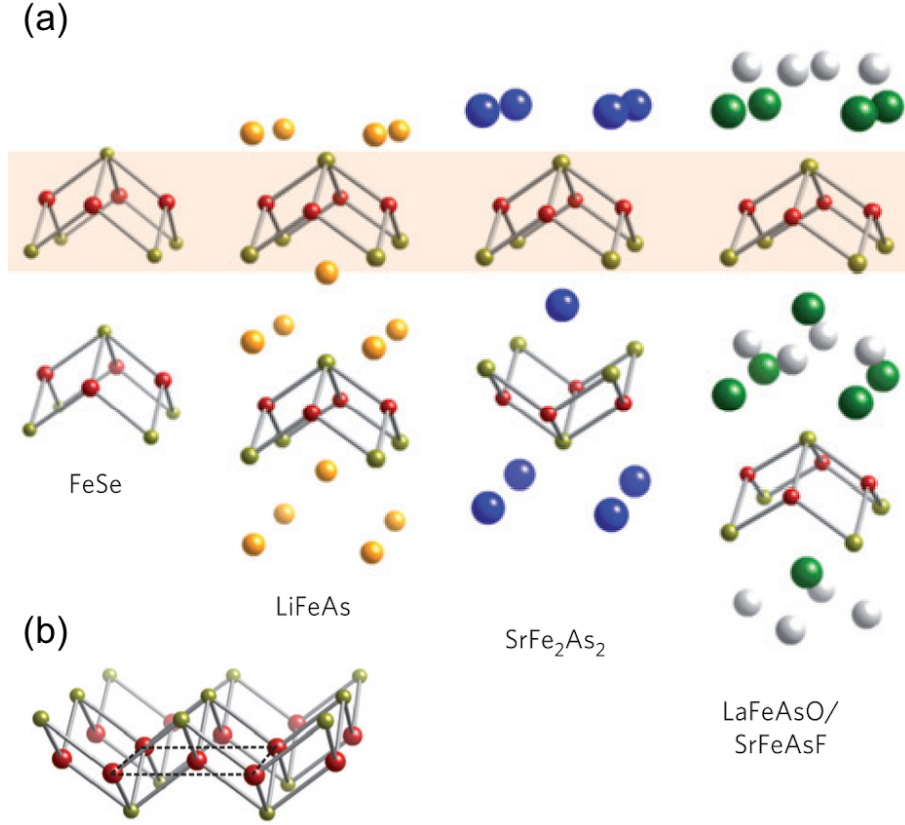


**Figure 1.1:** (a) Crystallographic structures of various families of iron-based superconductors. (b) Tetrahedral structure of the Fe-pnictide/chalcogen common to all superconducting compounds (iron in red, pnictogen/chalcogen in gold). Adapted from [29].

hedral Fe-pnictide/chalcogen layer separated by alkali, or rare-earth and oxygen/fluorine blocking layers. In Figure 1.1 some of the common structures are shown: 1111 are compounds with alternating FeAs and RE(O,F) sheets (RE= Rare Earth= La,Nd,Ce,etc.); 122 systems have two FeAs layers sandwiched between A (=Ba,Sr,K) layers; 111 as LiFeAs and NaFeAs are compounds with a single layer in between the FeAs plane: and 11, as FeSe, has the simplest structure as it does not have any filler species in between the iron-based layer.

## 1.2. Phase Diagram and tuning parameters

Superconductivity is only one of the several quantum phases of the matter that can be found in IBS. In Figure 1.2 we report the temperature-doping phase diagrams for different systems: (a) 1111 F-doped LaOFeAs [30] (b) 122 P-doped BaFe<sub>2</sub>As<sub>2</sub> [31] and (c) 11 S-doped FeSe [32]. Electron/hole doping, isovalent chemical substitutions or intercalations, and external pressure are typical tuning parameters that drives superconductivity [10, 11, 33].

In most IBS, the parent compounds is characterized by a spin-density wave (SDW) i.e. a metallic antiferromagnetic phase. The SDW transition is often coupled with a structural transition from a high-temperature tetragonal to a low-temperature orthorhombic phase. The region enclosed between the structural transition and the magnetic one is

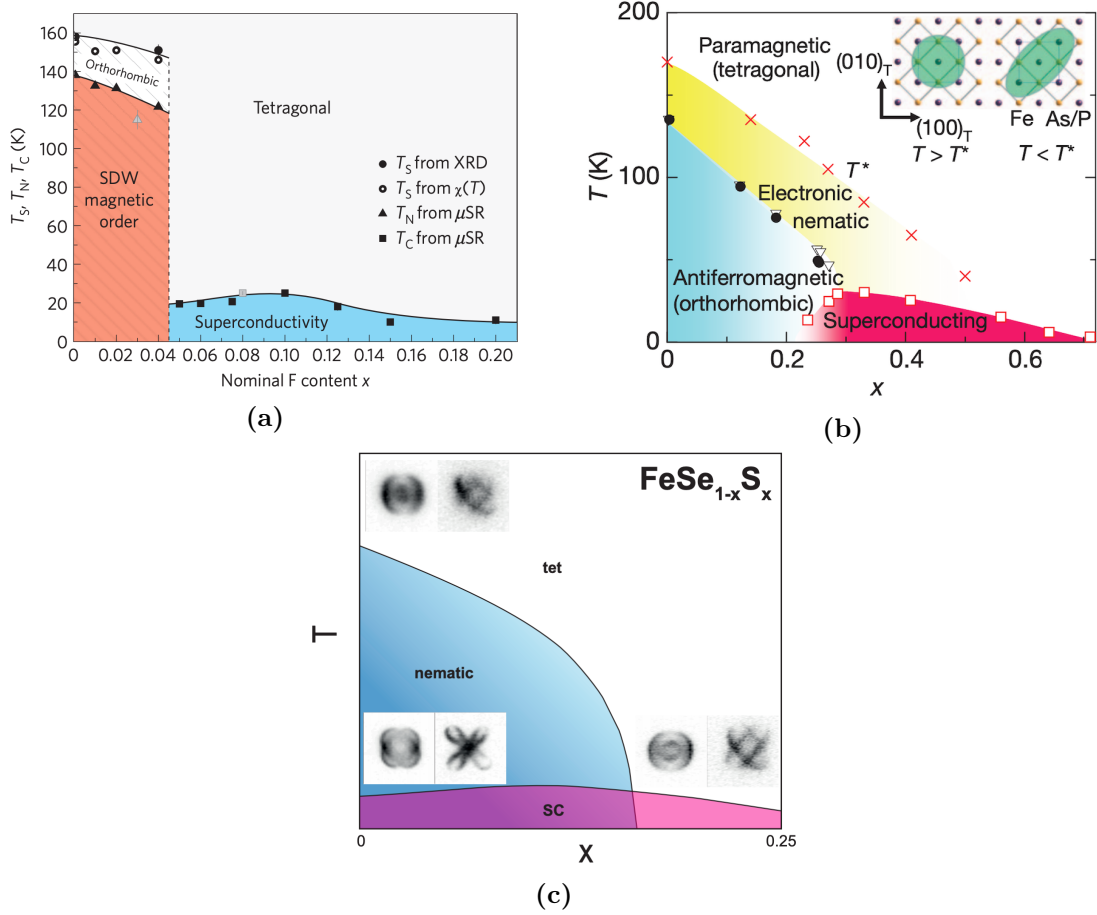


**Figure 1.2:** Phase diagrams for the  $x$ -doped systems (a) 1111  $\text{LaO}_{1-x}\text{F}_x\text{FeAs}$  [30], (b) 122  $\text{BaFe}_2(\text{As}_{1-x}\text{P}_x)_2$  [31] and (c) 11  $\text{FeSe}_{1-x}\text{S}_x$  [32].

the so-called nematic phase. This phase is characterized by a strong  $x/y$  anisotropy of the electronic properties of the system. The SDW and superconducting state are intimately related by either closely neighbouring (as in  $\text{LaOFeAs}$  and  $\text{CeFeAsO}$  systems), or interpenetrating to each other (as in  $\text{K}$ -doped  $\text{BaFe}_2\text{As}_2$ ). The normal phase from which superconductivity emerges at low-temperature is a metallic paramagnetic state characterized by strong correlations (bad metal). It is worth noticing that, even if IBS share similar crystal structures, their phenomenology can be very different as in the case of  $\text{FeSe}$  for which a nematic state, realized at  $T_S \sim 90\text{K}$ , evolves in a superconducting phase below  $T_c = 9\text{K}$  without the emergence of long-range magnetism.

We further discuss the instability and features of the ordered phases of IBS and the different phenomenology of  $\text{FeSe}$  vs 122 systems in Section 1.4.

### 1.3. Electronic Structure

Density Functional Theory (DFT) and local density (LDA) calculations [16–20] predicts a semimetallic behaviour for the parent compound with the density of states around the Fermi level dominated by the Fe–pnictogen (or chalcogen) planes. In undoped com-

pounds, Fe is in a  $(3d)^6$  valence state and the crystal field between the orbitals is much smaller than the bandwidth. This implies that all the  $d$ -orbitals participate to the formation of the low-energy electronic bands. Most IBS present two sets of disconnected Fermi surface sheets with two or three hole-pockets centered at the Brillouin zone center ( $\Gamma$ -point) and two electron-pockets near the zone boundary. Mainly three orbital,  $d_{xz}$ ,  $d_{yz}$ ,  $d_{xy}$ , participate to the formation of pocket at the Fermi level. Notice that because of the tetragonal symmetry the  $yz/xz$  orbitals are locally degenerate.

As mentioned above, while the Fe-ions sit on a planar two-dimensional square lattice, the pnictide/chalcogen ions are located alternatively above or below the Fe-plane. As a consequence the unit cell contains two inequivalent Fe positions. For many IBS, for the  $k_z = 0$  plane, there is a rigorous procedure of exact “unfolding” of bands to a reciprocal space corresponding to a single Fe atom per unit cell [34, 35]. In Figure 1.3 we show a sketch of the crystallographic unit cell contains the 1-Fe/2-Fe in real space (a) and the correspondent unfolded/folded Brillouin zone (b) for a generic IBS. One can discuss much of the essential physics in the 1-Fe unit cell in the unfolded Brillouin zone, this is the notation we use throughout this thesis unless mentioned otherwise.

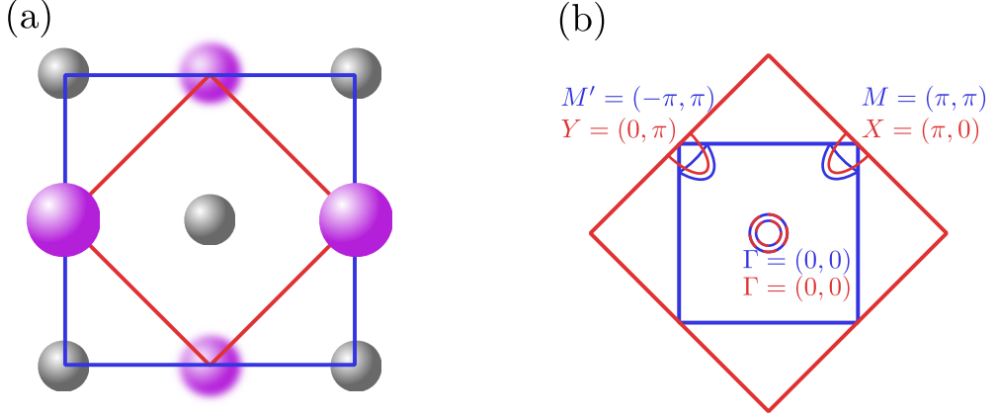


**Figure 1.3:** 1-Fe (red) and 2-Fe (blue) unit cells in (a) real and (b) momentum space. In (a), gray denotes Fe-atoms and purple denotes the pnictogen/chalcogen-atoms in staggered positions above and below the Fe-plane. In (b), the corresponding unit-cells in momentum space are shown with schematic Fermi surfaces overlaid. Adapted from [36].

From Figure 1.3 we can learn another important feature associated to the IBS Fermi surface: hole- and electron-pockets can be matched via a translation by momentum vector  $\mathbf{Q} = (\pi, 0)/(0, \pi)$ , which is the same wave-vector defining the periodicity of the IBS magnetic ordered state. This effect of *nesting* between matching Fermi surface can drives the system into certain particle-hole instabilities, e.g. the SDW.

The presence of multiple disconnected Fermi surfaces predicted by *ab initio* calculations has been widely confirmed by experiments. Well-defined Fermi surfaces having hole/electron character have been observed both in the parent compounds and doped IBS by quantum oscillations (QO) [37–44] and angle-resolved photoemission spectroscopy (ARPES) experiments [45–50] that also provide an experimental observation of the conditions of the  $\mathbf{Q} = (\pi, 0)/(0, \pi)$  nesting between hole and electron pockets [51–53]. The multi-orbital character of the Fermi surface has also been widely experimentally investigated e.g. using the polarization-sensitivity of the orbitals in ARPES to identify the orbital characters of band structure [21].



Although the qualitative agreement between *ab initio* calculations and experimental findings, two main discrepancies can be observed. First, by comparing *ab initio* bands with ARPES and QO measurements, a large band renormalization factor  $> 3$  can be estimated (see e.g. [42–44, 46, 54–56]), i.e. *ab initio* calculations consistently give bands that are more dispersive than the measured ones. This is a clear indication that electron-electron correlations are important in IBS, although their metallic behaviour [57, 58]. The second discrepancy is found at low-energy, i.e. around the Fermi level, where we find a substantial shrinking of the experimental Fermi pockets with respect to the ones predicted by LDA [37, 40, 41, 59]. Such a discrepancy is quite large in some cases as e.g. in FeSe, where of the two hole-pockets predicted by DFT at  $\Gamma$ , only one is experimentally found crossing the Fermi level [55, 60]. This effect has been theoretically analyzed in terms of self-energy renormalizations induced by repulsive interband spin-fluctuations [60–62] as we will discuss in Section 2.3.

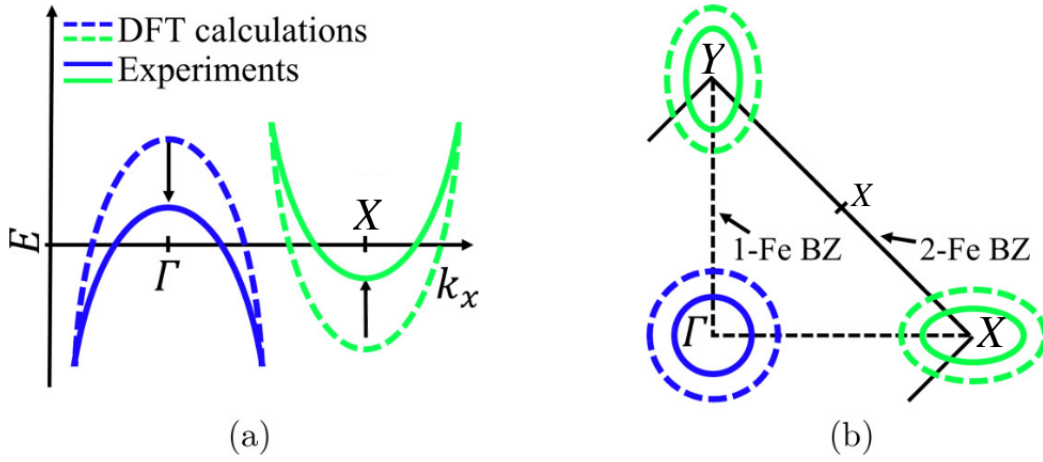


**Figure 1.4:** Schematic plot showing (a) band structure along  $k_x$  direction and (b) corresponding Fermi surface of a generic IBS in the 1-Fe BZ. The dashed lines represent DFT-predicted  $\Gamma$ -centered holes (blue) and  $X/Y$ -centered electron (green) bands. The solid lines represent the renormalized bands, as observed in dHvA and ARPES experiments, with energy shifts giving rise to a Fermi pocket shrinkage. Adapted from [62].

## 1.4. Instabilities and ordered phases

**Magnetism** The parent compounds of many IBS develop below  $T_N$  a metallic long-range SDW order, whose magnetic arrangement can vary depending on the material [11, 22, 63]. In many IBS the long-range order is a columnar SDW, with two interpenetrated Néel spin lattices such that antiferromagnetic stripes form along one direction which ferromagnetic stripes along the perpendicular direction. Notice that the columnar SDW ground state is actually doubly degenerated i.e. the  $\mathbf{Q} = (\pi, 0)$  magnetic order in which we have antiferromagnetic order in the  $x$ -direction and ferromagnetic in the  $y$ -direction of the Fe-Fe first neighbours direction is degenerate with the  $\mathbf{Q} = (0, \pi)$  in which the ferromagnetic/antiferromagnetic arrangement is realized along the perpendicular directions. Notice that this SDW is characterized by the same wave vector of the nesting match.

Two opposite view can be used as starting point of a theoretical description of magnetism in IBS: an itinerant view in which electrons are delocalized and a strong coupling one in which electrons are localized on the atomic lattice and can be consider as localized spins. The itinerant approach was supported by the metallicity of the parent compounds, the low magnetic moment, and the apparent nesting on the Fermi surface with a wave-vector. The strong coupling approach was motivated by the observed band renormalization, the bad metallicity and later by the discovery of families of IBS whose magnetic order could not be explained by Fermi surface nesting [22].

In what follows we will perform our theoretical analysis starting from an itinerant description of the electrons in which the effect of the band renormalization is taking into account phenomenologically to describe the IBS phase diagram.

**Superconductivity** Since the discovery of IBS, various experimental probes [45, 48, 64–68] indicate that quite different symmetries of the superconducting order parameter can be realized in IBS. Nowadays there is a general consensus, based on nuclear magnetic resonance (NMR) [68, 69] and inelastic neutron scattering (INS) [67] experiments, that in moderated doped IBS the gap symmetry is  $s_{\pm}$  (see Figure 1.5): a gap function which changes sign between electron and hole pockets but not necessarily within the same pocket. Notice that this implies that the electron/hole gap is s-wave but can present accidental nodes [34, 70].

In Figure 1.5 we show two other states that have also been proposed for at least some IBS: one is a conventional  $s$ -wave state where the gap function has the same sign over the whole Brillouin Zone ( $s_{++}$ ) [29]; the other is the  $d_{x^2-y^2}$ -wave [71], where the interpocket repulsion between two electron pockets become dominant over other interactions in the Brillouin Zone.

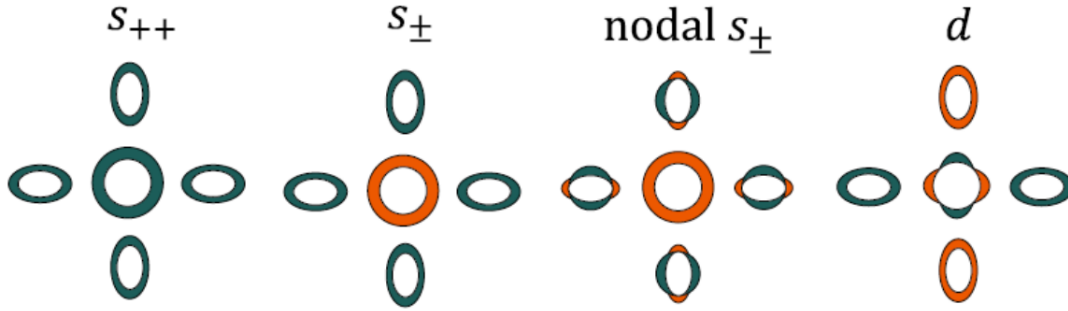


**Figure 1.5:** Different gap symmetry (s-wave and d-wave) and structure in IBS represented in the 1-Fe Brillouin zone. Different colors stands for different signs of the gap. Adapted from [34].

To determine the structure and symmetry of the superconducting order parameter is crucial to get information about the microscopic pairing interaction in IBS [72]. As already mention, IBS are unconventional superconductors since the calculated electron-phonon coupling can not account for the high values of  $T_c$  [73]. That leaves a nominally repulsive screened Coulomb interaction as the most likely source of the pairing. The excitations that pair electrons are now those of the electronic medium itself, either spin or charge fluctuations. Those, however, mediate pairing in different channels: a sign-preserving  $s_{++}$  s-wave state is expected from orbital-fluctuation mediated pairing [74, 75], whereas a  $s_{\pm}$  or a d-wave state is promoted by spin-fluctuation mediated pairing [19, 70, 76].



In this Thesis, we do not investigate different pairing channels. We assume spin-fluctuation mediating the pairing and analyze the relevance of the orbital-degree of freedom in determining the main features of the superconducting gap functions.

**Nematicity** The term nematic first appears in the context of isotropic liquid crystals as a phase characterized by a broken rotational symmetry and an unbroken translational symmetry [77, 78]. In crystalline solids, being in a lattice, the rotational and translational symmetries are always broken. In this context we use the term nematic to indicate a phase in which the point group symmetry of the lattice is reduced from tetragonal to orthorhombic, i.e. a phase characterized by a  $C_4 \rightarrow C_2$  breaking symmetry, whereas translational symmetry is preserved (for further details see Appendix A).

Nematic states have been reported in many IBS [11, 29, 79]. A structural transition from a high-temperature tetragonal phase to an orthorhombic one spontaneously breaks the discrete fourfold rotational symmetry of the lattice, making the  $x/y$  directions of the Fe-Fe plane non-equivalent. The nematic state, can be interpreted as a regular structural transition driven by the vibrations of the ions of the lattice [80] (see Figure 1.6a). However, several experimental probes highlight a much larger anisotropy in the electronic properties of the system than expected from the structural changes alone [81–83] (see Figure 1.6b).

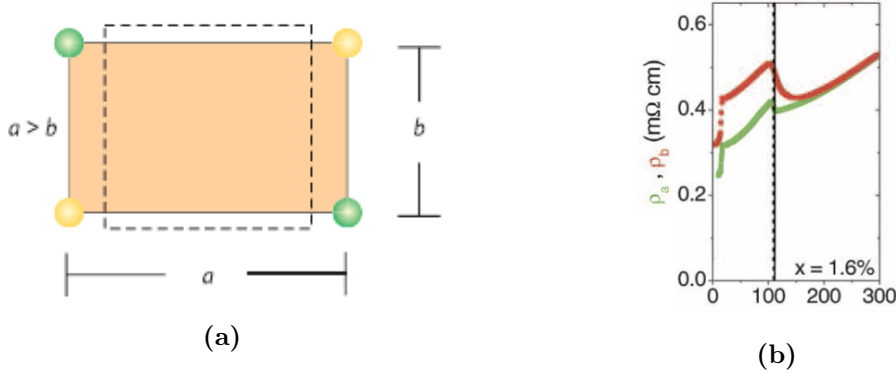


**Figure 1.6:** (a) Structural distortion from a tetragonal (dashed line) to an orthorhombic (solid line) unit cell. Adapted from [23]. (b) Temperature dependence of the in-plane resistivity of underdoped  $\text{Ba}(\text{Fe}_{1-x}\text{Co}_x)_2\text{As}_2$ ,  $x = 0.016$ . Solid and dashed vertical lines mark critical temperatures for the structural and magnetic phase transitions  $T_S$  and  $T_N$  respectively. The parallel ( $\rho_a$ ) and perpendicular ( $\rho_b$ ) components of the in-plane resistivity start to differentiate already before  $T_S$  and remain different until reach very low temperatures where they drop due to the superconducting transition. Adapted from [84].

This observation suggests an electronic origin of the nematic transition, however does not provide a clear indication about which electronic degree of freedom drives the transition [23]. Within a spin-fluctuation driven scenario, the nematic phase is a precursor effect of the SDW order that usually emerges at lower temperature by selecting an ordering wave vector along the  $x$  direction. In this scenario, the static spin susceptibility becomes different along the  $q_x$  and  $q_y$  directions of the Brillouin zone before the conventional SDW state develops. Within an orbital-fluctuation scenario, nematicity is driven by the charge unbalance created by a different occupation  $n_{xz}/n_{yz}$  of the  $xz/yz$  orbitals. As orbital and spin degrees of freedom are strongly entangled, it is not easy to discriminate their respective role. The fact that both those quantities, spin-fluctuations along  $x/y$  and  $xz/yz$

polarization, are anisotropic in the nematic phase leads to a typical ‘chicken and egg problem’.

In that respect, it is relevant to ask a more general question: should we expect to find the same mechanism driving the nematic instability in different materials, or should we invoke different fluctuation mechanisms? It could seem, in fact, hard to develop a unified picture that could account for the variety of the different realization of nematicity in different family of IBS. For example, in 122 the nematic instability is always found slightly above the magnetic transition, making the spin-driven mechanism the main candidate for explaining the origin of nematicity. On the other hand, the lack of magnetic order in FeSe and the orbital ordering measured by ARPES experiments [85, 86], seem to support model for nematicity as due to orbital ordering [87–93]. Another aspect that seems difficult to reconcile assuming nematicity driven by a common mechanism in IBS is the variety of anisotropy in the electronic properties found for different compounds. For example, if we analyze the dc resistivity anisotropy in the nematic phase of IBS we find that the anisotropy measured in 122 hole-doped systems [94] and FeSe [95] is opposite with respect to the one found in the electron-doped 122 [82].

In this Thesis we do not investigate the origin of the nematic phase. We adopt a spin-nematic view [23] and address the question whether it is possible to reconcile within a single theoretical framework the variety found in the realization of nematicity in different family of IBS.

## 1.5. Modeling iron-based superconductors within a spin-driven scenario

In this section we provide a compact overview of theoretical models used to describe the low-energy physics of IBS, highlighting the differences between orbital- and band-based modelings. The scope of this review is to point out the main advantages/disadvantages of multiorbital/multiband descriptions and introduce the Orbital Selective Spin-Fluctuations (OSSF) model used in this Thesis.

As already mentioned, in what follows we adopt an *itinerant view*. We use effective low-energy models that capture the electronic states near the Fermi level and their interactions, to describe the properties of the ordered phases appearing in the phase diagram. However, this weakly electron correlated view is not completely appropriated. In fact, extensive theoretical and experimental studies in IBS have highlighted the relevance of electron correlations driven by local interactions and there is now a general consensus that the bad metallic behavior of the normal state can be described in terms of the Hund’s metal physics [57, 58]. At the same time, the interplay between those electronic correlations and low-energy fluctuating modes is still poorly investigated. Recent analysis [96, 97] show that Hund’s driven correlations could potentially enhance the tendency of the system towards certain instabilities, e.g. superconductivity. Although extremely promising, the analysis of electronic correlations from local interactions and their effects at low-energy is beyond the scope of this Thesis. In what follows we adopt an effective approach in which the renormalization of the bands due to local interactions is already taken into account and projected into a low-energy effective interaction.

### 1.5.1. Multiband models

Within a spin-fluctuation driven scenario, all the instabilities observed in the phase diagram of IBS follows from the near nesting between hole-like and electron-like Fermi surfaces. Multiband models are band-basis low-energy model with phenomenologically-derived interactions between low-energy electronic states. They offer an appealing and simple framework to study magnetism, superconductivity and spin-nematic order. They ignore, however, the orbital content of the low-energy states, and as such they are generally blind to phenomena involving orbital physics. Multiband models has been extensively studied using a variety of methods involving different approximations e.g. mean-field, random phase approximation (RPA) calculations, Ginzburg-Landau analysis and renormalization group (RG) [25, 98–101].

In order to illustrate the strengths and weaknesses of this approach, we consider a minimal model with three-band, one hole band centered in  $\Gamma$ , and two electron bands centered in  $X$  and  $Y$ . The non-interacting Hamiltonian in the band basis reads

$$H_0^{band} = \sum_m \sum_{\mathbf{k}\sigma} \left( \epsilon_{\mathbf{k}}^m c_{m\mathbf{k}\sigma}^\dagger c_{m\mathbf{k}\sigma} \right) \quad (1.1)$$

where  $m = \Gamma, X, Y$  labels the hole/electron bands.  $c_{m\mathbf{k}\sigma}^\dagger$  is the fermionic operator that creates an electron in the band  $m$  with spin  $\sigma$  and momentum  $\mathbf{k}$ . The band dispersions,  $\epsilon_{\mathbf{k}}^m$ , are parametrized as simple tight-binding or parabolic dispersions, with no reference to their orbital content. The typical Fermi surface described by Eq. 1.1 is sketched in Figure 1.7a. Multiband models of interacting Hamiltonian containing all possible interactions between the low-energy electronic states can be studied via e.g. RG [98]. Here, we focus on interactions in the spin channel only and we explicitly consider the exchange of spin-fluctuations between nested Fermi surface i.e. with momenta near  $\mathbf{Q}_X = (\pi, 0)$  and  $\mathbf{Q}_Y = (0, \pi)$

$$H_{int}^{band} = -\frac{1}{2} u_{spin} \sum_{\mathbf{q}} \left( \vec{S}_{\mathbf{q}}^X \cdot \vec{S}_{-\mathbf{q}}^X + \vec{S}_{\mathbf{q}}^Y \cdot \vec{S}_{-\mathbf{q}}^Y \right) \quad (1.2)$$

$$\text{with} \quad \vec{S}_{\mathbf{q}}^{X/Y} = \sum_{\mathbf{k}ss'} \left( c_{\mathbf{k}s}^\dagger \vec{\sigma}_{ss'} c_{\mathbf{k}+\mathbf{q}s'}^{X/Y} \right) \quad (1.3)$$

Here  $u_{spin}$  is the coupling constant,  $\sigma_{ss'}$  the Pauli matrices and  $\vec{S}_{\mathbf{q}}^{X/Y}$  is the interband spin operator that describes the spin exchange between the hole pocket at  $\Gamma$  and the electron pocket at  $X/Y$ . The consequences of nesting can be illustrated already considering the bare static spin-susceptibility,  $\chi_{X/Y}(\mathbf{q}) = \langle \vec{S}_{\mathbf{q}}^{X/Y} \vec{S}_{\mathbf{q}}^{X/Y} \rangle$ , associated to the spin-exchange at  $\mathbf{Q}_{X/Y}$ . This can be rewritten as

$$\chi_{X/Y}(\mathbf{q}) = \sum_{\mathbf{k}} \frac{f(\epsilon_{\mathbf{k}+\mathbf{q}}^{X/Y}) - f(\epsilon_{\mathbf{k}}^\Gamma)}{\epsilon_{\mathbf{k}+\mathbf{q}}^{X/Y} - \epsilon_{\mathbf{k}}^\Gamma} \quad (1.4)$$

where  $f(\epsilon_{\mathbf{k}}^m)$  are the Fermi distribution function for the  $m$ -band and  $\mathbf{q}$  indicates the small momentum around  $\mathbf{Q}_{X/Y}$ . In the presence of nesting between the bands, i.e.  $\epsilon_{\mathbf{k}}^\Gamma = -\epsilon_{\mathbf{k}}^{X/Y}$ , the  $\chi_{X/Y}(\mathbf{q} = 0)$  diverges logarithmically. Notice that the susceptibility develops initially two equivalent peaks at  $\mathbf{Q}_{X/Y}$  (see Figure 1.7b) with the system eventually ordering along one of the two stripe magnetic ordering vectors below the Néel temperature  $T_N$  (not shown).

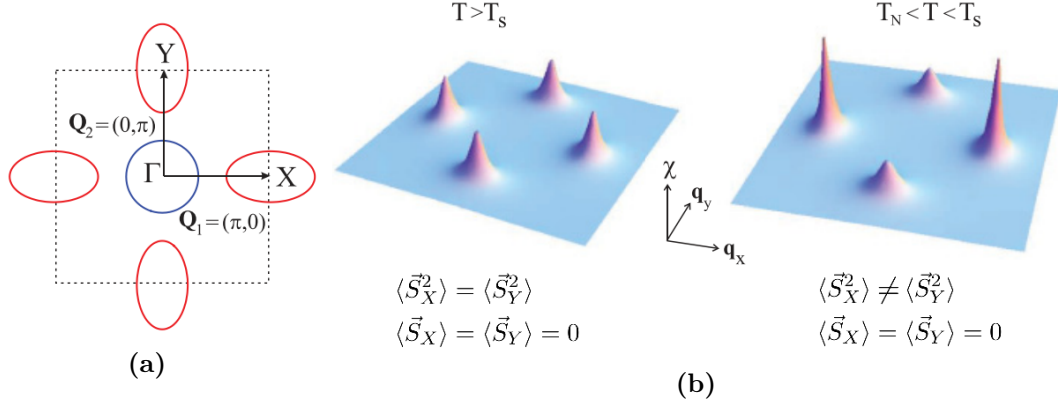


**Figure 1.7:** (a) Fermi surface for three-band model with a circular hole pocket at  $\Gamma$  and two elliptical electron pockets at  $X$  and  $Y$  connected by the vectors  $\mathbf{Q}_X = (\pi, 0)$  and  $\mathbf{Q}_Y = (0, \pi)$ . (b) Static magnetic susceptibility  $\chi(\mathbf{q})$  across the Brillouin zone lowering the temperature from above to below the structural transition temperature  $T_S$ . Adapted from [28].

Moving away from perfect nesting the divergence of  $\chi_{X/Y}(\mathbf{q} = 0)$ , Eq. 1.4, is not realized i.e. the magnetic instability is suppressed, however the exchange of magnetic excitation between the hole and electron pockets can mediate an effective pairing interaction at low-energy [19, 20, 98]. The BCS equation in this case reads

$$\Delta_{\mathbf{k}} = - \sum_{\mathbf{k}'} \frac{V_{eff}(\mathbf{k} - \mathbf{k}')}{2E_{\mathbf{k}'}} \Delta_{\mathbf{k}'} \quad (1.5)$$

where  $\mathbf{k}' - \mathbf{k}$  is the transferred momentum and  $V_{eff}$  the effective pairing interaction. Given the repulsive and interband character of the spin interaction mediating the pairing we can assume  $V_{eff}(\mathbf{k} - \mathbf{k}')$  to be a constant for  $\mathbf{k}' - \mathbf{k} \sim \mathbf{Q}_{X/Y}$  and vanish at other momentum, i.e.  $V_{eff}(\mathbf{Q}_{X/Y}) = V > 0$ . As a consequence we get a set of coupled BCS equations for the gap functions of the different pocket. As one can see from Eq. 1.5 a gap function having a preserving sign s-wave symmetry is not a solution. However, if the gap function changes sign between the nested hole and electron Fermi surfaces,  $\Delta^\Gamma = -\Delta^X$ , as in a  $s_\pm$  or  $d$ -wave symmetry, then a solution is allowed.

The three-band model also offers a suitable platform to study the onset of nematic order [23, 28]. Within this approach, nematicity is a precursor effect of the stripe magnetic order. The idea is illustrated schematically in Figure 1.7b. At high temperatures, above the structural transition  $T_S$ , spin-fluctuations near the two stripe magnetic ordering vectors  $\mathbf{Q}_{X/Y}$  are equally strong  $\langle \vec{S}_X^2 \rangle = \langle \vec{S}_Y^2 \rangle$  and the system has tetragonal symmetry  $C_4$ . Below  $T_S$  the system spontaneously selects one direction along which fluctuation becomes stronger lowering the symmetry from  $C_4$  to  $C_2$ . This means that  $\langle \vec{S}_X^2 \rangle \neq \langle \vec{S}_Y^2 \rangle$  before the long-range stripe order is established below  $T_N$ . In that respect the nematic instability is described in terms of a spontaneous symmetry breaking in which a nematic order parameter,  $\phi = \vec{S}_X^2 - \vec{S}_Y^2$ , acquires a final mean-field value across the nematic transition temperature, defined by the divergence of the nematic susceptibility (see also discussion in Appendix A). We will revise in more details the emergence of nematicity within the three-band model in Section 2.1.

A similar multiband model has been used to explain the phenomenon of the Fermi pocket shrinkage, illustrated in Figure 1.4 in Section 1.3. This effect is explained, in [61],

in terms of renormalization effects induced by repulsive interband interactions. These effects are computed within an Eliashberg framework via a self-energy function for each band. Due to the multiband character of the electronic structure and the strong particle-hole asymmetry of the IBS bands the real part of the self-energy is finite and renormalize the low-energy bands leading to the shrinking of the Fermi Surface. We will revise the derivation of [61] in Section 2.3.

Working in the band-basis representation simplifies substantially the modeling of IBS. As we summarize above, minimal three-band models can successfully reproduce a number of experimental features of IBS e.g. emergence of stripe magnetism,  $s_{\pm}$  superconductivity, nematicity as precursor of magnetism and Fermi pocket shrinkage. However, this description does not include information about the orbital composition of the low-energy bands, thus within a multiband modeling we cannot study phenomena involving orbital physics nor spin-orbital interplay.

A first consequence of the lack of spin-orbital interplay in multiband approach is the difficulty to reproduce the angular modulation of the superconducting gap functions. As already discussed in Section 1.4, in fact, the gap functions in IBS can present different structures (with or without accidental nodes) depending on the specific compound, despite the  $s_{\pm}$  symmetry. Using a multiband description the exchange of spin-fluctuations is homogeneous along the Fermi surfaces at perfect nesting and any angular dependence follows from a deviation from that condition, such modulations are however quite small and cannot reproduce the experimental findings. This was early noticed already in 2009, e.g. in [102], where it is discussed as the orbital make-up of the states on the Fermi surface together with the momentum dependence of the fluctuation-exchange pairing interaction play a key roles in favouring an anisotropic gap.

Another consequence of the lack of orbital information within a multiband approach is that band nesting is the only model parameter controlling the phenomenology of the system. Thus, we cannot explain how systems with similar band structure can present a very different realization of nematicity. For example, FeSe presents a single hole-pocket at  $\Gamma$  nested with electron  $X/Y$ -pockets. A similar situation is realized in underdoped 122 compounds where, although two hole bands cross the Fermi Level, only the inner hole-band presents a good nesting with the electron pockets. Despite the similarity of the electronic structure the nematic instability is realized slightly above the magnetic transition in 122, while a much stronger nematicity without magnetism is found in FeSe. Another example is the variety of dc-resistivity anisotropy found in the nematic phase of IBS that can have different signs and magnitude depending on the compound under study.

In the next Chapters we show that the inclusion of the orbital degrees of freedom within a low-energy modeling is the key solve those discrepancies. In particular, in Chapter 2 we review the results discussed in [27] that demonstrates that the inclusion of the orbital information allows us to discriminate between similar band structures and that different phenomenology is expected based on the orbital composition of the nested bands. In Chapter 3 we show that, once the orbital physics is taken into account, the orbital composition of the nested Fermi surface introduces an additional angular modulation in the spin-fluctuations and as a consequence in the various observable e.g. superconducting gaps. In Chapter 4 we study, instead, the anisotropy of the dc resistivity in the nematic phase of IBS [103] and show that the spin-nematic scenario driven by orbital-selective spin-fluctuations can reconcile the experimental observations reported in different families of IBS within a single picture due to the orbital-spin interplay encoded in the model.

### 1.5.2. Multiorbital Hubbard models

As discussed in Section 1.3, DFT calculations find the density of states of IBS dominated by the Fe- $d$  orbitals. States due to the pnictogen/chalcogen orbitals are located at much higher energy (approximately 2eV) below the Fermi level. Nonetheless, the pnictogen/chalcogen orbitals allow for hybridization with the Fe- $d$  states, therefore, an effective Fe-Fe hopping Hamiltonian on a square lattice defined by the Fe-sites can be constructed, provided the symmetries of the entire Fe-pnictogen/chalcogen layer are respected.

The observation that mainly three of the five Fe- $d$  orbitals ( $xz$ ,  $yz$ ,  $xy$ ) contribute to the Fermi surface, motivated early two/three-orbital tight-binding models [104–106]. However, it was soon realized the minimal tight-binding model that respect all the symmetries of the Fe-pnictogen/chalcogen plane and correctly reproduce the geometry of the Fermi surface requires to include all the five Fe- $3d$  orbitals [25, 76, 107, 108]. In Figure 1.8 we show the bands for the tight-binding model for iron-pnictides proposed in [109]. The electron pockets at  $X/Y$  formed by  $xy$  and  $yz/xz$  orbitals and the two hole-pockets at  $\Gamma$  given by an opposite arrangement of the  $yz/xz$  orbital. Notice that the third hole  $xy$ -pocket at the  $M$ -point is parameter sensitive (i.e. not common to all IBS families).

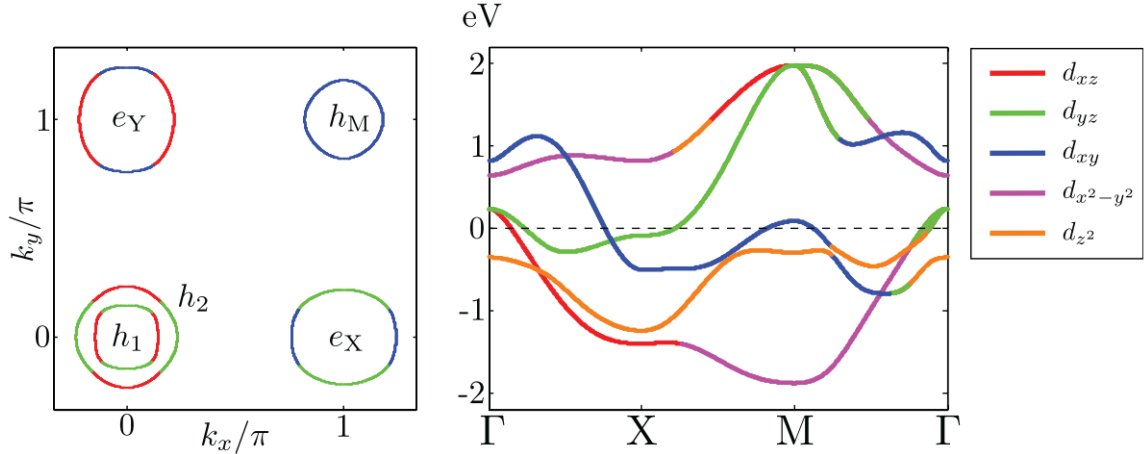


**Figure 1.8:** Five-orbital tight-binding model for iron-pnictides from [109]. Fermi surface in the 1-Fe BZ (left panel) and bands dispersion (right panel). The bands are colored according to the orbital that contributes the largest spectral weight. Adapted from [25].

The non-interacting tight-binding Hamiltonian reads

$$H_0^{orb} = \sum_{ij\sigma} \sum_{\eta\eta'} t_{ij}^{\eta\eta'} d_{\eta i\sigma}^\dagger d_{\eta' j\sigma} + \sum_{i\sigma} \sum_{\eta} \epsilon_{\eta} n_{\eta i\sigma}. \quad (1.6)$$

$\eta, \eta' = \{1, 2, 3, 4, 5\}$  are orbital indices for the Fe- $d$  orbitals ( $d_{xz}, d_{yz}, d_{xy}, d_{x^2-y^2}, d_{3z^2-r^2}$ ),  $t_{ij}^{\eta\eta'}$  are the tight-binding hopping parameters from the  $\eta$  orbital on site  $i$  to the  $\eta'$  orbital on site  $j$ ,  $\epsilon_{\eta}$  the on-site energy of the  $\eta$  orbital and  $n_{\eta i\sigma} = d_{\eta i\sigma}^\dagger d_{\eta i\sigma}$  the occupation number with  $d_{\eta i\sigma}^\dagger$  is the fermionic creation. By diagonalizing Eq. 1.6 we obtain the quasiparticle dispersions (as shown in Figure 1.8). The orbital spectral weights are defined by the matrix elements  $a_m^\eta(\mathbf{k}) = m\mathbf{k}|\eta$  associated with the rotation from the orbital to the band space.



In first approximation, the electron-electron interactions are assumed to be heavily screened and therefore can be approximated as local. The interacting Hamiltonian for multiorbital models reads

$$H_{int}^{orb} = \sum_{i\eta} \left( n_{\eta i \uparrow} n_{\eta i \downarrow} + U' \sum_{i\sigma, \eta' < \eta} n_{\eta i \sigma} n_{\eta' i \sigma} - J \sum_{i, \eta' \neq \eta} \vec{S}_{\eta i} \cdot \vec{S}_{\eta' i} + J' \sum_{i, \eta' \neq \eta} \left( d_{\eta i \uparrow}^\dagger d_{\eta i \downarrow}^\dagger d_{\eta' i \downarrow} d_{\eta' i \uparrow} \right. \right. \quad (1.7)$$

and can be generated using a Hubbard-type approach [110–112]. Here,  $\vec{S}_{\eta i} = \frac{1}{2} d_{\eta i \sigma}^\dagger \vec{\sigma}_{\sigma \sigma'} d_{\eta i \sigma'}$  is the intraorbital spin operator in the orbital basis,  $U$  is the Hubbard repulsion between electrons on the same orbitals,  $U'$  is the onsite repulsion between electrons on different orbitals,  $J$  is the Hund's exchange that tends to align spins at different orbitals and  $J'$  another exchange term usually called a pair-hopping term. Notice that interactions are assumed to be independent on orbitals. The number of independent parameters can be further reduced assuming  $J' = J$  and  $U' = U - 2J$  the last condition is exact in the case of spin-rotational invariance [113].

Multiorbital models described by Eqs. 1.6 and 1.7 have been extensively studied using different methods. In what follows we focus on the results provided by RPA. For magnetism, such analysis revealed magnetic instabilities towards a SDW order with momenta  $\mathbf{Q}_X$  or  $\mathbf{Q}_Y$ , as well as a subleading instability towards a Neel order with  $\mathbf{Q}_M = (\pi, \pi)$  order [76, 114, 115]. Assuming that the pairing interaction responsible for the occurrence of superconductivity in IBS arises from the exchange of spin and charge fluctuations, the pairing vertex can be computed using the fluctuation exchange approximation [116]. Within the range of parameters typical of underdoped IBS, RPA studies find an anisotropic sign-changing  $s$ -wave state and a nearly degenerate  $d_{x^2-y^2}$  [76]. The orbital information included in the model and the momentum dependence of the spin-interactions lead to an anisotropic solution for the gap even in the  $s$ -wave case [34, 102]. In Section 3.2 we review the main steps of the RPA analysis and the results for magnetism and superconductivity within a five-orbital model.

The main issue with microscopic multiorbital descriptions is that they do not distinguish high-energy and low-energy states, which makes it difficult to implement methods beyond RPA [25]. This is particularly important if we want to study the nematic phase, in fact, in contrast to usual electronic instabilities, such as magnetic and charge order, this fluctuation-driven phenomenon cannot be captured by the standard RPA method and requires the inclusion of fluctuations beyond RPA in the multiorbital interacting model.

An early attempt to describe nematicity within a multiorbital description has been proposed in [26]. Here one starts from a multiorbital interacting Hamiltonian of Eq. 1.7 and, after projecting it at low energy, i.e. considering only electronic states around the high-symmetry points, derives the effective action in term of the  $\mathbf{Q}_{X/Y}$  spin-excitations up to the quartic order. This allows the analysis of the spin-mediated nematicity retaining the information of the orbital degree of freedom. This study analyzed for the first time the role of the orbitals in the nematic instability driven by spin-excitations and found out a number of outcomes of the model that are qualitatively different with respect to the results obtained within a band-basis description. It was shown, for example, how the orbital symmetry of the bands connected by spin-fluctuations affects the attractive/repulsive character of the nematic coupling and how the orbital-weights of the low-energy states affects the momentum dependence of the spin-fluctuations peaked at  $\mathbf{Q}_X/\mathbf{Q}_Y$ . Moreover, this analysis provided a theoretical frame to study the spin-orbital interplay showing explicitly how the

anisotropy of the spin-fluctuations reflects in the break of the  $xz/yz$  symmetry in the charge-orbital sector.

Such analysis, however, is remarkably complex given the number of orbitals involved. The nematic order parameter is now a matrix in the orbital space,

$$\phi_{\mu\nu} = S_X^\mu S_X^\nu - S_Y^\mu S_Y^\nu \quad (1.8)$$

and, as a consequence, the nematic susceptibility is a tensor  $\chi^{\mu\nu\rho\eta} \propto \langle \phi_{\mu\nu} \phi_{\rho\eta} \rangle$ . The same definition of the nematic order parameter and susceptibility is found in [117], where, following the same strategy of [26], the free energy up to the quartic order for the orbital-dependent spin-fluctuations is derived and the orbital components of the nematic susceptibility tensor are numerically studied.

### 1.5.3. Orbital selective nature of the spin excitations

A way to deal with the complexity given by the multiorbital description is to reduce the number of orbitals included in the calculation. For example, one can start from the five-orbital Hamiltonian of Eq. 1.6 and restrict the analysis to the subspace of the two or three orbitals that dominate the low-energy states near the high-symmetry points. By diagonalizing the quadratic Hamiltonian, one obtains the dispersion of low-energy states in the band basis in terms of the original tight-binding parameters of the multiorbital model. The low-energy fermionic operator defined via the diagonalization are used to build up the orbital-dependent spin-excitations connecting the hole and electron bands. This idea has been implemented in [26], in which the analysis is restricted to the  $xz - yz$  orbital subsector. This approximation made possible analytical calculations and highlighted a crucial feature of the spin-nematic model in the orbital basis. In fact, by projecting the microscopic interaction of Eq. 1.7 on the low-energy state of  $xz - yz$  orbitals only, one finds that spin fluctuations at different  $\mathbf{Q}$ -vectors become orbital selective, i.e. they involve only a specific orbital.

The drawback of this procedure is that one builds up the spin-excitations using the low-energy states obtained from the truncated tight-binding model. These do not respect all the symmetries of the system and can actually differ from the actual low-energy dispersions, e.g. extracted from ARPES experiments, due to interaction-driven renormalizations not accounted within this procedure. To overcome these limitations we need to project the interacting Hamiltonian into a symmetry adapted low-energy model as the one derived [118] exploiting the symmetry properties of the Fe-layer and constructing a minimal model using the Luttinger's method of invariants. This strategy has been implemented in Ref. [27] and led to the definition of the Orbital Selective Spin-Fluctuations (OSSF) model used in this Thesis.

In [27] the low-energy effective description derived in [118] has been used as the starting Hamiltonian for the derivation of the spin-nematic action in the orbital-basis. By projecting the general microscopic interaction of Eq. 1.7 on the low-energy multiorbital model of [118] one derives an effective spin-nematic action that respects all the symmetry of the systems while retaining the orbital information of the low-energy excitations using only three orbitals. This description not only reproduces the orbital-selective nature of the spin-fluctuation already found in [26], but also leads to a new definition of the nematic order parameter

$$\phi = S_X^{yz} S_X^{yz} - S_Y^{xz} S_Y^{xz} \quad (1.9)$$



that is now a scalar and formally equivalent to the nematic order parameter defined in the band basis. Notice that the tensorial form of the nematic order parameter, Eq. 1.8 defined in [26, 117] does not contain this result, which in turn is dictated by the only possible nematic contribution to the quartic order action of the model.

We will discuss more the nature of the nematic order parameter defined within the OSSF model in Chapter 2 where we derive and discuss the OSSF model reviewing the results of [27, 60]. In Chapter 3, instead, we will focus on the analysis of the spin-excitations of the OSSF model and on the superconductivity mediated by orbital selective spin-fluctuations within RPA and compare our results to analogous calculations performed within microscopic five-orbital models. We will show that the orbital selectivity, encoded in the OSSF model, simplified substantially the analysis, allowing for analytical treatments while retaining the main features of the spin-excitations computed using five-orbital models.

The body of work collected in Chapter 2 and Chapter 3 aims to provide both a complete description of the OSSF model and an extensive comparison of the model with multiorbital and multiband descriptions. We will show that the OSSF offers a theoretical frame in which the simplicity of multiband models merges with the orbital information characteristic of multiorbital descriptions and it allows us to gain a deeper understanding of the IBS physics.

# 2

## Orbital Selective Spin Fluctuation (OSSF) Model

In this Chapter we provide a general description of the OSSF model. First, we review the main steps of the derivation of the spin-nematic model in the band-basis [28]. We then analyze how the phenomenology of the model changes once the orbital degree of freedom is taken into account [26] and introduce the Orbital Selective Spin-Fluctuations (OSSF) model [27]. Finally, we discuss the self-energy corrections due to spin-fluctuations both in the paramagnetic and nematic phase of IBS. Also in this case, we start by briefly reviewing the derivation obtained in the band-basis and summarizing the results of [61], in which the idea of shrinking of the Fermi pockets as due to self-energy effects was originally proposed. We then derive the self-energy corrections within the OSSF model and discuss the orbital-selective shrinking of the Fermi Surface analyzed in [60]. The self-energy corrections from OSSF will be used in Chapter 4 as input for the calculation of the anisotropy of the dc-conductivity in the nematic phase of IBS.

### 2.1. Spin-nematic model in the band-basis

As we discussed in Section 1.5.1, within a multiband description, the three-band model provides the minimal low-energy model to explain the emergence of striped magnetism,  $s_{\pm}$  superconductivity and nematicity within a spin-driven scenario. In this context, the nematic state is a precursor of magnetism that is realized when the system spontaneously breaks the  $Z_2$ -symmetry of the lattice, while still preserving the  $O(3)$  spin-rotational symmetry (see also Appendix A). This idea has been originally discussed in [28] in which the low-energy effective action for the collective magnetic excitations has been derived. In what follows we review the main steps of this analysis.

The derivation of the effective action in terms of the spin fluctuations requires the standard implementation of the Hubbard-Stratonovich (H-S) method [119]. Starting from a microscopic generic Hamiltonian  $\hat{H}[c_i(\tau)]$ , the microscopic action is defined as

$$S[c_i(\tau)] = \int_0^\beta d\tau c_i^\dagger(\tau) [\partial_\tau - \mu] c_i(\tau) + \hat{H}[c_i(\tau)] \quad (2.1)$$

with  $\tau$  the imaginary time and  $\beta = 1/T$ . The partition function of the system can be computed as the integral over Grassmann variables as

$$Z = \int \mathcal{D}c e^{-S[c_i(\tau)]} \quad (2.2)$$

The H-S transformation allows us to decouple the interacting term of  $S[c_i(\tau)]$ , i.e. the quartic term in the fermionic operators, by using the functional identity

$$e^{\frac{ax^2}{2}} = \int \mathcal{D}y e^{(-\frac{y^2}{2a} + yx)} \quad a > 0. \quad (2.3)$$

with  $y$  an auxiliary variable, i.e. the H-S field associated to the bilinear fermionic operator  $x$ . After performing the H-S transformation, the action becomes quadratic with respect to the fermionic operators, so that we can integrate out the fermions from Eq. 2.2. The results of this operation is recast back into the exponent, and the partition function is expressed in terms of the effective action  $S_{eff}[y]$

$$Z = \int \mathcal{D}y e^{-S_{eff}[y]}. \quad (2.4)$$

We now apply this machinery to the low-energy three-band model discussed in Section 1.5.1. We report here for simplicity the model Hamiltonian  $H^{band} = H_0^{band} + H_{int}^{band}$  given in Eqs. 1.1 - 1.2

$$H^{band} = \sum_m \sum_{\mathbf{k}\sigma} \left( \epsilon_{\mathbf{k}}^m c_{m\mathbf{k}\sigma}^\dagger c_{m\mathbf{k}\sigma} - \frac{1}{2} u_{spin} \sum_{\mathbf{q}} \left( \vec{S}_{\mathbf{q}}^X \cdot \vec{S}_{-\mathbf{q}}^X + \vec{S}_{\mathbf{q}}^Y \cdot \vec{S}_{-\mathbf{q}}^Y \right) \right) \quad (2.5)$$

with  $m = \Gamma, X, Y$ ,  $\epsilon_{\mathbf{k}}^m$  the band dispersions,  $u_{spin}$  the coupling constant and  $\vec{S}_{\mathbf{q}}^{X/Y} = \sum_{\mathbf{k}ss'} c_{\mathbf{k}s}^\dagger \vec{\sigma}_{ss'} c_{\mathbf{k}+\mathbf{q}s'}$  the interband electronic spin operator that describes the spin-exchange between hole and electron pockets connected by  $\mathbf{Q}_X = (\pi, 0)$  and  $\mathbf{Q}_Y = (0, \pi)$ . We introduce the six-dimensional destruction (creation) operator  $\Psi_{\mathbf{k}}^{(\dagger)}$

$$\Psi_{\mathbf{k}}^\dagger = (c_{\mathbf{k}\uparrow}^\dagger, c_{\mathbf{k}\downarrow}^\dagger, c_{\mathbf{k}\uparrow}^\dagger, c_{\mathbf{k}\downarrow}^\dagger, c_{\mathbf{k}\uparrow}^\dagger, c_{\mathbf{k}\downarrow}^\dagger) \quad (2.6)$$

and the auxiliary bosonic fields  $\vec{M}_{X/Y}(\mathbf{q})$  coupled to  $\vec{S}_{\mathbf{q}}^{X/Y}$ .  $\vec{M}_X$  and  $\vec{M}_Y$  are the H-S fields and play the role of the magnetic order parameters in the Landau functional. Applying the H-S transformation, Eq. 2.3, the partition function reads

$$Z = \int \mathcal{D}M_X \mathcal{D}M_Y \mathcal{D}\Psi e^{-S^{band}[\Psi, M_X, M_Y]} \quad (2.7)$$

with

$$S^{band}[\Psi, \vec{M}_X, \vec{M}_Y] = \frac{2}{u_{spin}} \int_q (M_X^2(q) + M_Y^2(q)) + \iint_{\mathbf{k}, \mathbf{k}'} \Psi_{\mathbf{k}}^\dagger \hat{\mathcal{A}}_{\mathbf{k}\mathbf{k}'} \Psi_{\mathbf{k}'}. \quad (2.8)$$

We use here  $k - k' = q$ , with  $k = (\omega_n, \mathbf{k})$ ,  $q = (\Omega_m, \mathbf{q})$ .  $\omega_n$  and  $\Omega_m$  are the fermionic and bosonic Matsubara frequencies respectively. The  $\hat{\mathcal{A}}_{\mathbf{k}\mathbf{k}'}$  matrix is composed by the blocks

$$\hat{\mathcal{A}}_{\mathbf{k}, \mathbf{k}'}|_{mm} = -\hat{G}_{m\mathbf{k}\mathbf{k}'}^{-1} \delta_{\mathbf{k}\mathbf{k}'} \quad (2.9)$$

$$\hat{\mathcal{A}}_{\mathbf{k}, \mathbf{k}'}|_{\Gamma X/Y} = -\hat{M}_{X/Y}(q) \quad (2.10)$$

where we use a compact notation for the spin sector defining  $\hat{G}_{m\mathbf{k}} = G_{m\mathbf{k}} \hat{\mathbb{I}}$  and  $\hat{M}_{X/Y} = \vec{M}_{X/Y} \cdot \vec{\sigma}$ . Here  $G_{m\mathbf{k}} = (i\omega_n - \xi_{\mathbf{k}}^m)^{-1}$  is the non-interacting single-particle Green's function,  $\xi_{\mathbf{k}}^m = \epsilon_{\mathbf{k}}^m - \mu$ ,  $\hat{\mathbb{I}}$  and  $\sigma_i$  are the identity and the Pauli matrices in the spin-space.

By integrating out the fermions from Eq. 2.7 we obtain the effective action in terms of the H-S fields only

$$S_{eff}^{band}[\vec{M}_X, \vec{M}_Y] = \frac{2}{u_{spin}} \int_q \left( M_X^2(q) + M_Y^2(q) \right) + \text{Tr} \ln \left( \hat{\mathcal{A}}_{kk'} \right) \left( \quad \right) \quad (2.11)$$

where the integral and the trace act over momentum, frequency, and spin indices. It is convenient to decompose the second term of Eq. 2.11 by separating in Eqs. 2.9-2.10 the part with the explicit structure of  $\delta_{kk'}$  from the rest  $\hat{\mathcal{A}}_{kk'} = -\hat{\mathcal{G}}_0^{-1} + \hat{\mathcal{M}}_{kk'}$ . This separation allows us to rewrite in our action

$$\text{Tr} \ln \mathcal{A}_{kk'} = \text{Tr} \ln \hat{\mathcal{G}}_0^{-1} + \text{Tr} \ln \left[ \hat{1} - \hat{\mathcal{G}}_0 \hat{\mathcal{M}} \right] \left( \quad \right) \quad (2.12)$$

Now we separate the H-S fields  $M_{X/Y}(q) = M_{X/Y}(0) + \delta M_{X/Y}(q)$  in its homogeneous and constant part and its fluctuating part. By minimizing the action with respect to  $M_{X/Y}(0)$  we obtain the mean-field equations of the magnetic problem that admit two degenerate non trivial solutions with finite magnetization,  $\langle M_{X/Y} \rangle$ , below a critical temperature,  $T_N$ . We are interested in the analysis of the nematic phase, thus we have to study the fluctuations of the spin-fields in the paramagnetic phase above  $T_N$ , i.e. for  $\langle M_{X/Y} \rangle = 0$ . To do that we need to expand the effective action, Eq. 2.11, up to quartic order in  $\delta M_{X/Y}$ . It is easy to verify that

$$\text{Tr} \ln \left[ \hat{1} - \hat{\mathcal{G}}_0 \hat{\mathcal{M}} \right] = \sum_n \frac{1}{n} \text{Tr} (\hat{\mathcal{G}}_0 \hat{\mathcal{M}})^n$$

By using the above expansion up to  $n = 4$  and performing the traces, we are left with

$$S_{eff}^{band}[\vec{M}_X, \vec{M}_Y] = \sum_{i=X,Y} \chi_{0,i}^{-1} M_i^2 + \sum_{i,j=X,Y} \left( u_{ij} M_i^2 M_j^2 \right) \quad (2.13)$$

where the Gaussian propagator  $\chi_{0,i}^{-1}$  and the quartic coefficients  $u_{ij}$  are defined as

$$\chi_{0,i}^{-1} = \frac{2}{u_{spin}} + 2 \int_k G_{\Gamma k} G_{i,k}, \quad u_{ij} = \int_k G_{\Gamma k}^2 G_{i,k} G_{j,k}. \quad (2.14)$$

and we simplified a bit the notation using  $\delta M_{X/Y} \rightarrow M_{X/Y}$ , dropping the  $k, q$  dependencies of the variables and focusing only on the  $q = 0$  contributions. The multiband model is invariant under  $\pi/2$ -rotation so that  $\chi_{0,X}^{-1} = \chi_{0,Y}^{-1} = \chi_0^{-1}$  and  $u_{XX} = u_{YY}$ . We diagonalize the quartic term of the action and rewrite Eq. 2.13 as

$$S_{eff}^{band}[\vec{M}_X, \vec{M}_Y] = \chi_0^{-1} (M_X^2 + M_Y^2) + \frac{\lambda_\psi}{2} (M_X^2 + M_Y^2)^2 + \frac{\lambda_\phi}{2} (M_X^2 - M_Y^2)^2 \quad (2.15)$$

where we defined  $\lambda_\psi = u_{XX} + u_{XY}$  and  $\lambda_\phi = u_{XX} - u_{XY}$ . The magnetic instability is controlled by the Gaussian propagator  $\chi_0^{-1}$  that diverges at the Néel temperature  $T_N$ .  $\lambda_\psi$  and  $\lambda_\phi$  are the couplings of the  $x/y$  isotropic and anisotropic fluctuations of the spin-excitations. The coefficient of the action explicitly read:

$$\chi_0^{-1} = \frac{2}{u_{spin}} + 2 \int_k G_{\Gamma k} G_{Xk} \quad (2.16)$$

$$\lambda_\psi = \frac{1}{2} \int_k G_{\Gamma k}^2 (G_{Xk} + G_{Yk})^2 \quad (2.17)$$

$$\lambda_\phi = \frac{1}{2} \int_k G_{\Gamma k}^2 (G_{Xk} - G_{Yk})^2 \quad (2.18)$$

From Eq. 2.15 one immediately sees that a nematic instability is possible only for  $\lambda_\phi < 0$  when making the spin fluctuations along  $x/y$  different lowers the energy of the system. Notice that  $\lambda_\phi \sim G_X - G_Y$ , thus it vanishes within a parabolic band approximation in which the two electron bands are completely degenerate, i.e.  $G_X^0 = G_Y^0 = G^0$ . However, if one takes into account the ellipticity of the electron pockets the result changes. In first approximation we can account for the ellipticity perturbatively, i.e. we can approximate the electron Green's functions as  $G_{X/Y} = G^0(1 \mp \delta_e \cos(2\theta)G^0)$ , with the ellipticity parameter  $\delta_e \sim (m_x - m_y)/(2m_x m_y)$ . By substituting the elliptical Green's functions  $G_{X/Y}$  in Eq. 2.18 and performing the integral, we find that  $\lambda_\phi \sim -\delta_e^2$ . That means, we have an attraction in the nematic channel. This implies that within the spin-nematic model in the band-basis the ellipticity of the electron pockets is a necessary condition for nematicity.

In order to analyze the nematic instability, we need to perform a second H-S transformation on the effective action of Eq. 2.15 using as auxiliary fields  $\psi$  and  $\phi$  associated to  $M_X^2 + M_Y^2$  and  $M_X^2 - M_Y^2$  respectively. The action now reads

$$S_{eff}^{band}[\vec{M}_X, \vec{M}_Y, \phi, \psi] = \chi_0^{-1}(M_X^2 + M_Y^2) + \iint \left( \frac{\phi^2}{2\lambda_\phi} - \frac{\psi^2}{2\lambda_\psi} \right) + \int \psi(M_X^2 + M_Y^2) + \iint \phi(M_X^2 - M_Y^2) \quad (2.19)$$

$\psi$  gives an isotropic correction to the magnetic susceptibility, while  $\phi$  is the nematic field that renormalizes in an anisotropic way the  $X/Y$  spin propagators. Both these effects can be seen explicitly by integrating out the spin degree of freedom  $M_X$  and  $M_Y$ . In this way the action reads

$$S_{eff}^{band}[\phi, \psi] = \frac{\phi^2}{2\lambda_\phi} - \frac{\psi^2}{2\lambda_\psi} + \frac{3}{2} \ln \left[ (\chi_0^{-1} + \psi)^2 - \phi^2 \right] \quad (2.20)$$

This means that once the nematic order parameter  $\phi$  acquires a finite value the static susceptibilities for  $\vec{M}_X$  and  $\vec{M}_Y$  become non-equivalent

$$\chi_X(q=0) = \frac{1}{\tilde{\chi}^{-1} - \langle \phi \rangle}, \quad \chi_Y(q=0) = \frac{1}{\tilde{\chi}^{-1} + \langle \phi \rangle} \quad (2.21)$$

where we define  $\tilde{\chi}^{-1} = \chi_0^{-1} + \langle \psi \rangle$ , i.e. we included the isotropic correction given by the  $\psi$  field in the definition of the propagator. Eq. 2.21 represents the main result of [28]. From this we understand that (i) the nematic phase is a precursor state of magnetism: before the divergence of the magnetic susceptibility, when the long-range magnetic order is not developed  $\langle M_{X/Y} \rangle = 0$ , the difference between the spin propagators in the  $x/y$ -direction makes the spin fluctuations along  $x/y$  inequivalent, i.e.  $\langle M_X^2 \rangle \neq \langle M_Y^2 \rangle$ ; (ii) the nematic order selects a preferred direction and decides along which direction the striped magnetism is eventually established; (iii) when  $\langle \phi \rangle \neq 0$  the magnetic transition occurs in the  $X/Y$  channel at  $\tilde{\chi}^{-1} = |\phi|$ , i.e. at a temperature larger than before. This means the nematic transition may occur just before that the magnetic transition takes place as indeed experimentally found in many IBS.

## 2.2. Spin-nematic scenario driven by orbital selective spin-fluctuations

The main limitation of a spin-nematic model in the band-basis is the absence of the information of the orbital composition of the low-energy states. As a consequence, the band nesting of the Fermi surfaces is the only parameter controlling the phenomenology of the system and compounds with similar band structures and nesting conditions are expected to display a close phenomenology. However, as we already mentioned, it is experimentally found that different compounds can present a very different realization of nematicity despite having similar band structures. In what follows we will explicitly show how by taking into account the orbital make-up of the low-energy states near the Fermi level we can reconcile within a single theoretical frame the variety of the nematic realization in IBS.

The idea proposed in [26] is that one can derive a spin-nematic action that retains the orbital information by projecting the multiorbital interacting Hamiltonian at low-energy energy and then deriving the effective action following the same strategy used in the band spin-nematic model [28] discussed in the previous section. A remarkable feature of this theoretical description is unveiled by the low-energy projection that shows a strong orbital selectivity of spin-fluctuations at  $\mathbf{Q}_{X/Y}$ , i.e. spin-fluctuations at different momenta involve only specific orbitals.

The orbital selective nature of the spin-fluctuations is a robust feature of the modeling and does not depend on the particular procedure implemented to derive the spin-nematic action. On the other hand, the low-energy model one uses to perform the projection can affect the definition of the nematic order parameter and the symmetries incorporated into the model. In particular, in Section 1.5.3 we showed that by using as starting point a symmetry adapted low-energy model, e.g. [118], one obtains a definition of the nematic order extremely elegant and simple that makes the physical interpretation of the results straightforward while allowing for analytical treatment. Thus, in what follows we focus on the Orbital Selective Spin Fluctuations (OSSF) model derived in [27] using the symmetry adapted low-energy model of [118].

### 2.2.1. Model Hamiltonian

We consider a general four-pocket model with two hole pockets at  $\Gamma$ ,  $\Gamma_{\pm}$  and two electron pockets at  $X$  and  $Y$ , that can be easily adapted to describe different compounds among the 122 and 11 families. In Figure 2.1 we show a sketch of the orbital content of the Fermi surface for a generic IBS. Mainly three orbitals participate the formation of the Fermi surfaces,  $yz$  and  $xz$  orbitals at  $\Gamma$  and  $yz/xz$  and  $xy$  orbitals at  $X/Y$ .

#### Symmetry adapted low-energy model

The kinetic Hamiltonian is derived adapting the low-energy model considered in [118], where the electronic states around the high-symmetry points  $l = \Gamma, X, Y$  are described using a spinor representation in the pseudo-orbital space

$$H_0^l = \sum_{\mathbf{k}, \sigma} \left( \phi_{\mathbf{k}\sigma}^\dagger \hat{H}_{0\mathbf{k}}^l \psi_{\mathbf{k}\sigma}^l \right). \quad (2.22)$$

Here  $\psi_{\mathbf{k}\sigma}^\Gamma = (c_{\mathbf{k}\sigma}^{yz}, c_{\mathbf{k}\sigma}^{xz})$ ,  $\psi_{\mathbf{k}\sigma}^{X/Y} = (c_{\mathbf{k}\sigma}^{yz/xz}, c_{\mathbf{k}\sigma}^{xy})$  and  $\hat{H}_{0\mathbf{k}}^l = h_{0\mathbf{k}}^l \hat{\tau}_0 + \vec{h}_{\mathbf{k}}^l \cdot \vec{\tau}$  with  $\hat{\tau}$  the Pauli matrices representing the orbital isospin. Diagonalizing  $\hat{H}_0^l$  we find the dispersion relations and the orbital composition for the bands

$$H_0^l = \sum_{\mathbf{k}, \sigma} \phi_{\mathbf{k}\sigma}^{\dagger l} \hat{\Lambda}_{0\mathbf{k}}^l \phi_{\mathbf{k}\sigma}^l. \quad (2.23)$$

with  $\phi^l = \hat{\mathcal{U}}^l \psi^l$  the fermionic operator in the band basis and  $\hat{\Lambda}^l = \hat{\mathcal{U}}^l \hat{H}_0^l \hat{\mathcal{U}}^{l-1} = \text{diag}(E^{l+}, E^{l-})$  the diagonal matrix containing the band dispersions  $E^{l\pm} = h_0^l \pm h^l$  with  $h^l = |\vec{h}^l|$ . The components of the unitary matrix  $\hat{\mathcal{U}}^l$ , that connect the orbital-space to the band-space, are the coherence factors that represent the orbital content of the  $l_{\pm}$ -pockets. All the above quantities still depends on momentum and spin, we drop those labels to make the equations more readable.

Explicitly, for  $l = \Gamma$  for example, the fermionic operator in the band basis reads

$$\phi^\Gamma = \begin{pmatrix} h_+ \\ h_- \end{pmatrix} \begin{pmatrix} u^\Gamma & -v^\Gamma \\ v^{*\Gamma} & u^{*\Gamma} \end{pmatrix} \begin{pmatrix} c^{yz} \\ c^{xz} \end{pmatrix} \quad (2.24)$$

and analogous expressions can be derived for the  $X/Y$  pockets, provided that the corresponding orbital spinors and  $\hat{H}_0^{X/Y}$  are used (full expression are available in Appendix B.1). Notice that at  $X/Y$  only the  $E^{X/Y+}$  band crosses the Fermi level, so in the following we will use  $e^{X/Y}$  for the corresponding fermionic operators and  $E^{X/Y}$  for the bands dropping the  $+$  subscript.

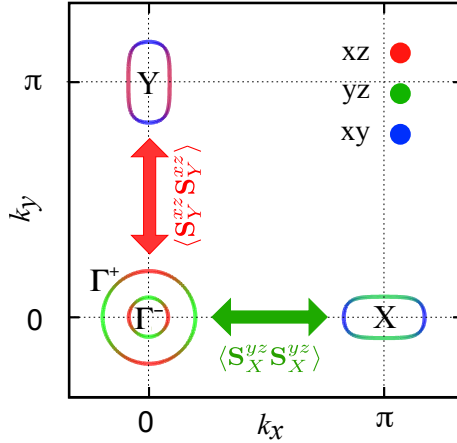


**Figure 2.1:** General sketch of the Fermi surface for a generic four-pocket model for IBS. The orbital composition of the pockets is shown using the color code: red for  $xz$ , green for  $yz$  and blue for  $xy$ . The arrows show the spin-fluctuation exchange between the nested Fermi surfaces. The color code represents the orbital selectivity of the spin-fluctuations having  $yz$  character along  $x$  direction and  $xz$  character along  $y$ .

The explicit expressions of  $(h_0^l, \vec{h}^l)$  that reproduce a four-pocket model as the one shown Figure 2.1 are detailed in Appendix B.1. Notice that in order to lift the degeneracy of the inner and outer  $xz/yz$  pockets at  $\Gamma$  we need to account for the spin-orbit coupling in the Hamiltonian. We added it explicitly by replacing  $h^\Gamma \rightarrow \sqrt{(h^\Gamma)^2 + \lambda^2/4}$  in the expression for  $E^{\Gamma\pm}$ .

The the non-interacting Green's functions in the orbital space are given by  $\hat{G}^{l-1} = \omega \hat{1} - \hat{H}_0^l$  and we can express them via the band Green's functions using  $\hat{G}^{l-1} = \hat{\mathcal{U}}^{l-1}(\omega \hat{1} - \hat{\Lambda}^l) \hat{\mathcal{U}}^l$  that reads explicitly

$$\hat{G}^l = g^{l+} \begin{pmatrix} (u^l)^2 & u^l v^l \\ v^l u^l & (v^l)^2 \end{pmatrix} + g^{l-} \begin{pmatrix} (v^l)^2 & -v^l u^l \\ -u^l v^l & (u^l)^2 \end{pmatrix} \quad (2.25)$$

where we defined  $g_{(\mathbf{k}, i\omega_n)}^{l\pm} = (i\omega_n - E_{\mathbf{k}}^{l\pm})^{-1}$ .

### Interacting Hamiltonian

We consider the full multiorbital Hubbard Hamiltonian defined by Eq. 1.7 in Section 1.5.2. By transforming by Fourier and considering only the spin channel of the interactions we find

$$H_{int} = -\frac{1}{2} \sum_{\mathbf{q}} \left( U_{\eta\eta'} \vec{S}^\eta(\mathbf{q}) \cdot \vec{S}^{\eta'}(-\mathbf{q}) \right). \quad (2.26)$$

Here,  $\eta, \eta' = yz, xz, xy$  are the orbital indices and  $U_{\eta\eta'} \sim U\delta_{\eta\eta'} + J(1 - \delta_{\eta\eta'})$  the effective coupling, with  $U$  and  $J$  being the Hubbard and Hund's couplings. Notice that Eq. 2.26 contains only spin operators with intraorbital character  $\vec{S}^\eta(\mathbf{q}) = \sum_{\mathbf{k}ss'} c_{\mathbf{k}s}^{\eta\dagger} \vec{\sigma}_{ss'} c_{\mathbf{k}+\mathbf{q}s'}$  with  $\sigma_{ss'}$  the Pauli matrices for the spin operator. This choice is motivated by the general finding that intraorbital magnetism is the dominant channel in IBS [22, 76, 120–122].

We project the interacting Hamiltonian, Eq. 2.26, into the low-energy model defined by Eqs. 2.23–2.24 focusing on spin-excitations with momentum close to  $\mathbf{Q}_X/\mathbf{Q}_Y$  only. The low-energy projection establishes a precise correspondence between the orbital and the momentum character of the spin operators  $\vec{S}_{X/Y}^\eta \equiv \vec{S}^\eta(\mathbf{q} = \mathbf{Q}_{X/Y})$ :

$$\begin{aligned} \vec{S}_X^{yz} &= \sum_{\mathbf{k}} \left( u^\Gamma h_+^\dagger + v^\Gamma h_-^\dagger \right) \vec{\sigma} u^X e^X \\ \vec{S}_Y^{xz} &= \sum_{\mathbf{k}} \left( -v^\Gamma h_+^\dagger + u^\Gamma h_-^\dagger \right) \vec{\sigma} u^Y e^Y \end{aligned} \quad (2.27)$$

As a consequence, the interacting Hamiltonian of Eq. 2.26 simplifies substantially and once the spin-exchange interaction is projected at low energy it reduces to

$$H_{int} = -\frac{\tilde{U}}{2} (\vec{S}_X^{yz} \cdot \vec{S}_X^{yz} + \vec{S}_Y^{xz} \cdot \vec{S}_Y^{xz}) \quad (2.28)$$

where  $\tilde{U}$  is the intraorbital interaction renormalized at low energy.

This is a crucial result of the OSSF model [27]: the projection of the generic interaction Hamiltonian into the low-energy model, Eq. 2.23, generates a one to one correspondence between momentum  $\mathbf{Q}_{X/Y}$  and orbital character  $yz/xz$  of the spin-fluctuations. In fact, as one can see also from Figure 2.1, at low energy the  $yz/xz$ -fermionic states exist only around  $\mathbf{Q}_X/\mathbf{Q}_Y$ , thus spin operators  $\vec{S}_X^\eta$  with  $\eta \neq yz$  and  $\vec{S}_Y^\eta$  with  $\eta \neq xz$  are absent in Eq. 2.28.

The orbital selective character of the low-energy spin-excitations makes the interacting Hamiltonian for the spin-channel, Eq. 2.28, considerably simpler than the one obtained within a five-orbital tight-binding model, Eq. 2.26. As a matter of fact, Eq. 2.28, while retaining the orbital dependence of the spin excitations does not acquire a complex tensorial



form and is instead formally equivalent to the spin-spin interacting Hamiltonian written in the band-basis, Eq. 1.2. This implies that in order to derive the effective action we can simply use the derivation of [28] that we revised in Section 2.1. Notice that although formally equivalent to a band-model, the OSSF model allows the analysis of orbital physics and as we will discuss, it is able to describe a much richer phenomenology due to the spin-orbital interplay encoded in the model.

### 2.2.2. Effective action for orbital selective spin excitations

We exploit the orbital-selective character of the OSSF model that makes the model Hamiltonian, Eqs. 2.23 and 2.28, formally equivalent to the multiband model, Eq. 2.5, and decouple the interaction term by means of two H-S field  $\vec{M}_X^{yz}$  and  $\vec{M}_Y^{xz}$  following the same derivation of Section 2.1. The effective action up to quartic order becomes

$$S_{\text{eff}} = \begin{pmatrix} M_X^{yz} & M_Y^{xz} \end{pmatrix} \begin{pmatrix} \chi_X^{-1} & 0 \\ 0 & \chi_Y^{-1} \end{pmatrix} \begin{pmatrix} M_X^{yz} \\ M_Y^{xz} \end{pmatrix} + \begin{pmatrix} (M_X^{yz})^2 & (M_Y^{xz})^2 \end{pmatrix} \begin{pmatrix} u_{11} & u_{12} \\ u_{12} & u_{22} \end{pmatrix} \begin{pmatrix} (M_X^{yz})^2 \\ (M_Y^{xz})^2 \end{pmatrix}. \quad (2.29)$$

Here  $\chi_{X/Y}^{-1} = 1/2\tilde{U} + \Pi_{X/Y}^{yz/xz}$  is the Gaussian susceptibility that controls the magnetic instability, with  $\tilde{U}$  the effective interactions between low-energy quasiparticles, and  $\Pi_{X/Y}^{yz/xz}$  the propagator in the long-wavelength and zero-frequency limit

$$\Pi_X^{yz} = 2T \sum_{\mathbf{k}, i\omega_n} \left( u_\Gamma^2 u_X^2 g_+ g_X + v_\Gamma^2 u_X^2 g_- g_X \right), \quad (2.30)$$

$$\Pi_Y^{xz} = 2T \sum_{\mathbf{k}, i\omega_n} \left( v_\Gamma^2 u_Y^2 g_+ g_Y + u_\Gamma^2 u_Y^2 g_- g_Y \right). \quad (2.31)$$

The coefficients of the quartic part of the action in Eq. 2.29 are

$$u_{11} = T \sum_{\mathbf{k}, i\omega_n} \left( u_X^2 g_X \right)^2 (u_\Gamma^2 g_+ + v_\Gamma^2 g_-)^2, \quad (2.32)$$

$$u_{22} = T \sum_{\mathbf{k}, i\omega_n} \left( u_Y^2 g_Y \right)^2 (v_\Gamma^2 g_+ + u_\Gamma^2 g_-)^2, \quad (2.33)$$

$$u_{12} = T \sum_{\mathbf{k}, i\omega_n} u_X^2 g_X u_Y^2 g_Y u_\Gamma^2 v_\Gamma^2 (g_+ - g_-)^2. \quad (2.34)$$

Notice that as a consequence of the orbital selectivity of the low-energy spin-excitations, we find the same fermionic loops found in effective action derived in the band basis given by Eqs. 2.14 weighted by the coherence factors  $u^l, v^l$  defining the orbital content of each pocket. It is easy to verify, in fact, that if we neglect the orbital weight, i.e. set  $u^l = v^l = 1$  in Eq. 2.32-2.34, we recover indeed the expressions, Eqs. 2.14, obtained in the band-basis.

Since  $u_{11} = u_{22}$  due to  $C_4$  symmetry, the quartic part of the action, Eq. 2.29 can be simply diagonalized as

$$S_{\text{eff}}^{(4)} = \lambda_\psi \psi^2 + \lambda_\phi \phi^2 \quad (2.35)$$

where in analogy with the band case we have define  $\lambda_\psi$  and  $\lambda_\phi$  and  $\psi$  and  $\phi$  as

$$\psi = \frac{1}{\sqrt{2}} \left( (M_X^{yz})^2 + (M_Y^{xz})^2 \right), \quad \lambda_\psi = u_{11} + u_{12} \quad (2.36)$$

$$\phi = \frac{1}{\sqrt{2}} \left( (M_X^{yz})^2 - (M_Y^{xz})^2 \right), \quad \lambda_\phi = u_{11} - u_{12}. \quad (2.37)$$

It is worth noticing again that the tensorial forms of the nematic order parameter proposed in [26, 117] do not contain the result of Eq. 2.37, which in turn is dictated by the only possible nematic contribution in Eq. 2.29 for the OSSF model (see also discussion in Section 1.5.3).

To compute the nematic transition temperature we have to perform a second H-S and study the divergence of the nematic susceptibility. However, as we already pointed out in the previous section, a necessary condition to have nematicity is to have attraction in the nematic coupling i.e.  $\lambda_\phi < 0$ . While in the band spin-nematic model this is only controlled by the shape of the electron pockets, here the orbital composition of the nested band plays an important role. This feature allows us to explain why systems having similar band structure can display a very different realization of nematicity as we shown in the next section.

### 2.2.3. Role of the orbital nesting in the OSSF model

To make a first estimate of the role of the orbital weights in affecting the magnetic and nematic instabilities we consider the simple case where the hole and the electron pockets are perfectly nested circular Fermi surface, so that the orbital weights and the Green's functions reduce to

$$u_\Gamma = u_Y = v_X = \cos \theta, \quad v_\Gamma = v_Y = u_X = \sin \theta \quad (2.38)$$

$$g_+ = g_- = g_h = (i\omega_n + \epsilon)^{-1} \quad g_X = g_Y = g_e = (i\omega_n - \epsilon)^{-1} \quad (2.39)$$

with  $\epsilon = -\epsilon_0 + \mathbf{k}^2/2m - \mu$ .  $\epsilon_0$  is the off-set energy,  $m$  the parabolic band mass and  $\mu$  the chemical potential (further details in Appendix B.2). Within this approximation we can carry out explicitly the integration in Eqs. 2.30-2.34 using the usual decomposition

$$\sum_{\mathbf{k}} \left( \iint_{\mathbb{R}^2} \frac{d^2 \mathbf{k}}{(2\pi)^2} = \int_0^{2\pi} \frac{d\theta}{2\pi} \int d\epsilon N_F \right) \quad (2.40)$$

where  $\theta$  the azimuthal angle and  $N_F = m/2\pi$  is the two-dimensional density of state per spin at the Fermi level. In fact, the coherence weights, Eq. 2.38, depend on  $\theta$  only, and the Green's functions, Eq. 2.39, only on  $\epsilon$ . For what concerns the magnetic instability, the spin-fluctuations bubbles  $\Pi_{X/Y}^{yz/xz}$ , Eqs. 2.30-2.31, are both proportional to  $\Pi_{eh} = T \sum_{\mathbf{k}, i\omega_n} g_e g_h$  that lead to the usual log divergence:  $\Pi_{eh} \sim -N_F \log \omega_0/T$  where  $N_F$  is the density of states and  $\omega_0$  an upper cut-off. On the other hand, the orbital renormalization of the  $S_{\text{eff}}^{(4)}$  action is much more severe. Indeed, considering two hole pockets of same size, one immediately finds from Eq. 2.33 that  $u_{12} = 0$ . This leads to a large *positive* nematic eigenvalue  $\lambda_\phi$  in Eq. 2.37, which prevents the occurrence of nematicity, in agreement with renormalization group studies on the four-pocket model [123].

To simulate the case of specific compounds we consider two three-pocket models in which a single hole pocket at  $\Gamma$  is well-nested with the elliptical electron pocket

- (a) The  $3p_+$  model which reproduces FeSe (see Figure 2.2a), where only the outer pocket  $\Gamma_+$  crosses the Fermi level while the inner pocket  $\Gamma_-$  sinks below it before the nematic transition [32, 60].
- (b) The  $3p_-$  model which simulate 122 systems (see Figure 2.2b), where the outer pocket  $\Gamma_+$  is much larger than the electron ones, so it weakly contributes to the nesting [45].

Notice that these two cases are completely equivalent and indistinguishable within a band-based description. On the contrary, within the OSSF model, they are different as the orbital composition of the hole pocket is opposite in the two case, as one can see from Figure 2.2. As a consequence the two systems are characterized by a different degree of orbital nesting. In fact, by translating the Fermi surfaces of  $\mathbf{Q}_{X/Y}$  we observe the orbitals matching between the hole and electron pocket of the 122 system, while in the FeSe case there is a clear orbital mismatch.

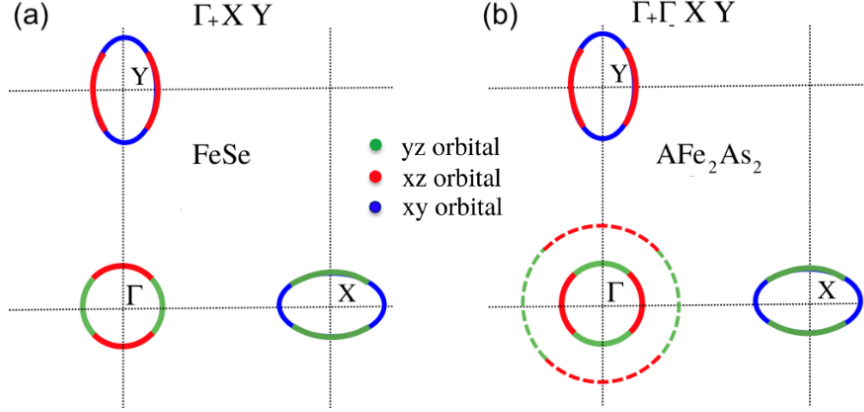


**Figure 2.2:** Sketch of the orbital content of the Fermi surface for (a) FeSe in which only the outer hole pocket is present. A clear orbital mismatch between the hole and electron pocket is shown. (b) 122 in which the outer hole pocket is much larger than the inner hole pocket, so it can be neglected in first approximation. An orbital matching between the inner hole and the electron pockets is shown and thus a robust orbital nesting. Adapted from [27].

We focus first, on a perfect nested parabolic band approximation, see Eqs. 2.38 - 2.39. In the  $3p_+$  model for FeSe it is easy to verify from Eqs. 2.32 - 2.34 that  $u_{11}^0 = u_{12}^0$ , and thus the nematic coupling  $\lambda_\phi^{0\Gamma+XY} = 0$ . In the  $3p_-$  model for 122 instead, thanks to the perfect orbital nesting, we have  $u_{11} \sim \sin^8\theta g_e^2 g_h^2$  while  $u_{12} \sim \sin^4\theta \cos^4\theta g_e^2 g_h^2$ . As a consequence, once performed the angular integration we find that  $u_{11}$  is much larger than the  $u_{12}$ , so that  $\lambda_\phi^{0\Gamma-XY} > 0$  is finite and positive, preventing a nematic transition.

We can go beyond this approximation and account for the ellipticity of the electron pockets, as done in the analysis of spin-nematic model in the band basis. We introduce the ellipticity  $\delta_e$  at a perturbative level, and approximate the electron Green's functions as  $g_{X/Y} = g_e(1 \mp \delta_e \cos(2\theta)g_e)$  with  $\delta_e = \epsilon_0 m(m_x - m_y/2m_x m_y)$ . As one can see, we can still analytically compute Eqs. 2.30 - 2.37 as each additional term due to the ellipticity go with a  $\cos(2\theta)g_e$  factor that can be integrated analytically over  $\theta$  and  $\epsilon$ . By explicitly performing the computation of each terms we find that the nematic couplings for the three-pocket models are

$$\lambda_\phi^{3p_+} = -\mathcal{K}(T) \frac{b \delta_e^2}{T^2} \quad \lambda_\phi^{3p_-} = \mathcal{K}(T) \left( 16 - \frac{25}{2} \frac{b \delta_e^2}{T^2} \right), \quad (2.41)$$

with  $\mathcal{K}(T) = 7N_F \zeta(3)/(8^3 \pi^2 T^2)$ ,  $b > 0$  [27]. As one can see, as soon as a finite ellipticity is included, we have in both cases a negative correction to results obtained within the parabolic approximation. This means that in the  $3p_+$  model for FeSe  $\lambda_\phi < 0$  at any temperature, while for the  $3p_-$  model for 122,  $\lambda_\phi^{3p_-}$  changes sign only below a temperature  $T^* \sim \delta_e$  [27]. A quantitative analysis for  $\delta_e = 0.55\epsilon_0$  is shown in Figure 2.3b.

The orbital composition of the nested bands also affects the magnetic instability. Already within the parabolic band approximation one can verify the magnetic tendency is enhanced in presence of a good orbital nesting. In fact, the magnetic transition is pushed to higher temperatures within the  $3p_-$  model for 122 with respect to the  $3p_+$  case [27]. The magnetic susceptibility for FeSe and 122 system is shown in Figure 2.3a.

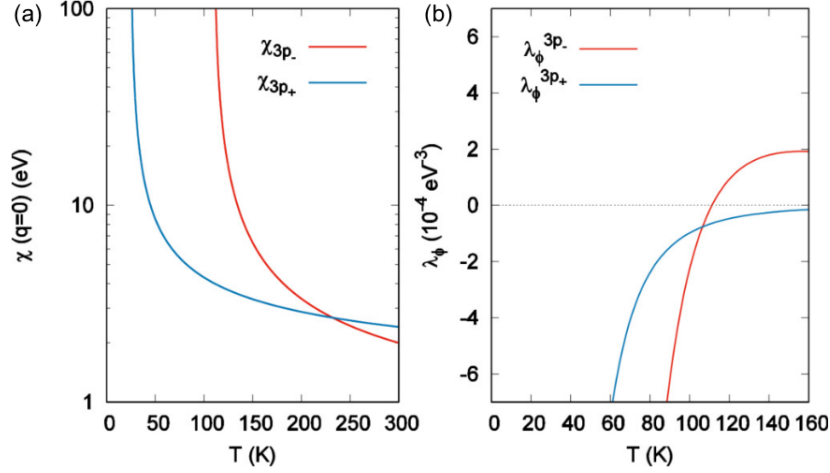


**Figure 2.3:** (a)  $\chi_{X/Y}^{yz/xz}$  spin susceptibilities and (b)  $\lambda_\phi$  nematic couplings for the  $3p_-$  and  $3p_+$  model. The Néel temperature for the  $3p_-$  model is  $T_N^{p-} = 110\text{K}$  and for the  $3p_+$  model is  $T_N^{p+} = 24\text{K}$ . The change of sign of  $\lambda_\phi^{p-}$  occurs around  $112\text{K}$ . Adapted from [27].

The main result of [27], is that despite being formally equivalent to the spin-nematic model in the band-basis, the OSSF model is able to explain the different phenomenology displayed by systems having similar band structures. In fact within the OSSF model, *orbital nesting* is equally important as *band nesting* to determine the magnetic and nematic properties of a system. In particular, in systems in which the nested pockets have a good orbital nesting, as 122, the coherence factors favour magnetism while suppressing nematicity, so that the nematic channel becomes attractive only at temperature close to the magnetic transition. On the contrary, the orbital mismatch of the nested bands boosts nematicity and is detrimental for magnetism. This is the case of FeSe.

As argued in [27], this result offers also a possible explanation for the suppression of nematicity in FeSe under internal and external pressure. Indeed, it has been reported that sulphur isoelectronic substitution [32, 124] brings back the inner hole pocket above the Fermi level. This finding is also supported by *ab-initio* calculations, which usually miss the experimental position of the Fermi level but report in general an increase of the hole-pockets size with pressure [125]. The emergence of the inner hole pocket changes the FS topology of FeSe towards the more symmetric four-pocket model, which has been shown before to be detrimental for nematicity. On the other hand, the same mechanism could also enhance magnetism, as observed.

In Chapter 5 we extend the analysis of the spin-nematic model due to OSSF to a five-pockets model, in order to be able to study the phenomenology of the 1111 IBS family.

### 2.3. Self-energy corrections from interband spin-fluctuations

In a quantum system the low-energy interaction between particles results in a renormalization of the particle properties that can affect for example the electronic and transport properties of the system. We defined self-energy corrections the effects that renormalize the single-particle properties (i.e. the single particle Green's function) and vertex corrections the renormalization of the two-particle interaction.

In what follows we will compute self-energy due to spin-fluctuations following Ref.s [60, 61] in which the spin-propagator is assumed momentum-independent. In this case self-energy are momentum independent too and vertex corrections vanish identically. We will use this self-energy in Chapter 4 where we consider its effects in the nematic phase of IBS to analyze the anisotropy of the dc resistivity in 122 and FeSe compounds. Notice that the choice of neglecting the effects of vertex corrections is justified by the analysis performed in [126] in which the momentum dependence of the spin-mode is taken into account and the effects of the vertex renormalizations on the dc resistivity is found to be negligible with respect the self-energy renormalizations.

#### 2.3.1. Self-energy effects due to spin-fluctuation in a multiband model

We consider the three-band spin-nematic model described in Section 1.5.1 and Section 2.1. The self-energy due to the spin-fluctuation exchange between the hole and electron pockets in the Matsubara space reads

$$\begin{aligned}\Sigma^\Gamma(k) &= V_s \sum_q \left( \sum_{i=X,Y} \langle \vec{S}_i(q) \cdot \vec{S}_i(-q) \rangle G^i(k-q) \right) \\ \Sigma^i(k) &= V_s \sum_q \langle \vec{S}_i(q) \cdot \vec{S}_i(-q) \rangle G^\Gamma(k-q)\end{aligned}\quad (2.42)$$

where  $i = X, Y$ ,  $\vec{S}_{X/Y}$  is the spin-operator that connects the hole pocket at  $\Gamma$  and the electron pockets at  $X/Y$ ,  $V_s \propto u_{spin}^2$  is the interband coupling and  $G^{\Gamma/X/Y}$  are the local Green's function. Notices that given the interband nature of the spin-interaction, in Eq. 2.42 the self-energy of the hole-band depends on the electron Green's functions and *vice versa*.

We follow the derivation from [61] where the momentum dependence of the interaction is neglected and the spin-mode propagator is modelled as  $D(\omega_n) = \int d\Omega 2\Omega B(\Omega) / (\Omega^2 + \omega_n^2)$ , where  $B(\Omega)$  is the density of the states of the bosonic excitations. (Eqs. 2.42 can be rewritten as

$$\Sigma^l(i\omega_n) = -T \sum_{m,l'} V^{l,l'} D(\omega_n - \omega_m) G^{l'}(i\omega_m) \quad (2.43)$$

where  $l, l'$  are band indices and  $V^{l,l'} > 0$  is the multiband interaction and  $G^{l'}(i\omega_m)$ .

The dressed Green's functions for each band are obtained via the Dyson equation  $G^{l-1}(\mathbf{k}, i\omega_n) = G_0^{l-1}(\mathbf{k}, i\omega_n) - \Sigma^l(i\omega_n)$  where  $G_0^{l-1}(\mathbf{k}, i\omega_n) = (i\omega_n - \xi_{\mathbf{k}})$  is the non-interacting Green's function. The self-energy Eq. 2.43 is a complex quantity. The real part  $Re\Sigma^l(i\omega_n)$  renormalize the band dispersion and the imaginary part  $Im\Sigma^l(i\omega_n)$  renormalizes the scattering rate.

**Fermi surface shrinking in IBS** The multiband character of IBS and the strong particle-hole asymmetry of the bands allow for a peculiar self-energy effect that concerns the real part of the self-energy and is usually neglected in the Eliashberg approach for a single particle-hole symmetric band [61]. As discussed in Section 1.5.1, the self-energy correction induced by repulsive interband spin-fluctuations in IBS, has been used to explain the shrinking of the Fermi surfaces found when comparing the experimentally measured Fermi surfaces to the one expected by LDA [37, 40, 41, 59].

In the conventional Eliashberg analysis [127], is usually assumed that the distance of the chemical potential  $\mu$  from the band edges is much larger than the typical boson energy scale, and thus one can safely assume the system to be particle-hole symmetric. In this way the Matsubara self-energy, Eq. 2.43 is purely imaginary. In systems in which the particle-hole symmetry is not fulfilled (for example if we are far from half filling) the situation changes. By taking into account the particle-hole asymmetry in a single-band system, the self-energy acquires a finite real part that can be adsorbed in a redefinition of the chemical potential. However, in multiband systems, like IBS, the self-energy acquires a finite real part generally different for each band. In this case, we cannot simply redefine the chemical potential as we need to account for a relative change in the bands. The sign of the energy dependent shifts of the various bands with respect to the Fermi level depends on the repulsive/attractive nature of the bosonic mode and in the case of an interband spin-mode leads to a shrinking of the non-interacting Fermi surface [61].

A simple way to understand this effect is to compute explicitly the self-energy for a system of two parabolic bands, an electron band and a hole one. We consider a two-dimensional system, this means that given the top for band for hole band we fix the lower edge from the density of states  $N^l = 1/(E_{max}^l - E_{min}^l)$  knowing that  $N^l = m/\pi$  (*vice versa* for the electron band). We compute the self-energy at the lowest order in the perturbation theory, i.e. we replace  $G''(i\omega_m)$  with the non-interacting one in Eq. 2.43. We also consider an Einstein mode  $B(\Omega) = (\omega_0/2)\delta(\Omega - \omega_0)$ . Within these approximations we can derive an analytical expression for the real part of the self-energy

$$Re\Sigma^l = -\frac{\omega_0}{2} \sum_{l'} \left( \gamma^{l,l'} N^{l'} \ln \frac{\omega_0 - \mu + E_{max}^{l'}}{\omega_0 + \mu - E_{min}^{l'}} \right) \approx -\frac{\omega_0}{2} \sum_{l'} \left( \gamma^{l,l'} N^{l'} \ln \frac{E_{max}^{l'} - \mu}{E_{min}^{l'} - \mu} \right) \quad (2.44)$$

where we also assumed  $T \approx 0$  and used that the exchanged boson-energy is negligible with respect the rest. In a particle-hole symmetric system,  $Re\Sigma^l = 0$  as  $|E_{max}^{l'} - \mu| = |E_{min}^{l'} - \mu|$ . On the contrary, in a particle-hole asymmetric system, this correction is finite and has opposite sign for hole and electron bands. In fact, in an electron-like band  $|E_{max}^{l'} - \mu| > |E_{min}^{l'} - \mu|$  thus the energy shift is negative (downward), while for a hole-like band  $|E_{max}^{l'} - \mu| < |E_{min}^{l'} - \mu|$  and the renormalization produces a positive shift (upward). Therefore, Eq. 2.44, describes a shrinking of the Fermi surfaces in agreement with experiments in IBS. Notice that, while within the analytical calculation of Eq. 2.44 the correction reduces to a constant, in the full numerical evaluation of Eq. 2.43 performed in [61] this is an energy-dependent renormalization,  $Re\Sigma^l(\omega)$ , whose effect cannot be simply reproduced by rigid shift of the bands.

### 2.3.2. Self-energy effects in the OSSF model

Here we discuss the self-energy due to OSSF following the derivation performed in [60]. We show that those corrections lead to a renormalization of the scattering rates and the band dispersions analogous to the ones found in the multiband approach. However, due to the spin-orbital interplay encoded in the OSSF model, those also affect the *shape* and *orbital content* of the Fermi surface. All these effects will be accounted in the analysis of the dc-resistivity contained in Chapter 4.

At the end of this section we also summarized the main results of [60], in particular (i) the orbital ordering resulting from the orbital-selective shrinking in the nematic phase of IBS and (ii) the interplay between spin and orbital in the OSSF model that makes possible, via the analysis of the Fermi surface reconstruction in the nematic phase, to establish the sign of the anisotropy of the spin-fluctuations.

The spin fluctuation exchange and the associated self-energy corrections must preserve the orbital character of the electrons, thus within the OSSF model they both become orbital selective. In particular, as one can see from Eq. 2.28, we have a single orbital component for the spin-fluctuation connecting hole and electron pockets  $\Gamma_{-X/Y}$  i.e.  $S_X^{yz}$  and  $S_Y^{xz}$ . As a consequence, only the intraorbital components of the self-energy  $\Sigma_{yz/xz}^l$  are defined. In the Matsubara space the orbital selective self-energies read

$$\begin{aligned}\Sigma_{yz}^\Gamma(k) &= V_s \sum_q \langle \vec{S}_X^{yz}(q) \cdot \vec{S}_X^{yz}(-q) \rangle G_{yzyz}^X(k-q) \\ \Sigma_{xz}^\Gamma(k) &= V_s \sum_q \langle \vec{S}_Y^{xz}(q) \cdot \vec{S}_Y^{xz}(-q) \rangle G_{xzxz}^Y(k-q) \\ \Sigma_{yz}^X(k) &= V_s \sum_q \langle \vec{S}_X^{yz}(q) \cdot \vec{S}_X^{yz}(-q) \rangle G_{yzyz}^\Gamma(k-q) \\ \Sigma_{xz}^Y(k) &= V_s \sum_q \langle \vec{S}_Y^{xz}(q) \cdot \vec{S}_Y^{xz}(-q) \rangle G_{xzxz}^\Gamma(k-q)\end{aligned}\tag{2.45}$$

where  $\langle \vec{S}_{X/Y}^{yz/xz} \cdot \vec{S}_{X/Y}^{yz/xz} \rangle$  is the propagator of the spin-fluctuations connecting hole and electron pockets along  $x/y$ ,  $V_s \propto \tilde{U}^2$  and  $G_{\eta\eta}^l$  is the  $\eta\eta$ -intraorbital component of the Green's functions  $\hat{G}^l$  given in Eq. 2.25.

In what follows we use the same approximation of [61], and neglect the momentum dependence of the spin propagator. The self-energy for each band can be written as matrices in the orbital space

$$\hat{\Sigma}^\Gamma(\omega) = \begin{pmatrix} \Sigma_{yz}^\Gamma(\omega) & 0 \\ 0 & \Sigma_{xz}^\Gamma(\omega) \end{pmatrix} \left( \Sigma_0^\Gamma(\omega) \hat{\tau}_0 + \Sigma_3^\Gamma(\omega) \hat{\tau}_3, \right)\tag{2.46}$$

$$\hat{\Sigma}^{X/Y}(\omega) = \begin{pmatrix} \Sigma_{yz/xz}^{X/Y}(\omega) & 0 \\ 0 & 0 \end{pmatrix} \left( \Sigma_0^{X/Y}(\omega) \hat{\tau}_0 + \Sigma_3^{X/Y}(\omega) \hat{\tau}_3 \right)\tag{2.47}$$

with  $\Sigma_0^\Gamma(\omega) = [\Sigma_{yz}^\Gamma(\omega) + \Sigma_{xz}^\Gamma(\omega)]/2$  and  $\Sigma_3^\Gamma(\omega) = [\Sigma_{yz}^\Gamma(\omega) - \Sigma_{xz}^\Gamma(\omega)]/2$  for the holes and  $\Sigma_0^{X/Y}(\omega) = \Sigma_3^{X/Y}(\omega) = \Sigma_{yz/xz}^{X/Y}(\omega)/2$  for the electrons where the  $\Sigma_{xy}^{X/Y}(\omega) = 0$  as a consequence of the lack of a  $xy$  orbital component on the hole pockets.



The local Green's functions are given by the corresponding Dyson equation for each pocket as

$$\hat{G}_R^{l-1}(\mathbf{k}, \omega) = \hat{G}^{l-1}(\mathbf{k}, \omega) - \hat{\Sigma}^l(\omega), \quad (2.48)$$

with  $\hat{G}_{(\mathbf{k}, \omega)}^{l-1} = \omega \hat{\mathbb{1}} - \hat{H}_{0\mathbf{k}}^l$  the non-interacting Green's function and  $\hat{\Sigma}^l(\omega) = \Sigma_0^l(\omega) \hat{\tau}_0 + \Sigma_3^l(\omega) \hat{\tau}_3$  the orbital selective self-energy given in the Eqs. 2.46 and 2.47.

By rotating the orbital Hamiltonian into the band basis we can write

$$\hat{G}_{R(\mathbf{k}, \omega)}^l = \hat{\mathcal{U}}_{R(\mathbf{k}, \omega)}^l [\omega \hat{\mathbb{1}} - \hat{\Lambda}_{R(\mathbf{k}, \omega)}^l]^{-1} \hat{\mathcal{U}}_{R(\mathbf{k}, \omega)}^{l-1} \quad (2.49)$$

where  $\hat{\Lambda}_R^l = \text{diag}(E_R^{l+}, E_R^{l-})$  with  $E_R^{l\pm}$  the renormalized quasiparticle energy and  $\hat{\mathcal{U}}_R^l$  the corresponding rotation matrix. Both the  $\hat{\tau}_0$  and  $\hat{\tau}_3$  components of the self-energy renormalize the quasiparticle energy of the  $l^{\text{th}}$  pockets as

$$E_R^{l\pm} = h_0^l + \Sigma_0^l \pm h_R^l = h_0^l + \Sigma_0^l \pm \sqrt{(\hbar_1^l)^2 + (\hbar_2^l)^2 + (\hbar_3^l + \Sigma_3^l)^2} \quad (2.50)$$

where the real part of the self-energy corrections renormalizes the band dispersion as

$$\epsilon_R^{l\pm} = \text{Re} E_R^{l\pm} \quad (2.51)$$

and the imaginary part renormalizes the scattering rate as

$$\Gamma_R^{l\pm} = \delta\Gamma + |\text{Im} E_R^{l\pm}| \quad (2.52)$$

with  $\delta\Gamma$  a residual constant broadening term. Notice that within the OSSF model, the self-energy changes also the orbital composition of the bands. In fact, the unitary matrix  $\hat{\mathcal{U}}^l$  that diagonalizes the bare Hamiltonian is different from  $\hat{\mathcal{U}}_R^l$ . This means that also the coherence factors  $u^l$  and  $v^l$  are renormalized.

The effect of the orbital selective self-energy corrections is analyzed in Chapter 4, where the anisotropy of the dc conductivity is computed in the tetragonal and nematic phase of IBS. In what follows we discuss the orbital selective shrinking due to OSSF as discussed in [60].

**Orbital Selective Shrinking: the FeSe case** As in the multiband case discussed previously, the real part of the self-energy leads to a shrinking of the bands that, in this case, inherits the orbital selectivity of the self-energy (Eq. 2.45) and thus, gives rise to an orbital selective shrinking of the pockets. This effect renormalizes not only the *size*, but also the *shape* of the Fermi surfaces, due to the orbital dependence of the shrinking and the *orbital composition* of the Fermi surface, due to a change in the orbital weights. All these effects are linked to the spin-orbital interplay encoded in the OSSF model and could not be analyzed within a multiband approach.

In Ref. [60] the temperature evolution of the Fermi surface of FeSe has been studied both experimentally via ARPES and theoretically within the OSSF model. The theoretical description starts from a four-pocket model adapted from [118] and compute the effect of the self-energy both in the tetragonal and the nematic phase.

In the tetragonal state, above the structural transition  $T_S$ , the spin fluctuations along  $x$  and  $y$  directions are isotropic

$$\langle \mathbf{S}_X^{yz} \cdot \mathbf{S}_X^{yz} \rangle = \langle \mathbf{S}_Y^{xz} \cdot \mathbf{S}_Y^{xz} \rangle \quad \Rightarrow \quad \Sigma_{yz}^\Gamma(\omega) = \Sigma_{xz}^\Gamma(\omega) \quad \text{and} \quad \Sigma_{yz}^X(\omega) = \Sigma_{xz}^X(\omega). \quad (2.53)$$



This leads to equivalent self-energies for the  $C_4$  symmetric  $xz/yz$  orbitals with opposite signs for the hole and electron pockets. Notice that Eq. 2.53 can be rewritten as

$$\Sigma_3^\Gamma(\omega) = 0, \quad \Sigma_3^X(\omega) = \Sigma_3^Y(\omega) \quad (2.54)$$

This means that both  $\Gamma^\pm$  pockets are shifted by the  $\Sigma_0^\Gamma$  part of the self-energy modifying their size, but not their circular shape, as  $\Sigma_3^\Gamma = 0$ . The electron pockets in addition to be shifted by  $\Sigma_0^{X/Y}$ , also become more elliptical, in agreement with experiments. Notice that the combined effect of the spin-orbit coupling that lifts the degeneracy in the hole sector and a sizeable correction due to  $\Sigma_0^\Gamma$  we find that the inner hole pocket is pushed below the Fermi level already in the tetragonal phase (see Figure 2.4a).

In the nematic phase, the anisotropy of the spin fluctuations induces a  $x/y$  differentiation in the self-energy

$$\langle \mathbf{S}_X^{yz} \cdot \mathbf{S}_X^{yz} \rangle \neq \langle \mathbf{S}_Y^{xz} \cdot \mathbf{S}_Y^{xz} \rangle \Rightarrow \Sigma_{yz}^\Gamma(\omega) \neq \Sigma_{xz}^\Gamma(\omega) \quad \text{and} \quad \Sigma_{yz}^X(\omega) \neq \Sigma_{xz}^Y(\omega). \quad (2.55)$$

Due to the spin-orbital entanglement, taken into account within the OSSF model, the anisotropy of the spin-fluctuations reflects in anisotropic Fermi surface shrinking in which the degeneracy of the  $yz/xz$  orbitals in the charge sector is broken via orbital-selective self-energy corrections. Eq. 2.55 can be written as

$$\Sigma_3^\Gamma(\omega) \neq 0, \quad \Sigma_3^X(\omega) \neq \Sigma_3^Y(\omega), \quad (2.56)$$

i.e. all the pockets are modified in size, shape and orbital content (see Figure 2.4b). Notice that the orbital-dependent renormalization of the quasiparticle energy ( $\sim \hat{\tau}_3$ ) due to the OSSF in the  $C_2$  phase can be interpreted as an effective  $yz/xz$  crystal field. This is one of the main results of [60] and explains why a soft nematic transition can give rise to an order-parameter like behavior of the electronic structure. This result reconciles within a spin-driven scenario the experimental observations of orbital-ordering in the nematic phase of FeSe [86, 90, 128–132].

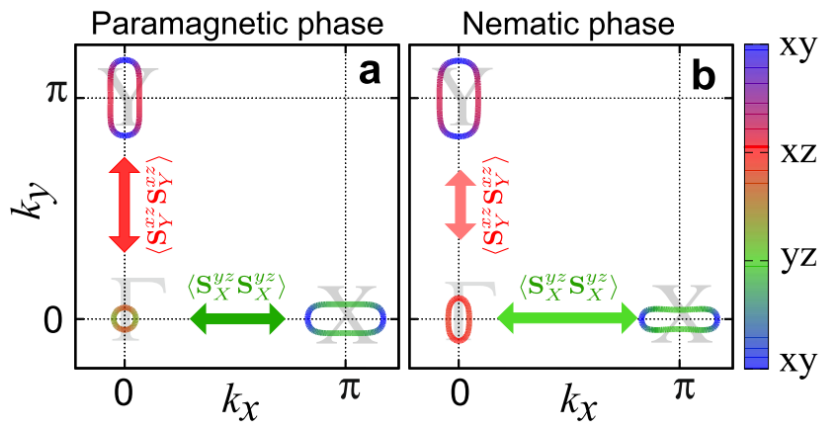


**Figure 2.4:** FeSe Fermi surfaces at  $k_z = 0$ . (a). Paramagnetic phase. (b). Nematic phase. The colors represent the main orbital character of the Fermi surface. The green/red arrows denote the OSSF, connecting hole and electron pockets at different momenta. The spin fluctuations along  $\Gamma X$  and  $\Gamma Y$  are equivalent in the paramagnetic phase and become stronger along  $x$  in the nematic one. Adapted from [133].

Ref. [60] also contains a quantitative analysis to reproduce in details the experimental ARPES data. In order to do that the spin-mode is modeled in analogy to [61] as

$$B_{X/Y}(\omega) = \frac{1}{\pi} \frac{\omega \omega_0}{(\omega_{X/Y}(T))^2 + \Omega^2}, \quad (2.57)$$

where  $\omega_0$  is a constant while  $\omega_{X/Y}(T)$  is the characteristic energy scale of spin modes. The self-energy functions are then computed as

$$\Sigma_{yz}^\Gamma(i\omega_n) = -VT \sum_{\mathbf{k}, m} \hat{p}_X(\omega_n - \omega_m) g^X(\mathbf{k}, i\omega_m) \quad (2.58)$$

$$\Sigma_{xz}^\Gamma(i\omega_n) = -VT \sum_{\mathbf{k}, m} \hat{p}_Y(\omega_n - \omega_m) g^Y(\mathbf{k}, i\omega_m) \quad (2.59)$$

where  $D_{X/Y}(\omega_n) = \int d\Omega \, 2\Omega B_{X/Y}(\Omega) / (\Omega^2 + \omega_n^2)$  is the propagator for the spin-mode along  $x/y$ ,  $B_{X/Y}$  is its spectral function given by Eq. 2.57 above,  $V$  is the strength of the coupling and  $g^{l\pm}(\mathbf{k}, i\omega_m)$  denotes the Greens function of the  $E^\pm$  band at  $l$ . Analogous expressions hold for the electron pockets. To reproduce quantitatively the experimental data, the spectral functions are computed by using as fitting parameter the splitting of the spin-fluctuation energies  $\omega_{X/Y}$  (see Figure 2.5).

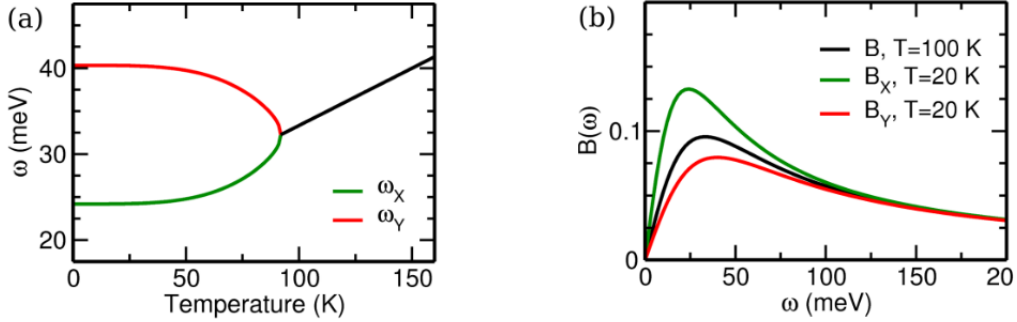


**Figure 2.5:** Evolution of the spin fluctuation with temperature. (a) Temperature evolution of the spin-fluctuations energies  $\omega_{X/Y}$  across the nematic transition. (b) Spin-fluctuations propagator above and below the structural transition  $T_S$ . Notice that in the nematic phase ( $T < T_S$ ) the spin propagator along  $x$  and  $y$  becomes different due to the differentiation of  $\omega_{X/Y}$ . Adapted from [60].

We refer the reader to [60] for further details. Here we, only point out that the crucial prediction of [60] is that, given the experimentally observed nematic Fermi surfaces reconstruction in FeSe, one can establish the sign of the anisotropy of the spin-fluctuations below  $T_S$ . In fact, in order to reproduce shape and orbital content of the ARPES Fermi surface one need to assume

$$\langle (\mathbf{S}_X^{yz})^2 \rangle > \langle (\mathbf{S}_y^{xz})^2 \rangle$$

i.e. spin-fluctuations along  $x$  are larger with respect to spin-fluctuations along  $y$ . This is a result that one can only get accounting for the spin-orbital entanglement into the spin-nematic approach. This prediction has been confirmed later by neutron scattering experiment in FeSe [134] and it is consistent with the analysis of the superconductivity mediated by nematic OSSF [133] in which the specific nematic orbital ordering induced by the nematic OSSF (with the elliptical Gamma pocket almost completely  $xz$  at the Fermi level See Figure 2.4) makes necessary to invoke a very strong nematic pairing with the superconducting coupling along  $x$  much stronger than the one along  $y$ .

# 3

## Magnetic excitations and superconductivity in the OSSF model

### 3.1. Introduction

The discovery of iron-based superconductors (IBS) raised immediate questions about the nature of the superconducting state and the pairing mechanism. From the very beginning it was proposed that pairing could be unconventional [19, 20]. This proposal has been triggered, from one side, by the small estimated value of the electron-phonon coupling [73], and, from the other side, by the proximity in the phase diagram of a magnetic instability nearby the superconducting one. As discussed in Section 1.5.1, within an itinerant-electron picture pairing is provided by repulsive spin-fluctuations between hole and electron pockets, connected by the same wavevector characteristic of the spin modulations in the magnetic phase [98, 99, 101, 135–137]. Given the repulsive and interband character of the interaction the expected symmetry for the gap function is the so-called  $s_{\pm}$ , i.e. an isotropic s-wave on each pocket with opposite sign between hole and electron pockets. This picture has been discussed within a more realistic description for IBS using multiorbital Hubbard model [34, 76, 98, 108, 109, 114] that provide a quantitative estimate of the superconducting properties starting from RPA-based description of the spin-susceptibility. As we discussed in Section 1.5.2, the inclusion of the orbital degree of freedom in the analysis open the possibility to find anisotropic  $s_{\pm}$  gap functions, in which the amplitude of the angular modulation and the presence of accidental nodes depends on the system parameters [34, 76, 102].

As we widely discuss in Section 1.5.2, the main issue with multiorbital models is that the implementation of these methods is complicated due to the number of the orbitals considered so that analytical treatments of the problems are often unattainable. Moreover the inclusion of fluctuations beyond RPA to describe spin-nematicity is not straightforward as instead in the band-language. In the previous Chapter, we discuss the Orbital Selective Spin Fluctuations (OSSF) model as the minimal model to describe the spin-nematic phase within a simple multiband language while at the same time retaining the orbital information. We showed that the orbital-selectivity makes the model extremely simple as the spin-fluctuation along  $x/y$  are given by a single orbital component  $yz/xz$ .

In this Chapter we aim to discuss in detail the magnetic excitations of the OSSF model and of the superconductivity mediated by OSSF. The main question we want to address is: Is it possible within the OSSF to reproduce the main features of the spin-excitations computed within microscopic five-orbital models? In Sections 3.2 - 3.3 we prove

that the OSSF qualitatively reproduce all the relevant features characterizing the RPA spin susceptibilities obtained within microscopic multiorbital models. This is a remarkable results, especially considering that the OSSF is based on the symmetric adapted model derived in [118] that only involved three orbitals, and that the orbital-selectivity of the spin-fluctuation reduces the computation of the spin susceptibility to a few scalar components.

A direct consequence of the orbital selectivity then, is that it makes possible to perform analytical calculations that allows us to easily interpret our results. A clear example of this is the momentum dependence of the RPA spin-susceptibility that is found within both microscopic five-orbital models and OSSF model. Within the OSSF the modulation can be directly linked to the orbital nesting properties of the low energy states connected by orbital-selective interband interaction.

In Section 3.4 we compute the superconducting vertex mediated by the spin fluctuations obtained in Section 3.3 and show how the pairing vertex inherits the orbital modulation given by the orbital-selective spin fluctuations. By solving the the corresponding gap equations, we find gap function characterized by anisotropic  $s_{\pm}$  gap functions that can also present accidental nodes when the interaction between electron pockets is taking into account in agreement with results obtained for a multiorbital Hubbard model [102]. A main result of the gap analysis is that the simplified description provided by the OSSF model unveils the dominant role of the orbital nesting over the band nesting in establishing the hierarchy of the band gaps.

## 3.2. Magnetic excitations and superconductivity in the multiorbital Hubbard model

The non-interacting tight-binding Hamiltonian for a five orbital model in the orbital basis takes the following form

$$H_0^{orb} = \sum_{ij\sigma} \sum_{\eta\eta'} t_{ij}^{\eta\eta'} d_{\eta i\sigma}^\dagger d_{\eta' j\sigma} + \sum_{i\sigma} \sum_{\eta} \epsilon_{\eta} n_{\eta i\sigma} \quad (3.1)$$

with the orbital indices  $\eta, \eta' = \{1, 2, 3, 4, 5\}$  denoting the five different  $Fe$ -d orbitals ( $d_{xz}, d_{yz}, d_{xy}, d_{x^2-y^2}, d_{3z^2-r^2}$ ),  $t_{ij}^{\eta\eta'}$  the tight-binding one-electron hopping parameters [18, 76] from the  $\eta$  orbital on site  $i$  to the  $\eta'$  orbital on site  $j$ ,  $d_{\eta i\sigma}^\dagger$  the creation operator of an electron in  $\eta$  orbital on the  $i$  site with spin  $\sigma = \{\uparrow, \downarrow\}$ ,  $\epsilon_{\eta}$  the site energy of the  $\eta$  orbital and  $n_{\eta i\sigma} = d_{\eta i\sigma}^\dagger d_{\eta i\sigma}$  the occupation number.

Within standard RPA analysis [20, 34, 76, 108], the pairing is assumed to be mediated by spin and charge fluctuations. It has been shown [76], that the charge susceptibility is more than one order of magnitude smaller than the spin susceptibility, therefore hereafter we focus on the spin channel only.

The spin susceptibility is a four orbital indices tensor,  $\chi_{\delta\delta'}^{\eta\eta'}(\mathbf{q}, \Omega)$ . This is obtained from the analytical continuation  $i\Omega_m \rightarrow \Omega + i0^+$  of the Matsubara spin-spin correlation function

$$\chi_{\delta\delta'}^{\eta\eta'}(\mathbf{q}, i\Omega_m) = \int_0^\beta d\tau e^{i\Omega_m \tau} \left\langle T_\tau \vec{S}^{\eta\delta}(\mathbf{q}, \tau) \vec{S}^{\eta'\delta'}(-\mathbf{q}, 0) \right\rangle \quad (3.2)$$

where  $\mathbf{q}$  is the momentum vector,  $\beta = 1/k_B T$  is the inverse temperature,  $\tau$  is the imaginary time and  $\Omega_m = 2m\pi k_B T$  is the bosonic Matsubara frequency. The spin operator in the

orbital space for the  $\eta, \delta$  orbitals is defined as

$$\vec{S}^{\eta\delta}(\mathbf{q}, \tau) = \sum_{\mathbf{k}s s'} \left( d_{\mathbf{k}s}^{\eta\dagger} \vec{\sigma}_{ss'} d_{\mathbf{k}+\mathbf{q}s'}^{\delta} \right) \quad (3.3)$$

with  $\vec{\sigma}_{ss'}$  the Pauli matrices for the spin operator being  $s, s'$  spin indices. Using this explicit definition given by Eq. 3.3 and applying the Wick's theorem to Eq. 3.2 the non-interacting spin susceptibility can be rewritten as

$$\chi_{\delta\delta'}^{\eta\eta'}(\mathbf{q}, \Omega_m) = -\frac{1}{\beta} \sum_{\mathbf{k}, n} Tr \left[ \left( G^{\delta\eta}(\mathbf{k}, i\omega_n) G^{\delta'\eta'}(\mathbf{k} + \mathbf{q}, i\omega_n + i\Omega_m) \right) \right] \quad (3.4)$$

where the spectral representation of the Green's function is given by the rotation to the orbital basis of the non-interacting Green's function in the band basis

$$G^{\delta\eta}(\mathbf{k}, i\omega_n) = \sum_m \frac{a_m^{\delta}(\mathbf{k}) a_m^{\eta*}(\mathbf{k})}{i\omega_n - E_m(\mathbf{k})} \quad (3.5)$$

where  $\omega_n = (2n + 1)\pi k_B T$  is the fermionic Matsubara frequency and  $a_m^{\eta}(\mathbf{k})$  the matrix elements connecting the orbital ( $\eta$ ) and the band space ( $m$ ) determined by diagonalization of the tight-binding Hamiltonian, Eq. 3.1. Performing the Matsubara frequency summation and setting  $\Omega \rightarrow 0$ , the static spin susceptibility for a generic multiorbital system is given by

$$\chi_{\delta\delta'}^{\eta\eta'}(\mathbf{q}) = - \sum_{\mathbf{k}, mn} \left( \frac{a_m^{\delta}(\mathbf{k}) a_m^{\eta*}(\mathbf{k}) a_n^{\eta'}(\mathbf{k} + \mathbf{q}) a_n^{\delta'*}(\mathbf{k} + \mathbf{q})}{E_n(\mathbf{k} + \mathbf{q}) - E_m(\mathbf{k})} f(E_n(\mathbf{k} + \mathbf{q})) - f(E_m(\mathbf{k})) \right) \quad (3.6)$$

with  $f(E_m(\mathbf{k}))$  the Fermi distribution function. The RPA spin-fluctuation is given in the form of Dyson-type equation

$$(\chi_{RPA}^S)_{\delta\delta'}^{\eta\eta'}(\mathbf{q}) = \frac{\chi_{\delta\delta'}^{\eta\eta'}(\mathbf{q})}{1 - (U_S)_{\delta\delta'}^{\eta\eta'} \chi_{\delta\delta'}^{\eta\eta'}(\mathbf{q})} \quad (3.7)$$

with  $(U_S)_{\delta\delta'}^{\eta\eta'}$  the non-zero components of the interaction spin matrix  $\hat{U}_S$  in terms of the interaction parameters [20, 76].

The singlet pairing vertex driven by spin-fluctuation is a four orbital indices tensor and can be computed on the low-energy sector in terms of the RPA spin susceptibility [76, 138] as

$$(\Gamma_{RPA})_{\delta\delta'}^{\eta\eta'}(\mathbf{k}, \mathbf{k}') = \frac{1}{2} (U_S)_{\delta\delta'}^{\eta\eta'} + \frac{3}{2} \frac{(U_S^2)_{\delta\delta'}^{\eta\eta'} \chi_{\delta\delta'}^{\eta\eta'}(\mathbf{k} - \mathbf{k}')}{1 - (U_S)_{\delta\delta'}^{\eta\eta'} \chi_{\delta\delta'}^{\eta\eta'}(\mathbf{k} - \mathbf{k}')} = \frac{1}{2} (U_S)_{\delta\delta'}^{\eta\eta'} + \frac{3}{2} (\chi_{RPA}^S)_{\delta\delta'}^{\eta\eta'}(\mathbf{k} - \mathbf{k}'). \quad (3.8)$$

Notice that the variety of possible diagrams given by Eq. 3.8 makes it unfeasible to draw the possible Feynman's diagrams up to orders larger than one.

The gap equation for the multiorbital model can be computed numerically by taking into account the singlet pairing vertex given by Eq. 3.8 as an eigenvalue problem in which the largest eigenvalue will lead to the highest transition temperature and its eigenfunction determines the symmetry of the gap (see e.g. [34, 76, 108, 139]). The main result is that an anisotropic sign changing s-wave  $s_{\pm}$  state is found as the dominant symmetry (for system parameters compatible with moderated-doped IBS), in agreement to experiments [67–69].

### 3.3. Magnetic excitations in the OSSF model: RPA analysis

We now compute the spin-excitation of the OSSF model within an RPA approach and compare our results to the ones obtained within the analysis of microscopic five-orbital model and three-band spin-nematic model. For that purpose, we focus on the tetragonal phase of the OSSF four-pocket model discussed in Section 2.2.

Within our OSSF model, the situation is substantially simplified as compared with the five-orbital tight-binding RPA approach due to the orbital-selective nature of the spin-fluctuations. Within the OSSF model we assume the spin operator to be intraorbital. Notice that this already reduces the spin-susceptibility of Eq. 3.2 to a two-orbital indices matrix

$$\chi^{\eta\eta'}(\mathbf{q}, i\Omega_m) = \int_0^\beta d\tau e^{i\Omega_m \tau} \left\langle T_\tau \vec{S}^\eta(\mathbf{q}, \tau) \vec{S}^{\eta'}(-\mathbf{q}, 0) \right\rangle \quad (3.9)$$

with  $\vec{S}^\eta(\mathbf{q}, \tau) = \sum_{\mathbf{k}ss'} c_{\mathbf{k}s}^{\eta\dagger} \vec{\sigma}_{ss'} c_{\mathbf{k}+\mathbf{q}s'}$  the intraorbital spin operator. Moreover, the low-energy projection further simplified the spin-susceptibility structure as the low-energy states are defined only around high symmetry point and have a well defined orbital character described by Eq. 2.23. As a consequence also the Green's functions are defined only for  $l = \Gamma, X, Y$  as  $G^l(\mathbf{k}, i\omega_n) = \hat{\mathcal{U}}^l(\mathbf{k}, i\omega_n) \text{diag}(g^{l+}(\mathbf{k}, i\omega_n), g^{l-}(\mathbf{k}, i\omega_n)) \hat{\mathcal{U}}^{l-1}(\mathbf{k}, i\omega_n)$ . Here  $\hat{\mathcal{U}}^l$  are the matrices that diagonalize the  $l$ -Hamiltonian given by Eq. 2.24 and  $g^{l\pm}(\mathbf{k}, i\omega_n) = (i\omega_n - E_{\mathbf{k}}^{l\pm})^{-1}$  the Green's functions in the band basis. Substituting the intraorbital spin operator  $\vec{S}^\eta(\mathbf{q}, \tau)$  and applying Wick's theorem to Eq. 3.9, the intraorbital spin susceptibility in the low-energy projection can be read as

$$\chi^{ll'}(\mathbf{q}, i\Omega_m) = -\frac{1}{\beta} \sum_{\mathbf{k}, n} \text{Tr} \left[ \hat{G}^l(\mathbf{k}, i\omega_n) \hat{G}^{l'}(\mathbf{k} + \mathbf{q}, i\omega_n + i\Omega_m) \right] \quad (3.10)$$

Eq. 3.10 represents the spin susceptibility between two pockets  $l$  and  $l'$  and depends on the transferred momentum  $\mathbf{q} = \mathbf{k}' - \mathbf{k}$  and the external frequency  $\Omega$ .

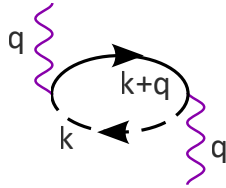


**Figure 3.1:** Intraorbital non-interacting spin susceptibility with transferred momentum  $\mathbf{q}$  in the OSSF model. The solid line represents an electron particle and the dashed line a hole particle.

In Figure 3.1 it is shown the Feynman's diagram representation for the intraorbital non-interacting spin susceptibility given by Eq. 3.10 within the OSSF model. The low energy spin susceptibility connects an electron (solid line) with a hole (dashed line) with the same orbital content, that is, it is an interpocket and intraorbital spin susceptibility. Performing the Matsubara frequency summation and setting  $\Omega \rightarrow 0$  in Eq. 3.10, we find the static susceptibility for the  $l_{\pm}$  pockets in terms of the Fermi distribution function  $f(E_{\mathbf{k}}^{l\pm})$  and the matrix element of each pocket  $|(u/v)^l(\mathbf{k})|$  connecting the orbital and the

band space is

$$\chi_{\eta}^{l_{\pm}l'_{\pm}}(\mathbf{q}) = \sum_{\mathbf{k}} \frac{f(\epsilon_{\mathbf{k}+\mathbf{q}}^{l'_{\pm}}) - f(\epsilon_{\mathbf{k}}^{l_{\pm}})}{\epsilon_{\mathbf{k}+\mathbf{q}}^{l'_{\pm}} - \epsilon_{\mathbf{k}}^{l_{\pm}}} |(u/v)_{\mathbf{k}}^l|^2 |(u/v)_{\mathbf{k}+\mathbf{q}}^{l'}|^2 \quad (3.11)$$

which has a much simpler expression than for the multiorbital model given in Eq. 3.6.

Within the OSSF model, we only consider magnetic fluctuations close to momenta  $\mathbf{Q}_X = (\pi, 0)$  and  $\mathbf{Q}_Y = (0, \pi)$ , so the two most relevant spin susceptibilities for a four-pocket model will involve the  $yz$  orbital coming from the interaction between the  $\Gamma_{\pm}$  holes with the  $X$  electron pockets, and the  $xz$  orbital coming from the  $\Gamma_{\pm}$  holes with the  $Y$  electron pockets near  $\mathbf{Q}_X$  and  $\mathbf{Q}_Y$  respectively. The spin susceptibility around  $\mathbf{Q}_M = (\pi, \pi)$  that involves the  $xy$  orbital from the interaction between the  $X$  and  $Y$  electron pockets is also taken into account in order to better compare with the results for the multiorbital model in which all five orbital contributions are considered. Notice that the inclusion of the  $\mathbf{Q}_M = (\pi, \pi)$  susceptibility within the OSSF is straightforward due to the orbital selectivity of the spin fluctuation involved in the exchange process. In Appendix C.1.1 are shown all the details about the computation of Eq. 3.11.

The RPA spin susceptibilities are obtained in the form of Dyson-type equations as

$$\chi_{\eta RPA}^{l_{\pm}l'_{\pm}}(\mathbf{q}) = \frac{\chi_{\eta}^{l_{\pm}l'_{\pm}}(\mathbf{q})}{1 - \tilde{U} \chi_{\eta}^{l_{\pm}l'_{\pm}}(\mathbf{q})} \quad (3.12)$$

with  $\tilde{U}$  the intraorbital effective coupling and  $\chi_{\eta}^{l_{\pm}l'_{\pm}}(\mathbf{q})$  the non-interacting spin susceptibility given by Eq. 3.11. Notice that, due to the orbital selectivity of the spin fluctuations, the expressions for the spin susceptibility given by Eq. 3.11 and the RPA spin susceptibility given by 3.12, acquire a scalar structure in the orbital basis. This will be crucial in order to compute analytically in the following Sections 3.4 and 3.3 the pairing vertex and superconducting gaps respectively, making the computations much more manageable than for the multiorbital models.

To get insight into the previous result, we perform a numerical estimate for the RPA spin susceptibility given by Eq. 3.12 for a four-pocket model in the tetragonal phase. Figure 3.2 shows the  $\chi_{yzRPA}^{\Gamma+X}(\mathbf{q})$ ,  $\chi_{yzRPA}^{\Gamma-X}(\mathbf{q})$  and  $\chi_{xyRPA}^{XY}(\mathbf{q})$  orbital components of the RPA spin susceptibility, providing a significant qualitative insight into the role of the orbital degrees of freedom. In the upper panel we 3D color maps in  $\mathbf{q}_x, \mathbf{q}_y$ . In the bottom panel of we show the  $\mathbf{q}_x, \mathbf{q}_y$  2D cuts. The middle point for all the 2D plots is  $\mathbf{Q}_X = (\pi, 0)$  for the electron-hole spin susceptibilities and  $\mathbf{Q}_M = (\pi, \pi)$  for the electron-electron one. The right part of each graphics represents the  $\chi_{\eta RPA}^{l_{\pm}l'_{\pm}}$  by moving from the center of the 3D plots in the  $\mathbf{q}_x$  momentum, maintaining  $\mathbf{q}_y$  constant and analogously on the other side. This representation makes easier to compare the relative weight of the different susceptibilities.

The specific expressions of the non-interacting and the RPA spin susceptibility for the different pockets are given in Appendix C.1.2. Notice that the contributions of the  $Y$  pocket (not shown) are equivalent to those for the  $X$  pockets with a  $\pi/2$  rotation, since in the tetragonal phase the susceptibility is isotropic in both directions. From Figure 3.2 we can highlight some main results:

(i) The orbital-selective RPA spin susceptibilities peaked at  $\mathbf{Q}_X$  and  $\mathbf{Q}_M$  show a clear momentum-dependent structure of the peaks. This can be explained due to the degree of orbital nesting between pockets. The orbital nesting indicates the relative orbital composition between the two pockets involved in the spin-exchange mechanism. In Figure 3.2 we



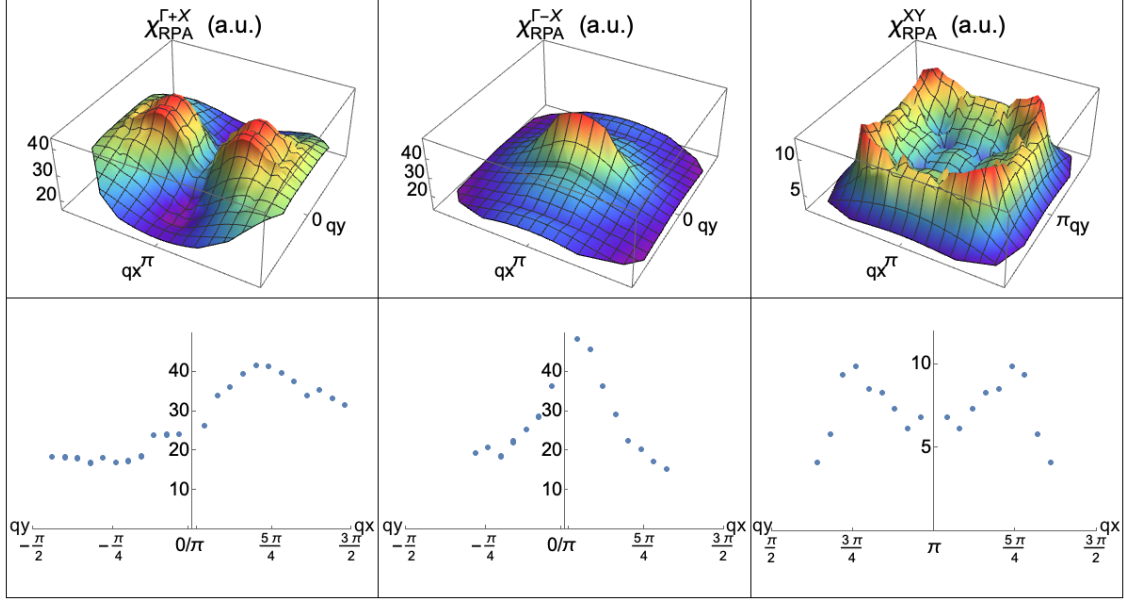


**Figure 3.2:** RPA spin susceptibility for a four-pocket model in the tetragonal phase in 3D (upper panel) and 2D cuts (bottom panel) around the high symmetry points  $X$  for the hole-electron sector and  $M$  for the electron-electron sector. The right-hand part of the 2D cuts represents the  $\mathbf{q}_x$  direction and the left-hand part the  $\mathbf{q}_y$  direction starting from  $X = (\pi, 0)$  or  $M = (\pi, \pi)$  points.

can see that when there is an orbital mismatch, as is the case of  $\Gamma_+$  and  $X$  pockets, the spin susceptibility develops two incommensurate peaks around  $\mathbf{Q}_X$ . In contrast, if there is an orbital match between pockets, i.e. the case of  $\Gamma_-$  and  $X$ , the spin susceptibility develops a single commensurate peak at the  $\mathbf{Q}_X = (\pi, 0)$ . For the  $\chi_{xyRPA}^{XY}(\mathbf{q})$  susceptibility there is a total mismatch between the  $xy$  orbital of the electrons pockets. Thus, the spin susceptibility is totally incommensurate and develops four symmetric peaks that correspond with the overlap of the  $xy$  orbital contribution around the  $M = (\pi, \pi)$  point.

(ii) From Figure 3.2 we can see that the RPA spin susceptibility at  $\mathbf{Q}_X$  is greater by moving in the  $\mathbf{q}_x$  direction than in the  $\mathbf{q}_y$ . This is due to the orbital selectivity of the spin fluctuation that connects the  $\Gamma_{\pm}$  with the  $X$ . Notice that for the  $\mathbf{Q}_M$  spin susceptibility we get a symmetric contributions in both directions  $\mathbf{q}_x$  and  $\mathbf{q}_y$  due to the equal contribution from the  $xy$  orbital.

(iii) The main contribution to the spin susceptibility comes from the  $\mathbf{Q}_X$  spin-mode, i.e.  $\chi_{yzRPA}^{\Gamma_{\pm}X}(\mathbf{q})$  (and analogously the  $\chi_{xzRPA}^{\Gamma_{\pm}Y}(\mathbf{q})$ ) contributions are much greater (four times greater) than the electron-electron exchange  $\chi_{xyRPA}^{XY}(\mathbf{q})$ . Among the two hole pockets, we find that the commensurate peak coming in  $\chi_{yzRPA}^{\Gamma_-X}(\mathbf{q})$  is bigger than the non-commensurate one in  $\chi_{yzRPA}^{\Gamma_+X}(\mathbf{q})$ . This can also be explained thanks to the better orbital nesting in the former case.

We now compare our results obtained within the OSSF model with a numerical calculation of the RPA spin susceptibility for a five-orbital tight-binding four-pocket model building on Eq. 3.6 and 3.7. By tuning the filling and the crystal field we consider two different cases: the first one corresponding to a four-pocket model with better nesting between the  $\Gamma_-$  and the electron pockets, and the second case is appropriate to describe a four-pocket model with better nesting between the  $\Gamma_+$  and the  $X/Y$  pockets. We obtained



for the first case a commensurability of the RPA spin susceptibility at the  $\mathbf{Q}_X = (\pi, 0)$ . Whereas in the second case we get an non-commensurate peaks around  $\mathbf{Q}_X = (\pi, 0)$ . Therefore, the same orbital modulation for the momentum dependence of the RPA spin susceptibility is obtained with both different models. We also compute the RPA spin susceptibility coming from the electron-electron sector within the five-orbital model. We obtain that the contribution from this sector is negligible in comparison with the one for the hole-electron sector. This result is also in agreement with other different studies of the RPA spin susceptibility within a multiorbital models given by Ref. [20, 76, 139].

Notice that, the orbital modulation of the RPA spin susceptibility is an effect that comes directly from taking into account the orbital degree of freedom of IBS. Within a low-energy multiband model, which is blind to the orbital content of the system, the spin susceptibility give to two equivalent peaks with the same commensurable narrow structure (see Figure 1.7b). Therefore, within this model is not possible to appreciate the orbital modulation in the momentum dependence of the spin susceptibility.

Our results are particularly important. In fact, while a generic correlation between the orbital-make up of the Fermi surface and the momentum-dependent structure of the RPA spin excitation has been already highlighted within multiobital models (e.g. [102]), the explicit link and precise relationship between orbital nesting and momentum dependence of the spin-susceptibility is a new results of the RPA analysis within the OSSF model.

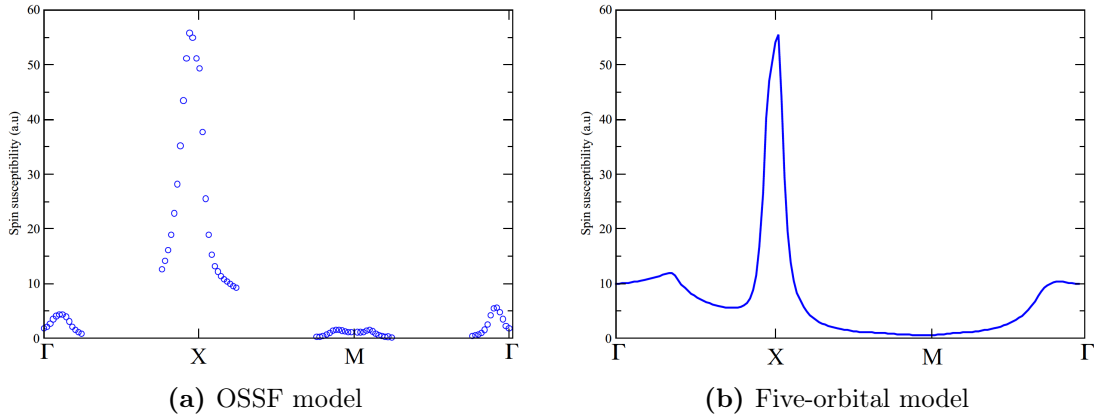


**Figure 3.3:** Cuts of the total RPA spin susceptibility along the high symmetry directions  $\Gamma XM\Gamma$  in the Brillouin zone within the (a) OSSF model (b) five-orbital tight-binding model. The interaction parameters have been chosen for (a) as  $\tilde{U} = 1\text{eV}$  and (b) as  $U = 1.2\text{eV}$ . Notice for the OSSF model the discontinuity of the susceptibility is due to the OSSF model is a low energy model and we only get the contribution near the Fermi surface around the high symmetry points  $\Gamma, X, M$ .

To conclude our comparative analysis, in Figure 3.3 we compare the cuts along the main symmetry directions of the RPA spin susceptibility (included the intraband ones) computed within the OSSF model and within the five-orbital tight-binding model. The calculation performed within the OSSF model reproduce remarkably well the overall momentum-dependence of the spin-spectrum as well as the relative height and width of the various peaks.

The comparative analysis performed in this Section is extremely encouraging as it proves that we can still obtain reliable description of the spin spectrum within the OSSF model of Eq. 3.11, without dealing with the tensorial form of the spin susceptibility given in the five-orbital model, Eq. 3.6.

### 3.4. Superconductivity mediated by the OSSF

Assuming that same spin fluctuations responsible for the magnetism, represented in Figure 3.1, are also responsible for the superconductivity in the IBS, in the present section we compute the pairing interaction that arises from the exchange of the spin fluctuations discussed in the previous section and the correspondent gap equations for a four-pocket model. We compare the results with the five-orbital microscopic model.

#### 3.4.1. Superconducting vertex: RPA analysis

To determine the superconducting vertex in the random phase approximation, we draw in Figure 3.4 all Feynman's diagrams that contains only the (scalar) spin susceptibilities up to finite order in perturbation of  $\tilde{U}$  for electrons of opposite spin and momentum. From Figure 3.4 we can draw some relevant conclusions:

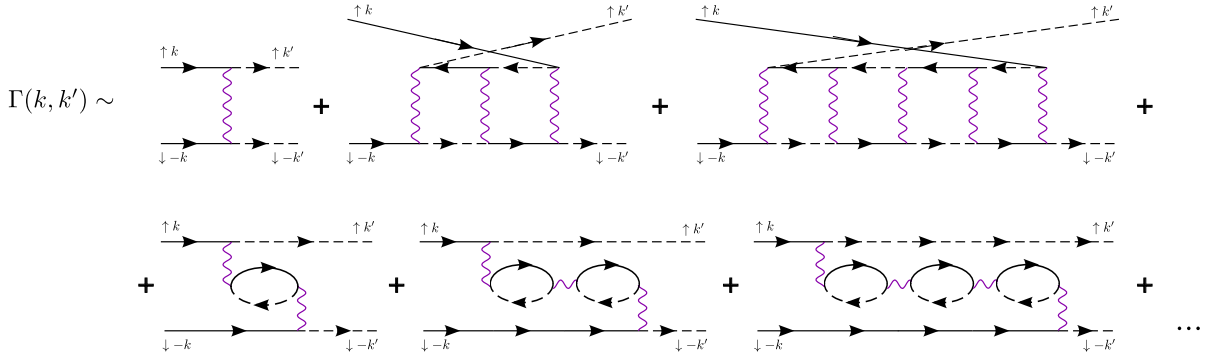


**Figure 3.4:** Pairing vertex in random phase approximation up to fifth order within the OSSF model.

(i) As we discussed in Section 3.2, within the five-orbital model to draw analytically all the Feynman's diagrams involved in the pairing interaction vertex is something almost unfeasible due to the large number of different possible diagrams. This is due to the complex tensorial structure of the pairing vertex, Eq. 3.8. On the contrary, given the scalar character of the low-energy orbital-selective spin susceptibility we can easily draw analytically all the possible diagrams.

(ii) Due to the simple orbital structure of the pairing vertex within the OSSF model, the diagrams involved represented in Figure 3.4 may look similar to those in the original spin fluctuation single-orbital Hubbard model to pattern the cuprates [140]. It is important to notice that only the mathematical treatment for the diagrams is similar between these two models, because the physical meaning is completely different. In the OSSF model the starting point is a three-orbital low energy model where the exchanged spin fluctuations come from the low energy-bands. In contrast, within the Hubbard model the full bands are taking into account.

(iii) As a consequence of the projection to a constrained orbital space within the OSSF model, the diagrammatic for the RPA pairing vertex is formally equivalent to the one for the band-basis model which does not contain the orbital information of the spin-fluctuations exchange. Within the multiband model the RPA pairing vertex is composed by the exchange of spin fluctuations connecting an electron pocket with a hole pocket.

While within the OSSF model, the essential difference is that the low energy exchanged spin fluctuations connect a hole with an electron pocket with the *same orbital content*  $yz$  or  $xz$ . In this way, we retain the simplicity of the analysis of the Feynman's diagrams within the multiband model and, at the same time, we account the orbital degree of freedom of the system.

By applying the RPA approach and symmetrizing the singlet pairing interaction vertex given in Figure 3.4, we get that the leading RPA diagrams for the vertex within the OSSF model can be read as

$$\Gamma_{\eta}^{l_{\pm}l'_{\pm}}(\mathbf{q}) = \tilde{U} + \frac{\tilde{U}^3 \chi_{\eta}^{l_{\pm}l'_{\pm}}(\mathbf{q})}{1 - \tilde{U}^2 \chi_{\eta}^{l_{\pm}l'_{\pm}}(\mathbf{q})} + \frac{\tilde{U}^2 \chi_{\eta}^{l_{\pm}l'_{\pm}}(\mathbf{q})}{1 - \tilde{U} \chi_{\eta}^{l_{\pm}l'_{\pm}}(\mathbf{q})} \quad (3.13)$$

where  $\mathbf{q} = \mathbf{k}' - \mathbf{k}$  is the transferred momentum,  $\tilde{U}$  is the intraorbital effective coupling and  $\chi_{\eta}^{l_{\pm}l'_{\pm}}(\mathbf{q})$  the intraorbital susceptibility given in formula Eq. 3.11. In Section C.2.1 the detailed computation of the RPA pairing vertex within the OSSF model is shown.

As follows, we perform a numerical estimates for the four-pocket model. We get the RPA vertex is proportional to the spin susceptibility and thus preserves the orbital dependence and all the physical properties as the RPA spin susceptibility given by Eq. 3.12. For instance, we get the same criterion of commensurability or incommensurability depending on the orbital nesting between pockets. In the same way, we also obtained that the dominant contribution to the RPA pairing vertex is given by the spin-fluctuations exchange between hole-electron pockets, i.e. the  $\Gamma_{yz}^{\Gamma_{\pm}X}(\mathbf{q})$  and  $\Gamma_{xz}^{\Gamma_{\pm}Y}(\mathbf{q})$  contributions, being the  $\Gamma_{\eta}^{\Gamma_{\pm}l}(\mathbf{q})$  the greater.

### 3.4.2. Superconducting gaps

In this section we solve the BCS gap equation mediated by the orbital selective spin fluctuation exchanged computed in the previous section for a four pocket model within the OSSF model. Let's consider first the pairing Hamiltonian involving only the  $yz$  and  $xz$  orbital contributions

$$\begin{aligned} H_{yz,xz}^{pairing} = & - \sum_{\mathbf{k},\mathbf{k}'} \Gamma_{yz}^{\Gamma_{+}X} \left[ \left( u_{\mathbf{k}}^{\Gamma} \right)^2 h_{\mathbf{k}}^{+\dagger} h_{-\mathbf{k}}^{+\dagger} (u_{\mathbf{k}}^X)^2 e_{\mathbf{k}'}^X e_{-\mathbf{k}'}^X \right] \left( \right. \\ & - \sum_{\mathbf{k},\mathbf{k}'} \Gamma_{yz}^{\Gamma_{-}X} \left[ \left( v_{\mathbf{k}}^{\Gamma} \right)^2 h_{\mathbf{k}}^{-\dagger} h_{-\mathbf{k}}^{-\dagger} (u_{\mathbf{k}}^X)^2 e_{\mathbf{k}'}^X e_{-\mathbf{k}'}^X \right] \left( \right. \\ & - \sum_{\mathbf{k},\mathbf{k}'} \Gamma_{xz}^{\Gamma_{+}Y} \left[ \left( v_{\mathbf{k}}^{\Gamma} \right)^2 h_{\mathbf{k}}^{+\dagger} h_{-\mathbf{k}}^{+\dagger} (u_{\mathbf{k}}^Y)^2 e_{\mathbf{k}'}^Y e_{-\mathbf{k}'}^Y \right] \left( \right. \\ & \left. - \sum_{\mathbf{k},\mathbf{k}'} \Gamma_{xz}^{\Gamma_{-}Y} \left[ \left( u_{\mathbf{k}}^{\Gamma} \right)^2 h_{\mathbf{k}}^{-\dagger} h_{-\mathbf{k}}^{-\dagger} (u_{\mathbf{k}}^Y)^2 e_{\mathbf{k}'}^Y e_{-\mathbf{k}'}^Y \right] \right) + h.c. \end{aligned} \quad (3.14)$$

where  $\Gamma_{\eta}^{l_{\pm}l'_{\pm}}$  with  $\eta = yz/xz$  is the RPA pairing vertex given by Eq. 3.13 for the different pockets  $l_{\pm}l'_{\pm}$ . The coefficient  $(u_{\mathbf{k}}^l)^2$  and  $(v_{\mathbf{k}}^l)^2$  are the coherence factors that connect the orbital and the band basis and account for the pockets orbital character.

The pairing Hamiltonian given by Eq. 3.14 is solved in the mean field approximation by defining the orbital dependent superconducting order parameters for the hole sector  $(\Delta_{yz}^+, \Delta_{yz}^-, \Delta_{xz}^+, \Delta_{xz}^-)$  and for the electron sector  $(\Delta_{yz}^{e+}, \Delta_{yz}^{e-}, \Delta_{xz}^{e+}, \Delta_{xz}^{e-})$ . The precise definition of these parameter is shown in Appendix C.2.2.

The resulting linearized gap equations at  $T=0$  read as

$$\Delta_{yz\mathbf{k}'}^+ = - \sum_k \frac{\Gamma_{yz\mathbf{k}\mathbf{k}'}^{\Gamma+X}}{|v_{F\mathbf{k}}^X|} (u_{\mathbf{k}}^X)^2 \left[ (u_{\mathbf{k}}^X)^2 \Delta_{yz\mathbf{k}}^{e+} + (u_{\mathbf{k}}^X)^2 \Delta_{yz\mathbf{k}}^{e-} \right] \left( \quad \right) \quad (3.15)$$

$$\Delta_{yz\mathbf{k}'}^- = - \sum_k \frac{\Gamma_{yz\mathbf{k}\mathbf{k}'}^{\Gamma-X}}{|v_{F\mathbf{k}}^X|} (u_{\mathbf{k}}^X)^2 \left[ (u_{\mathbf{k}}^X)^2 \Delta_{yz\mathbf{k}}^{e+} + (u_{\mathbf{k}}^X)^2 \Delta_{yz\mathbf{k}}^{e-} \right] \quad (3.16)$$

$$\Delta_{xz\mathbf{k}'}^+ = - \sum_k \frac{\Gamma_{xz\mathbf{k}\mathbf{k}'}^{\Gamma+Y}}{|v_{F\mathbf{k}}^Y|} (u_{\mathbf{k}}^Y)^2 \left[ (u_{\mathbf{k}}^Y)^2 \Delta_{xz\mathbf{k}}^{e+} + (u_{\mathbf{k}}^Y)^2 \Delta_{xz\mathbf{k}}^{e-} \right] \left( \quad \right) \quad (3.17)$$

$$\Delta_{xz\mathbf{k}'}^- = - \sum_k \frac{\Gamma_{xz\mathbf{k}\mathbf{k}'}^{\Gamma-Y}}{|v_{F\mathbf{k}}^Y|} (u_{\mathbf{k}}^Y)^2 \left[ (u_{\mathbf{k}}^Y)^2 \Delta_{xz\mathbf{k}}^{e+} + (u_{\mathbf{k}}^Y)^2 \Delta_{xz\mathbf{k}}^{e-} \right] \quad (3.18)$$

$$\Delta_{yz\mathbf{k}'}^{e+} = - \sum_k \frac{\Gamma_{yz\mathbf{k}\mathbf{k}'}^{\Gamma+X}}{|v_{F\mathbf{k}}^{h+}|} (u_{\mathbf{k}}^\Gamma)^2 \left[ (u_{\mathbf{k}}^\Gamma)^2 \Delta_{yz\mathbf{k}}^+ + (v_{\mathbf{k}}^\Gamma)^2 \Delta_{xz\mathbf{k}}^+ \right] \left( \quad \right) \quad (3.19)$$

$$\Delta_{yz\mathbf{k}'}^{e-} = - \sum_k \frac{\Gamma_{yz\mathbf{k}\mathbf{k}'}^{\Gamma-X}}{|v_{F\mathbf{k}}^{h-}|} (v_{\mathbf{k}}^\Gamma)^2 \left[ (v_{\mathbf{k}}^\Gamma)^2 \Delta_{yz\mathbf{k}}^- + (u_{\mathbf{k}}^\Gamma)^2 \Delta_{xz\mathbf{k}}^- \right] \left( \quad \right) \quad (3.20)$$

$$\Delta_{xz\mathbf{k}'}^{e+} = - \sum_k \frac{\Gamma_{xz\mathbf{k}\mathbf{k}'}^{\Gamma+Y}}{|v_{F\mathbf{k}}^{h+}|} (v_{\mathbf{k}}^\Gamma)^2 \left[ (u_{\mathbf{k}}^\Gamma)^2 \Delta_{yz\mathbf{k}}^+ + (v_{\mathbf{k}}^\Gamma)^2 \Delta_{xz\mathbf{k}}^+ \right] \left( \quad \right) \quad (3.21)$$

$$\Delta_{xz\mathbf{k}'}^{e-} = - \sum_k \frac{\Gamma_{xz\mathbf{k}\mathbf{k}'}^{\Gamma-Y}}{|v_{F\mathbf{k}}^{h-}|} (v_{\mathbf{k}}^\Gamma)^2 \left[ (v_{\mathbf{k}}^\Gamma)^2 \Delta_{yz\mathbf{k}}^- + (u_{\mathbf{k}}^\Gamma)^2 \Delta_{xz\mathbf{k}}^- \right] \quad (3.22)$$

with  $v_{F\mathbf{k}}^l = \partial_{\mathbf{k}}(\epsilon_{\mathbf{k}}^{l\pm})$  the Fermi velocity for the pocket  $l$ . Eqs. 3.15-3.22 represent the orbital components for each gap. Then, we define the total low-energy band gaps  $\Delta_{\mathbf{k}}^l$  as

$$\Delta_{\mathbf{k}}^{\Gamma+} = (u_{\mathbf{k}}^\Gamma)^2 \Delta_{yz\mathbf{k}}^+ + (v_{\mathbf{k}}^\Gamma)^2 \Delta_{xz\mathbf{k}}^+ \quad (3.23)$$

$$\Delta_{\mathbf{k}}^{\Gamma-} = (v_{\mathbf{k}}^\Gamma)^2 \Delta_{yz\mathbf{k}}^- + (u_{\mathbf{k}}^\Gamma)^2 \Delta_{xz\mathbf{k}}^- \quad (3.24)$$

$$\Delta_{\mathbf{k}}^X = (u_{\mathbf{k}}^X)^2 \Delta_{yz\mathbf{k}}^{e+} + (u_{\mathbf{k}}^X)^2 \Delta_{yz\mathbf{k}}^{e-} \quad (3.25)$$

$$\Delta_{\mathbf{k}}^Y = (u_{\mathbf{k}}^Y)^2 \Delta_{xz\mathbf{k}}^{e+} + (u_{\mathbf{k}}^Y)^2 \Delta_{xz\mathbf{k}}^{e-} \quad (3.26)$$

where each low-energy band gap involves the sum of the different orbital contributions weighted by the correspondent coherent factors of the pocket. The gap functions  $\Delta_{\mathbf{k}}^l$ , given by the set of coupled equations in 3.23-3.26, contain information on the spatial and orbital structures of the pairs.

To get insight into these results, we solve numerically the linearized gap equations for a four pocket model given by Eqs. 3.15-3.22, by searching for the largest eigenvalue that corresponds to the leading instability of the system. Then, we calculate the eigenfunction corresponding to the leading instability that determines the symmetry and the structure of the gap function. In Figure 3.5 the solution for the low-energy band gaps functions  $\Delta_{\mathbf{k}}^l$  given by Eqs. 3.23-3.26 is shown.

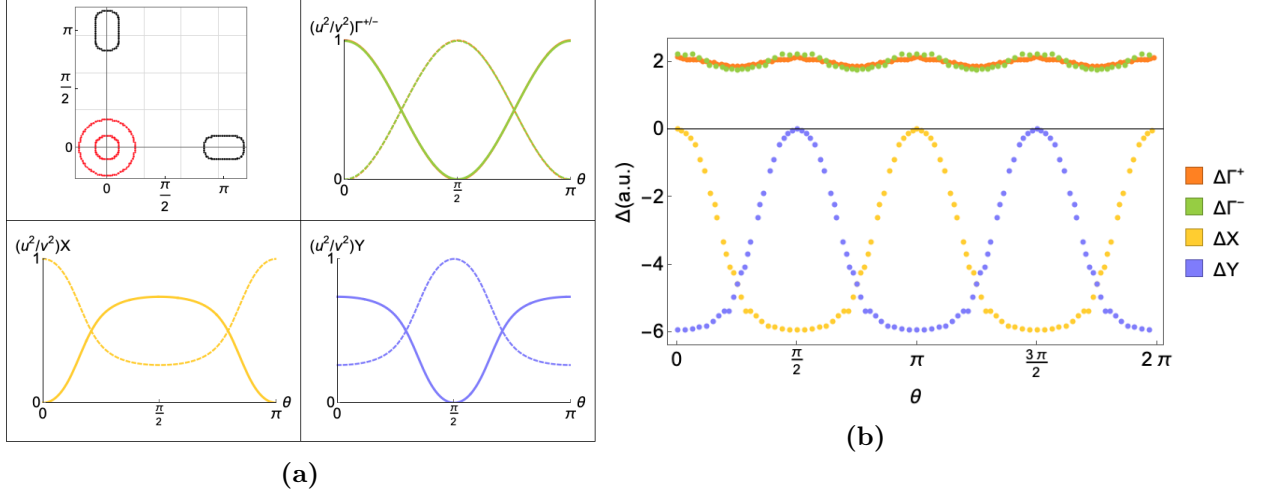


**Figure 3.5:** (a) Gap function plotted on the Fermi surfaces (red positive and black negative values) and orbital content of the  $\Gamma_{\pm}$  (green and orange) X (yellow) and Y (blue) pockets a function of the angle  $\theta$  in the tetragonal phase. Solid and dashed lines represent the  $u_{\mathbf{k}}^l$  and  $v_{\mathbf{k}}^l$  orbital coherence factor respectively. (b) Angular dependence of the superconducting band gaps given in Eqs. 3.23-3.26. An anisotropic s-wave symmetry is obtained within the OSSF model. The band parameter are specified in Appendix B.3 and  $\tilde{U} = 1\text{eV}$ .

In Figure 3.5 the band gaps symmetry and structure and the orbital composition for a four-pocket model are shown within our OSSF model. The following results are drawn:

(i) In the first panel in Figure 3.5a, the RPA band gaps (Eqs. 3.23-3.26) are plotted on the Fermi surface. From it we can read that the gap in the hole pocket sector is positive sign (red color), while the gap for the electron sector is negative sign (black color). Therefore, we obtain a sign changing s-wave gap between the hole and the electron pockets in agreement with five-orbital tight-binding model where a  $s_{\pm}$  symmetry is also achieved [76, 102] and as also expected for low-energy multiband models [19, 20, 98].

(ii) Besides that, we show in Figure 3.5b the angular dependence of the superconducting RPA band gaps (Eqs. 3.23-3.26). Therefore, we get an anisotropic momentum  $s_{\pm}$  gap symmetry. The momentum dependence can be explained as in terms of the orbital content of the Fermi surface  $u_{\mathbf{k}}^l$  and  $v_{\mathbf{k}}^l$  (plotted in Figure 3.5a) and the orbital nesting in the superconducting order parameters (given in Eqs. 3.15-3.22). This result is again in agreement with multiorbital models [102], but it cannot be reproduce within a perfect nested multiband model due to the lack of spin-orbital interplay.

(iii) Another interesting related result concerns the orbital momentum modulation of the gap bands. In Figure 3.5b it is shown that the maximum and the minimum values for the angular dependence of the different pockets correspond exactly with the angular position where there are better orbital nesting between the holes and the electrons. Thus, for the  $\Gamma$  sector, the maximum values for the angular dependence band gaps are located at the  $\theta = (0, \pi/2, \pi, 3\pi/2)$  angular positions corresponding with the position of the  $yz$  and  $xz$  orbitals. While for the electron sector X/Y the maximum values of the band gaps correspond to the  $yz/xz$  orbitals position at  $\theta = (\pi/2, 3\pi/2)$  and  $\theta = (0, \pi)$  for the X/Y pockets respectively and it is zero where the  $xy$  orbital is placed.

In conclusion, from the analysis of Figure 3.5 we get that within the OSSF model applied to a prototypical four-pocket model for IBS we find an anisotropic sign changing

s-wave gap symmetry, i.e., a  $s_{\pm}$  s-wave band gap. This result is in agreement with calculations performed within five-orbital tight-binding models in which the gap anisotropy found for the  $s_{\pm}$  s-wave state in RPA spin fluctuations is discussed in Ref. [76, 102]. We illustrate that the overall momentum dependence of the band gaps is determined by the momentum-dependence of the pairing vertex and the orbital-make of the Fermi surface. A key parameter that control the angular modulation of the gap is the orbital nesting between the low-energy states connected by the spin-fluctuations that determine the structure of the spin-susceptibilities (and thus of the pairing vertex).

To provide a quantitative analysis to these results, we compare them with the ones obtained in Ref. [102], where the anisotropy of the gaps for a five-orbital model is discussed in detail by using RPA calculations for the exchange of spin and charge fluctuations. The authors conclude that the anisotropy of the gap on the different Fermi surfaces has been shown to arise from an interplay of the orbital make-up of the states on the Fermi surface together with the momentum dependence of the fluctuation-exchange pairing interaction. Moreover, to minimize the repulsion between the electron Fermi surfaces, the electron can present accidental nodes.

To provide a more accurate comparison we use a set of band parameters to generate similar Fermi surface to the ones used in [102] (see Appendix C.2.3).

We also take into account the pairing mediated by  $xy$ -spin-fluctuation peaked at  $\mathbf{Q}_M$ . This means that we have to add to the pairing Hamiltonian, Eq. 3.27 the  $xy$ -pairing term

$$H_{xy}^{pairing} = - \sum_{\mathbf{k}, \mathbf{k}'} \Gamma_{xy \mathbf{k}\mathbf{k}'}^{XY} \left[ (v_{\mathbf{k}}^X)^2 e_{\mathbf{k}'}^X e_{-\mathbf{k}'}^X (v_{\mathbf{k}}^Y)^2 e_{\mathbf{k}'}^Y e_{-\mathbf{k}'}^Y \right] + h.c. \quad (3.27)$$

where  $\Gamma_{xy \mathbf{k}\mathbf{k}'}^{XY}$  is the RPA pairing vertex given by Eq. 3.13 for the electron pockets  $X$  and  $Y$  around  $\mathbf{Q}_M = (\pi, \pi)$ .

By defining the new orbital dependent superconducting order parameters for the electron sector ( $\Delta_{xy}^{eY}, \Delta_{xy}^{eX}$ ) (see Appendix C.2.2) and then by solving the pairing Hamiltonian given in Eqs. 3.14 and 3.27 in a mean field approximation, the resulting linearized gap equations at  $T=0$  read as

$$\Delta_{yz\mathbf{k}'}^+ = - \sum_{\mathbf{k}} \frac{\Gamma_{yz\mathbf{k}\mathbf{k}'}^{\Gamma+X}}{|v_{F\mathbf{k}}^X|} (u_{\mathbf{k}}^X)^2 \left[ (u_{\mathbf{k}}^X)^2 \Delta_{yz\mathbf{k}}^{e+} + (u_{\mathbf{k}}^X)^2 \Delta_{yz\mathbf{k}}^{e-} + (v_{\mathbf{k}}^X)^2 \Delta_{xy\mathbf{k}}^{eX} \right] \left( \quad (3.28) \right.$$

$$\Delta_{yz\mathbf{k}'}^- = - \sum_{\mathbf{k}} \frac{\Gamma_{yz\mathbf{k}\mathbf{k}'}^{\Gamma-X}}{|v_{F\mathbf{k}}^X|} (u_{\mathbf{k}}^X)^2 \left[ (u_{\mathbf{k}}^X)^2 \Delta_{yz\mathbf{k}}^{e+} + (u_{\mathbf{k}}^X)^2 \Delta_{yz\mathbf{k}}^{e-} + (v_{\mathbf{k}}^X)^2 \Delta_{xy\mathbf{k}}^{eX} \right] \quad (3.29)$$

$$\Delta_{xy\mathbf{k}'}^{eY} = - \sum_{\mathbf{k}} \frac{\Gamma_{xy\mathbf{k}\mathbf{k}'}^{XY}}{|v_{F\mathbf{k}}^X|} (v_{\mathbf{k}}^X)^2 \left[ (u_{\mathbf{k}}^X)^2 \Delta_{yz\mathbf{k}}^{e+} + (u_{\mathbf{k}}^X)^2 \Delta_{yz\mathbf{k}}^{e-} + (v_{\mathbf{k}}^X)^2 \Delta_{xy\mathbf{k}}^{eX} \right] \left( \quad (3.30) \right.$$

$$\Delta_{xz\mathbf{k}'}^+ = - \sum_{\mathbf{k}} \frac{\Gamma_{xz\mathbf{k}\mathbf{k}'}^{\Gamma+Y}}{|v_{F\mathbf{k}}^Y|} (u_{\mathbf{k}}^Y)^2 \left[ (u_{\mathbf{k}}^Y)^2 \Delta_{xz\mathbf{k}}^{e+} + (u_{\mathbf{k}}^Y)^2 \Delta_{xz\mathbf{k}}^{e-} + (v_{\mathbf{k}}^Y)^2 \Delta_{xy\mathbf{k}}^{eY} \right] \left( \quad (3.31) \right.$$

$$\Delta_{xz\mathbf{k}'}^- = - \sum_{\mathbf{k}} \frac{\Gamma_{xz\mathbf{k}\mathbf{k}'}^{\Gamma-Y}}{|v_{F\mathbf{k}}^Y|} (u_{\mathbf{k}}^Y)^2 \left[ (u_{\mathbf{k}}^Y)^2 \Delta_{xz\mathbf{k}}^{e+} + (u_{\mathbf{k}}^Y)^2 \Delta_{xz\mathbf{k}}^{e-} + (v_{\mathbf{k}}^Y)^2 \Delta_{xy\mathbf{k}}^{eY} \right] \quad (3.32)$$

$$\Delta_{xy\mathbf{k}'}^{eX} = - \sum_{\mathbf{k}} \frac{\Gamma_{xy\mathbf{k}\mathbf{k}'}^{XY}}{|v_{F\mathbf{k}}^Y|} (v_{\mathbf{k}}^Y)^2 \left[ (u_{\mathbf{k}}^Y)^2 \Delta_{xz\mathbf{k}}^{e+} + (u_{\mathbf{k}}^Y)^2 \Delta_{xz\mathbf{k}}^{e-} + (v_{\mathbf{k}}^Y)^2 \Delta_{xy\mathbf{k}}^{eY} \right] \left( \quad (3.33) \right.$$

where we only report the equations that changed due to the  $xy$ -pairing channel, while the rest are identical to Eqs. 3.19-3.22. Notice that two new gaps equations Eqs. 3.33 and 3.30 are taking into account due to the inclusion of the  $XY$  pairing vertex  $\Gamma_{xy\mathbf{k}\mathbf{k}'}$ . Moreover, the orbital components for the gap equations for the hole sectors is modified by a new term coming from the new order parameters for the electron sector given by  $(\Delta_{xy}^{eY}, \Delta_{xy}^{eX})$ .

Then, we define the total low-energy band gaps  $\Delta_{\mathbf{k}}^l$  as

$$\Delta_{\mathbf{k}}^{\Gamma+} = (u_{\mathbf{k}}^{\Gamma})^2 \Delta_{yz\mathbf{k}}^+ + (v_{\mathbf{k}}^{\Gamma})^2 \Delta_{xz\mathbf{k}}^+ \quad (3.34)$$

$$\Delta_{\mathbf{k}}^{\Gamma-} = (v_{\mathbf{k}}^{\Gamma})^2 \Delta_{yz\mathbf{k}}^- + (u_{\mathbf{k}}^{\Gamma})^2 \Delta_{xz\mathbf{k}}^- \quad (3.35)$$

$$\Delta_{\mathbf{k}}^X = (u_{\mathbf{k}}^X)^2 \Delta_{yz\mathbf{k}}^{e+} + (u_{\mathbf{k}}^X)^2 \Delta_{yz\mathbf{k}}^{e-} + (v_{\mathbf{k}}^X)^2 \Delta_{xy\mathbf{k}}^{eX} \quad (3.36)$$

$$\Delta_{\mathbf{k}}^Y = (u_{\mathbf{k}}^Y)^2 \Delta_{xz\mathbf{k}}^{e+} + (u_{\mathbf{k}}^Y)^2 \Delta_{xz\mathbf{k}}^{e-} + (v_{\mathbf{k}}^Y)^2 \Delta_{xy\mathbf{k}}^{eY} \quad (3.37)$$

where each low-energy band gap involves the sum of the two different orbital contributions weighted by the correspondent coherent factors of the pocket.

In Figures 3.6a and 3.7a the Fermi surface used for the OSSF model and for the multiorbital model [102] are shown respectively. Notice that the electron Fermi surfaces are much bigger than the holes and there is a better band nesting between the  $\Gamma_+$  and the  $X/Y$  pocket than for the  $\Gamma_-$ .

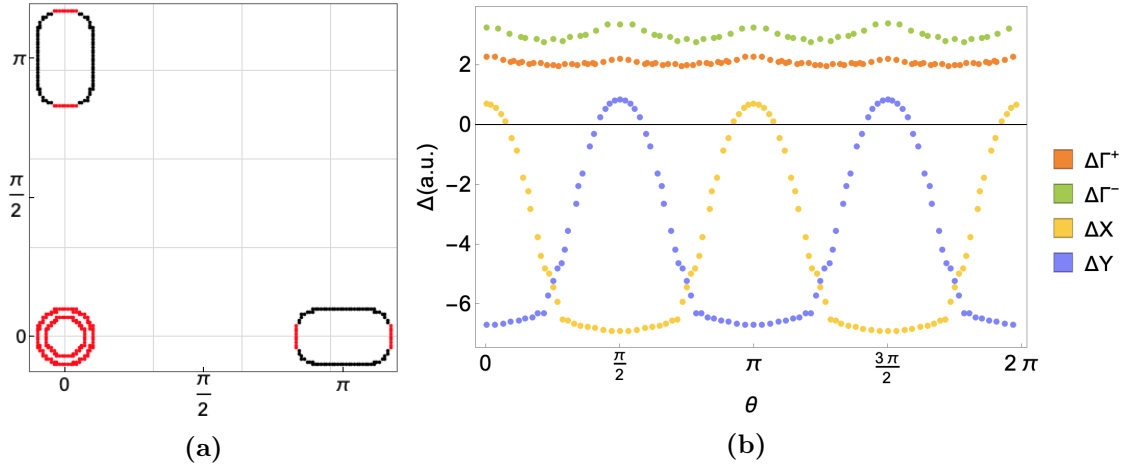


**Figure 3.6:** RPA gap function within the OSSF model (a) plotted on the Fermi surfaces (red circles positive and black circles negative), (b) plotted as a function of angle from 0 to  $2\pi$ . The band parameter are specified in Appendix C.2.3

Results for the gap function are summarized in Figures 3.6 and 3.7. From the comparison we find:

(i) The inclusion of the charge channel within the RPA analysis of the five-orbital model. In the five-orbital model [102] does not change qualitatively the results. We still find a good agreement within the OSSF model calculation in which only the spin-channel is considered and the microscopic model in which the charge channel is considered in the RPA resummation. This confirms that the spin channel provides the dominant pairing contribution and that this is well described within the OSSF model which is able to reproduce in a much simpler way the same results.



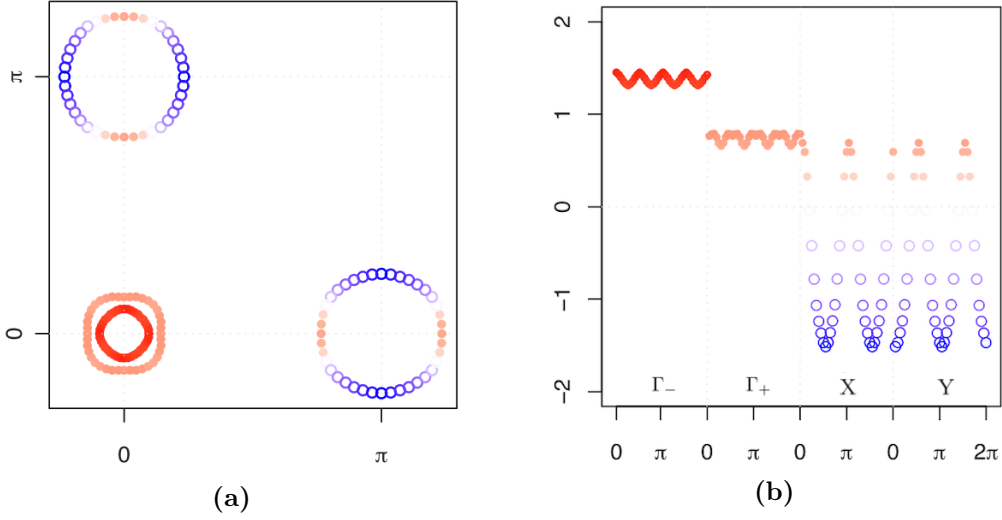


**Figure 3.7:** RPA gap function within the five-orbital model (a) plotted on the Fermi surfaces (red/solid circles positive and blue/open circles negative), (b) plotted as a function of angle from 0 to  $2\pi$ . Adapted from [102].

(ii) An anisotropic s-wave sign changing band gaps are obtained within both models with the same modulation in momentum. We already discussed in the previous section as the modulation is a direct consequences of the orbital composition of the nested pockets.

(iii) We reproduce the correct hierarchy of the band gap  $|\Delta_{\mathbf{k}}^{\Gamma_-}| > |\Delta_{\mathbf{k}}^{\Gamma_+}|$ . It is interesting that the larger gap is found for the  $\Gamma_-$  pocket despite the stronger band nesting of the  $\Gamma_+$  with the electron pockets. The result can be easily interpreted within the OSSF modeling as a consequence of the orbital matching between the  $\Gamma_-$  and the electron Fermi surfaces. This finding show that the orbital nesting (more than the band nesting) controls the strength of the pairing.

(iv) When the interaction between the electron pockets  $X$  and  $Y$  is taken into account, we find accidental nodes for the electron gaps  $\Delta_{\mathbf{k}}^X$  and  $\Delta_{\mathbf{k}}^Y$  in agreement with the microscopic analysis. As explained in [102] this is a way to reduces the effects of the repulsive scattering between the electron-sheets.

### 3.5. Conclusion Chapter 3

In Chapter 3 we show that the OSSF model provide a reliable description of the magnetic excitations and pairing interactions. We compare our results with the five-orbital tight-binding RPA model and with the three-band spin-nematic model.

In Section 3.3 we compute the spin susceptibility for a four pocket model in the tetragonal phase and we compare the results with the ones obtained for a five-orbital tight-binding RPA model. One of the most relevant results, is that depending on the degree of orbital nesting between pockets, we get an orbital modulation of the spin susceptibility that rises to commensurate or incommensurate peaks in the spin susceptibility when there is an orbital match or mismatch between the holes and the electrons respectively. Moreover we see that the main contribution to the spin susceptibility is given by the spin-fluctuation exchange between hole and electron pockets and the the larger contributions comes for



the hole pocket whose orbital composition match better the orbital composition of the electrons.

We also compare the total spin susceptibility and plot it along the high-symmetry points. The OSSF reproduces qualitatively well the overall momentum dependence and the relative heights and widths of the peaks located at different momenta. This is a remarkable result considering that the OSSF model is a low-energy effective model that only consider the  $yz, xz, xy$  orbitals and we compare with results obtained within the microscopic five-orbital model.

Within a spin-driven scenario, in Section 3.4, we compute the RPA pairing vertex and the correspondent gap equation for a four pocket model. The RPA pairing interaction, estimated in Section 3.4.1, is given by the irreducible particle-particle vertex that can be computed from all possible Feynman's diagrams containing the orbital selective spin fluctuation exchanged susceptibilities. It is interesting to notice that within the OSSF model it is possible to draw analytically all the Feynman's diagrams involved in the pairing vertex, something which is almost unfeasible within the five-orbital model due to the large number of different possible diagrams. As a result, the same features of the spin susceptibilities are transmitted to the pairing vertex obtaining commensurate or incommensurate peaks depending on the degree of orbital nesting. In Section 3.4.2 we solve the BCS gap equations mediated by the RPA pairing vertex computed in Section 3.4.1. We analyse the gap symmetry and structure of the band gaps for the different pockets and we compare with the results obtained for a five-orbital model. We find an anisotropic  $s_{\pm}$  gap function due to the orbital degree of freedom.

A deep analysis of the bands gap structure shows that the angular dependence and the magnitudes of the different gaps depend directly on the degree of orbital nesting between the holes and the electrons pockets, and what is more important, that the degree of orbital nesting is a stronger condition than the degree of band nesting between the different Fermi surfaces. This result proves that a minimal theoretical model to understand superconductivity in IBS has to account for the spin-orbital interplay. In that respect, the OSSF model is a perfect candidate.

Despite its simplicity, the OSSF model is able to reproduce qualitatively well all the relevant features of the spin-excitations and pairing interactions of the multiorbital description. It allows for analytical treatment making easy and straightforward the interpretation of the results. Moreover, due to the orbital-selectivity of the spin-fluctuations, it allows to include in a very simple way additional interacting channel, as we showed explicitly by considering the electron-electron interaction beside the hole-electron spin-exchange. Also in this case we find a perfect agreement with the multiorbital analysis in which it was shown as the presence of an electron-electron interaction leads to the appearance of accidental nodes in the electron gap bands.

# 4

## Anisotropy of the dc conductivity in the nematic phase

### 4.1. Introduction

Resistivity anisotropy is a hallmark of nematicity in iron-based superconductors (IBS). As discussed in Section 1.4 the experimental evidences appear extremely puzzling and difficult to be explained using a single theoretical frame. In fact, the dc-resistivity anisotropy measured in the nematic phase of IBS can have different signs and magnitude depending on the compound.

In detwinned electron-doped 122 compounds  $\Delta\rho = \rho_x - \rho_y < 0$  is found below the structural transition [82, 141–144] while detwinned hole-doped compounds present the opposite anisotropy [94]. There is an on-going debate in the literature on whether the observed dc anisotropy is due to the anisotropy in the scattering rate or to the anisotropy in Fermi surface parameters [95, 145–152]. In principle, within an orbital-ordering scenario the different occupation of the various orbitals affects mainly the Fermi surface [74, 153, 154], while within a spin-driven scenario the largest effect is expected to come from an anisotropy in the inelastic scattering rate [145, 155–158]. Specifically, in the band spin-nematic scenario, depending on the Fermi surface shape and size, the band nesting is active at the so called hot spots on the Fermi surface, where the scattering rate is maximum. It has been argued that the location of the hot spots could explain the different signs between electron-doped compounds and hole-doped compounds [94] in pnictides. Besides the spin-nematic or orbital order scenario, further attempts to explain the dc anisotropy in pnictides taking into account the spin-orbital interplay has been performed using effective spin-fermion model [159] or multiorbital microscopic model in the magnetic phase [22, 160, 161]. Experiments in FeSe have found the opposite anisotropy with respect to the electron-doped 122 compounds [162], i.e.  $\Delta\rho = \rho_x - \rho_y > 0$ . The significant Fermi surface reconstruction observed in the nematic phase of FeSe [24, 32], suggests that both scattering rate and velocity could play a role in contributing to the anisotropy of the dc resistivity, in particular in the light of the results obtained in [60] in which the temperature evolution of the Fermi Surface (size, shape and orbital composition) of FeSe across the nematic transition has been quantitatively explained within the orbital selective spin-fluctuations (OSSF) scenario.

In this Chapter, which is based on [103], we analyze the anisotropy of the dc resistivity in the nematic phase of IBS within the theoretical frame of the OSSF model presented in Chapter 2. The model, due to the spin-orbital entanglement encoded in the theory, is

able to account for the different phenomenology of 122 and FeSe regarding magnetism and nematicity [27] and provides a simple scheme to understand both nematicity and superconductivity of FeSe [60, 133].

To compute the conductivity of the system, we implement a quantum field theory approach as discussed in Section 4.2 starting from the definition of the current-current correlator in the bare bubble approximation. This means we account for self-energy effects only. As we already discussed in Section 2.3, the OSSF self-energy we use do not depend on momentum, thus vertex corrections vanish identically. However, our results do not depend crucially on this approximation and are expected to hold even in a calculation in which the self-energy is given by spin-mode having a momentum dependence. This idea is supported by the work performed in [126, 163], where it is shown that self-energy corrections to resistivity are dominant (over the vertex ones) in IBS.

We focus in the analysis of the nematic phase where the OSSF self-energy are not longer degenerate for the  $xz/yz$  orbital as consequences of the  $x/y$  anisotropy of the spin-fluctuations. The analysis is contained in Section 4.3. To gain physical insight and disentangle the effects of anisotropy coming from scattering rate or velocity, we first perform analytical calculation using the perfectly-nested parabolic-band approximation and treating the nematic order parameter perturbatively. This analysis allow us to define simple analytical equation for the dc conductivity anisotropy of each band. We find that, in contrast to the band spin-nematic scenario [23, 28] where just the scattering rate contributes to the dc anisotropy, also the velocity contributes. The contribution of the scattering rate to the resistivity anisotropy is dominated by the location of the cold spots where the scattering rate is minimum, which, within our model, is determined by the orbital composition of the Fermi surface and by the spin-orbital interplay of the OSSF. The contribution of the velocity to the resistivity anisotropy is counter-intuitive and opposite to the one of the scattering rate. We find indeed that the conductivity is larger in the direction where the self-energy is also larger. This interesting new effect is due to an orbital character exchange in the pockets arising from the OSSF self-energy in the nematic phase.

To check the validity of the analytical approximation, we compute numerically the dc conductivity using realistic band parameters for 122 compounds and FeSe compounds, i.e. accounting for spin-orbit coupling elliptical electron pockets. We verified that for 122 compounds due to a smaller spin-orbital coupling and a weaker nematic order numerical results are very close to the analytical ones, while more important deviation from the analytical analysis are found in FeSe.

Last, in Section 4.4 we discuss our results and put them in the context of experiments in IBS. Our study shows that the sign of the anisotropy of the dc conductivity depends on whether scattering rate or velocity anisotropy dominates on each pocket, as well as other parameters such as the ellipticity and the quasiparticle renormalization due to local interactions. Thus, different experimental results among the various families of IBS can be explained within the same OSSF scenario.

## 4.2. Conductivity in the OSSF model: a quantum field theory approach

Consider a system of electrons subjected to an external electromagnetic field. In linear response theory, the conductivity tensor  $\sigma$  is the proportionality function between

the induced electric density  $\mathbf{J}$  and the applied external electric field  $\mathbf{E}$

$$J_i(\mathbf{q}, \Omega) = \sigma_{ij}(\mathbf{q}, \Omega) E_j(\mathbf{q}, \Omega) \quad (4.1)$$

with  $i = \{x, y, z\}$  the spatial coordinate and  $\mathbf{q}$  and  $\Omega$  the transferred momentum and frequency respectively. The spatial components of the conductivity tensor  $\sigma_{ij}$  are defined as

$$\sigma_{ij}(\mathbf{q}, \Omega) = -\frac{ie^2}{V\Omega} [\Pi_{ij}(\mathbf{q}, \Omega) - \langle \tau_{ii} \rangle \delta_{ij}] \quad (4.2)$$

where  $V$  is the unit-cell volume,  $\Pi_{ij}$  is the current-current correlation function and  $\tau_{ii}$  is the diamagnetic tensor, where the current operator and the diamagnetic term are given by

$$j_i(\mathbf{q}) = \frac{1}{N} \sum_{\mathbf{k}, \sigma} \mathbf{v}(\mathbf{k}) c_{\mathbf{k}-\mathbf{q}\sigma}^\dagger c_{\mathbf{k}\sigma} \quad \text{and} \quad \tau_{ii} = \frac{1}{N} \sum_{\mathbf{k}, \sigma} \frac{\partial^2 \epsilon_{\mathbf{k}}}{\partial k_i^2} n_{\mathbf{k}, \sigma} \quad (4.3)$$

with  $N$  the number of unit cells,  $\mathbf{v}(\mathbf{k}) = \partial \epsilon_{\mathbf{k}} / \partial k_i$  the velocity,  $\epsilon_{\mathbf{k}}$  the band dispersion and  $n_{\mathbf{k}, \sigma}$  the electron density. Eq. 4.2 represents a powerful result that defines the electromagnetic response of the system.

The  $\mathbf{q} \rightarrow 0$  limit of Eq. 4.2 defines the optical conductivity in which the off-diagonal component of the conductivity tensor vanish by symmetry (if the system is time-reversal symmetric e.g. in the absence of magnetic field). The real and the imaginary part of the conductivity represent the dissipative and the absorptive part respectively. The optical properties of the system are expressed through the optical response functions which are determined by the real part of the optical conductivity tensor given by

$$\text{Re } \sigma_\alpha(\Omega) = \frac{e^2}{V} \frac{\text{Im } \Pi_\alpha(\mathbf{q} = 0, \Omega)}{\Omega}, \quad (4.4)$$

where we simplified the notation  $\alpha \equiv ii = \{x, y\}$ . The dc conductivity is defined as the  $\Omega \rightarrow 0$  limit of the longitudinal optical conductivity

$$\sigma_{dc\alpha} = \frac{e^2}{V} \lim_{\Omega \rightarrow 0} \frac{\text{Im } \Pi_\alpha(\mathbf{q} = 0, \Omega)}{\Omega} \quad (4.5)$$

Therefore, the conductivity of a given system reduces to the computation of the current-current correlation function  $\Pi_\alpha$ .

In what follows we summarize the main step of the computation the current-current correlation function and dc conductivity within the OSSF model. We refer the reader to Appendix D.1.1 and D.1.2 for the complete derivation.

#### 4.2.1. Current-current correlation function

The current-current correlation function  $\Pi_\alpha$  can be evaluated as usual from the standard analytic continuation  $i\Omega_m \rightarrow \Omega + i\eta$  of the equivalent correlation function in the Matsubara formalism as

$$\Pi_{ij}(\mathbf{q}, i\Omega_m) = \frac{T}{N} \iint_0^\beta d\tau e^{i\Omega_m \tau} \langle T_\tau j_i(\mathbf{q}, \tau) j_j(-\mathbf{q}, 0) \rangle \quad (4.6)$$

with  $\tau$  the imaginary time,  $\Omega_m = 2\pi mT$  the bosonic Matsubara frequency and  $j_i(\mathbf{q}, \tau)$  is the current operator given by Eq. 4.3. According the diagrammatic technique this can

be decomposed in a series of diagrams with increasing numbers of single-particle Green's functions and interactions lines [164]. If we consider a non-interacting electron system we have

$$\Pi_{ij}(\mathbf{q}, i\Omega_m) = 2 \sum_{lkn} \text{Tr} \{ \hat{G}^l(\mathbf{k} - \mathbf{q}/2, i\omega_n) \hat{V}_{\mathbf{k}_i}^l \hat{G}^l(\mathbf{k} + \mathbf{q}/2, i\omega_n + i\Omega_m) \hat{V}_{\mathbf{k}_j}^l \} \quad (4.7)$$

where the factor 2 is due to the spin summation and we are summing over  $l = \Gamma, X, Y$ . Here  $\omega_n = 2\pi(n + 1/2)T$  the fermionic Matsubara frequency,  $\hat{G}^l(\mathbf{k}, i\omega_n)$  is the non-interacting Green's function from the OSSF model, Eq. 2.25, and  $\hat{V}_{\mathbf{k}_i}^l = \partial_{\mathbf{k}_i} \hat{H}^l$  are the bare velocity in the direction  $i = \{x, y\}$ . As soon as interactions are present in the system, we have to consider their effect on  $\Pi_{ij}(\mathbf{q}, i\Omega_m)$ . It is easy to demonstrate [164] that one can perform a partial summation of diagrams to all orders by replacing in Eq. 4.7 each bare Green's function by the full Green's function defined by the Dyson equation Eq. 2.48. The current-current correlation function computed within this approximation is the so-called bare-bubble. In what follows we work within this approximation and compute the current-current correlator from Eq. 4.7 in which we dress the bare Green's functions with the OSSF self-energy as discussed in Section 2.3.

When can now set  $\mathbf{q} = 0$  and use that  $\hat{G}^l(\mathbf{k}, i\omega_n) = \hat{\mathcal{U}}_R^l(\mathbf{k}, i\omega_n) [i\omega_n \hat{\mathbb{I}} - \hat{\Lambda}_R^l(\mathbf{k}, i\omega_n)]^{-1} \hat{\mathcal{U}}_R^{l-1}(\mathbf{k}, i\omega_n)$  (Eq. 2.49). By using the cyclic property of the trace, Eq. 4.6 can be rewritten as

$$\Pi_{ij}(i\Omega_m) = 2 \sum_{lkn} \text{Tr} \{ [i\omega_n \hat{\mathbb{I}} - \hat{\Lambda}_R^l(\mathbf{k}, i\omega_n)]^{-1} \hat{V}_{R(\mathbf{k}_i i\omega_n)}^l [(i\omega_n + i\Omega_m) \hat{\mathbb{I}} - \hat{\Lambda}_R^l(\mathbf{k}, i\omega_n + i\Omega_m)]^{-1} \hat{V}_{R(\mathbf{k}_j i\omega_n + i\Omega_m)}^l \} \quad (4.8)$$

with the renormalized velocity matrix defined as

$$\hat{V}_{R(\mathbf{k}_i i\omega_n)}^l = \hat{\mathcal{U}}_R^{l-1}(\mathbf{k}, i\omega_n) \hat{V}_{\mathbf{k}_i}^l \hat{\mathcal{U}}_R^l(\mathbf{k}, i\omega_n + i\Omega_m) \quad (4.9)$$

where  $\hat{\mathcal{U}}_R^{l-1}(u_R, v_R)$  is the rotation matrix with  $u_R$  and  $v_R$  the renormalized coherence factors Eq. D.22. Notice that the renormalized velocities are affected by the self-energy via the coherence factors. Notice that those depend on both the internal ( $\omega_n$ ) and external ( $\Omega_m$ ) frequencies. This effect does not enter in our calculation as we focus on the dc conductivity, but could be important in the analysis of the optical conductivity.

We replace the expressions for the velocity, Eq. 4.9, and the renormalized Green's functions  $\hat{G}^l(\mathbf{k}, i\omega_n) = [i\omega_n \hat{\mathbb{I}} - \hat{\Lambda}_R^l(\mathbf{k}, i\omega_n)]^{-1} = \text{diag}(g^+(\mathbf{k}, i\omega_n), g^-(\mathbf{k}, i\omega_n))$  in Eq. 4.8. By evaluating the trace over the orbital basis the current-current correlation function can be rewritten as

$$\begin{aligned} \Pi_{ij}(i\Omega_m) &= \Pi_{ij(i\Omega_m)}^{l_{11}++} + \Pi_{ij(i\Omega_m)}^{l_{11}+-} + \Pi_{ij(i\Omega_m)}^{l_{22}-+} + \Pi_{ij(i\Omega_m)}^{l_{22}--} = \\ &= 2 \sum_{lkn} \left( \left[ g_{i\omega_n}^+ V_R^{l_{11}} g_{i\omega_n+i\Omega_m}^+ V_R^{l_{11}} + g_{i\omega_n}^+ V_R^{l_{12}} g_{i\omega_n+i\Omega_m}^- V_R^{l_{21}} \right] \right. \\ &\quad \left. + \left[ g_{i\omega_n}^- V_R^{l_{21}} g_{i\omega_n+i\Omega_m}^+ V_R^{l_{12}} + g_{i\omega_n}^- V_R^{l_{22}} g_{i\omega_n+i\Omega_m}^- V_R^{l_{22}} \right] \right) \quad (4.10) \end{aligned}$$

where we drop the  $\mathbf{k}$  dependence. Notice that in Eq. 4.10,  $\Pi_{ij(i\Omega_m)}^{l_{11}++}$  and  $\Pi_{ij(i\Omega_m)}^{l_{22}--}$  represent intraband terms and  $\Pi_{ij(i\Omega_m)}^{l_{11}+-}$  and  $\Pi_{ij(i\Omega_m)}^{l_{22}-+}$  interband contributions to the optical conductivity given by Eq. 4.4.

We are interested in the intraband terms given by the  $\Pi_{ij}^{++/--}$  as we focus on the analysis of the dc conductivity and hereafter we use the compact notation  $\alpha = ii = \{x, y\}$

### 4.2.2. Dc conductivity

In order to compute the  $\Pi_{\alpha=ii}^{++/--}$  terms, we express the Green's functions  $g^\pm(i\omega_n)$  in terms of the spectral functions  $A_{\mathbf{k}}^{l\pm}(\omega)$ . After performing the Matsubara sum we can replace the current-current correlator in Eqs. 4.4 and 4.5. The dc conductivity for each pocket is then given by

$$\sigma_\alpha^{l\pm} = \frac{2\pi e^2}{N} \sum_{\mathbf{k}} \int_{-\infty}^{\infty} d\omega \left( -\frac{\partial f(\omega)}{\partial \omega} \right) [V_{R\mathbf{k}\alpha}^{l\pm}(\omega)]^2 [A_{\mathbf{k}}^{l\pm}(\omega)]^2. \quad (4.11)$$

where  $f(\omega)$  the Fermi distribution function and the spectral function reads

$$A_{\mathbf{k}}^{l\pm}(\omega) = \frac{1}{\pi} \frac{\Gamma_{R\mathbf{k}}^{l\pm}(\omega)}{[\Gamma_{R\mathbf{k}}^{l\pm}(\omega)]^2 + [\omega - \epsilon_{R\mathbf{k}}^{l\pm}(\omega)]^2} \quad (4.12)$$

The total dc conductivity is defined by the sum over the pockets  $l_\pm = \{\Gamma_+, \Gamma_-, X, Y\}$  as  $\sigma_{dc\alpha} = \sum_{l_\pm} \sigma_\alpha^{l\pm}$ . By direct inspection of Eq. 4.11 we see that the dc conductivity within the bare-bubble approximation depends on the self-energy via: (i) the renormalized energy dispersions and scattering rate contained in the spectral function Eq. 4.12 (ii) the renormalized velocity.

The dispersions and scattering rate for the interacting system, derived in Section 2.3, are given by

$$\epsilon_{R\mathbf{k}}^{l\pm}(\omega) = Re E_{R\mathbf{k}}^{l\pm}(\omega) \quad (4.13)$$

$$\Gamma_{R\mathbf{k}}^{l\pm}(\omega) = \delta\Gamma + |Im E_{R\mathbf{k}}^{l\pm}(\omega)| \quad (4.14)$$

where  $E_{R\mathbf{k}}^{l\pm}(\omega)$  is

$$E_{R\mathbf{k}}^{l\pm}(\omega) = h_0^l + \Sigma_{0\mathbf{k}}^l(\omega) \pm \sqrt{(h_{1\mathbf{k}}^l)^2 + (h_{2\mathbf{k}}^l)^2 + (h_{3\mathbf{k}}^l + \Sigma_{3\mathbf{k}}^l(\omega))^2} \quad (4.15)$$

derived in Eq. 2.50 in Section 2.2.1.

$V_{R\mathbf{k}\alpha}^{l\pm}$ , Eq. 4.9, is the bare velocity operator rotated (using the rotation matrix of the interacting system) into the band basis. We take the  $\Omega \rightarrow 0$  limit and consider the intraband component only

$$V_{R\mathbf{k}\alpha}^{l\pm} = V_{\mathbf{k}\alpha}^{l11} |u_R^l|^2 \pm V_{\mathbf{k}\alpha}^{l12} u_R^{*l} v_R^{*l} \pm V_{\mathbf{k}\alpha}^{l21} u_R^l v_R^l + V_{\mathbf{k}\alpha}^{l22} |v_R^l|^2 \quad (4.16)$$

$V_{\mathbf{k}\alpha}^{l\eta\eta'}$  are the  $\eta\eta'$  component of the velocity,  $(u/v)_R^l$  are the renormalized coherence factors and hereafter we omit the dependence on the internal frequency  $\omega$  for simplicity.  $V_{R\mathbf{k}\alpha}^{l\pm}$  depends on the self-energy via the coherence factors. It is worth noticing that Eq. 4.16 show a dependence on the orbital  $\hat{\tau}_3$  component of the self-energies,  $\Sigma_3^l(\omega)$  that mixes the orbital content of each pocket. This can be easily check by looking at the analytical expressions for  $u_R/v_R$  that can be derive within the parabolic approximation (see Appendix D.2) as

$$\begin{aligned} |u_R^l|^2 &= |u^l|^2 \left( 1 + \frac{2Re\Sigma_3^l}{h^l} |v^l|^2 \right) \left( \right. \\ |v_R^l|^2 &= |v^l|^2 \left( 1 - \frac{2Re\Sigma_3^l}{h^l} |u^l|^2 \right) \left( \right. \end{aligned} \quad (4.17)$$

In the  $T \rightarrow 0$  limit we can approximate the Fermi function with a  $\delta(\omega)$  which selects only states at the Fermi level  $\omega = 0$ . Moreover, we assume  $\Gamma_R^{l\pm}$  to be small so that  $(A_{\mathbf{k}}^{l\pm})^2 \rightarrow \frac{1}{2\pi\Gamma_R^{l\pm}} \delta(\epsilon_{R\mathbf{k}}^{l\pm})$  and the pocket conductivity reduces to

$$\sigma_{\alpha}^{l\pm} = \frac{e^2}{N} \sum_{\mathbf{k}} \frac{(V_{R\mathbf{k}\alpha}^{l\pm})^2}{\Gamma_R^{l\pm}} \delta(\epsilon_{R\mathbf{k}}^{l\pm}). \quad (4.18)$$

In the next Section we will perform analytical and numerical analysis of Eq. 4.18 to analyze the dc conductivity in the nematic phase of IBS. Further details can be found in Appendix D.2.

### 4.3. 122 and FeSe dc conductivity within the OSSF model

The general sketch of the orbital content of the Fermi surface for a generic four-pocket model for IBS is shown in Figure 4.1.

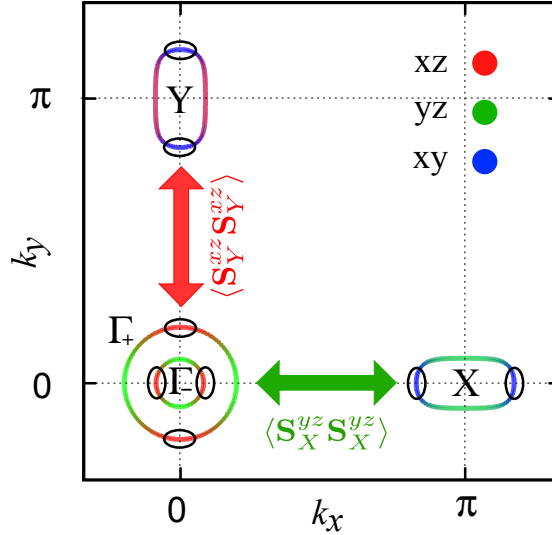


**Figure 4.1:** General sketch of the orbital content of the Fermi surface of the 4 pocket model for IBS. The green and red arrows show the OSSF with  $yz$  content in the  $x$ -direction and  $xz$  content in the  $y$ -direction. Cold spots, where the scattering rate is minimum, are shown by a circle and they are found on the  $xy$  and  $xz$  orbitals in the nematic phase due to anisotropic self-energy corrections.

The qualitative behavior of the self-energies in the nematic phase allows us to easily localize the minimum value of  $\Gamma_R^{l\pm}$  on the Fermi surface (FS), i.e. the cold spots shown in Figure 4.1. As is discussed in Ref. [60], within the OSSF model, the reconstruction of the FS below  $T_S$  is consistent with the spin-fluctuations being bigger at  $Q_X$  than at  $Q_Y$ . This implies that self-energy corrections are stronger on the  $yz$  orbital than on the  $xz$  one. As a consequence on the hole pockets the smaller scattering rate corresponds to the  $xz$  orbital. On the electron pockets instead, the smaller scattering rate is found for the  $xy$  orbital, given the absence of  $xy$ -SF within our model. The result is an example of the spin-orbital interplay retained by the OSSF approach that allows us to directly link the cold spots position with the FS orbital character and is not present in the band-based spin-nematic scenario [28].



### 4.3.1. Analytical estimate of the dc-conductivity anisotropy

To gain physical insight on the dc anisotropy and disentangle the effect of the velocity and scattering rate in Eq. 4.18, we estimate analytically  $\sigma_\alpha$ . In order to do that we performed two main approximations. First, we approximate the hole and electron bands with perfectly nested parabolic bands (see also Appendix B.2). Second, with respect to the self-energy, we define the nematic splitting as symmetric around the isotropic value  $\Sigma_0^l$  of the tetragonal phase and assume that the nematic order is small enough to allow for a perturbative expansion of the renormalized energy  $E_R^{l\pm}$  given in Eq. 4.15.

By expanding  $E_R^{l\pm}$  at first order in the  $\hat{\tau}_3$  self-energy component we can estimate analytically for each pocket  $V_{R\mathbf{k}\alpha}^{l\pm}$ ,  $\epsilon_R^{l\pm}$  and  $\Gamma_{R\mathbf{k}}^{l\pm}$  via Eqs. 4.13 and 4.14.

**Renormalized velocity** By neglecting the imaginary part of the self-energy in the coherence factors  $(u/v)_R^l$ , it is easy to check the velocity given in Eq. 4.16 can also be written as the derivative of the renormalized dispersion relation

$$V_{R\mathbf{k}\alpha}^{l\pm} = \partial \epsilon_R^{l\pm}(\mathbf{k}) / \partial k_\alpha. \quad (4.19)$$

Let's perform explicitly the derivation for one pocket. Deriving, for example with respect  $k_x$  the renormalized energy of the pocket  $\Gamma_+$  we find

$$V_{R\mathbf{k}x}^{\Gamma_+} = -\frac{k \cos \theta}{m^{\Gamma_+}} + 4 Re \Sigma_3^\Gamma \sin^2 \theta^2 \frac{k \cos \theta}{k^2} \quad (4.20)$$

where  $m^{\Gamma_+}$  is the bare mass of the  $\Gamma_+$  pocket whose definition in terms of the Hamiltonian parameters. The first term on the right hand side of Eq. 4.20, is the  $\alpha$  component of the bare velocity, while the second term  $\mathcal{O}(Re \Sigma_3^l)$  is an additional contribution due to the orbital mixing induced by the nematic order as expected from the  $(u, v)_R^l$  coherence factors in Eq. 4.16. The expression of the renormalized velocities for the different pockets in the  $k_x$  and  $k_y$  directions are specified in Appendix D.2.

To compute the  $\mathbf{k}$  integration in Eq. 4.18 we will use the delta function and evaluate  $V_{R\mathbf{k}x}^{\Gamma_+}$  at the renormalized Fermi surface. Notice that, in the nematic phase  $k_F^{\Gamma_+}(\theta)$  is no longer constant but gets deformed because of the anisotropic self-energy renormalization. This effect is also of order  $\mathcal{O}(Re \Sigma_3^l)$  and has to be taken into account.

We estimate the change in the Fermi wave vector at the first order in the self-energy. Replacing the expression of  $k_F^{\Gamma_+}(\theta)$  into Eq. 4.20 we find

$$V_{R\mathbf{k}x}^{\Gamma_+} = V_{0\mathbf{k}x}^{\Gamma_+} \left( 1 + \cos 2\theta \frac{Re \Sigma_3^\Gamma}{2\epsilon_0^h} - 4 \sin^2 \theta \frac{Re \Sigma_3^\Gamma}{2\epsilon_0^h} \right) \quad (4.21)$$

where  $\epsilon_0^h = \epsilon^\Gamma + Re \Sigma_0^\Gamma$  and  $V_{0\mathbf{k}x}^{\Gamma_+} = -k_{0F_x}^{\Gamma_+} / m^{\Gamma_+}$  are the  $x$  component of the bare velocity in the tetragonal state with  $k_{0F}^{\Gamma_+} = \sqrt{\epsilon_0^\Gamma / (2m^{\Gamma_+})}$ .

From Eq. 4.21, one sees that the bare Fermi velocity in the nematic phase has two contributions  $\mathcal{O}(Re \Sigma_3^l)$  opposite in sign: the first one is due to the change in  $k_F^{l\pm}$ , while the second one comes from the orbital mixing produced by the nematic order.

Analogous calculation of the velocity contributions along  $k_y$  for the  $\Gamma_+$  as well as for the other pockets lead to similar expressions (see Appendix D.2) with the band velocity of the tetragonal phase renormalized by two additional contributions  $\mathcal{O}(Re \Sigma_3^l)$  of opposite sign.



**Renormalized scattering rate** The scattering rate is analytically estimated from Eq. 4.14 using again the expansion of  $E_R^{\Gamma+}$  at the first order in  $\Sigma_3^\Gamma$

$$\Gamma_R^{\Gamma+} = \Gamma_0^h + \cos 2\theta |Im\Sigma_3^\Gamma| \quad (4.22)$$

where we separate the tetragonal phase scattering rate,  $\Gamma_0^h = \delta\Gamma + |Im\Sigma_0^\Gamma|$ , from the angular dependent correction due to the nematic effect  $\sim Im\Sigma_3^\Gamma$ . By looking Eq. 4.22 and comparing it with Figure 4.1, is easy to understand where are the minimum values of the scattering rate at the Fermi surface, that is, where are the cold spot located in each pocket. Analogous calculation of the renormalized scattering rate for the  $\Gamma_-$ ,  $X$ ,  $Y$  pockets are specified in Appendix D.2.

**dc conductivity** By replacing the analytical expressions found for the velocity, Eq. 4.21, and for the scattering rate, Eq. 4.22 in Eq. 4.18 the expression of the  $\Gamma_+$  pockets dc conductivity read as

$$\begin{aligned} \sigma_x^{\Gamma+} &= \sigma^h \left( \left( \pm \frac{Re\Sigma_3^\Gamma}{2\epsilon_0^h} \mp \frac{Re\Sigma_3^\Gamma}{\epsilon_0^h} \mp \frac{|Im\Sigma_3^\Gamma|}{2\Gamma_0^h} \right) \right) = \\ &= \sigma^h \left( \left( -\frac{\Phi^h}{2\epsilon_0^h} + \frac{\Phi^h}{\epsilon_0^h} - \frac{\Delta\Gamma^h}{2\Gamma_0^h} \right) \right) \end{aligned} \quad (4.23)$$

where  $\epsilon_0^h$ ,  $\Gamma_0^h$  and  $\sigma^h = e^2\epsilon_0^{h/e}/(2\pi\hbar)\Gamma_0^h$  are respectively the Fermi energy, the scattering rate and the dc conductivity in the tetragonal phase for the hole pocket. We also defined the real and imaginary part of the nematic order parameter ( $\Phi^h, \Delta\Gamma^h$ ) for the hole pocket as

$$\Phi^h \equiv -Re\Sigma_3^\Gamma, \quad \Delta\Gamma^h \equiv |Im\Sigma_3^\Gamma|, \quad (4.24)$$

taking also into account that stronger spin-fluctuation at  $\mathbf{Q}_X$  implies  $Re\Sigma_3^\Gamma < 0$ , so that now the nematic order parameters are positive defined. Via analogous calculations we derive the dc conductivities along  $x$  and  $y$  for each pockets.

The dc conductivity components for the hole pocket at  $\Gamma$  point read as

$$\begin{aligned} \sigma_{x/y}^{\Gamma+} &= \sigma^h \left( \left( \mp \frac{\Phi^h}{2\epsilon_0^h} \pm \frac{\Phi^h}{\epsilon_0^h} \mp \frac{\Delta\Gamma^h}{2\Gamma_0^h} \right) \right) \left( \right. \\ \sigma_{x/y}^{\Gamma-} &= \sigma^h \left( \left( \pm \frac{\Phi^h}{2\epsilon_0^h} \mp \frac{\Phi^h}{\epsilon_0^h} \pm \frac{\Delta\Gamma^h}{2\Gamma_0^h} \right) \right) \left( \right. \end{aligned} \quad (4.25)$$

In the absence of spin-orbit interaction the hole pockets have the same  $\epsilon_0^h$ , so they also have the same conductivity  $\sigma^h$  in the tetragonal phase. Additional terms proportional to  $\Phi^h$  and  $\Delta\Gamma^h$  arise in the nematic phase and make the conductivity different for the two hole pocket.

As discussed within the calculation of the velocity operator for the  $\Gamma_\pm$  pocket in Eq. 4.21, the nematic order has two opposite effects  $\mathcal{O}(\Phi^h)$  in the velocity and this is reflected into the pocket dc conductivity anisotropy as one sees from Eq. 4.25. The first correction comes directly from the  $k_F^{\Gamma\pm}$  changes due to the nematic Fermi surface reconstruction, while the second one, opposite in sign, is due to the orbital mixing. Notice that this last term also determine the overall sign of the correction  $\sim \Phi^h$  in each pocket.

Due to the  $xz/yz$  orbital arrangement of the  $\Gamma_{\pm}$  Fermi surface, the two hole pockets contribute with opposite sign to the conductivity anisotropy i.e. in Eq. 4.25 we find the same sign of the nematic terms in the conductivity along  $x$  of the  $\Gamma_+$  pocket and in the conductivity along  $y$  of the  $\Gamma_-$  one. In particular, the opposite sign of the contribution  $\mathcal{O}(\Delta\Gamma^h)$  giving negative/positive anisotropy for the  $\Gamma_{+/-}$  pocket is a direct consequence of the cold spots physics, Figure 4.1, from where we can easily infer the sign of the anisotropic contribution for  $\Gamma_{\pm}$  having in mind that lower scattering implies a bigger conductivity.

By computing the hole dc conductivity anisotropy as the different of the dc conductivity in the  $x$  and  $y$  directions  $\Delta\sigma^{h\pm} \equiv \sigma_x^{\Gamma_{\pm}} - \sigma_y^{\Gamma_{\pm}}$ , we find

$$\begin{aligned}\Delta\sigma^{h+} &= \sigma^h \left( \frac{\Phi^h}{\epsilon_0^h} - \frac{\Delta\Gamma^h}{\Gamma_0^h} \right) \left( \right. \\ \Delta\sigma^{h-} &= \sigma^h \left( -\frac{\Phi^h}{\epsilon_0^h} + \frac{\Delta\Gamma^h}{\Gamma_0^h} \right) \left( \right.\end{aligned}\quad (4.26)$$

Within a parabolic band approximation, neglecting the effect of the spin-orbit coupling the hole pockets are completely degenerated, thus is no surprising to find that by summing up  $\Delta\sigma$  for the two hole pockets their anisotropic contributions cancel out. Therefore the sign of the anisotropy of the total dc conductivity is in this case completely controlled by the electron pockets.

The dc conductivity components for the electron pocket at  $X$  read as

$$\begin{aligned}\sigma_x^X &= \sigma^e \left( 1 - \frac{Re\Sigma_{yx}^X}{4\epsilon_0^e} + \frac{|Im\Sigma_{yz}^X|}{4\Gamma_0^e} \right) \left( \right. \\ \sigma_y^X &= \sigma^e \left( 1 + \frac{3Re\Sigma_{yx}^X}{4\epsilon_0^e} - \frac{|Im\Sigma_{yz}^X|}{4\Gamma_0^e} \right) \left( \right.\end{aligned}\quad (4.27)$$

where we used that  $\sigma_{x/y}^e = \sigma^e$  as within the parabolic approximation we neglect the ellipticity of the electron pockets. Same expressions hold for the  $Y$  pocket once replaced  $\Sigma_{yz}^X \rightarrow \Sigma_{xz}^Y$  and  $\mathbf{k}_x \rightarrow \mathbf{k}_y$ . This imply that  $X/Y$  pockets contribute with opposite sign to the overall dc conductivity.

We define the real and imaginary part of the nematic order parameter for the electron pockets  $(\Phi^e, \Delta\Gamma^e)$  as

$$\Phi^e \equiv \frac{Re\Sigma_{yz}^X - Re\Sigma_{xz}^Y}{2}, \quad \Delta\Gamma^e \equiv \frac{|Im\Sigma_{yz}^X| - |Im\Sigma_{xz}^Y|}{2} \quad (4.28)$$

which are all positive defined.

By using Eq. 4.28 we can write the electronic dc conductivity anisotropy  $\Delta\sigma^e \equiv \Delta\sigma^X + \Delta\sigma^Y$  as

$$\Delta\sigma^e = \sigma^e \left( -\frac{\Phi^e}{\epsilon_0^e} + \frac{\Delta\Gamma^e}{\Gamma_0^e} \right) \left( \right. \quad (4.29)$$

Also for the electron pockets we find that the renormalized velocity and the scattering rate contribute with opposite sign to the dc conductivity anisotropy. The balance between the two effects is controlled by the nematic order parameters normalized to the Fermi energy and isotropic scattering rate, respectively, i.e.  $\Phi^e/\epsilon_0^e$  vs  $\Delta\Gamma^e/\Gamma_0^e$ .

In conclusion, we computed analytically the anisotropy of the dc conductivity of the various pockets using the parabolic-band approximation Eq. 4.26 and 4.29 and treating the nematic order perturbatively. In each pocket, we find that the anisotropy of the dc conductivity is given by a contribution  $\mathcal{O}(Re\Sigma^l)$  and another  $\mathcal{O}(Im\Sigma^l)$ , opposite in sign with respect to each other, whose relevance is controlled by the relative values of  $\Phi^{h/e}/\epsilon_0^{h/e}$  vs  $\Delta\Gamma^{h/e}/\Gamma_0^{h/e}$ . Summing up the hole and electron pockets  $\Delta\sigma^{h/e}$  we find that the sign of the anisotropy of the total dc conductivity is controlled by the electron contribution and depends on which among  $X/Y$ -pocket contributes more to the total conductivity and on which effect, among the scattering rate and velocity renormalization, dominates.

The cancellation of the hole-contribution is an artifact of the approximation used in the calculation. In order to consider realistic system, we need to account for the presence of the spin-orbit interaction that splits the hole pockets at  $\Gamma$  and mixes their orbital content at the Fermi surface already in the tetragonal phase. Moreover, the parabolic band approximation is particularly inaccurate for the electron pockets that are strongly elliptical in IBS. Furthermore, especially for FeSe, the nematic self-energy components  $\Sigma_3^l$  are not small [60], thus the expansion of the renormalized energy in  $\Sigma_3^l$  performed above is not longer justified.

For realistic cases then, we cannot use the analytical expressions for the renormalized velocity Eq. 4.21 and scattering rate Eq. 4.22, and we need to compute the dc conductivity from Eq. 4.18 using a numerical estimate of the velocity and scattering rate from Eqs. 4.13-4.15.

### 4.3.2. Numerical estimate of the dc-conductivity anisotropy

We perform a numerical estimate of the conductivity anisotropy using realistic parameters for 122 and FeSe systems in order to assess the limits of validity of the analytical expressions Eq. 4.26 and 4.29 and qualitatively discuss our results in the context of the experimental outcomes found for 122 pnictides and FeSe.

We assume for both 122 and FeSe equivalent bare band structure parameters and real part of the self-energy capable of reproducing the 122 tetragonal Fermi surface shown in Figure 4.1. The Fermi surface topology of FeSe with just the outer hole pocket crossing the Fermi level at  $\Gamma$  already in the tetragonal phase is achieved in the calculation using a larger value of the spin-orbit interaction as well as a larger values of the real part of the self-energy renormalizations in agreement with previous analysis [60]. The numerical values of the parameters used in the following are detailed in Appendix D.3.

#### 122 pnictides

In Figure 4.2 we show for each pockets the Fermi surface wave-vectors and velocities along  $x/y$  computed by Eq. 4.16. To better appreciate the changes induced by the nematic order we plot in the first row the results for the tetragonal phase and in the second ones the results obtained in the nematic phase assuming  $\Phi^h = \Phi^e = 4$  meV.

The shrinking acts isotropically in the tetragonal phase, i.e. the hole pockets are still circular and  $k_F$  is constant. However due to the orbital-selectivity of the shrinking in the OSSF model, they are weakly deformed in the nematic phase (4.2a-d). The changes in the velocities for the  $\Gamma_{\pm}$  pockets appear to be quite small and do not follow monotonously

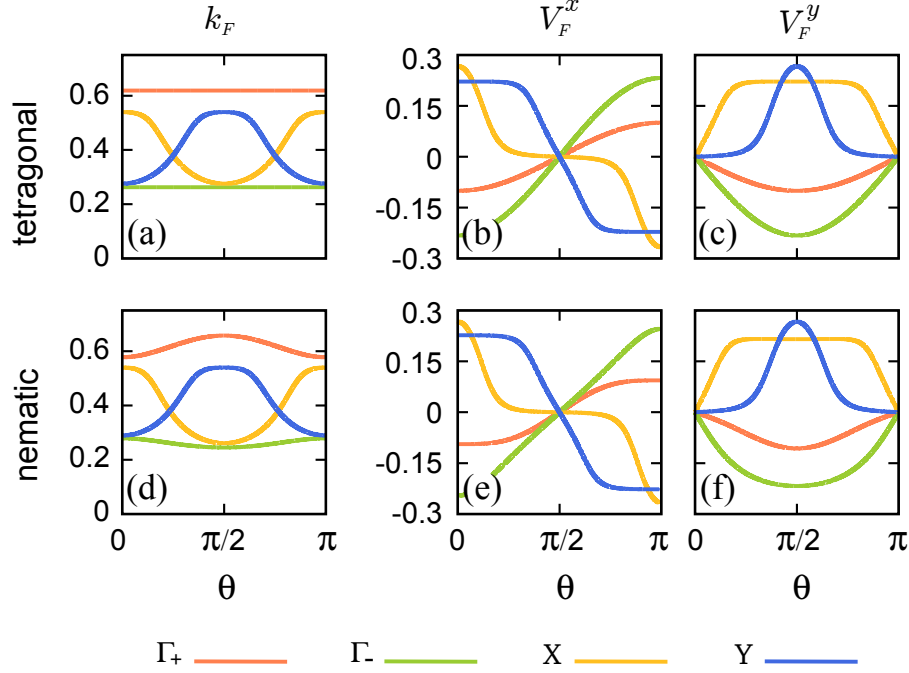


**Figure 4.2:** Numerical computation of FS wavevectors and velocity components for 122 system parameters in the tetragonal and nematic phase.  $\Phi_h = \Phi_e = 4$  meV, the spin-orbit interaction is 5 meV, other band parameters are detailed in Appendix B.3. The  $k_F$  are measured in units  $1/a \sim 0.375 \text{ \AA}^{-1}$ , where  $a = a_{FeFe}$  is the lattice constant of the 1-Fe unit cell. Velocities are in eV.

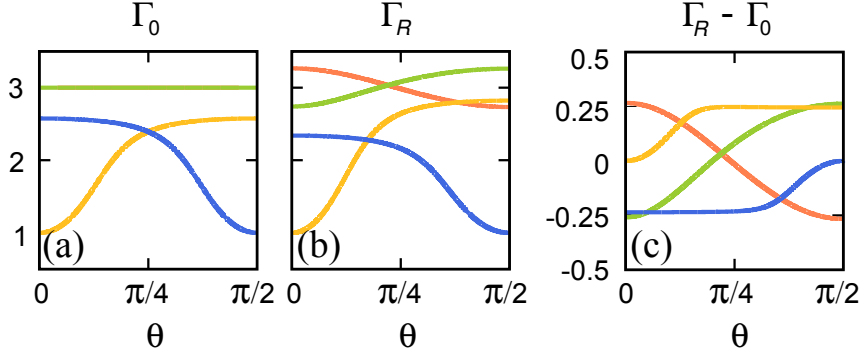


**Figure 4.3:** Renormalized scattering rate (in meV) computed using realistic 122 system parameters. Here  $\Gamma_0^h = 3$  meV and  $\Gamma_0^e = 2$  meV. We fix  $\Delta\Gamma^h$  and  $\Delta\Gamma^e$  considering the imaginary part of the self-energy for each pocket changing proportionally to the real part in the nematic phase (see Appendix D.3).

the renormalization of the Fermi vectors as one could have *naively* expected (4.2e-f). This is in agreement with the analytical calculation (see Eq. 4.21), where we found that the renormalization of the velocities is given by the combination of two opposite contributions, one due to the orbital mixing and the other from the shrinking (Fermi vector renormalization), reducing the overall anisotropic effect on the velocity. Due to the ellipticity of the Fermi surface, the electron pockets have anisotropic velocities already in the tetragonal phase (4.2b-c) with the X/Y pockets showing larger velocity along  $y/x$ . No qualitatively changes are visible in the nematic phase (4.2e-f).

In Figure 4.3 we show for each pocket the scattering rate obtained from Eq. 4.14. In the three panels we show the tetragonal value,  $\Gamma_0$ , the nematic one  $\Gamma_R$  and their difference.

We find again a good agreement between the analytical calculations and the numerical results for the hole pockets. As in Eq. 4.22 the angular dependence of the correction  $\Gamma_R^{\Gamma_{\pm}} - \Gamma_0^{\Gamma_{\pm}}$  goes almost as a  $\cos 2\theta$ , even if the weak ellipticity of the hole Fermi surface induced by the nematic order causes minor deviations, e.g. the correction vanishes for the  $\Gamma_+/\Gamma_-$  slightly before/after  $\pi/4$ . No renormalizations are found along  $x/y$  for the  $X/Y$  pockets since, within our model, no scattering is allowed in the  $xy$  channel (Figure 4.1). The location of the so-called cold spots i.e. the position of the minima of the scattering rate for both hole and electron pockets, does not change once a realistic Fermi surfaces are considered and corresponds to the ones shown in Figure 4.1.

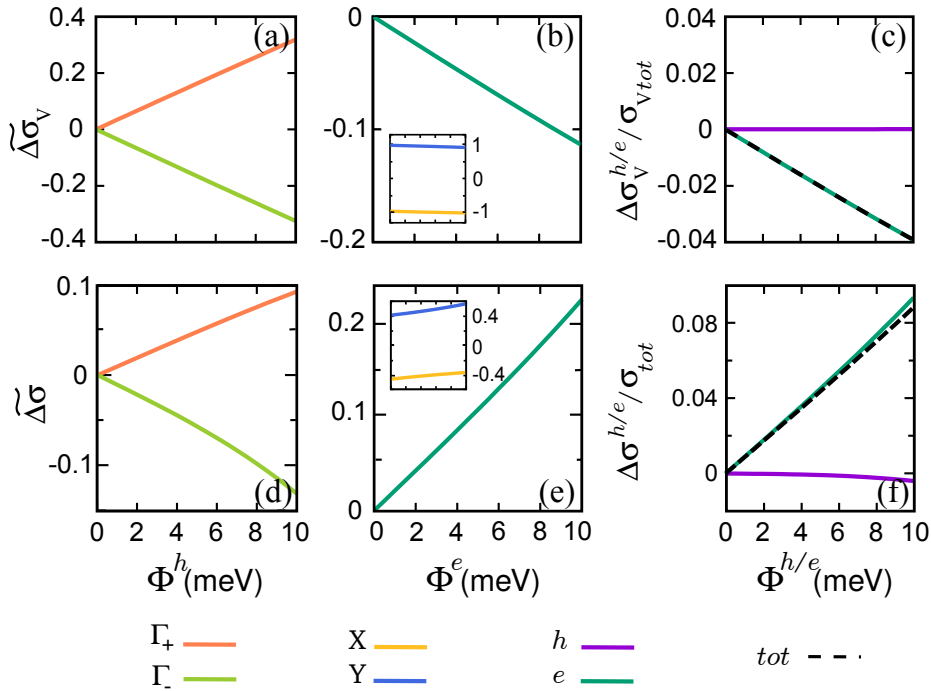


**Figure 4.4:** Numerical computation of the velocity contribution to the dc conductivity anisotropy  $\Delta\sigma_V$  and of the total dc conductivity anisotropy  $\Delta\sigma$  for realistic parameter for 122. In panels a-b we renormalized the pocket contributions to their value in the tetragonal phase i.e.  $\Delta\sigma_V^{\Gamma_{\pm}}(\Phi^{h/e} = 0)$  and analogously in panels d-e. In c and f panels instead we renormalize the hole and electron contributions to the total tetragonal values, i.e.  $\sigma_{V^{tot}} = \sigma_V(\Phi^{h/e} = 0)$  and  $\sigma_{tot} = \sigma(\Phi^{h/e} = 0)$ .

We can disentangle the effect of the velocity and of the scattering rate on the dc anisotropy by computing Eq. 4.18 using a constant scattering rate. This result just account for the anisotropic effects coming from the velocity so we will refer to it as  $\Delta\sigma_V$ . In Figure 4.4 we show for each pockets  $\Delta\sigma_V$  4.4a-c and the complete conductivity anisotropy  $\Delta\sigma$  4.4d-f as a function of  $\Phi^{h/e}$ . To easily compare the results of the numerics with the analytical estimate of Eq. 4.26 and 4.29 we renormalized the  $h_{\pm}/e$  pocket anisotropy in 4.4a-b and 4.4d-e to their value in the tetragonal phase. In 4.4c and 4.4f we renormalize instead the hole and electron anisotropy to the total values of  $\sigma_V$  and  $\sigma$  obtained summing all the pockets contributions in the tetragonal phase.

From the analysis of  $\Delta\sigma_V$  we find that the sign of the anisotropic contribution proportional to  $\Phi^{h/e}$  found in Eq. 4.26 and 4.29 is robust, with the  $\Gamma_{+/-}$  and the  $Y/X$  pockets contributing with positive/negative terms to the dc conductivity anisotropy (see panels 4.4a-b and inset of 4.4b). The hole pockets anisotropy due to the velocity, panels 4.4a-c, are opposite in sign and grows as  $\Phi^h/\epsilon_0^h$  in agreement with the analytical expectation. Even if the  $\Gamma_{\pm}$  are not longer equivalent due to a small spin-orbit interaction their anisotropic contributions almost cancel out so that the negative anisotropy of the electron pocket is the one that determines the final results. Once the effect of the scattering rate is included in the calculation we see in 4.4d a reduction of the conductivity anisotropy for the hole pocket that however still sum up to an anisotropic conductivity terms close to zero (4.4f). In contrast a change of sign in the overall electronic term is observed due to the larger positive contribution  $\Delta\sigma^Y$  of the  $Y$  pocket once that the anisotropic scattering rate is correctly taken into account. For the set of parameters used, thus, we find a final  $\Delta\sigma > 0$ . The result comes from the change in the relative weight of the contribution of the  $X$  and  $Y$  pockets in the electron term due to the different scattering rate  $\Gamma_R^{X/Y}$ .

The final outcome is thus particularly sensitive to the  $\Gamma_0^e$  and  $\Delta\Gamma^e$  used and could be strongly affected by any mechanism (temperature, disorder, interactions, ect..) affecting their absolute values.

## FeSe

We repeat the numerical analysis considering the case of FeSe. In Figure 4.5 we show the pockets Fermi surface wavevectors and velocities both in the tetragonal and in the nematic phase assuming  $\Phi^h = \Phi^e = 15$  meV.

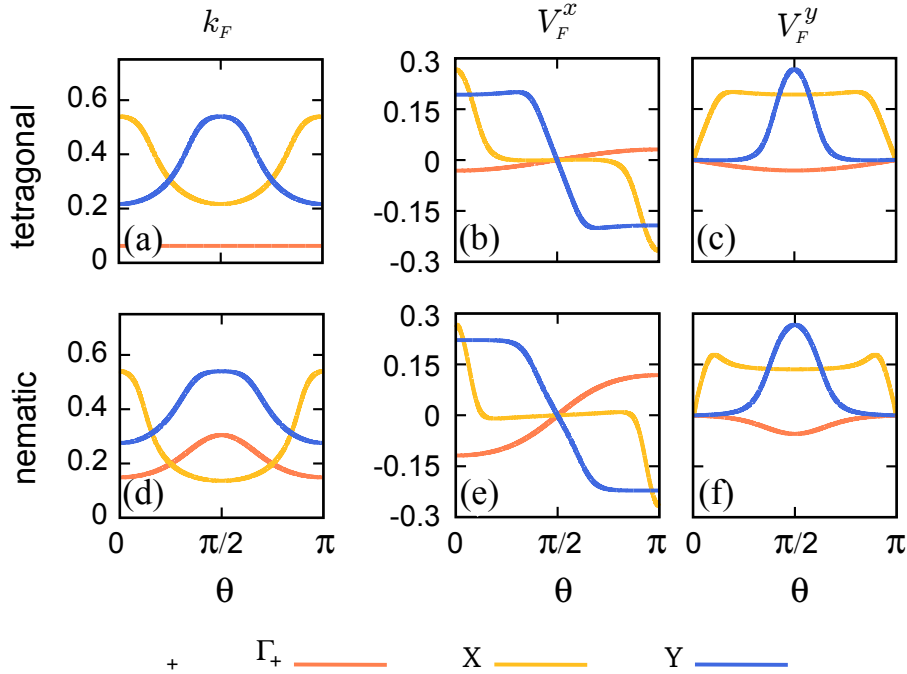


**Figure 4.5:** Numerical computation of the tetragonal and nematic Fermi surface and Fermi velocity components for FeSe parameters.  $\Phi_h = \Phi_e = 15$  meV, the spin-orbit interaction is 20 meV, the other band parameters are detailed in Appendix B.3.

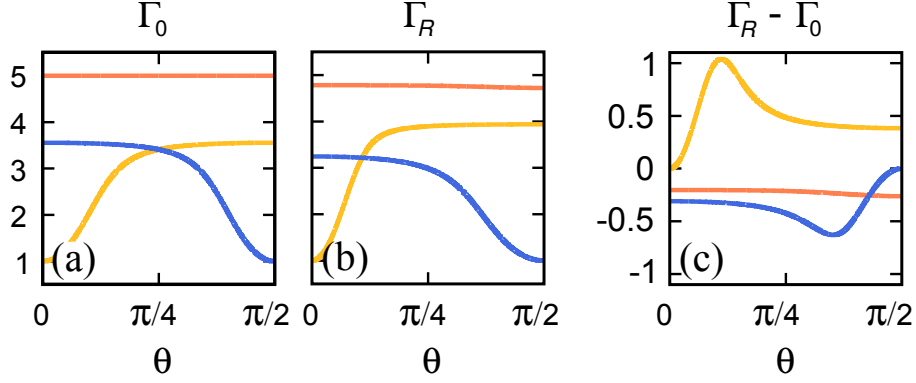


**Figure 4.6:** Renormalized scattering rate for FeSe.  $\Gamma_0^h = 5$  meV and  $\Gamma_0^e = 2.5$  meV.  $\Delta\Gamma^h$  and  $\Delta\Gamma^e$  are considered as proportional to the nematic variation of the real parts (App. D.3)

With respect to the previous case, here we clearly see that the outer hole pocket, the only one crossing the Fermi level, becomes strongly elliptical in the nematic phase due to the large nematic order which also makes the  $X/Y$  pockets consistently different in size (4.5a-d). The changes in the velocities (4.5e-f panels) are similar to the ones observed for the 122 case but quantitatively more pronounced here due to the larger value of the nematic order parameters.

The scattering rates for all the pockets are shown in Figure 4.6. For all the pockets we find a clear deviation of the renormalized scattering rate from the analytical estimate. In particular, the angular dependence of the  $\Gamma_+$  scattering rate is very weak and does not resemble the  $\cos 2\theta$  predicted by Eq. 4.14. This is a consequence of the Fermi surface nematic reconstruction of FeSe. In fact, the nematic order not only makes the  $\Gamma_+$  pocket elliptical but also affect its orbital content that becomes almost completely  $xz$  at the Fermi level [60, 86, 128]. As a consequence, the cold spots of the outer pocket shown in Fig. 4.1 do not represent anymore a minimum of the scattering since the  $\Gamma_+$  Fermi surface is mostly  $xz$  also at  $\theta = 0$ .

We study also in this case for each pocket the behaviour of  $\Delta\sigma_V$  and  $\Delta\sigma$  as a function of  $\Phi^{h/e}$ , Figure 4.7. We use the same renormalizations used in Figure 4.4.

The analysis of the velocity contribution reveals that the sign of the  $\Phi^{h/e}$  terms of Eq. 4.26 and 4.29 is robust also in this case. We are no longer in the perturbative regime as one can see from the non-linear behaviour of  $\Delta\sigma_V^{h+}$ , shown in 4.7a, where the  $\Gamma_+$  pocket anisotropy contribution grows much faster than what expected from the linear dependence in Eq. 4.26. The final anisotropy of  $\Delta\sigma_V$  is the result of the competition between the hole and electron terms.

The inclusion of the scattering rate in the calculation strongly affect the electron pockets contribution while leaving  $\Delta\sigma^{h+}$  almost unchanged. As a matter of fact, the scattering rate of the outer hole pocket  $\Gamma_R^{h+}$  is almost isotropic, see Figure 4.6, so that the anisotropic velocity is the only factor which contributes to the dc anisotropy of the  $\Gamma_+$  pocket.



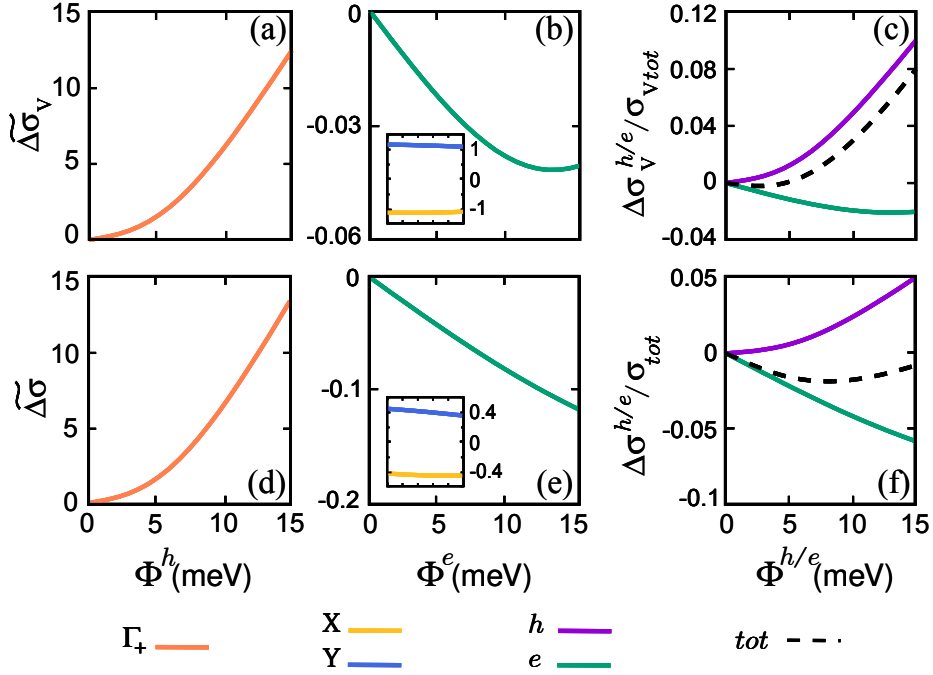


**Figure 4.7:** Numerical computation of the velocity contribution to the dc conductivity anisotropy and of the total dc conductivity anisotropy for realistic parameter for FeSe. All the pockets show consistent deviations of the dc anisotropy with respect the analytical expectations Eq. 4.26 and 4.29.

The final result for the dc conductivity strongly depends on the set of  $\Gamma_0^{h/e}$  and  $\Delta\Gamma^{h/e}$  used. In 4.7d-f, we show a case in which the inclusion of the scattering rate enhances the relative weight of the electron contribution with respect the hole term, so that overall the negative anisotropy of the electron part, due to the  $X$  pocket, determines the final results shown in 4.7f.

### High-energy renormalization and nesting

An effect neglected in the above calculation is the renormalization of the quasiparticle due to local electronic interactions. It is well established that in IBS the high-energy renormalizations of the quasiparticle  $Z_{orb}$  coming from local interactions are quite strong and orbital-dependent [57, 58]. The high-energy renormalizations have noticeable effects on the optical conductivity in the tetragonal phase of IBS, as discussed in Ref. [165] and should be included in the above calculation.

In order to assess the importance of this effect, we repeted the numerical analysis including phenomenologically the orbital renormalizations into the coherence factors  $(u/v)_R^l$  entering in Eq. 4.16. As expected, the inclusion of a severe reduction of the coherence of the  $xy$  orbital ( $Z_{xy} \sim 0.3$ ), that is the most correlated orbital in all IBS, leads to the suppression of the  $V_{X/Y}^{x/y}$  contributions enhancing the dc anisotropy in the electron pockets. Moreover, the small differentiation ( $\sim 10\%$ ) of the quasiparticle masses for the  $xz/yz$  orbitals in the nematic phase [97] contributes to enhance the differentiation of the  $\Gamma_{\pm}$  and  $X/Y$  pockets. However, the sign of the velocity contribution to the dc anisotropy is robust within the set of  $Z_{orb}$  considered. The quasiparticle renormalizations affect also the con-

ductivity via the renormalized scattering rate, however their relevance strongly depends on the set of parameters used, whose analysis goes beyond the scope of the present work.

Finally, it is worth noting that the analysis presented here does not include the physics of the band-nesting effects, which are the only ones to determine the location of the hot-spots in the band-based description [94, 155]. In particular the ellipticity of the  $X/Y$  pockets suggests that the scattering rate is maximum at the location where the nesting with the hole pockets is realized. Within the OSSF both, the orbital character and the degree of band nesting will contribute to the hot-spot location. Recent multiorbital RPA calculation in the paramagnetic state support the idea that the dominant effect in determining the scattering rate is still the orbital character of the Fermi surface [121, 166]. How these results evolve below  $T_S$  within an orbital selective spin-nematic scenario is still an open question which certainly deserves further investigation.

#### 4.4. Discussion and comparison with experiments

In the previous section we computed numerically the dc anisotropy for realistic parameters of 122 pnictides and FeSe. The values of the band structure parameters and self-energies used in the calculations quantitatively reproduce the main features of the Fermi surface, including the Fermi surface shrinking and the orbital Fermi surface reconstruction experimentally observed in the nematic phase of 122 and FeSe.

In 122, where the nematic order parameters  $\Phi^{h/e}$  are small, the hole pockets contribution to the dc conductivity anisotropy is well approximated by the analytical estimate Eq. 4.26, while we observe consistent deviations in FeSe. Nonetheless, for both 122 and FeSe systems the sign of the anisotropic contribution coming from the renormalized velocity,  $\Delta\sigma_V$ , is robust. In both cases considered in Section 4.3.2 we managed to match the experimental result,  $\Delta\sigma_{dc}(FeSe) < 0$  and  $\Delta\sigma_{dc}(122) > 0$ , once the renormalization of the scattering rate is included in the calculation. As already mentioned, the final result is still somehow sensitive to the set of parameters used. Thus, in this last section we discuss in general which are the possibilities to match the experimental results regardless the precise choice of parameters used in Section 4.3.2.

Concerning 122 systems, as long as the hole pockets contributions to the dc anisotropy cancel out, the final result is controlled by the electron pockets. Since they have a strong elliptical deformation, their overall contribution to the dc anisotropy cannot be predicted from the analytical result Eq. 4.29, and the final outcome depends on the relative weight of the  $X$  and  $Y$  pockets and on the relevance of the scattering rate anisotropy over the contribution  $\Delta\sigma_V^e$ . Even in doped 122 compounds the hole pocket contributions cancellation still occurs since the relatively small value of the spin-orbit splitting at  $\Gamma$  guarantees that the Fermi energy is the same for the hole pockets. However, doping changes both the size of the pockets and the degree of nesting between hole and electron pockets. Both effects contribute to change the relative weight of the  $X/Y$  electron pockets as well as the balance between the velocity vs scattering rate anisotropic contributions and can be at the origin of the different sign of  $\Delta\sigma_{dc}$  experimentally observed between the hole and electron doped side of 122 phase diagram.

For what concerns FeSe, the presence of a single hole pocket and its strong orbital reconstruction lead to rather different physics. In particular, since the nematic Fermi surface reconstruction makes the whole  $\Gamma_+$  Fermi surface mostly  $xz$  even at  $\theta = 0$ , the

expected anisotropy of the renormalized scattering rate is absent, see Figure 4.6. As a consequence the  $\Gamma_+$  anisotropic contribution is more likely controlled by the velocity anisotropy. This result should be contrasted with the outcomes of Ref. [167], where the difference between 122 and FeSe is fully ascribed to a different behavior of the scattering-rate anisotropy in the two compounds. In our picture the FeSe dc conductivity anisotropy emerges from a subtle interplay between the competing effects coming from the scattering rate and the velocity, as it has been recently suggested by optical conductivity experiments in FeSe [168].

It is worth noting that recent ARPES experiments reveal a strong  $k_z$  dependence of the orbital composition of the  $\Gamma_+$  Fermi surface [169], with the Fermi surface a  $k_z = \pi$  recovering  $yz$ -character at  $\theta = 0$ . As a consequence, also the scattering rate anisotropy on  $\Gamma_+$  is expected to be larger at  $k_z = \pi$  and its effect on the dc conductivity anisotropy can possibly compete with the velocity term at this  $k_z$ . This observation calls for a more complete analysis of the dc anisotropy involving also the  $k_z$ -dependence of the Fermi surface.

## 4.5. Conclusion Chapter 4

In conclusion, in the present Chapter we computed the dc-conductivity anisotropy in the nematic phase of IBS using the orbital selective spin-nematic scenario that accounts for the orbital content of the Fermi surface [26, 27]. In this scenario, the dc anisotropy of the nematic phase of IBS depends on the scattering rate and velocity renormalizations due to self-energy corrections. Both scattering rate and velocity are affected by the Fermi surface nematic reconstruction.

The scattering rate is strongly affected by the orbital content of the Fermi surface, and the location of its minima on the Fermi surface is found in correspondence of the less renormalized orbitals giving rise to cold spots. The velocity renormalization is sensitive both to the orbital mixing and to the shrinking of the Fermi surface induced by the nematic order, with the former effect dominating over the latter. Due to this effect we find the unexpected result that the conductivity increases in the direction in which the self-energy is larger and the shrinking is stronger.

For both, hole and electron carriers the contribution of the velocity to the dc anisotropy is opposite in sign to the one of the scattering rate. This is in agreement with optical conductivity experiment in FeSe [168] where it is shown that scattering rate and velocity contribute to the conductivity anisotropy with opposite signs.

Our results naturally follows from the spin-orbital entanglement implicit in the OSSF model and are new results in contrast to the band spin-nematic scenario [23, 28]. In particular we demonstrated that the usual expectation of anisotropic magnetic fluctuations giving rise only to an anisotropy in the inelastic scattering rate [155] is not longer valid once the orbital degree of freedom is taken into account in the theoretical description.

We performed numerical calculation for representative parameters for 122 pnictides and FeSe. We verified that for 122 system the analytical estimate represents a good approximation of the numerical with the overall hole pockets contribution vanishing even once a finite spin-orbit splitting at  $\Gamma$  is considered. Numerical results for FeSe instead deviate from the analytical expectations due to the huge nematic Fermi surface reconstruction. We also discuss how the conductivity anisotropy depends on the system parameters. It

can be dominated by either electron or hole pocket conductivity and depends on ellipticity and high-energy renormalizations.

The OSSF scenario provides then a suitable framework where the same mechanism due to orbital-spin interplay can reconcile the experimental observations reported in different families of iron-based superconductors.

# 5

## OSSF within a five-pockets model

### 5.1. Introduction

The Orbital Selective Spin Fluctuation (OSSF) model has been derived in [27] within a four-pocket model representative for IBS. This model offers the possibility to study qualitatively the different phenomenology of FeSe and 122 systems [27, 103] and it has been exploited to perform quantitative analysis of the nematic and superconducting phase of FeSe [60, 133].

In order address within a realistic calculation different compounds we need to consider the most general five-pockets that counts an additional pocket at the  $M = (\pi, \pi)$  point with  $xy$  orbital content. The analysis of this pocket is interesting as it has been shown that magnetic and superconducting properties vary with the size of this extra pocket [120, 139]. One well-known explanation for the change of the size of the  $M$  pocket is given in terms of the angle formed by the Fe-As bonds and the Fe-plane [107]. This angle differs among compounds [170, 171], and depends on doping [170, 172, 173] or applied pressure [174].

In the present Chapter we extend the OSSF model and generalize it to a five-pocket model. In Section 5.2 we introduce the extended OSSF model presenting the five-orbital kinetic and interacting Hamiltonian by adding the  $M$  hole pocket. The projection of the interaction into the low-energy five-pocket model unveils the orbital-selective character of the spin-fluctuations with  $yz/xz$  spin-fluctuations connecting the hole-pockets in  $\Gamma$  and the electron pockets in  $X/Y$  and  $xy$  spin-fluctuations connecting the hole-pockets in  $M$  with the  $X/Y$  electron pockets.

In Section 5.3, we derive the effective action for the five-pocket spin-nematic model following the same procedure discussed in Chapter 2 and we discuss the contribution to the magnetic and nematic instabilities coming from the  $\Gamma$ - $X/Y$  sector and from the  $M$ - $X/Y$  sector.

In order to analyse the effects on magnetism and nematicity due to the inclusion of the  $M$  hole pocket in the low-energy model, in Section 5.4 we perform a preliminary study of the three-band model  $MXY$ . The analysis represents an easy way to study the physics associated to the  $xy$  OSSF coming in absence of coupling with the  $\Gamma$ - $XY$  sector. The analysis is also motivated by the results of renormalization group study of the five-pocket model that show that such a three-band model represents a fix-point of the low-energy theory [123].

## 5.2. Model Hamiltonian

### 5.2.1. Kinetic Hamiltonian

We consider a general five-pocket model with two hole pockets,  $\Gamma_+$  and  $\Gamma_-$ , centered at the  $\Gamma = (0,0)$  point, two electron pockets,  $X$  and  $Y$ , centered at  $X = (\pi,0)$  and  $Y = (0,\pi)$  points respectively and a  $M$  hole pocket located at the  $M = (\pi,\pi)$  point. In Figure 5.1 it is shown a schematic representation of the orbital content of the Fermi surface for a generic five-pockets model for IBS. As within the four-pocket model, the hole pockets at  $\Gamma$  and the electron pockets at  $X/Y$  are composed by  $yz - xz$  orbitals and  $yz/xz - xy$  orbitals respectively. The fifth pocket at  $M$  pocket is composed exclusively of  $d_{xy}$  orbital.

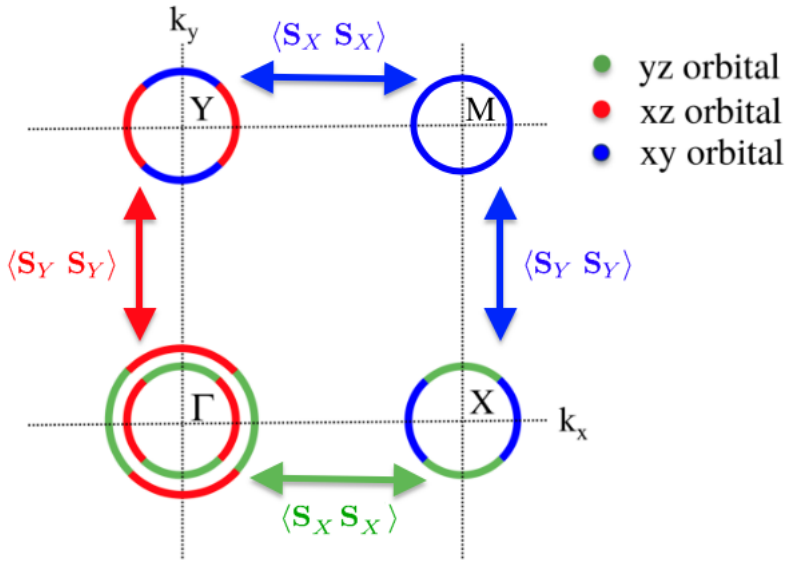


**Figure 5.1:** General sketch of the orbital content of the Fermi surface of the five-pocket model for IBS. The three dominant orbital weights,  $d_{xz}$ ,  $d_{yz}$  and  $d_{xy}$ , are taking into account. The green and red arrows show the OSSF carrying  $yz$  content in the  $x$  direction and  $xz$  content in the  $y$  direction, which connects the  $\Gamma$  hole pocket with an electron  $X$  and  $Y$  pocket respectively. The blue arrows show the OSSF carrying  $xy$  content in the  $x$  and  $y$  directions connecting the  $M$  hole pocket with both electron pockets  $X$  and  $Y$ .

The low-energy bands are modelled by the kinetic part of the Hamiltonian

$$H_0^l = \sum_{\mathbf{k}, \sigma} \psi_{\mathbf{k}\sigma}^\dagger \hat{H}_{0\mathbf{k}}^l \psi_{\mathbf{k}\sigma} \quad (5.1)$$

where  $l = \Gamma, X, Y, M$  and the spinors around the high-symmetry points are defined as  $\psi_{\mathbf{k}\sigma}^\Gamma = (c_{\mathbf{k}\sigma}^{yz}, c_{\mathbf{k}\sigma}^{xz})$ ,  $\psi_{\mathbf{k}\sigma}^{X/Y} = (c_{\mathbf{k}\sigma}^{yz/xz}, c_{\mathbf{k}\sigma}^{xy})$  and  $\psi_{\mathbf{k}\sigma}^M = c_{\mathbf{k}\sigma}^{xy}$ . As the hole pocket  $M$  is exclusively composed by the  $xy$  orbital, the corresponding fermionic operator has only one component.

The diagonalization of the  $\hat{H}_{0\mathbf{k}}^l$  leads to the band dispersion for the different pockets. The same rotation matrices that defines the bands for the four-pocket model diagonalize the  $l = \Gamma, X, Y$  Hamiltonian. For the  $\Gamma$  hole sector the fermionic spinor  $\psi_{\mathbf{k}\sigma}^\Gamma = (c_{\mathbf{k}\sigma}^{yz}, c_{\mathbf{k}\sigma}^{xz})$

rotates via the unitary matrix  $\hat{\mathcal{U}}_{\mathbf{k}}^\Gamma$  as

$$\begin{pmatrix} h^+ \\ h^- \end{pmatrix} = \begin{pmatrix} u^\Gamma & -v^\Gamma \\ v^\Gamma & u^\Gamma \end{pmatrix} \begin{pmatrix} c^{yz} \\ c^{xz} \end{pmatrix} \quad (5.2)$$

and for the  $X/Y$  electron sector the fermionic spinor  $\psi_{\mathbf{k}\sigma}^{X/Y} = (c_{\mathbf{k}\sigma}^{yz/xz}, c_{\mathbf{k}\sigma}^{xy})$  rotates via the unitary matrix  $\hat{\mathcal{U}}_{\mathbf{k}}^{X/Y}$  as

$$\begin{pmatrix} e^{X/Y+} \\ e^{X/Y-} \end{pmatrix} = \begin{pmatrix} u^{X/Y} & -v^{X/Y} \\ v^{X/Y} & u^{X/Y} \end{pmatrix} \begin{pmatrix} c^{yz/xz} \\ c^{xy} \end{pmatrix} \quad (5.3)$$

$\hat{H}_{0\mathbf{k}}^M$  only has one component thus does not require any rotation and we can use  $\psi_{\mathbf{k}\sigma}^M = c_{\mathbf{k}\sigma}^{xy}$  and

$$h^{xy} = c^{xy} \quad (5.4)$$

### 5.2.2. Interacting Hamiltonian

The interacting Hamiltonian, as for the four-pocket model (Eq. 2.26), is given by

$$H_{int} = -\frac{1}{2} \sum_{\mathbf{q}} \left( U_{\eta\eta'} \vec{S}^\eta(\mathbf{q}) \cdot \vec{S}^{\eta'}(-\mathbf{q}) \right) \quad (5.5)$$

with  $\eta, \eta' = yz, xz, xy$  the orbital indices and  $U_{\eta\eta'} \sim U\delta_{\eta\eta'} + J(1 - \delta_{\eta\eta'})$ , with  $U$  and  $J$  being the usual Hubbard and Hund couplings. We again consider only spin operators with intraorbital character  $\vec{S}^\eta(\mathbf{q}) = \sum_{\mathbf{k}ss'} c_{\mathbf{k}s}^{\eta\dagger} \vec{\sigma}_{ss'} c_{\mathbf{k}+\mathbf{q}s'}^\eta$  with  $\sigma_{ss'}$  the Pauli matrices for the spin operator and peaked at  $(\pi, 0)/(0, \pi)$  momenta. By projecting the interacting Hamiltonian Eq. 5.5 into the low-energy model Eqs. 5.2-5.4, the low-energy intraorbital spin operators are given by

$$\vec{S}_X^{yz} = \sum_{\mathbf{k}} (u^\Gamma h_+^\dagger + v^\Gamma h_-^\dagger) \vec{\sigma} u^X e^X \quad (5.6)$$

$$\vec{S}_Y^{xz} = \sum_{\mathbf{k}} (-v^\Gamma h_+^\dagger + u^\Gamma h_-^\dagger) \vec{\sigma} u^Y e^Y \quad (5.7)$$

$$\vec{S}_Y^{xy} = \sum_{\mathbf{k}} (\hat{h}_{xy}^\dagger) \vec{\sigma} (-v^X e^X) \quad (5.8)$$

$$\vec{S}_X^{xy} = \sum_{\mathbf{k}} (\hat{h}_{xy}^\dagger) \vec{\sigma} (-v^Y e^Y) \quad (5.9)$$

As already discuss within the analysis of the four-pocket model, the low-energy projection unveils a strong orbital-selectivity of the spin-fluctuations. The inclusion into the low-energy multiband description of the  $xy$ -hole pocket at  $M$  leads to the emergence of a spin-fluctuating mode connecting the hole pocket at  $M$  and the electron pockets at  $X/Y$  having  $xy$  character.

Consequently, the low energy for the five-pocket interacting Hamiltonian Eq. 5.5 reduces to

$$H_{int} = -\frac{\tilde{U}}{2} (\vec{S}_X^{yz} \cdot \vec{S}_X^{yz} + \vec{S}_Y^{xz} \cdot \vec{S}_Y^{xz} + \vec{S}_X^{xy} \cdot \vec{S}_X^{xy} + \vec{S}_Y^{xy} \cdot \vec{S}_Y^{xy}) \quad (5.10)$$



where  $\tilde{U}$  is the intraorbital interaction renormalized at low energy.

Due to the orbital-selectivity of the spin-fluctuation the inclusion of the  $xy$ -hole pocket at  $M$  in the OSSF model does not affect the interacting Hamiltonian describing the  $yz/xz$  spin-fluctuation exchange between  $\Gamma$ -X/Y and only appears via an additional interacting term representing the exchange of spin-fluctuation having  $xy$  character between the  $M$  hole pocket and the X/Y electrons. A schematic representation of the model is sketched in Figure 5.1.

### 5.3. Effective action for the five-pocket spin-nematic model

In this Section we derive the effective action for the five-pocket spin-nematic model using the same machinery discussed in Section 2.1 exploiting the Hubbard-Stratonovich (H-S) transformation to decouple the spin-spin interacting term Eq. 5.10.

We introduce the H-S fields  $\vec{M}_{X/Y}^{yz/xz}$  coupled to the OSSF connecting  $\Gamma$ -X/Y having  $yz/xz$  character and  $\vec{\tilde{M}}_{X/Y}^{xy/xy}$  coupled to the OSSF connecting  $M$ -X/Y having  $xy$  character

$$\begin{aligned}
 S_{\text{eff}} = & \begin{pmatrix} M_X & M_Y & \tilde{M}_X & \tilde{M}_Y \end{pmatrix} \begin{pmatrix} \chi_X^{-1} & 0 & 0 & 0 \\ 0 & \chi_Y^{-1} & 0 & 0 \\ 0 & 0 & \tilde{\chi}_X^{-1} & 0 \\ 0 & 0 & 0 & \tilde{\chi}_Y^{-1} \end{pmatrix} \begin{pmatrix} M_X \\ M_Y \\ \tilde{M}_X \\ \tilde{M}_Y \end{pmatrix} \\
 & + \begin{pmatrix} (M_X)^2 & (M_Y)^2 & (\tilde{M}_X)^2 & (\tilde{M}_Y)^2 \end{pmatrix} \begin{pmatrix} u_{11} & u_{12} & 0 & k_{12} \\ u_{12} & u_{22} & k_{21} & 0 \\ 0 & k_{21} & \tilde{u}_{11} & \tilde{u}_{12} \\ k_{12} & 0 & \tilde{u}_{12} & \tilde{u}_{22} \end{pmatrix} \begin{pmatrix} (M_X)^2 \\ (M_Y)^2 \\ (\tilde{M}_X)^2 \\ (\tilde{M}_Y)^2 \end{pmatrix} \quad (5.11)
 \end{aligned}$$

We are using a notation in which the terms related to the  $xy$  OSSF are defined using a tilde character. Hereafter we refer to  $M$ -X/Y sector to indicate those quantities and  $\Gamma$ -X/Y sector for the other. Notice that the quartic order expansion contains coupling terms  $k_{12/21}$  that connect the Gaussian fluctuation of the  $yz/xz$  spin-mode along  $x$  with the  $xy$  along the same direction (idem along  $y$ ).

#### Quadratic terms

The Gaussian part of the action Eq. 5.11 is given by the magnetic susceptibilities  $\chi_{X/Y}^{-1} = 1/2\tilde{U} + \Pi_{X/Y}^{yz/xz}$  and  $\tilde{\chi}_{X/Y}^{-1} = 1/2\tilde{U} + \tilde{\Pi}_{X/Y}^{xy/xy}$ , where  $\tilde{U}$  is the effective interactions between low-energy quasiparticles, and  $\Pi_{X/Y}^{yz/xz}$  and  $\tilde{\Pi}_{X/Y}^{xy/xy}$  are the propagators in the zero-

frequency limit given by

$$\Pi_X^{yz} = 2T \sum_{\mathbf{k}, i\omega_n} \left( u_\Gamma^2 u_X^2 g_+ g_X + v_\Gamma^2 u_X^2 g_- g_X \right), \quad (5.12)$$

$$\Pi_Y^{xz} = 2T \sum_{\mathbf{k}, i\omega_n} \left( v_\Gamma^2 u_Y^2 g_+ g_Y + u_\Gamma^2 u_Y^2 g_- g_Y \right), \quad (5.13)$$

$$\tilde{\Pi}_X^{xy} = 2T \sum_{\mathbf{k}, i\omega_n} v_Y^2 g_M g_Y, \quad (5.14)$$

$$\tilde{\Pi}_Y^{xy} = 2T \sum_{\mathbf{k}, i\omega_n} v_X^2 g_M g_X. \quad (5.15)$$

Notice that the two first equations 5.12 and 5.13, are the same than Eqs. 2.30 and 2.31 for the four pocket model analyzed in Chapter 2 and represent the spin exchange of  $yz/xz$  spin-fluctuations between the  $\Gamma$ -X/Y sector. On the other hand, Eq. 5.14 and Eq. 5.15 are the magnetic propagators in the zero-frequency limit coming from the  $xy$  spin-fluctuation exchange between the  $M$ -X/Y

### Quartic terms

The coefficients of the quartic part of the action Eq. 5.11 are given by

$$u_{11} = T \sum_{\mathbf{k}, i\omega_n} \left( u_X^2 g_X \right)^2 (u_\Gamma^2 g_+ + v_\Gamma^2 g_-)^2, \quad (5.16)$$

$$u_{22} = T \sum_{\mathbf{k}, i\omega_n} \left( u_Y^2 g_Y \right)^2 (v_\Gamma^2 g_+ + u_\Gamma^2 g_-)^2, \quad (5.17)$$

$$u_{12} = T \sum_{\mathbf{k}, i\omega_n} u_X^2 g_X u_Y^2 g_Y u_\Gamma^2 v_\Gamma^2 (g_+ - g_-)^2, \quad (5.18)$$

$$\tilde{u}_{11} = T \sum_{\mathbf{k}, i\omega_n} (v_Y^2 g_Y g_M)^2, \quad (5.19)$$

$$\tilde{u}_{22} = T \sum_{\mathbf{k}, i\omega_n} (v_X^2 g_X g_M)^2, \quad (5.20)$$

$$\tilde{u}_{12} = T \sum_{\mathbf{k}, i\omega_n} v_X^2 g_X v_Y^2 g_Y g_M^2, \quad (5.21)$$

$$k_{12} = T \sum_{\mathbf{k}, i\omega_n} (u_X v_X g_X)^2 g_M (u_\Gamma^2 g_+ + v_\Gamma^2 g_-), \quad (5.22)$$

$$k_{21} = T \sum_{\mathbf{k}, i\omega_n} (u_Y v_Y g_Y)^2 g_M (v_\Gamma^2 g_+ + u_\Gamma^2 g_-). \quad (5.23)$$

The expression for the quartic order coefficients relative to the  $\Gamma$ -X/Y sector Eqs. 5.16-5.18, are the same found for the four pocket model Eqs. 2.32-2.34. Analogous expressions are found for the  $M$ -X/Y sector, Eqs. 5.19-5.21. The mixed contribution connect the two sector by combining the spin-fluctuation along  $x/y$  weighted with the correspondent orbital factors, Eq. 5.22 and 5.23.

In what follows we perform analytical calculation of the coefficients of the effective action first within the perfect nested parabolic band approximation and then accounting perturbatively deviation from the perfect nesting conditions. We refer to Appendix E.1 for further details of the analytical computation.

### 5.3.1. Perfect circular nested Fermi surfaces

To make a first estimate of the new physics coming from the inclusion of the  $M$  pocket in the OSSF model, we start considering the simple case where the hole and the electron pockets are described by perfect nested circular Fermi surfaces.

In this approximation the orbital weights and pocket Green's functions reduce to

$$u_\Gamma = u_Y = v_X = \cos \theta, \quad v_\Gamma = v_Y = u_X = \sin \theta \quad (5.24)$$

$$g_+ = g_- = g_M = g_h = (i\omega_n + \epsilon)^{-1} \quad g_X = g_Y = g_e = (i\omega_n - \epsilon)^{-1} \quad (5.25)$$

with  $\epsilon = -\epsilon_0 + \mathbf{k}^2/2m - \mu$ .  $\epsilon_0$  is the off-set energy,  $m$  the parabolic band mass and  $\mu$  the chemical potential and  $\omega_n = (2n+1)\pi k_B T$  is the fermionic Matsubara frequency (see Appendix E.1.1). Notice that Eq. 5.24 are the same used for the analysis of the four-pockets OSSF model given by Eq. 2.38 and describe the orbital composition of the  $\Gamma, X, Y$  pockets. The  $M$  hole-pocket has purely  $xy$  orbital character so there is no angular modulation in the orbital composition.

#### Quadratic terms

Within the perfect nested parabolic band approximation the quadratic terms for a five-pocket model given by Eqs. 5.12-5.15 become

$$\Pi_X^0 = 2T \sum_{\mathbf{k}, i\omega_n} \left( \cos^2 \theta \sin^2 \theta g_h g_e + \sin^2 \theta \sin^2 \theta g_h g_e \right), \quad (5.26)$$

$$\Pi_Y^0 = 2T \sum_{\mathbf{k}, i\omega_n} \left( \sin^2 \theta \cos^2 \theta g_h g_e + \cos^2 \theta \cos^2 \theta g_h g_e \right), \quad (5.27)$$

$$\tilde{\Pi}_X^0 = 2T \sum_{\mathbf{k}, i\omega_n} \sin^2 \theta g_h g_e, \quad (5.28)$$

$$\tilde{\Pi}_Y^0 = 2T \sum_{\mathbf{k}, i\omega_n} \cos^2 \theta g_h g_e \quad (5.29)$$

It easy to verify that within this approximation all the components of the propagator reduce to the same expression once performed angular integration over  $\theta$ . By evaluating the sum over the Matsubara frequency  $\omega_n$  we find

$$\Pi_{X/Y}^0 = \tilde{\Pi}_{X/Y}^0 = \Pi_{eh} \quad (5.30)$$

where we define  $\Pi_{eh} \equiv TN_F \sum_{i\omega_n} \int d\epsilon g_e g_h = -N_F (\ln(\omega_0/T) + \text{const})$  that leads to the usual logarithmic divergence. As a consequence the magnetic susceptibility associated to  $yz/xz$  OSSF exchange between  $\Gamma XY$  and the one relative to  $xy$  OSSF exchange between  $MXY$  are equivalent

$$\chi_{X/Y}^0(q=0)^{-1} = \tilde{\chi}_{X/Y}^0(q=0)^{-1} = N_F \ln \left( \frac{T}{T_N} \right) \quad (5.31)$$

where the Néel temperature is

$$T_N = \frac{\omega_0}{k_B} e^{-(1/(2N_F \tilde{U}))}. \quad (5.32)$$

### Quartic terms

The quartic coefficients involving the  $\Gamma$ -X/Y sector (Eqs. 5.16-5.18) are given by

$$u_{11}^0 = u_{22}^0 = \frac{48 N_F}{128} \mathcal{A}(T) \quad (5.33)$$

$$u_{12}^0 = 0 \quad (5.34)$$

with  $\mathcal{A}(T) \equiv \frac{7\zeta(3)}{8\pi^2 T^2}$  coming from the integration of the hole and electron Green's functions computed in detail in Appendix E.1.2.

The quartic terms for the  $M$ -X/Y sector are

$$\tilde{u}_{11}^0 = \tilde{u}_{22}^0 = \frac{48 N_F}{128} \mathcal{A}(T), \quad (5.35)$$

$$\tilde{u}_{12}^0 = \left( \frac{16 N_F}{128} \mathcal{A}(T) \right) \quad (5.36)$$

We find that the diagonal components  $u_{ii}^0$  and  $\tilde{u}_{ii}^0$  are equal for both sectors, while the off-diagonal components are different.  $\tilde{u}_{ij}^0$  is finite,  $u_{ij}^0$  instead vanishes for the  $\Gamma$ -X/Y sector due to the contribution from  $\Gamma^\pm$  pockets that cancel each other within the parabolic band approximation.

Notice that already within the parabolic band approximation the  $\Gamma$ -X/Y and the  $M$ -X/Y sectors are coupled at quartic level by

$$k_{12}^0 = k_{21}^0 = \frac{16 N_F}{128} \mathcal{A}(T) \quad (5.37)$$

that assumes the same value of  $\tilde{u}_{12}^0$  term given in Eq. 5.36.

Within the perfect nested parabolic case using that  $u_{12}^0 = 0$  and  $u_{11}^0 = \tilde{u}_{11}^0$ ,  $k_{12}^0 = \tilde{u}_{12}^0$ , we can rewrite

$$S_{\text{eff}}^{0\text{quartic}} = \begin{pmatrix} u_{11}^0 & 0 & 0 & \tilde{u}_{12}^0 \\ 0 & u_{11}^0 & \tilde{u}_{12}^0 & 0 \\ 0 & \tilde{u}_{12}^0 & u_{11}^0 & \tilde{u}_{12}^0 \\ \tilde{u}_{12}^0 & 0 & \tilde{u}_{12}^0 & u_{11}^0 \end{pmatrix} \quad (5.38)$$

with the quartic terms different from 0 given by a similar analytical expressions that only vary in the numerical factors (Eqs. 5.33-5.37).

To study the magnetic and the nematic instabilities, we have to define the analogous of the  $\psi$  and  $\phi$  order parameters for the four-pocket model given in Eq. 2.36 and 2.37 respectively and then, perform a second Hubbard-Stratonovich transformation by diagonalizing the quartic term of the effective action given by Eq. 5.38. Despite the complication due to the additional  $M$ -X/Y sector appearing in the effective action of the OSSF model for five-pockets, the computation of the eigenvalues and the corresponding eigenvectors is

still treatable analytically. The eigenvalues of Eq. 5.38 are given by

$$\begin{aligned}
 \lambda_1^0 &= u_{11}^0 + \frac{1}{2}(1 - \sqrt{5})\tilde{u}_{12}^0 = \frac{N_F}{16}c_1 \mathcal{A}(T) \\
 \lambda_2^0 &= u_{11}^0 - \frac{1}{2}(1 + \sqrt{5})\tilde{u}_{12}^0 = \frac{N_F}{16}c_2 \mathcal{A}(T) \\
 \lambda_3^0 &= u_{11}^0 + \frac{1}{2}(1 + \sqrt{5})\tilde{u}_{12}^0 = \frac{N_F}{16}c_3 \mathcal{A}(T) \\
 \lambda_4^0 &= u_{11}^0 - \frac{1}{2}(1 - \sqrt{5})\tilde{u}_{12}^0 = \frac{N_F}{16}c_4 \mathcal{A}(T)
 \end{aligned} \tag{5.39}$$

where  $c_i > 0$  are positive numerical factors. The corresponding eigenvectors are

$$\begin{aligned}
 \rho_1 &= \frac{1}{A} \left[ \left( (M_X)^2 + (M_Y)^2 \right) - \left( (\tilde{M}_X)^2 + a(\tilde{M}_Y)^2 \right) \right] \begin{pmatrix} \\ \\ \\ \end{pmatrix} \\
 \rho_2 &= \frac{1}{A} \left[ \left( (M_X)^2 - (M_Y)^2 \right) - \left( (\tilde{M}_X)^2 - a(\tilde{M}_Y)^2 \right) \right] \begin{pmatrix} \\ \\ \\ \end{pmatrix} \\
 \rho_3 &= \frac{1}{A} \left[ \left( (M_X)^2 - a(M_Y)^2 \right) + \left( a(\tilde{M}_X)^2 - (\tilde{M}_Y)^2 \right) \right] \begin{pmatrix} \\ \\ \\ \end{pmatrix} \\
 \rho_4 &= \frac{1}{A} \left[ \left( (M_X)^2 + a(M_Y)^2 \right) + \left( a(\tilde{M}_X)^2 + (\tilde{M}_Y)^2 \right) \right] \begin{pmatrix} \\ \\ \\ \end{pmatrix}
 \end{aligned} \tag{5.40}$$

where  $a = \frac{1}{2}(\sqrt{5} - 1)$ . Notice that in Eq. 5.40 we separated the contribution of the  $\Gamma$ -X/Y sector given by  $M_{X/Y}$  from the contribution of the  $M$ -X/Y sector given by  $\tilde{M}_{X/Y}$ . The specific computation of Eqs. 5.39 and 5.40 is shown in Appendix E.2.

As one can see from Eq. 5.40,  $\rho_1$  and  $\rho_4$  are the eigenvectors describing isotropic contributions to the magnetic fluctuations along the  $x/y$  directions, while  $\rho_2$  and  $\rho_3$  describe anisotropic fluctuations which are related with the nematic order. From Eq. 5.39 we see that for the perfect nested band approximation, all the eigenvalues are positive, this means that analogously to what found for the four-pocket model, the interaction in the nematic channel is always repulsive.

### 5.3.2. Effect of the ellipticity in the model

In this Section we include at perturbative level the electron pockets ellipticity  $\delta_e$  and the deviations from perfect circular nesting for the hole sector  $\delta_{m_{\pm},M}$  in order to study a more realistic case in which the form and size of the pockets are different. We follow the same strategy of Chapter 2 and analyze how the Fermi surface shapes affect to the quadratic and quartic terms of the effective action for the five-pocket model.

In this approximation, the pockets Green's function are

$$\begin{aligned}
 g_{\pm,M} &= g_h(1 + \delta_{m_{\pm},M}g_h) \\
 g_{X/Y} &= g_e(1 \mp \delta_e \cos(2\theta)g_e).
 \end{aligned} \tag{5.41}$$

with  $g_h$  and  $g_e$  the perfect nested circular Green's function given by Eq. 5.25. The effect of the ellipticity for the electron pockets is included in the perturbative parameter  $\delta_e = \epsilon_0 m \left( \frac{m_x - m_y}{2m_x m_y} \right)$ . (We account for a deviation from the perfect circular nesting condition (as results of doping for example) defining a perturbative parameter  $\delta_{m_{\pm},M} = \epsilon_0 \left( \frac{m_{\pm}/M - m}{m} \right)$ )

term, where subscript  $m_{\pm}/M$  refers to the  $\Gamma^{\pm}/M$  hole pockets. To reduce the number of parameters and make the result more readable for simplicity we set here  $\delta_{m_+} = 0$  as it is only necessary one  $\delta_m$  to differentiate the two gamma pockets. See Appendix E.1.1 for further details of the elliptical approximation.

### Quadratic term

The quadratic term for the  $\Gamma$ -X/Y sector is given by

$$\Pi_{X/Y} = \Pi_{eh} + \frac{N_F}{2} \mathcal{A}(T) \delta_{m_-} \delta_e \quad (5.42)$$

and for the  $M$ -X/Y sector is

$$\tilde{\Pi}_{X/Y} = \Pi_{eh} - \frac{N_F}{2} \mathcal{A}(T) \delta_M \delta_e \quad (5.43)$$

Notice that the corrections  $\sim \delta_e \delta_{m_{\pm}, M}$  appear in the propagator with same numerical coefficient but opposite sign for the two sectors. This is a direct consequence of the angular integration of the  $\cos(2\theta)$  angular factor coming from the  $\delta_e$  expansion Eq. 5.41 multiplied by the orbital weights  $(u/v)^l$  that are different from the  $\Gamma$ -X/Y sector and the  $M$ -X/Y sector.

As consequence, the magnetic susceptibility is now different for the  $yz/xz$  OSSF of the  $\Gamma$ -X/Y sector and the  $xy$  OSSF of the  $M$ -X/Y sector

$$\chi_{X/Y}^{-1}(q=0) = N_F \ln \left( \frac{T}{T_N^*} \right) \left( \frac{7N_F \zeta(3)}{16\pi^2} \delta_{m_-} \delta_e \left( \frac{1}{T_N^{*2}} - \frac{1}{T^2} \right) \right) \quad (5.44)$$

$$\tilde{\chi}_{X/Y}^{-1}(q=0) = N_F \ln \left( \frac{T}{T_N^*} \right) \left( - \frac{7N_F \zeta(3)}{16\pi^2} \delta_M \delta_e \left( \frac{1}{T_N^{*2}} - \frac{1}{T^2} \right) \right) \quad (5.45)$$

where  $T_N^*$  is the new Néel temperature that is still the degenerate for the  $yz/xz$  and  $xy$  OSSF. Notice that the corrections  $\sim \delta_e \delta_{m_{\pm}, M}$  differentiate the two subsectors for  $T > T_N^*$  and vanish approaching  $T_N^*$ .

### Quartic terms

The quartic terms for the  $\Gamma$ -X/Y sector are

$$u_{11} = u_{22} = \frac{N_F}{128} \left[ 48 \mathcal{A}(T) + \mathcal{B}(T) \left( 35 \delta_{m_-}^2 + 28 \delta_e^2 \right) \left( 120 \mathcal{C}(T) \delta_{m_-} \delta_e \right) \right] \quad (5.46)$$

$$u_{12} = \frac{2 N_F}{128} \mathcal{C}(T) \delta_{m_-}^2 \quad (5.47)$$

with

$$\mathcal{A}(T) \equiv \frac{7\zeta(3)}{8\pi^2 T^2}, \quad \mathcal{B}(T) \equiv -\frac{31\zeta(5)}{64\pi^4 T^4} \quad \text{and} \quad \mathcal{C}(T) \equiv -\frac{93\zeta(5)}{128\pi^4 T^4}$$

the different temperature dependence factors that come from the different Green's function integrals.

The quartic terms involving the  $M$ -X/Y are given by

$$\tilde{u}_{11} = \tilde{u}_{22} = \frac{N_F}{128} \left[ 48 \mathcal{A}(T) + \mathcal{B}(T) \left( 48\delta_M^2 + 28\delta_e^2 \right) \left( -128 \mathcal{C}(T) \delta_M \delta_e \right) \right] \left( \quad \right) \quad (5.48)$$

$$\tilde{u}_{12} = \frac{N_F}{128} \left[ 6 \mathcal{A}(T) + \mathcal{B}(T) \left( 16\delta_M^2 - 4\delta_e^2 \right) \right] \left( \quad \right) \quad (5.49)$$

where the  $\delta_M \delta_e$  term appears with opposite sign respect to the  $\Gamma$ -X/Y sector given by Eq. 5.46. The mixing terms are

$$k_{12} = k_{21} = \frac{N_F}{128} \left[ 16 \mathcal{A}(T) + \mathcal{B}(T) \left( 8\delta_M \delta_{m-} + 4\delta_e^2 \right) \left( +4 \mathcal{C}(T) \delta_{m-} \delta_e \right) \right] \left( \quad \right) \quad (5.50)$$

where an extra  $\delta_M \delta_{m-}$  term that connects the  $\Gamma$ -X/Y sector and the  $M$ -X/Y sector is obtained.

In Table 5.1 we summarize the different contributions for the quadratic and quartic terms in the perfect circular nested Fermi surfaces and elliptical approximation are shown.

Five-pocket model: $\Gamma^+ \Gamma^- XYM$		
Quadratic terms		
	From $\Gamma$ -X/Y sector	From $M$ -X/Y sector
$\Pi_{X/Y}^0, \tilde{\Pi}_{X/Y}^0$	$\Pi_{eh}$	$\Pi_{eh}$
$\Pi_{X/Y}, \tilde{\Pi}_{X/Y}$	$+N_F/2\mathcal{A}\delta_{m-}\delta_e$	$-N_F/2\mathcal{A}\delta_{m-}\delta_e$
Quartic terms		
	From $\Gamma$ -X/Y sector	From $M$ -X/Y sector
$u_{11}^0/\tilde{N}_F, \tilde{u}_{11}^0/\tilde{N}_F$	$48\mathcal{A}$	$48\mathcal{A}$
$u_{11}/\tilde{N}_F, \tilde{u}_{11}/\tilde{N}_F$	$+\mathcal{B}(35\delta_{m-}^2 + 28\delta_e^2) + 120\mathcal{C}\delta_{m-}\delta_e$	$+\mathcal{B}(48\delta_M^2 + 28\delta_e^2) - 128\mathcal{C}\delta_M\delta_e$
$u_{12}^0/\tilde{N}_F, \tilde{u}_{12}^0/\tilde{N}_F$	$0$	$16\mathcal{A}$
$u_{12}/\tilde{N}_F, \tilde{u}_{12}/\tilde{N}_F$	$+2\mathcal{C}\delta_{m-}^2$	$+\mathcal{B}(16\delta_M^2 - 4\delta_e^2)$
From mixed $\Gamma$ -X/Y and $M$ -X/Y sectors		
$k_{12}^0/\tilde{N}_F$	$16\mathcal{A}$	
$k_{12}/\tilde{N}_F$	$+\mathcal{B}(8\delta_M\delta_{m-} + 4\delta_e^2) + 4\mathcal{C}\delta_{m-}\delta_e$	

**Table 5.1:** Quadratic and quartic terms for the five-pockets model for the perfect circular nested Fermi surfaces and the case for elliptical electrons and deviated hole pockets from the perfect nested approximation. The quantities coming from the  $\Gamma$ -X/Y and  $M$  sectors are represented without or with a tilde  $\sim$  respectively.

The analytical computation of the eigenvalues and the corresponding eigenvectors for the quartic term of the effective action as a function of the ellipticity and pocket size is still working in progress. To gain physical in what follows we study two complementary three-band model  $\Gamma_-XY$  and  $MX Y$ . The analysis of the three-pocket model  $MX Y$  represents an easy way to study the physics associated to the  $xy$  OSSF coming from the presence of the  $M$  pocket in a simplified frame in which there is no coupling with the  $xz/yz$  OSSF of the  $\Gamma$ -XY sector. The analysis is also motivated by the results of renormalization group



study of the five-pocket model that show that such a three-band model represents a fix-point of the low-energy theory [123]. We compare the results of the  $MX Y$  model with the results of the  $\Gamma_-XY$  that present the same degree of orbital nesting (good matching between the orbitals in the nested hole and electron pockets) and has been already studied in [27].

## 5.4. Orbital selectivity in the $\Gamma_-XY$ vs $MX Y$ pocket model

### 5.4.1. $\Gamma_-XY$ model

As we discussed in Section 2.2.2, the  $\Gamma_-XY$  model is a prototypical three-pocket model in which the hole  $\Gamma_-$  pocket has optimal orbital  $yz/xz$  nesting with the electron pockets.

The interacting Hamiltonian for the  $\Gamma_-XY$  model is given by

$$H_{int} = -\frac{\tilde{U}}{2} \vec{S}_{X/Y}^{yz/xz} \cdot \vec{S}_{X/Y}^{yz/xz} \quad (5.51)$$

By decoupling the interacting term 5.51 by means of two vectorial H-S fields  $\vec{M}_X^{yz}$  and  $\vec{M}_Y^{xz}$  associated with the collective magnetic degree of freedom  $\vec{S}_X^{yz}$  and  $\vec{S}_Y^{xz}$  given by Eqs. 5.6 and 5.7 respectively setting  $h_+^\dagger = 0$ , the effective action for the  $\Gamma_-XY$  model is

$$S_{\text{eff}}^{\Gamma_-XY} = \begin{pmatrix} M_X^{yz} & M_Y^{xz} \end{pmatrix} \begin{pmatrix} \chi_X^{-1} & 0 \\ 0 & \chi_Y^{-1} \end{pmatrix} \begin{pmatrix} M_X^{yz} \\ M_Y^{xz} \end{pmatrix} + \begin{pmatrix} (M_X^{yz})^2 & (M_Y^{xz})^2 \end{pmatrix} \begin{pmatrix} u_{11} & u_{12} \\ u_{12} & u_{11} \end{pmatrix} \begin{pmatrix} (M_X^{yz})^2 \\ (M_Y^{xz})^2 \end{pmatrix} \quad (5.52)$$

with  $\chi_{X/Y}^{-1}(q=0) = \chi^{\Gamma_-XY^{-1}}(q=0)$  the static magnetic susceptibility equivalent for both directions  $X/Y$  given by

$$\chi^{\Gamma_-XY^{-1}}(q=0) = \frac{3N_F}{4} \ln \left( \frac{T}{T_N^{*\Gamma_-XY}} \right) \left( \frac{7N_F \zeta(3)}{16\pi^2} \delta_{m-} \delta_e \left( \frac{1}{(T_N^{*\Gamma_-XY})^2} - \frac{1}{T^2} \right) \right) \quad (5.53)$$

The coefficients of the quartic part of the action in Eq. 5.52 are

$$u_{11}^{\Gamma_-XY} = \frac{N_F}{128} \left[ 35 \mathcal{A}(T) + \mathcal{B}(T) \left( 35\delta_{m-}^2 + \frac{49\delta_e^2}{2} \right) \right] \left( + 112 \mathcal{C}(T) \delta_{m-} \delta_e \right) \quad (5.54)$$

$$u_{12}^{\Gamma_-XY} = \frac{N_F}{128} \left[ 3 \mathcal{A}(T) + \mathcal{B}(T) \left( 3\delta_{m-}^2 - \frac{\delta_e^2}{2} \right) \right] \left( \right) \quad (5.55)$$

Thus, the nematic coupling for  $\Gamma_-XY$  model the is defining as  $\lambda_\phi^{\Gamma_-XY} = u_{11}^{\Gamma_-XY} - u_{12}^{\Gamma_-XY}$  and is given by

$$\lambda_\phi^{\Gamma_-XY} = \frac{N_F}{128} \left[ 32 \mathcal{A}(T) + \mathcal{B}(T) (32\delta_{m-}^2 + 25\delta_e^2) + 112 \mathcal{C}(T) \delta_{m-} \delta_e \right] \left( \right) \quad (5.56)$$

which depends on both, the ellipticity of the electrons  $\delta_e$  and the deviation from perfect nested  $\Gamma_-$  Fermi surfaces  $\delta_{m-}$ .

### 5.4.2. MXY model

We perform the same analysis for the MXY model, in which the only the  $M$  hole is taken into account. The low-energy projection in this model leads to interacting Hamiltonian

$$H_{int} = -\frac{\tilde{U}}{2} \vec{S}_{X/Y}^{xy/xy} \cdot \vec{S}_{X/Y}^{xy/xy} \quad (5.57)$$

in which the spin-fluctuations connecting the  $M$  hole pocket and the  $X/Y$  electron pockets are fully  $xy$ . By decoupling the interacting term 5.57 by means of two H-S fields  $\vec{M}_X^{xy}$  and  $\vec{M}_Y^{xy}$  associated with magnetic degree of freedom  $\vec{S}_X^{xy}$  and  $\vec{S}_Y^{xy}$  given by Eqs. 5.8 and 5.9 respectively, the effective action for the MXY model is

$$S_{\text{eff}}^{MXY} = \begin{pmatrix} \vec{M}_X^{xy} & \vec{M}_Y^{xy} \end{pmatrix} \begin{pmatrix} \tilde{\chi}_X^{-1} & 0 \\ 0 & \tilde{\chi}_Y^{-1} \end{pmatrix} \begin{pmatrix} \vec{M}_X^{xy} \\ \vec{M}_Y^{xy} \end{pmatrix} + \begin{pmatrix} (\vec{M}_X^{xy})^2 & (\vec{M}_Y^{xy})^2 \end{pmatrix} \begin{pmatrix} \tilde{u}_{11} & \tilde{u}_{12} \\ \tilde{u}_{12} & \tilde{u}_{11} \end{pmatrix} \begin{pmatrix} (\vec{M}_X^{xy})^2 \\ (\vec{M}_Y^{xy})^2 \end{pmatrix} \quad (5.58)$$

with  $\tilde{\chi}_{X/Y}^{-1}(q=0) = \tilde{\chi}^{MXY-1}(q=0)$  the static magnetic susceptibilities for the  $X/Y$  directions are given by

$$\tilde{\chi}^{MXY-1}(q=0) = N_F \ln \left( \frac{T}{T_N^{*MXY}} \right) + \frac{7N_F \zeta(3)}{16\pi^2} \delta_M \delta_e \left( \left( \frac{1}{(T_N^{*MXY})^2} - \frac{1}{T^2} \right) \right) \quad (5.59)$$

Given the orbital composition of the M-pocket the angular integral makes the  $MXY$  spin-propagator larger than the one for the three pocket model  $\Gamma_-XY$ . This leads to a higher instability temperature for the  $xy$  OSSF of the  $MXY$  model with respect to the the  $xz/yz$  OSSF of the  $\Gamma_-XY$ . Notice that the term proportional to  $\delta_M \delta_e$  is equal to the term proportional to  $\delta_m \delta_e$  for the  $\Gamma_-XY$  model given in Eq. 5.53 but it contributes to the total static spin susceptibility with opposite sign.

The coefficients of the quartic part of the action in Eq. 5.58 are

$$u_{11}^{MXY} = \frac{N_F}{128} \left[ 48 \mathcal{A}(T) + \mathcal{B}(T)(48\delta_M^2 + 28\delta_e^2) - 128 \mathcal{C}(T) \delta_M \delta_e \right] \quad (5.60)$$

$$u_{12}^{MXY} = \frac{N_F}{128} \left[ 16 \mathcal{A}(T) + \mathcal{B}(T)(16\delta_M^2 - 4\delta_e^2) \right] \quad (5.61)$$

The nematic coupling for the  $MXY$  model  $\lambda_\phi^{MXY} = u_{11}^{MXY} - u_{12}^{MXY}$  is given by

$$\lambda_\phi^{MXY} = \frac{N_F}{128} \left[ 32 \mathcal{A}(T) + \mathcal{B}(T)(32\delta_M^2 + 32\delta_e^2) - 128 \mathcal{C}(T) \delta_M \delta_e \right] \quad (5.62)$$

where, as in the quadratic term, the term proportional to  $\delta_M \delta_e$  contribute with opposite sign in comparison with the  $\Gamma_-XY$  model term to the nematic coupling.

### 5.4.3. $\Gamma$ -XY model vs MXY model

**Effect of the ellipticity:**  $\delta_e \neq 0$ ,  $\delta_{m-} = \delta_M = 0$

We first consider the case in which only the electron pocket shapes are modified from the perfect nested condition.

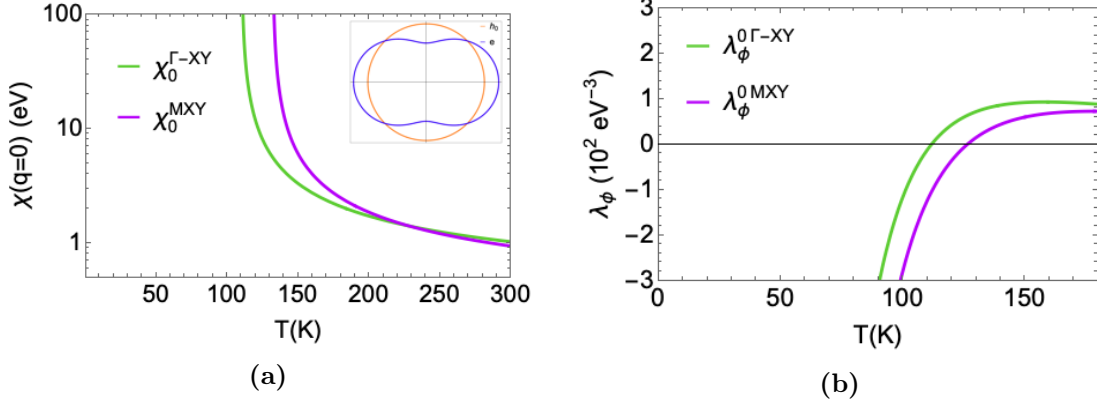


**Figure 5.2:** (a) Static spin susceptibilities  $\chi_0^{\Gamma-XY}(q=0)$ ,  $\chi_0^{MXY}(q=0)$  and (b) nematic couplings  $\lambda_\phi^{0\Gamma-XY}$ ,  $\lambda_\phi^{0MXY}$  for the two three-pocket models  $\Gamma$ -XY and MXY respectively. The Néel temperature is  $T_N^{\Gamma-XY} = 110 \text{ K}$  and  $T_N^{MXY} = 132 \text{ K}$ . The deviation of the hole pockets from the perfect nested Fermi surfaces is set to  $\delta_{m-} = \delta_M = 0$ . The ellipticity of the electron pockets is  $\delta_e = 0.55\epsilon_0$ . In the inset of (a) is shown the perfect nested hole pocket (orange) in comparison with the elliptical electron one (blue).

The ellipticity of the electron pocket does not affect the hierarchy of the magnetic instability and we still find the divergence of  $\chi_0^{MXY}(q=0)$  at higher temperature than the one for  $\chi_0^{\Gamma-XY}(q=0)$ . As we mentioned before this is the result of angular integration over the different orbital weights for the hole band. In fact, while the  $\Gamma$ - hole pocket has an angular orbital modulation given by  $h^- = \sin\theta_{cyz} - \cos\theta_{cxz}$ , the  $M$  pocket does not present orbital modulation since it is made exclusively of  $xy$  orbital component  $h^{xy} = c^{xy}$  (Eq. 5.4).

In Figure 5.2b the nematic coupling for the two three-band model taking into account elliptical electron Fermi surface is shown. The nematic coupling is positive at high temperature and changes sign lowering  $T$ . While  $\lambda_\phi^{0\Gamma-XY}$  changes sign slightly above the  $T_N^{\Gamma-XY}$  [27],  $\lambda_\phi^{0MXY}$  is always positive for any  $T > T_N^{MXY}$  and changes sign slightly below the  $T_N^{MXY}$ , this means that the nematic channel is always repulsive. Notice that, the homogeneous orbital modulation of the  $M$  pocket that appeared to boost magnetism appear detrimental for nematic instability.

**Effect of the deviation from perfect nesting:**  $\delta_{m-} = \delta_M \neq 0$ ,  $\delta_e \neq 0$

We consider  $\delta_{m-} = \delta_M \neq 0$  for the three-band models,  $\Gamma$ -XY and MXY, taking into account the same effect of the ellipticity  $\delta_e = 0.55\epsilon_0$  than in the previous case. We show the results for two different set of parameters  $\delta_{m-} = \delta_M = \{0.07\epsilon_0, 0.1\epsilon_0\}$ .

1.  $\delta_{m-} = \delta_M = 0.07\epsilon_0$ ,  $\delta_e = 0.55\epsilon_0$

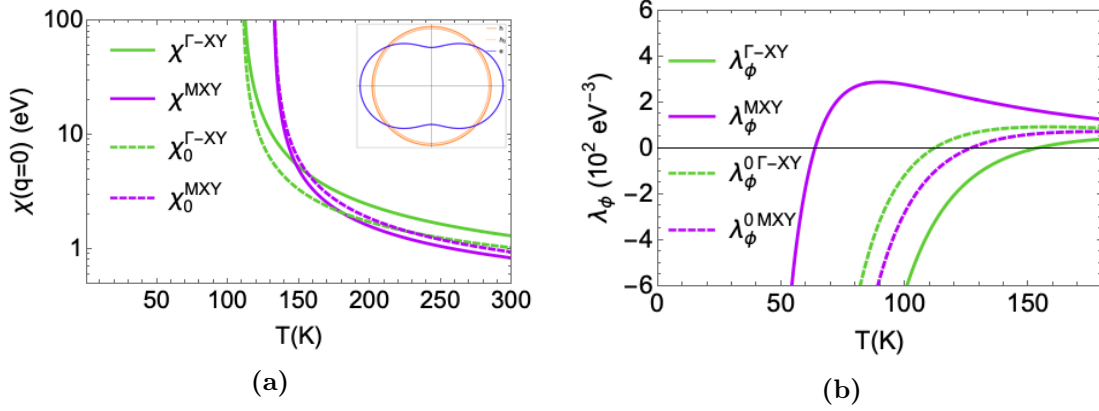


**Figure 5.3:** (a) Static spin susceptibilities ( $q=0$ ) and (b) nematic couplings for the two three-pocket models  $\Gamma_{-XY}$  and  $MXY$ . Solid lines represent these quantities by taking into account the deviation of the hole pockets from the perfect nested Fermi surfaces  $\delta_{m-} = \delta_M = 0.07\epsilon_0$  and the ellipticity of the electron pockets  $\delta_e = 0.55\epsilon_0$ . Dashed lines represent the previous case where  $\delta_{m-} = \delta_M = 0$  and  $\delta_e = 0.55\epsilon_0$  in order to compare them. In the inset of (a) is shown the effect of the deviation  $\delta_{m-}/M \neq 0$  (solid orange line) from the perfect nested hole pocket (dashed orange line) in comparison with the elliptical electron one (blue).

The Fermi surface for this range of parameters are shown in the inset panel of the Figure 5.3a in comparison with the perfect nested hole pocket.

The small variation in size of the hole-pocket does not introduce strong variation in the temperature behaviour of the magnetic susceptibility, Figure 5.3a. The hierarchy of the the Néel temperatures is the same as the parabolic approximation and the corrections proportional to  $\delta_e \delta_{m-}/M$ , opposite in signs for the two models, vanish when approaching the instability temperature as shown in Eqs. 5.53 and 5.59.

On the contrary, the nematic coupling is strongly affected by small variations of the hole-pockets sizes. In Figure 5.3b it is shown the results for the nematic coupling (Eqs. 5.56 and 5.62) represented by solid lines in comparison with the previous result for  $\delta_{m-} = \delta_M = 0$  represented by dashed lines. As one can reads from Eqs. 5.56 and 5.62 the term proportional to  $\delta_{m-}/M \delta_e$  contributes with opposite sign to the nematic coupling of the two models under exam. Nematicity in the  $\Gamma_{-XY}$  model is favoured by the variation of the hole-pocket size i.e. the nematic coupling changes sign for higher temperature compare to the case  $\delta_{m-} = 0$ . For the  $MXY$  model, instead we find the opposite results with the nematic coupling changing sign at even lower temperature.

2.  $\delta_{m-} = \delta_M = 0.1\epsilon_0$ ,  $\delta_e = 0.55\epsilon_0$

The above results are made more striking by the analysis of a slightly larger variation of the hole-pocket size  $\delta_{m-} = \delta_M = 0.1\epsilon_0$  (Fermi surface shown in the inset of Figure 5.4a)

While the the magnetic susceptibility shown in Figure 5.4a are robust with respect variation of the hole-pocket size, the nematic couplings, Figure 5.4b, are extremely sensitive to  $\delta_{m-}/M$  variations. Again the two model are affected by the pocket size variation in a opposite way with the interaction in the nematic channel attractive over a wider range of temperature for the  $\Gamma_{-XY}$  model and the nematic coupling for the  $MX/Y$  model found

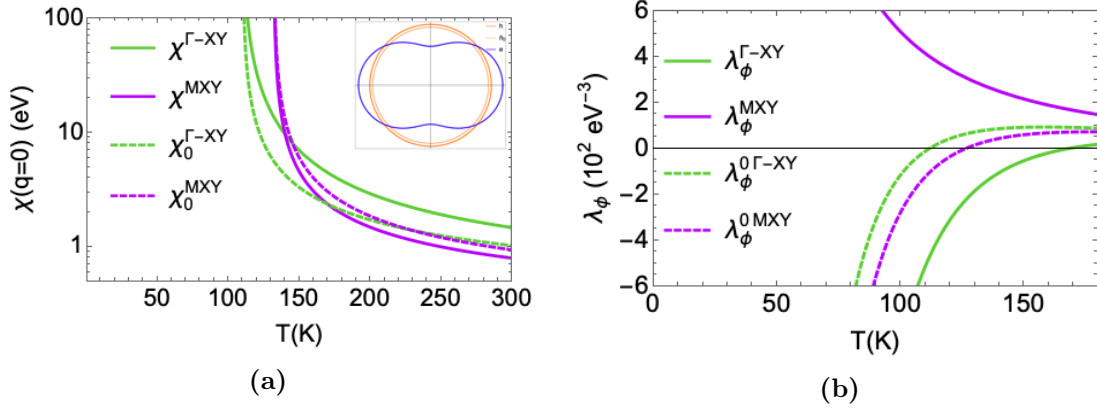


**Figure 5.4:** (a) Static spin susceptibilities ( $q=0$ ) and (b) nematic couplings for the two three-pocket models  $\Gamma_-XY$  and  $MXY$ . Solid lines represent these quantities by taking into account  $\delta_{m_-} = \delta_M = 0.1\epsilon_0$  and  $\delta_e = 0.55\epsilon_0$ . Dashed lines represent the case where  $\delta_{m_-} = \delta_M = 0$  and  $\delta_e = 0.55\epsilon_0$ . In the inset of (a) is shown the effect of the deviation  $\delta_{m_-/M} \neq 0$  (solid orange line) from perfect nested hole pocket (dashed orange line) in comparison with the electron one (blue).

out to be always repulsive.

From the previous analysis we can obtain the following results:

(i) Given two system with similar band and orbital nesting the magnetic transition is higher in system in which the angular integral is maximize by the orbital composition of the pockets, in our case, be the homogeneous composition of the  $M$  pocket.

(ii) Magnetism is robust and is not strongly not affected by deviation from the perfect nesting of the hole pockets.

(iii) The nematic coupling is very sensitive to to small variation of the hole-pocket size. Notice, that when increasing the value of the  $\delta_{m_-/M} \neq 0$  parameter, it affects in an opposite way to the orbital nesting for the  $\Gamma_-X/Y$  or  $M-X/Y$  models. When  $\delta_{m_-} > 0$  we are moving away from the perfect orbital matching between  $\Gamma_-$  and the electron pockets. That means  $\delta_{m_-} > 0$  values are detrimental for magnetism but enhance the appearance of the nematic instability. However, for the  $MXY$  moving away from  $\delta_M = 0$  implies a better orbital nesting with the elliptical electron pockets due to the position of the  $xy$  orbitals (see inset of Figure 5.4b). Therefore, when  $\delta_M > 0$  magnetism is enhanced and nematicity is suppressed.

## 5.5. Conclusion Chapter 5

In this Section we analyze the effective action up to the quartic order for the five-pocket model. The low-energy projection unveil within low-energy model the existence of two OSSF, one, having  $yz/xz$  character, describes the spin-exchange between the two-hole pockets at  $\Gamma$  and the  $X/Y$  electron pockets, the other, having  $xy$  character, describes the spin-exchange between the  $xy$ -hole pocket at  $M$  and the  $X/Y$  electron pockets. The two OSSF are decoupled at Gaussian level, while the quartic term of the action present coupling terms that combine the  $xz/yz$  OSSF and the  $xy$  OSSF along  $x$  and along  $y$ .

Within the perfect nested parabolic band approximation we find that the magnetic  $yz/xz$  susceptibility associated to the spin fluctuation exchange between  $\Gamma_{\pm}$  and  $X/Y$  in the four-pocket subsector and the  $xy$  susceptibility associated to the  $M$ - $X/Y$  pockets are equivalent as *naively* expected given the orbital composition of the hole-pockets involved. As mentioned at the OSSF are coupled at the quartic order and the analysis of the nematic instability cannot be performed studying the four-pocket  $yz/xz$  systems and the  $xy$  three-pocket separately. Diagonalizing the quartic action we find indeed a set of order parameters that contain a linear combination of the spin-fluctuations of the two subsectors. We identify the nematic order parameters as the two eigenvector having  $x/y$  anisotropic character and by analyzing the corresponding coupling we find that the nematic channel is always repulsive within the perfected nested parabolic band approximation.

We include perturbatively the ellipticity of the electron pocket  $\delta_e$ , and consider a deviation from the perfect nesting condition assuming a variation in the size of the hole pocket  $\delta_{m-,M}$ . The variation of the hole-pockets size can be the results for example of doping or pressure. We find that the correction proportional to  $\delta_{m-,M}\delta_e$  appear with opposite sign in the  $\Gamma$ - $X/Y$  and  $M$ - $X/Y$  subsectors. This is a direct consequence of the different orbital character of the hole pockets, this in fact affect the orbital weight factors appearing in the calculations.

The analysis of the nematic instability within the full model accounting for ellipticity and doping is still work in progress.

In order to gain physical insight we study two complementary three-band model  $\Gamma$ - $XY$  and  $MXY$ . The analysis of the three-pocket model  $MXY$  represents an easy way to study the physics associated to the  $xy$  OSSF coming from the presence of the  $M$  pocket in a simplified frame in which there is no coupling with the  $xz/yz$  OSSF of the  $\Gamma$ - $XY$  sector. The analysis is also motivated by the results of renormalization group study of the five-pocket model that show that such a three-band model represents a fix-point of the low-energy theory [123]. We compare the results of the  $MXY$  model with the results of the  $\Gamma$ - $XY$  model which both present the same degree of band and orbital nesting (good matching between the orbitals in the nested hole and electron pockets). We find:

(i) The orbital modulation of the hole pocket is an essential element in order to understand the magnetic instability. Given the same degree of band and orbital nesting the  $MXY$  band model present a stronger magnetic tendency as a consequence of homogeneous orbital composition of the  $M$  pocket. Notice that this result does not change even when ellipticity and variation of the hole-pocket size (that affect the degree of band and orbital nesting) are taken into account. This results is consistent with [120, 139] where the  $M$  pockets is considered as a key piece for the appearance of magnetism in 1111 systems.

(ii) The nematic channel is much more sensitive to deviation from the parabolic approximations and the  $MXY$  and the  $\Gamma$ - $XY$  models are affected by ellipticity and hole-pocket size variation in an opposite way. For the  $MXY$  model, nematicity is undermined and even is not realized, while for the  $\Gamma$ - $XY$  model, nematicity is boosted as we move away from the optimal orbital matching. The competition between this two kind of nematicity could be at the origin of the more elusive nematic phase recently observed in 1111 compounds [175, 176].

We leave for further work the study of magnetic and nematic instabilities for a realistic five-pockets model. With the analysis of the two three-pockets models  $\Gamma_{XY}$  and  $MY$  we study two limits cases which contain the relevant orbital information of the general five-pocket model. Thus, we could expect that when the study of the complete five-pocket model is done, a competition between the  $\Gamma$ -X/Y and  $M$ -X/Y hole sectors in the nematic transition will take place.



# 6

## Conclusions

This Thesis focuses on iron-based superconductors (IBS). The physics of these materials is so rich that it has placed their theoretical understanding as one of the most interesting open puzzles in the field of superconductivity. The phase diagram of IBS exhibits a wide range of different phases including the magnetic, nematic and superconducting. In these materials antiferromagnetism appears in the proximity of superconductivity suggesting that spin-fluctuations might play an important role in mediating pairing. Another key feature is the multiorbital character of their electronic structure at low-energy. There are two main theoretical approaches that have been used to explain the complex phenomenology of IBS in the spin-fluctuation driven scenario: multiband and multiorbital models. Multiband descriptions lack the information of the orbital degree of freedom of the system, while the complexity given by the inclusion of the multiorbital structure makes difficult to address the spin-orbital interplay in multiorbital models. In this Thesis we have studied the following issues: (i) can we describe the magnetic, nematic and superconducting phases of iron-based materials using a single modeling? (ii) can this theoretical frame account for the different phenomenology of the diverse compounds? and (iii) how does emerge and what are the effects of the spin-orbital interplay in the physics of IBS?.

We addressed these questions using the Orbital Selective Spin-Fluctuation (OSSF) model. The OSSF model is a minimal low-energy model for IBS that operates in the band basis but fully incorporates the orbital information of the low-energy excitations. The projection of the orbital information at low-energy unveils a non trivial spin-orbital interplay that results in a strong orbital selectivity of the Spin Fluctuations: Spin Fluctuations peaked around the  $\mathbf{Q}_X/\mathbf{Q}_Y$  vectors involve only the  $yz/xz$  orbitals, respectively. The description of the physical phenomena in terms of OSSF retains the simplicity of the band basis models, but fully account for the orbital degree of freedom.

We first analyzed the magnetic and the superconducting phases in a Random Phase Approximation (RPA) for a generic four-pocket model:  $\Gamma_+$ ,  $\Gamma_-$ ,  $X$  and  $Y$ , within the OSSF scenario. The orbital selectivity, encoded in our model, simplified substantially the analysis, allowing for analytical treatments, while retaining the main features of the spin-excitations computed using five-orbital models. The OSSF model in fact, reproduces qualitatively well the overall momentum dependence and the relative heights and widths of the peaks located at different momenta. This is a remarkable result considering that the OSSF model is a low-energy effective model that only consider the  $yz, xz, xy$  orbitals.

Another important result follows from the observation that the momentum-dependence of the peak of the RPA susceptibility depends on the degree of orbital nesting between the nested pockets: we find a commensurate/incommensurate peaks in the spin susceptibility depending if there is orbital match/mismatch between the nested pockets. Moreover we see that the main contribution to the spin susceptibility comes from the spin-fluctuations exchange between the hole and electron pockets and that the larger contributions comes from the hole pocket whose orbital composition match better the orbital composition of the electrons. Notice that, while a generic correlation between the orbital-make up of the Fermi surface and the momentum-dependent structure of the RPA spin excitation has been already highlighted within multiorbital models, the explicit link and precise relationship between orbital nesting and momentum dependence of the spin-susceptibility is a new results obtained from the RPA analysis within the OSSF model.

We analyzed the pairing interaction of IBS assuming that the same orbital selective spin-fluctuations responsible for magnetism are also responsible for superconductivity. We studied the superconducting pairing vertex and the resulting gap equations for these materials. Thanks to the orbital selectivity, the diagrammatic for the pairing vertex within the OSSF model become treatable via analytical computation and all the Feynman's diagrams can be explicitly drawn in an easy way in contrast to the complex diagrammatic of the full multiorbital description. We showed that both the pairing vertex and the band gaps inherit the orbital modulation in momentum given by the spin susceptibilities. Therefore, we obtained an anisotropic sign changing s-wave gap symmetry, i.e., a  $s_{\pm}$  s-wave band gap, in agreement with the experiments and multiorbital models. A deep analysis of the bands gap structure shows that the angular dependence and the magnitudes of the different gaps depend directly on the degree of orbital nesting between the holes and the electrons pockets, and what is more important, that the degree of orbital nesting (more than the band nesting) controls the strength of the pairing. This result proves that a minimal theoretical model to understand superconductivity in IBS has to account for the spin-orbital interplay. In that respect, the OSSF model is a perfect candidate.

We then analyzed the nematic phase of IBS by studying analytically and numerically the DC conductivity within the orbital-selective spin fluctuation scenario. Within this approach, the anisotropy of spin fluctuations below the spin-nematic transition at  $T_S$  is also responsible for the orbital ordering, induced by nematic self-energy corrections to the quasiparticle dispersion. As a consequence, the anisotropy of the DC conductivity below  $T_S$  is determined not only by the anisotropy of the scattering rates as expected within a spin-nematic scenario, but also by the modification of the Fermi velocity due to the orbital reconstruction (change in size, shape and orbital composition of the pockets). This is a remarkable example of the spin-orbital interplay in these systems. More interestingly, it turns out that these two effects contribute to the DC conductivity anisotropy with opposite signs. By using realistic band-structure parameters we compute the conductivity anisotropy for both 122 and FeSe compounds, discussing the possible origin of the different DC conductivity anisotropy observed experimentally in these two families of iron-based superconductors. We reproduced the experimental sign of the DC conductivity anisotropy for the 122  $\Delta\sigma_{DC}(122) > 0$  and for the FeSe  $\Delta\sigma_{DC}(FeSe) < 0$  when taking into account shrinking and the orbital reconstruction of the Fermi surface of those materials.

The OSSF model has been extensively studied to analyze the phenomenology of three- and four-pocket. In this Thesis we extended the OSSF model to the analysis of a more realistic five-pockets model, in which we account for the  $xy$ -hole pocket  $M$  at

$\mathbf{Q}_M = (\pi, \pi)$ . We have derived the effective action in terms of the spin excitation up to the forth order following the same strategy used to analyze the four-pocket model. Our analysis for the five-pocket model shows that also in this case the projection of the orbital information at low-energy unveils a strong orbital selectivity of the spin fluctuations. We found, in fact, two additional spin excitations connecting the  $M$  hole pocket with the  $X/Y$  electron pockets, having  $xy$ -orbital character. We showed how the spin-fluctuations in this model contribute within two different coupled subsectors:  $\Gamma$ - $X/Y$  and  $M$ - $X/Y$ , that give opposite contributions to the magnetic- and nematic-channel of the total effective action. In order to understand how the inclusion of the fifth pocket affects the magnetic and nematic instabilities, we perform a preliminary study of two limit cases in which we consider the two subsectors fully decoupled: in one case we consider only the  $yz/xz$  spin-fluctuations of the  $\Gamma$ - $X/Y$  sector, while in the other case we only account for the  $xy$  spin-fluctuations connecting the  $M$ - $X/Y$  sector. This analysis is also motivated by the result of renormalization group study of the five-pocket models that found the three-band  $M$ - $XY$  model as a fixed point of the theory at low energy. By comparing these two limit cases, we are able to gain physical insight on the new physics arising from the presence of the extra pocket. The contribution to magnetism and nematicity of the  $xy$  OSSF of the  $M$ - $X/Y$  appears to be in competition with the one coming from the  $yz/xz$  OSSF of the  $\Gamma$ - $X/Y$ . We realized that this effect can be understood in terms of the orbital degree of nesting between the hole and the electron pockets, which is again more effective than the band nesting of the Fermi surfaces in controlling the instabilities realized in the system. The competition between OSSF belonging to different subsectors could explain why different realizations of nematicity are found in different members of the IBS family, with certain compounds as e.g. 1111 showing more elusive nematicity with respect FeSe. In order to fully address this issue, we need to understand how the competition between the OSSF of the  $\Gamma$ - $X/Y$  and  $M$ - $X/Y$  sectors evolves once considered the full five-pockets model in which the two are coupled. This will be the subject of further investigation.

To conclude, in this Thesis we have shown how the diverse phenomenology of various families of IBS can be understood within a common framework: the Orbital Selective Spin Fluctuation scenario. We have seen that, thanks to the orbital selectivity of the magnetic excitations of the system, a spin-orbital interplay arises in the magnetic susceptibility, superconducting gaps and velocity and the scattering rate in the nematic phase of IBS. Given the success of the model, it could be used to make a complete study of most of the IBS phenomenology. In this respect, a complete study of the five-pocket model to analyze, magnetic, nematic and superconducting phases in different IBS compounds is already work in progress. In the next future, one could compute other response functions in order to compare with available experiments, e.g. the dynamical susceptibility in order to compare with Inelastic Neutron Scattering (INS) and Nuclear Magnetic Resonance (NMR) experiments. Another possible direction could be the extension of the analysis of the pairing vertex performed for the tetragonal phase into the nematic one. As the nematicity is an effect beyond RPA, this calculation would require to perform self-consistent calculations of the pairing vertex and superconducting gaps. Finally, orbital selectivity might also appear in other compounds in which the multiorbital character plays an important role. Without doubt, there are numerous avenues where orbital selectivity may play an important role, leaving many possibilities to be explored.

# Conclusiones

Esta Tesis se ha centrado en los superconductores basados en hierro (IBS). La física de estos materiales es tan rica que ha situado su comprensión teórica como uno de los rompecabezas más interesantes en el campo de la superconductividad. El diagrama de fases de los IBS exhiben un gran rango de fases diferentes incluyendo la magnética, nemática y superconductora. En estos materiales el antiferromagnetismo aparece en las proximidades de la superconductividad sugiriendo que las fluctuaciones de espín podrían jugar un papel importante en el mecanismo de la superconductividad. Otro factor clave es el carácter multiorbital de su estructura electrónica a baja energía. Hay dos principales propuestas teóricas que son usadas para explicar la compleja fenomenología de los IBS en el escenario mediado por fluctuaciones de espín: los modelos multibanda o multiorbitales. A los modelos multibanda les falta la información sobre el grado de libertad orbital del sistema, mientras que la complejidad al considerar estructuras multiorbitales hace difícil abordar la interacción entre el espín y el orbital en los modelos multiorbitales. En esta Tesis hemos estudiado los siguientes problemas: (i) ¿podemos describir la fase magnética, nemática y superconductora de los materiales basados en hierro usando un solo modelo? (ii) ¿puede este marco teórico explicar la diferente fenomenología entre los diversos compuestos? (iii) ¿cómo surge y cuáles son los efectos de la interacción entre el espín y el orbital en la física de los IBS?

Abordamos esas preguntas usando el modelo de Fluctuaciones de Espín con Selección Orbital (OSSF). El modelo OSSF es un modelo de baja energía que opera en la base de las bandas pero incorpora completamente la información orbital de las excitaciones de baja energía. La proyección del contenido orbital a baja energía descubre una relación no trivial entre el espín y el orbital que resulta en una fuerte selectividad orbital dada por las fluctuaciones de espín: las fluctuaciones de espín se vuelven máximas alrededor de los vectores  $\mathbf{Q}_X/\mathbf{Q}_Y$  involucrando a los orbitales  $yz/xz$  respectivamente. La descripción de los fenómenos físicos en términos de OSSF conserva la simplicidad de los modelos basados en la banda, pero teniendo además en cuenta el grado de libertad orbital.

Primero hemos analizado la fase magnética y superconductora en una Aproximación de Fase Aleatoria (RPA) un modelo genérico de cuatro áreas:  $\Gamma_+$ ,  $\Gamma_-$ ,  $X$  y  $Y$  en un escenario OSSF. La selectividad orbital, codificada en nuestro modelo, simplifica substancialmente el análisis, permitiendo tratamientos analíticos mientras se conservan las características principales de las excitaciones de espín calculadas usando un modelo de cinco orbitales. El modelo OSSF de hecho, reproduce cualitativamente bien la dependencia general del momento y las relativas alturas y anchuras de picos localizados en momentos diferentes. Esto es un resultado remarcable considerando que el modelo OSSF es un modelo efectivo a baja energía que solo considera los orbitales  $yz, xz, xy$ .

Otro resultado importante viene de la observación de que la dependencia en momento del pico de la susceptibilidad RPA depende del grado de coincidencia orbital entre las diferentes áreas: encontramos picos conmensurados/inconmensurados en la susceptibilidad de espín dependiendo de si hay buen grado de coincidencia orbital entre las áreas relacionadas. Además, vimos que la principal contribución a la susceptibilidad de espín viene del intercambio de fluctuaciones de espín entre las áreas de huecos y de electrones

siendo la mayor contribución la de el área de huecos con mejor coincidencia orbital con las áreas de electrones. Es importante darse cuenta de que mientras la correlación genérica entre la composición orbital de las superficies de Fermi y la estructura dependiente del momento en las excitaciones de espín en RPA ya ha sido destacado en modelos multiorbitales, el vínculo explícito y la relación precisa entre la coincidencia orbital y la dependencia en momento de la susceptibilidad de espín es un resultado nuevo obtenido desde el análisis RPA dentro del modelo OSSF.

Hemos analizado también el vértice de interacción de los IBS asumiendo que las mismas fluctuaciones de espín con selección orbital responsables del magnetismo, también son responsables de la superconductividad. Estudiamos el vértice superconductor y las ecuaciones de gap resultantes para estos materiales. Gracias a la selección orbital, los diagramas de Feynman's asociados al vértice de interacción se pueden tratar de forma analítica y se pueden representar de forma fácil en comparación con la compleja diagramática de la descripción en el modelo multiorbital. Demostramos que tanto el vértice superconductor como los gaps de las bandas heredan la modulación orbital en momento dada por las susceptibilidades de espín. Por lo tanto, obtuvimos un gap anisotrópico con una simetría de onda-s con cambio de signo, es decir, un gap de banda  $s_{\pm}$ , de acuerdo con los experimentos y con los modelos multiorbitales. Haciendo un análisis más profundo de la estructura de los gaps de banda, demostramos que la dependencia angular y las magnitudes de los diferentes gaps dependen directamente del grado de coincidencia orbital entre las áreas de huecos y las de electrones, y lo que es más importante, que el grado de coincidencia orbital (más que el de coincidencia de banda) es el que controla la fuerza del vértice superconductor. Este resultado es una prueba de que el modelo mínimo teórico usado para entender la superconductividad en IBS tiene que tener en cuenta la relación entre el espín y el orbital. En lo que respecta, el modelo OSSF es un candidato perfecto.

Después, analizamos la fase nemática de los IBS estudiando analíticamente y numéricamente la conductividad dc dentro del OSSF escenario. Bajo este enfoque, la anisotropía de las fluctuaciones de espín por debajo de la transición de espín nemática a  $T_S$  es también responsable del ordenamiento orbital, inducido por las correcciones de autoenergía nemáticas inducidas a la dispersión de la cuasipartícula. Como consecuencia, la anisotropía de la conductividad dc por debajo de  $T_S$  está determinada no sólo por la anisotropía en la tasa de dispersión de los electrones, sino que también está determinada por la modificación en la velocidad de Fermi debida a la reconstrucción orbital (cambio en tamaño, forma y composición orbital de las áreas). Esto es un ejemplo remarcable de la interacción entre el espín y el orbital en estos sistemas. Y lo que es más interesante, esto lleva a que los dos efectos contribuyan a la anisotropía en la conductividad dc con signos opuestos. Usando parámetros de banda realistas, calculamos la anisotropía en la conductividad para el FeSe y los compuestos 122, discutiendo el posible origen de la anisotropía en la conductividad dc observada experimentalmente en estas dos familias de superconductores basados en hierro. Logramos reproducir el signo experimental de la anisotropía en la conductividad dc para los 122  $\Delta\sigma_{DC}(122) > 0$  y para el FeSe  $\Delta\sigma_{DC}(FeSe) < 0$  cuando tenemos en cuenta la disminución y la reconstrucción orbital de la superficie de Fermi de esos materiales.

El modelo OSSF ha sido extensamente estudiado para analizar la fenomenología de los sistemas de tres y cuatro áreas. En esta Tesis extendemos el modelo OSSF para el análisis de sistemas más realistas de cinco áreas, en los que tenemos en cuenta el área de huecos  $M$  con  $xy$  localizada en  $\mathbf{Q}_M = (\pi, \pi)$ . Derivamos la acción efectiva en términos de

las excitaciones de espín hasta cuarto orden siguiendo la misma estrategia que se hizo para analizar el modelo de cuatro áreas. Nuestro análisis del modelo de cinco áreas, muestra que también en ese caso la proyección del contenido orbital a baja energía descubre una fuerte selección orbital de las fluctuaciones de espín. De hecho, encontramos dos fluctuaciones de espín adicionales que conectan el área de huecos  $M$  con el área de electrones  $X/Y$  teniendo contenido orbital  $xy$ . Demostramos como las fluctuaciones de espín en este modelo contribuyen a dos subsectores diferentes acoplados: el sector  $\Gamma$ - $X/Y$  y el sector  $M$ - $X/Y$ , que dan lugar a contribuciones opuestas en el canal magnético y nemático en la acción efectiva total. Para entender como afecta la inclusión de la quinta área a las inestabilidades magnéticas y nemáticas del sistema, llevamos a cabo un estudio preliminar de dos casos límites en los que consideramos los dos subsectores completamente desacoplados: en un caso consideramos solo las fluctuaciones de espín  $yz/xz$  del sector  $\Gamma$ - $X/Y$ , mientras que en el otro caso sólo tenemos en cuenta las fluctuaciones de espín  $xy$  que conectan el sector  $M$ - $X/Y$ . Este análisis está motivado también por el resultado del estudio del caso de cinco áreas en grupo de renormalización donde se encuentra que el modelo de tres bandas  $M - XY$  tiene un punto fijo de la teoría a baja energía. Comparando estos dos casos límites, somos capaces de adquirir conocimientos físicos sobre la nueva física que surge de la presencia de esta área extra. La contribución al magnetismo y a la nematicidad de las  $xy$  OSSF en el sector  $M$ - $X/Y$  parece competir con la que proveniente de las  $yz/xz$  OSSF en el sector  $\Gamma$ - $X/Y$ . Nos dimos cuenta que ese efecto podía ser entendido en términos del grado de coincidencia orbital entre las áreas de huecos y las de electrones, el cual una vez más era más importante que el grado de coincidencia de banda de las superficies de Fermi a la hora de controlar las inestabilidades que se llevaban a cabo en el sistema. La competición entre las OSSF que pertenecen a los diferentes subsectores podría explicar por qué se encuentran diferentes realizaciones de la nematicidad en distintos miembros de las familias de IBS, en ciertos compuestos como por ejemplo los 1111, mostrando una nematicidad más vaga respecto al FeSe. Para poder abordar de manera completa este hecho, necesitamos entender como evoluciona la competición entre las OSSF de los sectores  $\Gamma$ - $X/Y$  y  $M$ - $X/Y$  una vez consideremos el caso completo de cinco áreas en el que los dos sectores están acoplados. Esto será objeto de una mayor investigación.

Para concluir, en esta Tesis hemos demostrado que la diversa fenomenología de las diferentes familias de los IBS puede ser entendida con un marco común: el escenario de Fluctuaciones de Espín con Selección Orbital. Hemos visto que, gracias a la selectividad orbital de las excitaciones magnéticas del sistema, surge una relación entre el espín y el orbital en la susceptibilidad magnética, los gaps superconductores y en la velocidad y en la tasa de dispersión de los electrones en la fase nemática de los IBS. Dado el éxito del modelo, podría ser usado para hacer un estudio completo de la mayoría de la fenomenología de los IBS. En lo que respecta, un estudio completo del modelo de cinco áreas para analizar la fase magnética, nemática y superconductora en diferentes compuestos de los IBS es ya un trabajo en proceso. En el futuro cercano, uno podría calcular también otras funciones respuesta para comparar con experimentos disponibles como, por ejemplo, la susceptibilidad dinámica para comparar con experimentos de Dispersión Inelástica de Neutrones (INS) y con experimentos de Resonancia Magnética Nuclear (NMR). Otra dirección posible podría ser la extensión del análisis del vértice superconductor llevado a cabo en la fase tetragonal, a la fase nemática. como la nematicidad es un efecto más allá de RPA, este cálculo requeriría llevar a cabo cálculos autoconsistentes del vértice y de los gaps supercon-

ductores. Finalmente, la selectividad orbital debe aparecer también en otros compuestos en los que el carácter multiorbital juega un papel importante. Sin duda alguna, existen numerosas vías en las que la selectividad orbital puede desempeñar un papel importante, dejándonos muchas posibilidades que explorar.

# Appendices





## Spin-driven nematic transition as spontaneous $Z_2$ -symmetry breaking

We look into the concept of the nematic phase using symmetries arguments. The present discussion is mainly based on Ref.s [79] and [177].

When we study a spontaneous symmetry breaking we start from a disordered phase (such a paramagnetic phase) and we end in a ordered magnetic phase (such a magnetic SDW phase). In a paramagnetic phase, all the spins are indistinguishable, so the system has  $O(3)$  spin rotational symmetry. To end in an ordered magnetic phase, the system has to break at least, the  $O(3)$  spin rotational symmetry. To the  $O(3)$  symmetry breaking corresponds also a translational symmetry breaking, due to the increase in the size of the crystalline unit cell in the magnetically ordered phase. This is, indeed, the case of many antiferromagnets in which the symmetry that is broken at the magnetic transition temperature is the  $O(3)$  spin-rotational symmetry. However, in IBS the situation is more involved. In fact, the magnetically ordered state for most IBS is a SDW phase, that is actually doubly degenerate, as it is characterized by magnetic stripes of parallel spins along either the  $y$  axis with an ordering vector  $\mathbf{Q}_X = (\pi, 0)$  or the  $x$  axis with an ordering vector  $\mathbf{Q}_Y = (0, \pi)$ . This two degenerate ground states correspond to a  $Z_2$  (Ising-like) symmetry (see Figure A.1). In this case, thus, the system has to break not only the  $O(3)$  spin-rotational symmetry, but it also has to choose between one of the two degenerate ground states and thus has to break the  $Z_2$  symmetry. In real space, the  $Z_2$  symmetry breaking corresponds to a broken rotational symmetry of the lattice.

### Symmetry-based discussion

A generic  $d$ -dimensional rotation symmetry is represented by the rotational group  $O(d)$ . Although the rotational symmetry in crystalline solids is always broken, the point group of the symmetry, that is a subgroup of  $O(d)$ , is preserved. For a 2-dimensional systems, the point group that represents the  $n$ -fold rotational symmetry groups are the  $C_n$  cyclic groups. The  $C_n$  groups represent the discrete rotational symmetry of the  $n^{th}$  order with respect to a particular point, that means a rotation by an angle of  $360^\circ/n$  leaves the system invariant.

In crystalline solid, the point group symmetry for a 2-dimensional lattice with rotational symmetry is the  $C_4$  group. That means the system is invariant under all rotations given by an angle of  $360^\circ/4 = 90^\circ$  which represents a tetragonal structure of the lattice.

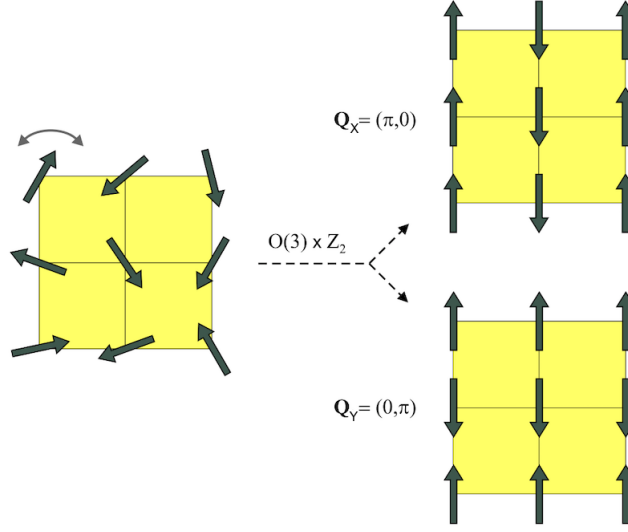


**Figure A.1:** The transition from the disordered phase to the SDW phase breaks an  $O(3) \times Z_2$  symmetry. The  $O(3)$  symmetry refers to rotations in spin space while the  $Z_2$  symmetry refers to the two degenerate ground states of magnetic stripes with parallel spins along the y axis with ordering vector  $\mathbf{Q}_X = (\pi, 0)$  or along the x axis with ordering vector  $\mathbf{Q}_Y = (0, \pi)$ . Adapted from [79].

The  $C_4$  group is, therefore, the cyclic group of order  $n = 4$ , that contains four elements, which can be represented as  $C_4 = \{1, e^{i\pi/2}, e^{i2\pi}, e^{i3\pi/2}\}$  referred to the lattice rotations by a  $\pi/2$  angle.

Let us now introduce the quotient group of the  $C_4$  as  $C_4/C_2$  with  $C_2$  the normal group of  $C_4$ . It can be shown that the quotient group  $C_4/C_2$  is isomorphic to  $Z_2$ , that is  $C_4/C_2 \cong Z_2$ . Here, the  $C_2$  and  $Z_2$  groups are the same cyclic group of order 2 (Ising-like), but we call it different because the  $Z_2$  group is referred to the two degenerated ground states and the  $C_2$  is referred to the lattice rotations by a  $\pi$  angle with  $C_2 = \{1, e^{i\pi}\}$ . What does the isomorphism  $C_4/C_2 \cong Z_2$  mean? On one hand, it means that a  $Z_2$  symmetry breaking corresponds to a  $C_4$  symmetry breaking, and thus a rotational symmetry breaking of the lattice. On the other, the isomorphism  $C_4/C_2 \cong Z_2$  also means that the remained symmetry of the lattice after such symmetry breaking is a  $C_2$  rotational symmetry.

This is the definition of the nematic phase: a broken rotation symmetry of the lattice  $C_4 \rightarrow C_2$ , but unbroken translational symmetry, i.e. unbroken spin rotational symmetry  $O(3)$ .

## Physical interpretation

In the disordered phase of a 2-dimensional crystalline solid the system preserves spin-rotational symmetry  $O(3)$  and rotational symmetry  $C_4$  of the lattice. That is, the total symmetry of the system is  $O(3) \times C_4$ . On the other hand, to end in a SWD phase, the system has to break the  $O(3)$  spin rotational symmetry, in order to acquire long-range magnetic order, and the  $Z_2$  rotational symmetry, in order to choose one of the two degenerated SWD ground states. So, in the SDW phase the system breaks  $O(3) \times Z_2$  symmetry (see Figure A.1). Since this is a discrete symmetry, the  $Z_2$ -symmetry breaking is expected to be less affected by magnetic fluctuations than the continuous  $O(3)$  symmetry breaking, and that suggest the possibility of the former happening before the latter. This

is just the idea of behind the Ising-nematic state: an intermediate phase preceding the SDW state, where the  $Z_2$  symmetry is broken but the  $O(3)$  symmetry is not.

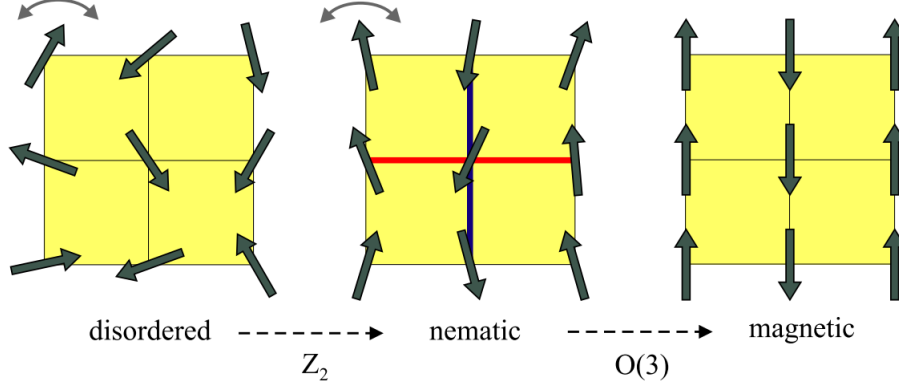


**Figure A.2:** The  $O(3) \times Z_2$  symmetry can be broken in two steps. First, only the  $Z_2$  symmetry is broken. The system is still paramagnetic since  $\langle \mathbf{S}_i \rangle = 0$  (gray double arrow on top of the spins), but the spin correlations break the tetragonal symmetry,  $\langle \mathbf{S}_i \cdot \mathbf{S}_{i+x} \rangle = -\langle \mathbf{S}_i \cdot \mathbf{S}_{i+y} \rangle$  (red and blue bonds, respectively). In the second step, the  $O(3)$  symmetry is broken and the system acquires long-range magnetic order with ordering vector  $\mathbf{Q}_X = (\pi, 0)$ . Adapted from [79].

Figure A.2 show a schematic of the transition from a disordered paramagnetic phase to a SDW through a nematic phase. Left-hand side of Figure A.2 represents the disordered paramagnetic phase. The symmetry of the system in this phase is  $O(3) \times C_4$ : we have translational symmetry  $O(3)$ , i.e. we do not have a long range magnetic order  $\langle \mathbf{S}_i \rangle = 0$  and at the same time we have a rotational symmetry  $C_4$ , so the spin correlations preserve the tetragonal symmetry  $\langle \mathbf{S}_i \cdot \mathbf{S}_{i+x} \rangle = \langle \mathbf{S}_i \cdot \mathbf{S}_{i+y} \rangle$ . In the nematic phase, middle of Figure A.2, magnetic fluctuations spontaneously lead the system to choose one of the two degenerated possible states and thus to break the  $Z_2$  symmetry. Therefore a  $Z_2$  breaking occurs already in the non-magnetic phase by making the spin correlations non equivalents along  $x/y$ , i.e.  $\langle \mathbf{S}_i \cdot \mathbf{S}_{i+x} \rangle \neq \langle \mathbf{S}_i \cdot \mathbf{S}_{i+y} \rangle$ . As the  $Z_2$  symmetry breaking corresponds to a broken  $C_4$  tetragonal symmetry, the symmetry that survives is just the  $C_2$  orthorhombic symmetry. It means that the system in the nematic phase is invariant under lattice rotations given by a  $\pi$  angle. On the other hand, the translational  $O(3)$  symmetry is still preserved, and thus the system does not develop a long range magnetic order  $\langle \mathbf{S}_i \rangle = 0$ . The total symmetry of the system in the nematic phase is  $O(3) \times C_2$ . It means in the nematic phase the rotational symmetry of the crystal is broken, going from tetragonal to orthorhombic  $C_4 \rightarrow C_2$ , but the translational symmetry  $O(3)$  is not. Last, on the right-hand side of Figure A.2 we have the ordered SDW phase. The translational  $O(3)$  symmetry of the system is not preserved anymore and the system develops a long-range magnetic order  $\langle \mathbf{S}_i \rangle \neq 0$  with an ordering vector  $\mathbf{Q}_X = (\pi, 0)$  (or  $\mathbf{Q}_Y = (\pi, 0)$ ).

# B

## Kinetic model for IBS

### B.1. Symmetry adapted low-energy model for the four-pocket model

The kinetic Hamiltonian is derived adapting the low-energy model considered in [118], where the electronic states around the high-symmetry points  $l = \Gamma, X, Y$  are described using a spinor representation in the pseudo-orbital space

$$H_0^l = \sum_{\mathbf{k}, \sigma} \left( \phi_{\mathbf{k}\sigma}^{\dagger l} \hat{H}_{0\mathbf{k}}^l \psi_{\mathbf{k}\sigma}^l \right). \quad (\text{B.1})$$

Here  $\psi_{\mathbf{k}\sigma}^{\Gamma} = (c_{\mathbf{k}\sigma}^{yz}, c_{\mathbf{k}\sigma}^{xz})$ ,  $\psi_{\mathbf{k}\sigma}^{X/Y} = (c_{\mathbf{k}\sigma}^{yz/xz}, c_{\mathbf{k}\sigma}^{xy})$  and  $\hat{H}_{0\mathbf{k}}^l = h_{0\mathbf{k}}^l \hat{\tau}_0 + \vec{h}_{\mathbf{k}}^l \cdot \vec{\tau}$  with  $\hat{\tau}$  Pauli matrices representing the orbital isospin. The  $(h_0^l, \vec{h}^l)$  components of the Hamiltonian at  $\Gamma$  are

$$\begin{aligned} h_{0\mathbf{k}}^{\Gamma} &= \epsilon_0^{\Gamma} - a^{\Gamma} \mathbf{k}^2, \\ h_{1\mathbf{k}}^{\Gamma} &= -2b^{\Gamma} k_x k_y, \\ h_{3\mathbf{k}}^{\Gamma} &= b^{\Gamma} (k_x^2 - k_y^2), \end{aligned} \quad (\text{B.2})$$

at  $X$  read

$$\begin{aligned} h_{0\mathbf{k}}^X &= (h_{\mathbf{k}}^{yz} + h_{\mathbf{k}}^{xy})/2 \\ h_{2\mathbf{k}}^X &= vk_y \\ h_{3\mathbf{k}}^X &= (h_{\mathbf{k}}^{yz} - h_{\mathbf{k}}^{xy})/2 - b(k_x^2 - k_y^2) \end{aligned} \quad (\text{B.3})$$

where  $h_{\mathbf{k}}^{yz} = -\epsilon^{yz} + a^{yz} \mathbf{k}^2$  and  $h_{\mathbf{k}}^{xy} = -\epsilon^{xy} + a^{xy} \mathbf{k}^2$ . Analogous expressions hold for  $(h_0^Y, \vec{h}^Y)$  by exchanging  $k_x$  by  $k_y$  and  $yz/xz$ .

The band dispersion and their orbital composition are obtained by diagonalizing the Hamiltonian, Eq. 2.22. For the hole sector  $\Gamma$  we have

$$H_0^{\Gamma} = \sum_{\mathbf{k}, \sigma} \psi_{\mathbf{k}\sigma}^{\dagger \Gamma} \hat{H}_{0\mathbf{k}}^{\Gamma} \psi_{\mathbf{k}\sigma}^{\Gamma} = \sum_{\mathbf{k}, \sigma} \phi_{\mathbf{k}\sigma}^{\dagger \Gamma} \hat{\Lambda}_{\mathbf{k}}^{\Gamma} \phi_{\mathbf{k}\sigma}^{\Gamma} \quad (\text{B.4})$$

where  $\phi_{\mathbf{k}\sigma}^{\Gamma} = (h_{\mathbf{k}\sigma}^{+}, h_{\mathbf{k}\sigma}^{-})$  are the fermionic operator for the  $\Gamma_{\pm}$  bands obtained by the  $\hat{\mathcal{U}}_{\mathbf{k}}^{\Gamma}$  rotation of the orbital spinor  $\psi_{\mathbf{k}\sigma}^{\Gamma}$

$$\phi^{\Gamma} = \hat{\mathcal{U}}^{\Gamma} \psi^{\Gamma} = \begin{pmatrix} u^{\Gamma} & -v^{\Gamma} \\ v^{*\Gamma} & u^{*\Gamma} \end{pmatrix} \begin{pmatrix} c^{yz} \\ c^{xz} \end{pmatrix} = \begin{pmatrix} h^{+} \\ h^{-} \end{pmatrix} \quad (\text{B.5})$$

where we omit the momentum and spin dependence for convenience. The components of the rotation matrix  $\hat{\mathcal{U}}^\Gamma$  are given by

$$\begin{aligned} u^\Gamma &= \frac{1}{\sqrt{2}} \sqrt{\left( + \frac{h_3^\Gamma}{h^\Gamma} \right)}, \\ v^\Gamma &= \frac{1}{\sqrt{2}} \text{sgn}(h_1^\Gamma) \sqrt{\left( - \frac{h_3^\Gamma}{h^\Gamma} \right)}. \end{aligned} \quad (\text{B.6})$$

and define the coherence factors representing the orbital content of the  $\Gamma$ -pockets.  $\hat{\Lambda}^\Gamma = \text{diag}(E^{\Gamma+}, E^{\Gamma-})$  is diagonal in the band space and contains the expression for the dispersions

$$E^{\Gamma\pm} = h_0^\Gamma \pm h^\Gamma = h_0^\Gamma \pm \sqrt{(h_1^\Gamma)^2 + (h_3^\Gamma)^2 + \lambda^2/4} \quad (\text{B.7})$$

Here we accounted explicitly the spin-orbit coupling  $\lambda$  by replacing  $|h^\Gamma| = \sqrt{|\vec{h}^\Gamma|^2 + \lambda^2/4}$ . This lifts the  $xz/yz$  degeneracy of the inner/outer pockets at  $\Gamma$ .

Analogously we derive the band dispersions and the orbital content at  $X$  and  $Y$ . We find

$$\phi^X = \hat{\mathcal{U}}^X \psi^X = \begin{pmatrix} u^X & -v^X \\ v^{*X} & u^{*X} \end{pmatrix} \begin{pmatrix} c^{yz} \\ c^{xy} \end{pmatrix} \begin{pmatrix} e^{X+} \\ e^{X-} \end{pmatrix} \quad (\text{B.8})$$

where we again drop the momentum and spin dependence for convenience. The rotation matrix  $\hat{\mathcal{U}}^X$  is defined around  $X$  as

$$\begin{aligned} u^X &= \frac{1}{\sqrt{2}} \sqrt{\left( + \frac{h_3^X}{h^X} \right)}, \\ v^{*X} &= \frac{1}{\sqrt{2}} i \text{sgn}(h_2^X) \sqrt{\left( - \frac{h_3^X}{h^X} \right)}. \end{aligned} \quad (\text{B.9})$$

and the band dispersions

$$E^{X\pm} = h_0^X \pm h^X = h_0^X \pm \sqrt{(h_2^X)^2 + (h_3^X)^2} \quad (\text{B.10})$$

where  $h_2^X$ ,  $h_3^X$  and  $h^X$  are given by Eq. B.3. Eqs. B.8 - B.10 are also valid for the  $Y$  electron pocket by substituting the  $X$  pocket index by the  $Y$  and the  $yz$  orbital label by the  $xz$ . Notice that since only the  $E^{X/Y+}$  band in Eq. B.10 crosses the Fermi level at  $X/Y$  points, we drop the  $+$  subscript from the electron pockets band dispersion  $E^{X/Y}$  and from the fermionic operator  $e^{X/Y}$ .

The the non-interacting Green's functions are given by

$$\hat{G}^{l-1} = \omega \hat{\mathbb{1}} - \hat{H}_0^l \quad (\text{B.11})$$

with  $\hat{H}_0^l$  the non-interacting Hamiltonian and  $\omega$  the fermionic frequency. By rotating it to the pocket basis we get the non-interacting pocket Green's function is given by  $\hat{G}^{l-1} = \hat{\mathcal{U}}^{l-1} (\omega \hat{\mathbb{1}} - \hat{\Lambda}^l) \hat{\mathcal{U}}^l$ , so that

$$\hat{G}^l = g^{l+} \begin{pmatrix} (u^l)^2 & u^l v^l \\ v^l u^l & (v^l)^2 \end{pmatrix} + g^{l-} \begin{pmatrix} (v^l)^2 & -v^l u^l \\ -u^l v^l & (u^l)^2 \end{pmatrix} \quad (\text{B.12})$$

where we introduced the pocket's Green's function as  $g_{(\mathbf{k}, i\omega_n)}^{l\pm} = (i\omega_n - E_{\mathbf{k}}^{l\pm})^{-1}$ .

## B.2. Perfect circular nested and elliptical Fermi surfaces

### *Perfect circular nested Fermi surfaces*

A useful approximation that allows for analytical treatment is to approximate any low-energy dispersion as a parabola and to assume a condition of perfect nesting between the hole and electron pockets.

Within the parabolic approximation we can rewrite the  $(h_0^l, \vec{h}^l)$  components given in Eqs. B.2 - B.3

$$\begin{aligned} h_0^\Gamma &= \epsilon^\Gamma - ak^2, \\ h_1^\Gamma &= -bk^2 \sin(2\theta), \\ h_3^\Gamma &= bk^2 \cos(2\theta) \end{aligned} \quad (\text{B.13})$$

and

$$\begin{aligned} h_0^{X/Y} &= -\epsilon^{X/Y} + ak^2, \\ h_2^{X/Y} &= bk^2 \sin(2\theta), \\ h_3^{X/Y} &= \mp bk^2 \cos(2\theta) \end{aligned} \quad (\text{B.14})$$

with  $\theta = \arctan k_y/k_x$  the polar angle and  $k = \sqrt{k_x^2 + k_y^2}$  the modulus of the momentum vector  $\mathbf{k} = (k_x, k_y)$ . The non-interacting energy for a pocket  $l$  is given by  $E^{l\pm} = h_0^l \pm h^l$  with  $h^l = \sqrt{(h_1^l)^2 + (h_2^l)^2 + (h_3^l)^2}$ , while the coherence factors reduce to

$$\begin{aligned} |u^\Gamma|^2 &= |u^Y|^2 = |v^X|^2 = \cos^2 \theta, \\ |v^\Gamma|^2 &= |v^Y|^2 = |u^X|^2 = \sin^2 \theta \end{aligned} \quad (\text{B.15})$$

Notice that the orbital content of the four-pocket model is still well described within the perfect nested parabolic bands approximation.

The non-interacting pocket Green's functions are given by

$$g_+ = g_- = g_h = (i\omega_n + \epsilon)^{-1} \quad (\text{B.16})$$

$$g_X = g_Y = g_e = (i\omega_n - \epsilon)^{-1} \quad (\text{B.17})$$

where  $\epsilon$  is the parabolic dispersion  $\epsilon = -\epsilon_0 + \mathbf{k}^2/2m$ , with  $\epsilon_0$  is the off-set energy with respect to the chemical potential, put conventionally to zero, and  $m$  the parabolic band mass. Notice that for a perfect nested Fermi surface, the Green's function of the system is only differentiate between the hole and electron sector, but inside each sector all the hole/electron pockets have the same energy.

### Elliptical approximation

We account for the deviations from the perfectly nested parabolic band approximation perturbatively. One can describe the ellipticity of the electronic band dispersion as

$$E^{X/Y} \simeq \epsilon \mp \delta_e \cos 2\theta_{\mathbf{k}}, \quad \delta_e = \epsilon_0 m \left( \frac{m_x - m_y}{2m_x m_y} \right), \quad (\text{B.18})$$

where  $\delta_e$  accounts for the ellipticity of the electron pocket via the  $x/y$  anisotropy of the masses with respect the parabolic band mass  $m$ . The expressions in Eqs. B.18 correctly reproduces the opposite ellipticity of the  $X/Y$  pockets. For the sake of completeness we also consider the deviation from perfect nesting due to, such as for example, a mass, off set energy, spin-orbit coupling mismatch of the hole pockets via

$$E^{\Gamma\pm} \simeq -\epsilon + \delta_{m\pm}, \quad \delta_{m\pm} = \epsilon_0 \left( \frac{m_{\pm} - m}{m} \right). \quad (\text{B.19})$$

These perturbations can be included in the estimate of the quadratic and quartic terms of the action by expanding the Green functions for small  $\delta_e, \delta_{m\pm}$

$$\begin{aligned} g_{\pm} &= g_h(1 + \delta_{m\pm} g_h) \\ g_{X/Y} &= g_e(1 \mp \delta_e \cos(2\theta_{\mathbf{k}}) g_e). \end{aligned} \quad (\text{B.20})$$

In principle the perturbations  $\delta_e$  and  $\delta_{m\pm}$  affect also the angular orbital factors, which should deviate from the  $\cos \theta / \sin \theta$  expressions of Eq. B.15. However in first approximation we will neglect these modifications and we will retain only the effects of  $\delta_e$  and  $\delta_{m\pm}$  on the Green's functions.

## B.3. Model parameters for the kinetic Hamiltonian

The parameters for the kinetic part of the Hamiltonian for a generic four-pocket model are given in Table B.1

$\Gamma$		$X/Y$			
$\epsilon_{\Gamma}$	46	$\epsilon_{xy}$	72	$\epsilon_{yz/xz}$	55
$a_{\Gamma}$	263	$a_{xy}$	93	$a_{yz/xz}$	101
$b_{\Gamma}$	182	$b$	154		
		$v$	144		

**Table B.1:** Model parameters for a generic four-pocket system. All the parameters are in meV.

The spin-orbit interaction for the 122 is set to  $\lambda = 5$  meV and for the FeSe  $\lambda = 20$  meV.



## Appendix Chapter 3

### C.1. Magnetic excitations in the OSSF model: RPA analysis

#### C.1.1. Computation of the spin susceptibility

In this appendix we compute the spin susceptibility induced by the orbital selective spin fluctuations within the OSSF model from the expression of the spin susceptibility in terms of the intraorbital Matsubara spin-spin correlation function given in Eq. 3.9 from the main text

$$\chi^{\eta\eta'}(\mathbf{q}, i\Omega_m) = \int_0^\beta d\tau e^{i\Omega_m \tau} \left\langle T_\tau \vec{S}^\eta(\mathbf{q}, \tau) \vec{S}^{\eta'}(-\mathbf{q}, 0) \right\rangle \quad (\text{C.1})$$

where  $\vec{S}^\eta(\mathbf{q}, \tau) = \sum_{\mathbf{k}ss'} c_{\mathbf{k}s}^{\eta\dagger} \vec{\sigma}_{ss'} c_{\mathbf{k}+\mathbf{q}s'}$  is the intraorbital spin operator. As we discussed in Section 3.3, the low-energy projection simplified considerably Eq. C.1 and thus substituting the intraorbital spin operator  $\vec{S}^\eta(\mathbf{q}, \tau)$  and applying Wick's theorem the spin susceptibility reads as

$$\chi^{ll'}(\mathbf{q}, i\Omega_m) = -\frac{1}{\beta} \sum_{\mathbf{k}, n} \text{Tr} \left[ \hat{G}^l(\mathbf{k}, i\omega_n) \hat{G}^{l'}(\mathbf{k} + \mathbf{q}, i\omega_n + i\Omega_m) \right] \quad (\text{C.2})$$

where the Green's function for the  $l$  pocket  $\hat{G}^l(\mathbf{k}, i\omega_n)$  are defined only around the high symmetry points  $\Gamma, X, Y$  (Eq. 3.10 from the main text). The Green's functions in the orbital basis  $\hat{G}^l(\mathbf{k}, i\omega_n)$  can be written in terms of the rotation matrices  $\hat{\mathcal{U}}^l$  that diagonalize the  $l$ -Hamiltonian and in terms of the Green's functions in the band basis  $g_{(\mathbf{k}, i\omega_n)}^{l\pm}$  as

$$\begin{aligned} \hat{G}_{(\mathbf{k}, i\omega_n)}^l &= \hat{\mathcal{U}}_{(\mathbf{k}, i\omega_n)}^l (\text{diag}(g^{l+}(\mathbf{k}, i\omega_n), g^{l-}(\mathbf{k}, i\omega_n))^{-1} \hat{\mathcal{U}}_{(\mathbf{k}, i\omega_n)}^{l-1}) = \\ &= \begin{pmatrix} u^l & -v^l \\ v^{*l} & u^{*l} \end{pmatrix} \begin{pmatrix} g^{l+} & 0 \\ 0 & g^{l-} \end{pmatrix} \begin{pmatrix} u^{*l} & v^l \\ -v^{*l} & u^l \end{pmatrix} \end{aligned} \quad (\text{C.3})$$

Then, by substituting in Eq. C.2 the expression for the orbital Green's functions given by Eq. C.3 we get the spin susceptibility read as

$$\begin{aligned} \chi^{ll'}(\mathbf{q}, i\Omega_m) &= \\ &= -\frac{1}{\beta} \sum_{\mathbf{k}, n} \text{Tr} \begin{pmatrix} u^l & -v^l \\ v^{*l} & u^{*l} \end{pmatrix} \begin{pmatrix} g^{l+} & 0 \\ 0 & g^{l-} \end{pmatrix} \begin{pmatrix} u^{*l} & v^l \\ -v^{*l} & u^l \end{pmatrix} \begin{pmatrix} u^{l'} & -v^{l'} \\ v^{*l'} & u^{*l'} \end{pmatrix} \begin{pmatrix} g^{l'+} & 0 \\ 0 & g^{l'-} \end{pmatrix} \begin{pmatrix} u^{*l'} & v^{l'} \\ -v^{*l'} & u^{l'} \end{pmatrix} \end{aligned} \quad (\text{C.4})$$



where we have omitted the momentum and frequency dependence for convenience but can be read from the  $l$  pocket which has the implicit dependence  $(\mathbf{k}, i\omega_n)^l$  and from the  $l'$  pocket which has the implicit  $(\mathbf{k} + \mathbf{q}, i\omega_n + i\Omega_m)^{l'}$  dependence. Operating Eq. C.4 and evaluating the trace over the orbital-basis, the spin susceptibility for a generic  $l, l'$  pockets can be expressed as

$$\begin{aligned} \chi^{ll'}(\mathbf{q}, i\Omega_m) = & -\frac{1}{\beta} \sum_{\mathbf{k}, n} \left[ g^{l+} g^{l'+} \left( |u^l|^2 |u^{l'}|^2 + u^l v^l u^{*l'} v^{*l'} + u^{*l} v^{*l} u^{l'} v^{l'} + |v^l|^2 |v^{l'}|^2 \right) + \right. \\ & + g^{l+} g^{l'-} \left( |u^l|^2 |v^{l'}|^2 - u^l v^l u^{*l'} v^{*l'} - u^{*l} v^{*l} u^{l'} v^{l'} + |v^l|^2 |u^{l'}|^2 \right) \left( \right. \\ & + g^{l'-} g^{l'+} \left( |v^l|^2 |u^{l'}|^2 - u^l v^l u^{*l'} v^{*l'} - u^{*l} v^{*l} u^{l'} v^{l'} + |u^l|^2 |v^{l'}|^2 \right) \left( \right. \\ & \left. \left. + g^{l'-} g^{l'-} \left( |v^l|^2 |v^{l'}|^2 + u^l v^l u^{*l'} v^{*l'} + u^{*l} v^{*l} u^{l'} v^{l'} + |u^l|^2 |u^{l'}|^2 \right) \right] \right) \quad (\text{C.5}) \end{aligned}$$

Selecting the intraorbital contribution for each term of Eq. C.5, i.e. the first and the latest terms for each summand, we get the intraorbital spin susceptibility can be expressed in a general way as

$$\begin{aligned} \chi^{ll'}(\mathbf{q}, i\Omega_m) = & -\frac{1}{\beta} \sum_{\mathbf{k}, n} \left[ g^{l+} g^{l'+} \left( |u^l|^2 |u^{l'}|^2 + |v^l|^2 |v^{l'}|^2 \right) + g^{l+} g^{l'-} \left( |u^l|^2 |v^{l'}|^2 + |v^l|^2 |u^{l'}|^2 \right) + \right. \\ & \left. + g^{l'-} g^{l'+} \left( |v^l|^2 |u^{l'}|^2 + |u^l|^2 |v^{l'}|^2 \right) + g^{l'-} g^{l'-} \left( |v^l|^2 |v^{l'}|^2 + |u^l|^2 |u^{l'}|^2 \right) \right] \quad (\text{C.6}) \end{aligned}$$

We can rewrite Eq. C.6 renaming each term as

$$\chi^{ll'}(\mathbf{q}, i\Omega_m) = \chi^{l+l'+}(\mathbf{q}, i\Omega_m) + \chi^{l+l'-}(\mathbf{q}, i\Omega_m) + \chi^{l-l'+}(\mathbf{q}, i\Omega_m) + \chi^{l-l'-}(\mathbf{q}, i\Omega_m) \quad (\text{C.7})$$

where the individuals terms of Eq. C.7 can be written as

$$\chi^{l\pm l'\pm}(\mathbf{q}, i\Omega_m) = \chi_{\eta}^{l\pm l'\pm}(\mathbf{q}, i\Omega_m) + \chi_{\eta'}^{l\pm l'\pm}(\mathbf{q}, i\Omega_m) \quad (\text{C.8})$$

Notice the two different contribution to the pocket susceptibility  $\chi^{l\pm l'\pm}(\mathbf{q}, i\Omega_m)$  come from different orbitals  $\eta$  and  $\eta'$ , since they correspond to the first and the latest terms for each summand of Eq. C.5 which carry on the orbital information from the rotation matrix  $\tilde{U}^l$  being different for each pocket  $l$ .

Last but not least, performing the Matsubara frequency summation with  $\omega_n = (2n + 1)\pi k_B T$  the fermionic Matsubara frequency and setting the external frequency  $\Omega \rightarrow 0$ , we find the static intraorbital susceptibility has the following expression

$$\chi_{\eta}^{l\pm l'\pm}(\mathbf{q}) = \sum_{\mathbf{k}} \frac{f(\epsilon_{\mathbf{k}+\mathbf{q}}^{l'\pm}) - f(\epsilon_{\mathbf{k}}^{l\pm})}{\epsilon_{\mathbf{k}+\mathbf{q}}^{l'\pm} - \epsilon_{\mathbf{k}}^{l\pm}} |(u/v)_{\mathbf{k}}^l|^2 |(u/v)_{\mathbf{k}+\mathbf{q}}^{l'}|^2 \quad (\text{C.9})$$

with  $f(\epsilon_{\mathbf{k}}^l) = (e^{\epsilon_{\mathbf{k}}^l / k_B T} + 1)^{-1}$  the Fermi distribution function. Eq. C.9 is just Eq. 3.11 from the main text.

The RPA spin susceptibilities are obtained in the form of Dyson-type equations (Eq. 3.12 from the main text) as

$$\chi_{\eta RPA}^{l\pm l'\pm}(\mathbf{q}) = \frac{\chi_{\eta}^{l\pm l'\pm}(\mathbf{q})}{1 - \tilde{U} \chi_{\eta}^{l\pm l'\pm}(\mathbf{q})} \quad (\text{C.10})$$

with  $\tilde{U}$  is the intraorbital effective coupling and  $\chi_{\eta}^{l_{\pm}l'_{\pm}}(\mathbf{q})$  the intraorbital spin susceptibility given in Eq. C.9.

### C.1.2. Four pocket model susceptibilities

Let us apply the current derivation for a four-pocket model  $\Gamma_+, \Gamma_-, X, Y$ . Within the OSSF model the spin fluctuations are orbital selective, so the two more relevant spin fluctuation propagators are around  $\mathbf{Q}_X = (\pi, 0)$  (involving the  $yz$  orbital component) and around  $\mathbf{Q}_Y = (0, \pi)$  (involving the  $xz$  orbital component). If we apply Eq. C.9 we will get for those two propagators the following contributions  $\chi_{yz}^{\Gamma_+X}(\mathbf{q})$  and  $\chi_{yz}^{\Gamma_-X}(\mathbf{q})$  referred to the  $yz$  orbital component and  $\chi_{xz}^{\Gamma_+Y}(\mathbf{q})$  and  $\chi_{xz}^{\Gamma_-Y}(\mathbf{q})$  referred to the  $xz$  orbital component. Still the spin susceptibility around  $\mathbf{Q} = (\pi, \pi)$   $\chi_{xy}^{XY}(\mathbf{q})$ , that represent the contribution of the  $xy$  orbital component is also computed for completeness.

$$\begin{aligned}
 \chi_{yz}^{\Gamma_+X}(\mathbf{q}) &= \sum_{\mathbf{k}} \frac{f(\epsilon_{\mathbf{k}+\mathbf{q}}^X) - f(\epsilon_{\mathbf{k}}^{\Gamma_+})}{\epsilon_{\mathbf{k}+\mathbf{q}}^X - \epsilon_{\mathbf{k}}^{\Gamma_+}} |u_{\mathbf{k}}^{\Gamma_+}|^2 |u_{\mathbf{k}+\mathbf{q}}^X|^2 \\
 \chi_{yz}^{\Gamma_-X}(\mathbf{q}) &= \sum_{\mathbf{k}} \frac{f(\epsilon_{\mathbf{k}+\mathbf{q}}^X) - f(\epsilon_{\mathbf{k}}^{\Gamma_-})}{\epsilon_{\mathbf{k}+\mathbf{q}}^X - \epsilon_{\mathbf{k}}^{\Gamma_-}} |v_{\mathbf{k}}^{\Gamma_-}|^2 |u_{\mathbf{k}+\mathbf{q}}^X|^2 \\
 \chi_{xz}^{\Gamma_+Y}(\mathbf{q}) &= \sum_{\mathbf{k}} \frac{f(\epsilon_{\mathbf{k}+\mathbf{q}}^Y) - f(\epsilon_{\mathbf{k}}^{\Gamma_+})}{\epsilon_{\mathbf{k}+\mathbf{q}}^Y - \epsilon_{\mathbf{k}}^{\Gamma_+}} |v_{\mathbf{k}}^{\Gamma_+}|^2 |u_{\mathbf{k}+\mathbf{q}}^Y|^2 \\
 \chi_{xz}^{\Gamma_-Y}(\mathbf{q}) &= \sum_{R\mathbf{k}} \left( \frac{f(\epsilon_{\mathbf{k}+\mathbf{q}}^Y) - f(\epsilon_{\mathbf{k}}^{\Gamma_-})}{\epsilon_{\mathbf{k}+\mathbf{q}}^Y - \epsilon_{\mathbf{k}}^{\Gamma_-}} |u_{\mathbf{k}}^{\Gamma_-}|^2 |u_{\mathbf{k}+\mathbf{q}}^Y|^2 \right. \\
 \chi_{xy}^{XY}(\mathbf{q}) &= \sum_{R\mathbf{k}} \frac{f(\epsilon_{\mathbf{k}+\mathbf{q}}^Y) - f(\epsilon_{\mathbf{k}}^X)}{\epsilon_{\mathbf{k}+\mathbf{q}}^Y - \epsilon_{\mathbf{k}}^X} |v_{\mathbf{k}}^X|^2 |v_{\mathbf{k}+\mathbf{q}}^Y|^2
 \end{aligned} \tag{C.11}$$

where we have simplified the notation  $(X/Y)^+$  as  $X/Y$  due to the  $(X/Y)^-$  contribution is not in the Fermi level for the electron pockets. Notice that for a three pocket model (for example simulating the FeSe case) the  $\Gamma^-$  contributions, i.e.  $\chi_{yz}^{\Gamma_-X}(\mathbf{q})$  and  $\chi_{xz}^{\Gamma_-Y}(\mathbf{q})$ , are absent.

The RPA spin susceptibilities for the FeSe and 122 systems are obtained in the form of Dyson-type equations based on Eq. C.10 with Eq. C.11 as

$$\begin{aligned}
 \chi_{yzRPA}^{\Gamma_{\pm}X}(\mathbf{q}) &= \frac{\chi_{yz}^{\Gamma_{\pm}X}(\mathbf{q})}{1 - \tilde{U}\chi_{yz}^{\Gamma_{\pm}X}(\mathbf{q})} & \chi_{xzRPA}^{\Gamma_{\pm}Y}(\mathbf{q}) &= \frac{\chi_{xz}^{\Gamma_{\pm}Y}(\mathbf{q})}{1 - \tilde{U}\chi_{xz}^{\Gamma_{\pm}Y}(\mathbf{q})} & \chi_{xyRPA}^{XY}(\mathbf{q}) &= \frac{\chi_{xy}^{XY}(\mathbf{q})}{1 - \tilde{U}\chi_{xy}^{XY}(\mathbf{q})}
 \end{aligned} \tag{C.12}$$

Eqs. C.12 are exactly those represented in Fig. 3.2 from the main text.

## C.2. Superconductivity mediated by OSSF

### C.2.1. Computation of the RPA pairing vertex

The RPA pairing interaction is given by the irreducible particle-particle vertex that can be computed from all possible Feynman's diagrams containing the orbital selective spin

susceptibility. In Figure C.1, that corresponds to Figure 3.4 in the main text, we draw again for convenience all Feynman's diagrams that contains only the spin susceptibilities up to finite order in perturbation of  $\tilde{U}$  for electrons of opposite spin and momentum.

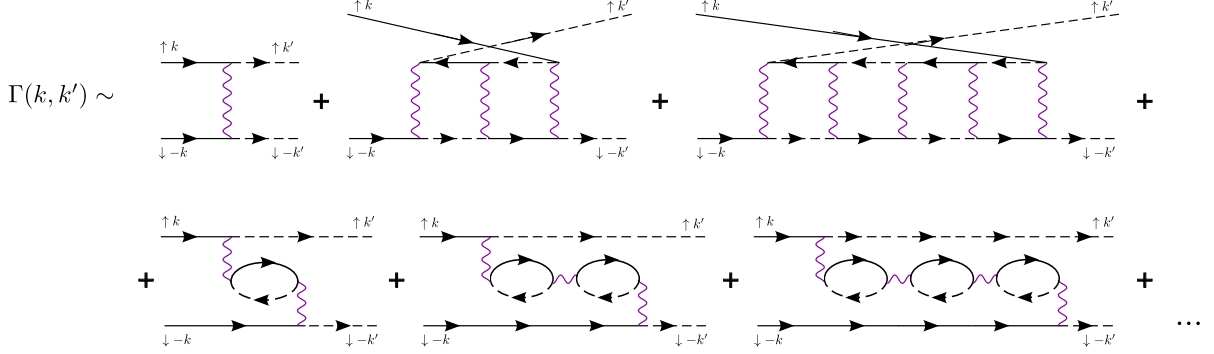


**Figure C.1:** Pairing vertex in random phase approximation up to fifth order in the OSSF model.

At first order perturbation in  $\tilde{U}$ , we find only one diagram given by

$$\Gamma_0^{l\pm l'\pm}(\mathbf{k}, \mathbf{k}') = \tilde{U} \quad (\text{C.13})$$

At higher orders we can differentiate between ladder diagrams or bubble diagrams. The ladder diagrams (first line in Figure C.1) can be expressed as

$$\Gamma_{ladder}^{l\pm l'\pm}(\mathbf{k}, \mathbf{k}') = \tilde{U}^3 \chi^{l\pm l'\pm 2}(\mathbf{k}' + \mathbf{k}) + \tilde{U}^5 \chi^{l\pm l'\pm 4}(\mathbf{k}' + \mathbf{k}) + \mathcal{O}(\tilde{U}^7) \quad (\text{C.14})$$

Eq. C.14 can be rewrite using a geometrical series as

$$\Gamma_{ladder}^{l\pm l'\pm}(\mathbf{k}, \mathbf{k}') = \frac{\tilde{U}^3 \chi^{l\pm l'\pm 2}(\mathbf{k}' + \mathbf{k})}{1 - \tilde{U}^2 \chi^{l\pm l'\pm 2}(\mathbf{k}' + \mathbf{k})} \quad (\text{C.15})$$

The bubble diagrams (second line in Figure C.1) can be expressed as

$$\Gamma_{bubble}^{l\pm l'\pm}(\mathbf{k}, \mathbf{k}') = \tilde{U}^2 \chi^{l\pm l'\pm}(\mathbf{k}' - \mathbf{k}) + \tilde{U}^3 \chi^{l\pm l'\pm 2}(\mathbf{k}' - \mathbf{k}) + \mathcal{O}(\tilde{U}^4) \quad (\text{C.16})$$

and it can be rewrite using a geometrical series as

$$\Gamma_{bubble}^{l\pm l'\pm}(\mathbf{k}, \mathbf{k}') = \frac{\tilde{U}^2 \chi^{l\pm l'\pm}(\mathbf{k}' - \mathbf{k})}{1 - \tilde{U} \chi^{l\pm l'\pm}(\mathbf{k}' - \mathbf{k})} \quad (\text{C.17})$$

So, the singlet pairing vertex can be expressed as the sum of this three contribution like

$$\Gamma^{l\pm l'\pm}(\mathbf{k}, \mathbf{k}') = \Gamma_0^{l\pm l'\pm}(\mathbf{k}, \mathbf{k}') + \Gamma_{ladder}^{l\pm l'\pm}(\mathbf{k}, \mathbf{k}') + \Gamma_{bubble}^{l\pm l'\pm}(\mathbf{k}, \mathbf{k}') \quad (\text{C.18})$$

Symmetrizing Eq. C.18 due to the  $\mathbf{k} \rightarrow -\mathbf{k}$  invariance of the gap, we get that in the weak coupling limit, the leading RPA diagrams for vertex in the OSSF model pairing interaction can be expressed

$$\Gamma_{\eta}^{l\pm l'\pm}(\mathbf{q}) = \tilde{U} + \frac{\tilde{U}^3 \chi_{\eta}^{l\pm l'\pm 2}(\mathbf{q})}{1 - \tilde{U}^2 \chi_{\eta}^{l\pm l'\pm 2}(\mathbf{q})} + \frac{\tilde{U}^2 \chi_{\eta}^{l\pm l'\pm}(\mathbf{q})}{1 - \tilde{U} \chi_{\eta}^{l\pm l'\pm}(\mathbf{q})} \quad (\text{C.19})$$

which is just Eq. 3.13 in the main text where  $\mathbf{q} = \mathbf{k}' - \mathbf{k}$  and  $\chi_{\eta}^{l\pm l'\pm}(\mathbf{q})$  the spin susceptibility given in formula Eq. C.9. Notice that in Eq. C.19 we recover the orbital dependant notation and also we simplify it by calling  $\eta$  to  $\eta\eta$  indices.

### C.2.2. Orbital-dependent superconducting order parameters

In order to reduce the two-particle operators to single-particle operators we apply mean field theory to Eq. 3.14 from the main text. The mean-field equations for the mean field Hamiltonian, can be easily derived by defining the orbital-dependent superconducting order parameters for the hole sector ( $\Delta_{yz}^+, \Delta_{yz}^-, \Delta_{xz}^+, \Delta_{xz}^-$ ) and the electron sector ( $\Delta_{yz}^{e+}, \Delta_{yz}^{e-}, \Delta_{xz}^{e+}, \Delta_{xz}^{e-}$ ) as

$$\begin{aligned}
 \Delta_{yz\mathbf{k}'}^+ &= -\Gamma_{yz\mathbf{k}\mathbf{k}'}^{+e} \langle (u_{\mathbf{k}}^X)^2 e_{\mathbf{k}}^X e_{-\mathbf{k}}^X \rangle \\
 \Delta_{yz\mathbf{k}'}^- &= -\Gamma_{yz\mathbf{k}\mathbf{k}'}^{-e} \langle (u_{\mathbf{k}}^X)^2 e_{\mathbf{k}}^X \mathbf{k} e_{-\mathbf{k}}^X \rangle \\
 \Delta_{xz\mathbf{k}'}^+ &= -\Gamma_{xz\mathbf{k}\mathbf{k}'}^{+e} \langle (u_{\mathbf{k}}^Y)^2 e_{\mathbf{k}}^Y \mathbf{k} e_{-\mathbf{k}}^Y \rangle \\
 \Delta_{xz\mathbf{k}'}^- &= -\Gamma_{xz\mathbf{k}\mathbf{k}'}^{-e} \langle (u_{\mathbf{k}}^Y)^2 e_{\mathbf{k}}^Y e_{-\mathbf{k}}^Y \rangle \\
 \Delta_{yz\mathbf{k}'}^{e+} &= -\Gamma_{yz\mathbf{k}\mathbf{k}'}^{+e} \langle (u_{\mathbf{k}}^{*\Gamma})^2 h_{\mathbf{k}}^+ h_{-\mathbf{k}}^+ \rangle \\
 \Delta_{yz\mathbf{k}'}^{e-} &= -\Gamma_{yz\mathbf{k}\mathbf{k}'}^{-e} \langle (v_{\mathbf{k}}^\Gamma)^2 h_{\mathbf{k}}^- h_{-\mathbf{k}}^- \rangle \\
 \Delta_{xz\mathbf{k}'}^{e+} &= -\Gamma_{xz\mathbf{k}\mathbf{k}'}^{+e} \langle (v_{\mathbf{k}}^{*\Gamma})^2 h_{\mathbf{k}}^+ h_{-\mathbf{k}}^+ \rangle \\
 \Delta_{xz\mathbf{k}'}^{e-} &= -\Gamma_{xz\mathbf{k}\mathbf{k}'}^{-e} \langle (u_{\mathbf{k}}^\Gamma)^2 h_{\mathbf{k}}^- h_{-\mathbf{k}}^- \rangle
 \end{aligned} \tag{C.20}$$

The superscript  $l = +/-$  is referred to the hole pockets  $\Gamma^+$  or  $\Gamma^-$  respectively and the superscript  $e$  is referred to the electron pockets  $X$  or  $Y$ .

By considering the electron-electron interaction we can define the  $xy$  order parameters ( $\Delta_{xy}^{eY}, \Delta_{xy}^{eX}$ ) as:

$$\begin{aligned}
 \Delta_{xy\mathbf{k}'}^{eY} &= -\Gamma_{xy\mathbf{k}\mathbf{k}'}^{XY} \langle (v_{\mathbf{k}}^X)^2 e_{\mathbf{k}}^X e_{-\mathbf{k}}^X \rangle \\
 \Delta_{xy\mathbf{k}'}^{eX} &= -\Gamma_{xy\mathbf{k}\mathbf{k}'}^{XY} \langle (v_{\mathbf{k}}^Y)^2 e_{\mathbf{k}}^Y \mathbf{k} e_{-\mathbf{k}}^Y \rangle
 \end{aligned} \tag{C.21}$$

with which we then solve the mean-field equations for the  $xy$  pairing Hamiltonian given in Eq. 3.27 from the main text.

### C.2.3. Band parameters to reproduced the multiorbital model

The modified parameters for reproduce the four pockets Fermi surface in [102] are given in Table B.1

$\Gamma$		$X/Y$	
$\epsilon_\Gamma$	10	$\epsilon_{xy}$	72
$a_\Gamma$	150	$a_{xy}$	93
$b_\Gamma$	50	$b$	154
		$v$	144

**Table C.1:** Low-energy model parameters used in Fig. 3.6. All the parameters are in meV.

The spin-orbit interaction is set to  $\lambda = 0$  meV.

# D

## Appendix Chapter 4

### D.1. Computation of the dc conductivity from the optical conductivity in the OSSF model

#### D.1.1. Current-current correlation function

In this Appendix we perform the complete derivation for the current-current correlation function within the OSSF model. We start from the expression of the current-current correlation function in the Matsubara formalism  $\Pi_\alpha$  (Eq. 4.6 from the main text)

$$\Pi_{ij}(\mathbf{q}, i\Omega_m) = \frac{T}{N} \int_0^\beta d\tau e^{i\Omega_m \tau} \langle T_\tau j_i(\mathbf{q}, \tau) j_j(-\mathbf{q}, 0) \rangle \quad (\text{D.1})$$

with  $\tau$  the imaginary time,  $\beta = 1/T$  and  $\Omega_m = 2\pi mT$  the bosonic Matsubara frequency.

In the bubble approximation, the current-current correlation function D.1 can be expressed as

$$\Pi_{ij}(\mathbf{q}, i\Omega_m) = 2 \sum_{lkn} \text{Tr} \{ \hat{G}^l(\mathbf{k} - \mathbf{q}/2, i\omega_n) \hat{V}_{\mathbf{k}_i}^l \hat{G}^l(\mathbf{k} + \mathbf{q}/2, i\omega_n + i\Omega_m) \hat{V}_{\mathbf{k}_j}^l \} \quad (\text{D.2})$$

with  $l = \Gamma, X, Y$  denoting the pocket index,  $\omega_n = 2\pi(n + 1/2)T$  the fermionic Matsubara frequency and the factor 2 is due to the spin summation.

In Eq. D.2,  $\hat{G}^l(\mathbf{k}, i\omega_n)$  is the renormalized Green's function from the OSSF (defined in Eq. 2.48 in the main text) and  $\hat{V}_{\mathbf{k}_i}^l$  are the velocity operator in the direction  $i = \{x, y\}$ . Since the self energy corrections computed within an Eliashberg-like treatment are momentum independent,  $\hat{V}_{\mathbf{k}_i}^l = \partial_{\mathbf{k}_i} \hat{H}^l = \partial_{\mathbf{k}_i} (\hat{H}_0^l + \hat{\Sigma}^l) = \partial_{\mathbf{k}_i} \hat{H}_0^l = \hat{V}_{0\mathbf{k}_i}^l$  so that vertex corrections vanish identically and the interacting velocity is the same than the bare velocity.

As we are interested in the dc conductivity, we set  $\mathbf{q} = 0$  in Eq. D.2

$$\Pi_{ij}(i\Omega_m) = 2 \sum_{lkn} \text{Tr} \{ \hat{G}^l(\mathbf{k}, i\omega_n) \hat{V}_{\mathbf{k}_i}^l \hat{G}^l(\mathbf{k}, i\omega_n + i\Omega_m) \hat{V}_{\mathbf{k}_j}^l \} \quad (\text{D.3})$$

We rotate Eq. D.3 into the band basis  $\hat{G}^l(\mathbf{k}, i\omega_n) = \hat{\mathcal{U}}_R^l(\mathbf{k}, i\omega_n) [i\omega_n \hat{\mathbb{1}} -$

$\hat{\Lambda}_R^l(\mathbf{k}, i\omega_n)]^{-1} \hat{\mathcal{U}}_R^{l-1}(\mathbf{k}, i\omega_n)$  and we get the current-current correlation is given by

$$\Pi_{ij}(i\Omega_m) = 2 \sum_{lkn} \left( \text{Tr} \left\{ \hat{\mathcal{U}}_R^l(\mathbf{k}, i\omega_n) [i\omega_n \hat{\mathbb{1}} - \hat{\Lambda}_R^l(\mathbf{k}, i\omega_n)]^{-1} \hat{\mathcal{U}}_R^{l-1}(\mathbf{k}, i\omega_n) \hat{V}_{\mathbf{k}_i}^l \right. \right. \\ \left. \left. \hat{\mathcal{U}}_R^l(\mathbf{k}, i\omega_n + i\Omega_m) [(i\omega_n + i\Omega_m) \hat{\mathbb{1}} - \hat{\Lambda}_R^l(\mathbf{k}, i\omega_n + i\Omega_m)]^{-1} \hat{\mathcal{U}}_R^{l-1}(\mathbf{k}, i\omega_n + i\Omega_m) \hat{V}_{\mathbf{k}_j}^l \right\} \right) \quad (\text{D.4})$$

Using the cyclic property of the trace allows us to define the renormalized velocity matrix  $\hat{V}_{R(\mathbf{k}_i, i\omega_n)}^l$  and redefine Eq. D.4 as

$$\Pi_{ij}(i\Omega_m) = 2 \sum_{lkn} \left( \text{Tr} \left\{ [i\omega_n \hat{\mathbb{1}} - \hat{\Lambda}_{R(\mathbf{k}, i\omega_n)}^l]^{-1} \hat{V}_{R(\mathbf{k}_i, i\omega_n)}^l [(i\omega_n + i\Omega_m) \hat{\mathbb{1}} - \hat{\Lambda}_{R(\mathbf{k}, i\omega_n + i\Omega_m)}^l]^{-1} \hat{V}_{R(\mathbf{k}_j, i\omega_n + i\Omega_m)}^l \right\} \right) \quad (\text{D.5})$$

with the renormalized velocity matrix defined as

$$\hat{V}_{R(\mathbf{k}_i, i\omega_n)}^l = \hat{\mathcal{U}}_R^{l-1}(\mathbf{k}, i\omega_n) \hat{V}_{\mathbf{k}_i}^l \hat{\mathcal{U}}_R^l(\mathbf{k}, i\omega_n + i\Omega_m), \quad (\text{D.6}) \\ \hat{V}_{R(\mathbf{k}_j, i\omega_n + i\Omega_m)}^l = \hat{\mathcal{U}}_R^{l-1}(\mathbf{k}, i\omega_n + i\Omega_m) \hat{V}_{\mathbf{k}_j}^l \hat{\mathcal{U}}_R^l(\mathbf{k}, i\omega_n)$$

If we substitute the unitary matrix  $\hat{\mathcal{U}}_R^l(\mathbf{k}, i\omega_n)$ , the explicit result for the renormalized velocity matrix is

$$\hat{V}_{R(\mathbf{k}_i, i\omega_n)}^l = \begin{pmatrix} V_R^{11} & V_R^{12} \\ V_R^{21} & V_R^{22} \end{pmatrix}_{\mathbf{k}_i}^l = \begin{pmatrix} u_R^* & v_R \\ -v_R^* & u_R \end{pmatrix}_{(\mathbf{k}, i\omega_n)}^l \begin{pmatrix} V^{11} & V^{12} \\ V^{21} & V^{22} \end{pmatrix}_{\mathbf{k}_i}^l \begin{pmatrix} u_R & -v_R \\ v_R^* & u_R^* \end{pmatrix}_{(\mathbf{k}, i\omega_n + i\Omega_m)}^l \quad (\text{D.7})$$

with  $u_R$  and  $v_R$  the renormalized coherence factors defined in Eq. D.22. Operating Eq. D.7 we get that, as a consequence of the orbital structure, the explicit components of  $\hat{V}_{R(\mathbf{k}_i, i\omega_n)}^l$  read as

$$\begin{aligned} V_R^{l11} &= V^{l11} u_{R\omega}^* u_{R\omega+\Omega}^l + V^{l21} v_{R\omega}^l u_{R\omega+\Omega}^l + V^{l12} u_{R\omega}^* v_{R\omega+\Omega}^* + V^{l22} v_{R\omega}^l v_{R\omega+\Omega}^*, \\ V_R^{l21} &= -V^{l11} v_{R\omega}^* u_{R\omega+\Omega}^l + V^{l21} u_{R\omega}^l u_{R\omega+\Omega}^l - V^{l12} v_{R\omega}^* v_{R\omega+\Omega}^* + V^{l22} u_{R\omega}^l v_{R\omega+\Omega}^*, \\ V_R^{l21} &= -V^{l11} u_{R\omega}^* v_{R\omega+\Omega}^l - V^{l21} v_{R\omega}^l v_{R\omega+\Omega}^l + V^{l12} u_{R\omega}^* u_{R\omega+\Omega}^* + V^{l22} v_{R\omega}^l u_{R\omega+\Omega}^*, \\ V_R^{l22} &= V^{l11} v_{R\omega}^* v_{R\omega+\Omega}^l - V^{l21} u_{R\omega}^l v_{R\omega+\Omega}^l - V^{l12} v_{R\omega}^* u_{R\omega+\Omega}^* + V^{l22} u_{R\omega}^l u_{R\omega+\Omega}^* \end{aligned} \quad (\text{D.8})$$

where we have dropped the  $\mathbf{k}$  indices and we call  $\omega$  to the Matsubara frequency  $i\omega_n$  for simplicity. Analogous expressions for the  $\hat{V}_{R(\mathbf{k}_j, i\omega_n + i\Omega_m)}^l$  and its components hold, by replacing  $k_i$  by  $k_j$  and exchanging  $i\omega_n$  by  $i\omega_n + i\Omega_m$  in Eq. D.7 and Eq. D.8.

By using Eq. D.7, the current-current correlation function D.5 can be rewritten as

$$\Pi_{ij}(i\Omega_m) = 2 \sum_{lkn} \begin{pmatrix} g^+ & 0 \\ 0 & g^- \end{pmatrix}_{(\mathbf{k}, i\omega_n)}^l \begin{pmatrix} V_R^{11} & V_R^{12} \\ V_R^{21} & V_R^{22} \end{pmatrix}_{\mathbf{k}_i}^l \begin{pmatrix} g^+ & 0 \\ 0 & g^- \end{pmatrix}_{(\mathbf{k}, i\omega_n + i\Omega_m)}^l \begin{pmatrix} V_R^{11} & V_R^{12} \\ V_R^{21} & V_R^{22} \end{pmatrix}_{\mathbf{k}_j}^l \quad (\text{D.9})$$

with  $\hat{G}^l(\mathbf{k}, i\omega_n) = [i\omega_n \hat{\mathbb{1}} - \hat{\Lambda}_R^l(\mathbf{k}, i\omega_n)]^{-1} = \text{diag}(g^+(\mathbf{k}, i\omega_n), g^-(\mathbf{k}, i\omega_n))$  as the renormalized Green function.

Operating the trace over the orbital basis we get

$$\begin{aligned} \Pi_{ij}(i\Omega_m) &= \left[ \Pi_{ij}^{l11}(i\Omega_m) \right] + \left[ \Pi_{ij}^{l22}(i\Omega_m) \right] = \\ &= 2 \sum_{lkn} \left( \left[ g_{i\omega_n}^+ V_R^{l11} g_{i\omega_n + i\Omega_m}^+ V_R^{l11} + g_{i\omega_n}^+ V_R^{l12} g_{i\omega_n + i\Omega_m}^- V_R^{l21} \right] \left( + \right. \right. \\ &\quad \left. \left. + \left[ g_{i\omega_n}^- V_R^{l21} g_{i\omega_n + i\Omega_m}^+ V_R^{l12} + g_{i\omega_n}^- V_R^{l22} g_{i\omega_n + i\Omega_m}^- V_R^{l22} \right] \right) \right) \quad (\text{D.10}) \end{aligned}$$

We can write Eq. D.10 in a simple way as

$$\Pi_{ij}(i\Omega_m) = \Pi_{ij(i\Omega_m)}^{l_{11}++} + \Pi_{ij(i\Omega_m)}^{l_{11}+-} + \Pi_{ij(i\Omega_m)}^{l_{22}-+} + \Pi_{ij(i\Omega_m)}^{l_{22}--} \quad (\text{D.11})$$

where explicitly the components of  $\Pi_{ij}(i\Omega_m)$  are given by

$$\begin{aligned} \Pi_{ij(i\Omega_m)}^{l_{11}++} &= 2 \sum_{lkn} g_{i\omega_n}^+ V_{R,\omega}^{l_{11}} g_{i\omega_n+i\Omega_m}^+ V_{R,\omega+\Omega}^{l_{11}}, \\ \Pi_{ij(i\Omega_m)}^{l_{11}+-} &= 2 \sum_{lkn} g_{i\omega_n}^+ V_{R,\omega}^{l_{12}} g_{i\omega_n+i\Omega_m}^- V_{R,\omega+\Omega}^{l_{21}}, \\ \Pi_{ij(i\Omega_m)}^{l_{22}-+} &= 2 \sum_{lkn} g_{i\omega_n}^- V_{R,\omega}^{l_{21}} g_{i\omega_n+i\Omega_m}^+ V_{R,\omega+\Omega}^{l_{12}}, \\ \Pi_{ij(i\Omega_m)}^{l_{22}--} &= 2 \sum_{lkn} g_{i\omega_n}^- V_{R,\omega}^{l_{22}} g_{i\omega_n+i\Omega_m}^- V_{R,\omega+\Omega}^{l_{22}} \end{aligned} \quad (\text{D.12})$$

In Eq. D.12,  $\Pi_{ij(i\Omega_m)}^{l_{11}++}$  and  $\Pi_{ij(i\Omega_m)}^{l_{22}--}$  are the intraband terms and  $\Pi_{ij(i\Omega_m)}^{l_{11}+-}$  and  $\Pi_{ij(i\Omega_m)}^{l_{22}-+}$  the interband terms.

### D.1.2. Dc conductivity

We start from the expression of the dc conductivity (Eq. 4.5 from the main text), as the  $\Omega \rightarrow 0$  limit of the longitudinal optical conductivity given by

$$\sigma_{dc\alpha} = \frac{e^2}{V} \lim_{\Omega \rightarrow 0} \frac{\text{Im} \Pi_\alpha(\mathbf{q} = 0, \Omega)}{\Omega} \quad (\text{D.13})$$

Therefore, we are interested in the intraband terms given by the  $\Pi^{++/--}$  components of Eq. D.12 and also in the diagonal terms of the current-current function  $\Pi_{ii}$  which we call as  $\Pi_\alpha$  with  $\alpha = \{x, y\}$  equivalent to the index  $ii = \{xx, yy\}$ .

In order to compute the  $\Pi_{ii}^{++/--}$  terms, we express the Green's functions  $g^\pm(i\omega_n)$  in terms of the spectral functions  $A_{\mathbf{k}}^{l\pm}(\omega)$  in Eq. D.12, by introducing the spectral representation

$$g^\pm(i\omega_n) = \int \left( dz \frac{A^\pm(z)}{i\omega_n - z} \right) \quad (\text{D.14})$$

Then, we perform the Matsubara sum, take the imaginary part of the current-current diagonal terms and take the  $\Omega \rightarrow 0$  limit and we finally arrive to the pocket dc conductivity expression  $\sigma_\alpha^{l\pm}$ . The  $\alpha = \{x, y\}$  component of the dc conductivity in the band basis is obtained from the sum over all the pockets  $l_\pm = \{\Gamma_+, \Gamma_-, X, Y\}$

$$\sigma_{dc\alpha} = \sum_{l_\pm} \sigma_\alpha^{l_\pm} \quad (\text{D.15})$$

The pocket conductivity is

$$\sigma_\alpha^{l\pm} = \frac{2\pi e^2}{N} \sum_{\mathbf{k}} \left( \int_{-\infty}^{\infty} d\omega \left( -\frac{\partial f(\omega)}{\partial \omega} \right) [V_{R\mathbf{k}\alpha}^{l\pm}(\omega)]^2 [A_{\mathbf{k}}^{l\pm}(\omega)]^2 \right). \quad (\text{D.16})$$

where  $f(\omega)$  the Fermi distribution function. In this basis the spectral function is diagonal

$$A_{\mathbf{k}}^{l\pm}(\omega) = \frac{1}{\pi} \frac{\Gamma_{R\mathbf{k}}^{l\pm}(\omega)}{[\Gamma_{R\mathbf{k}}^{l\pm}(\omega)]^2 + [\omega - \epsilon_{R\mathbf{k}}^{l\pm}(\omega)]^2} \quad (\text{D.17})$$

with the renormalized energy dispersion relation as

$$\epsilon_{R\mathbf{k}}^{l\pm}(\omega) = \text{Re} E_{R\mathbf{k}}^{l\pm}(\omega) \quad (\text{D.18})$$

and the renormalized scattering rate as

$$\Gamma_{R\mathbf{k}}^{l\pm}(\omega) = \delta\Gamma + |\text{Im} E_{R\mathbf{k}}^{l\pm}(\omega)| \quad (\text{D.19})$$

The eigenvalue matrix  $E_{R\mathbf{k}}^{l\pm}(\omega)$  is given by

$$E_{R\mathbf{k}}^{l\pm}(\omega) = h_0^l + \Sigma_{0\mathbf{k}}^l(\omega) \pm \sqrt{(h_{1\mathbf{k}}^l)^2 + (h_{2\mathbf{k}}^l)^2 + (h_{3\mathbf{k}}^l + \Sigma_{3\mathbf{k}}^l(\omega))^2} \quad (\text{D.20})$$

$V_{R\mathbf{k}\alpha}^{l\pm}$  is the bare velocity operator rotated into the band basis. As we take the  $\Omega \rightarrow 0$  limit and we only consider the intraband component, the velocity given by Eq. D.8 reduces to

$$V_{R\mathbf{k}\alpha}^{l\pm} = V_{\mathbf{k}\alpha}^{l11} |u_R^l|^2 \pm V_{\mathbf{k}\alpha}^{l12} u_R^{*l} v_R^l \pm V_{\mathbf{k}\alpha}^{l21} u_R^l v_R^l + V_{\mathbf{k}\alpha}^{l22} |v_R^l|^2 \quad (\text{D.21})$$

Hereafter we omit the dependence on  $\omega$  for simplicity.  $V_{\mathbf{k}\alpha}^{l\eta\eta'}$  are the  $\eta\eta'$  component of the velocity and  $(u/v)_R^l$  are the renormalized coherence factors which are renormalized by the self-energy correction as

$$u_R^l = \frac{1}{\sqrt{2}} \sqrt{1 + \frac{h_3^l + \Sigma_3^l}{h_R^l}}, \quad v_R^{*l} = \frac{1}{\sqrt{2}} \frac{h_1^l + ih_2^l}{\sqrt{(h_1^l)^2 + (h_2^l)^2}} \sqrt{\left(-\frac{h_3^l + \Sigma_3^l}{h_R^l}\right)} \quad (\text{D.22})$$

In the  $T \rightarrow 0$  limit we can approximate the Fermi function  $-\frac{\partial f(\omega)}{\partial \omega} \rightarrow \delta(\omega)$  which selects only states at the Fermi level  $\omega = 0$ .

$$\sigma_{\alpha}^{l\pm} = \frac{2\pi e^2}{N} \sum_{\mathbf{k}} (V_{R\mathbf{k}\alpha}^{l\pm})^2 (A_{\mathbf{k}}^{l\pm})^2 \quad (\text{D.23})$$

By further assuming  $\Gamma_R^{l\pm}$  to be small  $\Gamma_R^{l\pm} \rightarrow 0$ , we can also approximate the spectral function as  $(A_{\mathbf{k}}^{l\pm})^2 \rightarrow \frac{1}{2\pi\Gamma_{R\mathbf{k}}^{l\pm}} \delta(\epsilon_{R\mathbf{k}}^{l\pm})$  and the pocket conductivity reduces to

$$\sigma_{\alpha}^{l\pm} = \frac{e^2}{N} \sum_{\mathbf{k}} \frac{(V_{R\mathbf{k}\alpha}^{l\pm})^2}{\Gamma_{R\mathbf{k}}^{l\pm}} \delta(\epsilon_{R\mathbf{k}}^{l\pm}). \quad (\text{D.24})$$

which is Eq. 4.18 from the main text.

Moreover, if we express the delta in energy  $\delta(\epsilon_{R\mathbf{k}}^{l\pm})$  in terms of the momentum we get

$$\sigma_{\alpha}^{l\pm} = \frac{e^2}{N} \int \frac{d\mathbf{k}^2}{(2\pi)^2} \frac{(V_{R\mathbf{k}\alpha}^{l\pm})^2}{\Gamma_{R\mathbf{k}}^{l\pm}} \frac{\delta(\mathbf{k} - \mathbf{k}_F)}{|\nabla \epsilon_{R\mathbf{k}}^{l\pm}|} \quad (\text{D.25})$$

where the gradient  $|\nabla \epsilon_{R\mathbf{k}}^{l\pm}| = |(V_{R\mathbf{k}_x}^{l\pm})^2 + (V_{R\mathbf{k}_y}^{l\pm})^2|$  is different to the velocity term  $(V_{R\mathbf{k}\alpha}^{l\pm})^2$  in the numerator given by Eq. D.21 which is in the direction of the dc conductivity  $\alpha = \{x, y\}$ .



## D.2. Analytical computation of the anisotropy of the dc conductivity for the 122 and FeSe

### D.2.1. Perfect nested circular Fermi surfaces

To allow analytical treatment for the renormalized system in the parabolic approximation, we assume that the self-energy correction  $\Sigma_3$  is small enough to allow one for a perturbative expansion up to first order in  $\Sigma_3$ . The imaginary part of the self-energy is neglected since it goes to zero at low  $\omega$  and  $T = 0$ . Thus, the dressed coherence factors  $(u/v)_R^l$  in the analytical approach become

$$\begin{aligned} |u_R^l|^2 &= |u^l|^2 \left( 1 + \frac{2\text{Re}\Sigma_3^l}{h^l} |v^l|^2 \right) \\ |v_R^l|^2 &= |v^l|^2 \left( 1 - \frac{2\text{Re}\Sigma_3^l}{h^l} |u^l|^2 \right) \end{aligned} \quad (\text{D.26})$$

with  $u^l$  and  $v^l$  the bare coherence factors appearing in Eq. B.15. From Eq. D.26 we can see that the correction term  $\text{Re}\Sigma_3^l$  mixes the orbital character in each pocket, that is, contribute to  $u_R^l$  with a term proportional to  $v^l$  and vice versa. This effect of the OSSF self-energy in the coherence factors will have important consequences for the renormalized velocities in the nematic phase as we show below.

The dressed dispersion relations  $\epsilon_R^{l\pm} = \text{Re}E_R^{l\pm}$  is given by

$$\epsilon_R^{l\pm} = \epsilon^{l\pm} + \text{Re}\Sigma_0^l \pm \frac{h_3^l}{h^l} \text{Re}\Sigma_3^l. \quad (\text{D.27})$$

Replacing the values for the case of circular Fermi surface given in Eq. B.13 and Eq. B.14 we get

$$\begin{aligned} \epsilon_R^{\Gamma\pm} &= \epsilon_0^h \pm \cos 2\theta \text{Re}\Sigma_3^\Gamma, \\ \epsilon_R^{X/Y} &= -\epsilon_0^e \mp \cos 2\theta \text{Re}\Sigma_3^{X/Y}, \end{aligned} \quad (\text{D.28})$$

where we defined the tetragonal band energy for the hole pockets as  $\epsilon_0^h = \epsilon^\Gamma + \text{Re}\Sigma_0^\Gamma$  and  $\epsilon_0^e = \epsilon^e - \text{Re}\Sigma_0^{X/Y}$  for the electron pockets. For simplicity we further assume that  $\epsilon^X \equiv \epsilon^Y \equiv \epsilon^e$ .

The scattering rate  $\Gamma^{l\pm} = \delta\Gamma + |\text{Im}E_R^{l\pm}|$  acquires the expression

$$\Gamma_R^{l\pm} \approx \delta\Gamma + |\text{Im}\Sigma_0^l| \pm \frac{h_3^l}{h^l} |\text{Im}\Sigma_3^l|, \quad (\text{D.29})$$

Replacing Eq. B.13 and Eq. B.14 we get

$$\begin{aligned} \Gamma_R^{\Gamma\pm} &= \Gamma_0^h \pm \cos 2\theta |\text{Im}\Sigma_3^\Gamma|, \\ \Gamma_R^{X/Y} &= \Gamma_0^e \mp \cos 2\theta |\text{Im}\Sigma_3^{X/Y}|, \end{aligned} \quad (\text{D.30})$$

where we have separated the angular dependent renormalization  $\sim |\text{Im}\Sigma_3^l|$  from the tetragonal constant part,  $\Gamma_0^{h/e} = \delta\Gamma + |\text{Im}\Sigma_0^{\Gamma/e}|$ . From Eq. D.30 it is very easy to find analytically the locations of the cold spots on the Fermi surface by substituting the  $\text{Im}\Sigma_0^l$

and  $Im\Sigma_3^l$  expressions in terms of its orbital components. Thus, the minimum value of the scattering rate for each pocket is found at

$$\begin{aligned}\Gamma_R^{\Gamma+}(\theta = \frac{\pi}{2}) &= \delta\Gamma + |Im\Sigma_{xz}^\Gamma|, \\ \Gamma_R^{\Gamma-}(\theta = 0) &= \delta\Gamma + |Im\Sigma_{xz}^\Gamma|, \\ \Gamma_R^X(\theta = 0) &= \Gamma_R^Y(\theta = \frac{\pi}{2}) = \delta\Gamma\end{aligned}\tag{D.31}$$

The qualitative behavior of the self-energies in the nematic phase allows us to easily localize the minimum value of  $\Gamma_R^{l\pm}$  on the Fermi surface, that is, the cold spots.

As it is discussed in Ref. [60], the reconstruction of the Fermi surface below  $T_S$  is consistent with the Ising-nematic spin-fluctuations being bigger at  $\mathbf{Q}_X$  than at  $\mathbf{Q}_Y$ . This implies that self-energy corrections are stronger on the  $yz$  orbital than on the  $xz$  one. As a consequence for the holes, the smaller scattering rate corresponds to the  $xz$  orbital. Instead for the electrons, the smaller scattering rate is found for the  $xy$  orbital, given the absence of  $xy$  spin fluctuation between hole and electron pockets.

This result analysed in Chapter 4, is an example of the spin-orbital interplay retained by the OSSF approach that allows us to directly link the cold spots position with the Fermi surface orbital character and is not present in the band-based spin-nematic scenario.

### D.2.2. Anisotropy of the dc conductivity

In order to gain physical insight on the DC anisotropy given by Eq. D.25 we compute in this Appendix the expression for the renormalized velocity and scattering rate for each pocket  $l_{\pm} = \{\Gamma_+, \Gamma_-, X, Y\}$ .

#### Renormalized velocity

By neglecting the imaginary part of the self-energy in the coherence factors  $(u/v)_R^l$  given by Eq. D.26, it is easy to check the velocity given in Eq. D.21 can also be written as the derivative of the renormalized dispersion relation

$$V_{R\mathbf{k}\alpha}^{l\pm} = \partial\epsilon_R^{l\pm}(\mathbf{k})/\partial k_\alpha.\tag{D.32}$$

Explicitly for the hole pockets at  $\Gamma$  we have

$$V_{R\mathbf{k}\alpha}^{\Gamma\pm} = \partial_{k_\alpha} h_0^\Gamma \pm \partial_{k_\alpha} h_1^\Gamma \frac{h_1^\Gamma}{h^\Gamma} \pm \partial_{k_\alpha} h_3^\Gamma \frac{h_3^\Gamma}{h^\Gamma} \pm Re\Sigma_3^\Gamma \frac{h_1^\Gamma}{(h^\Gamma)^2} \left[ \partial_{k_\alpha} h_3^\Gamma \frac{h_1^\Gamma}{h^\Gamma} - \partial_{k_\alpha} h_1^\Gamma \frac{h_3^\Gamma}{h^\Gamma} \right]\tag{D.33}$$

and analogous expressions  $V_{R\mathbf{k}\alpha}^X$  and  $V_{R\mathbf{k}\alpha}^Y$  for the electron pockets. The first three terms in Eq. D.33 corresponds to the bare velocity, while the term multiplied by  $Re\Sigma_3^\Gamma$  accounts for the renormalization in the velocity due to OSSF self-energy corrections.

Using the explicit definition of  $h_0^l$  and  $h^l$  given by Eq. B.13 and Eq. B.14 in the analytical approximation, and deriving with respect to  $\mathbf{k}_x$  and  $\mathbf{k}_y$ , the velocities for the

different pockets read as

$$\begin{aligned}
 V_{R\mathbf{k}_x}^{\Gamma\pm} &= -\frac{k \cos \theta}{m^{\Gamma\pm}} \pm 4 \operatorname{Re} \Sigma_3^{\Gamma} \sin^2 \theta \frac{k \cos \theta}{k^2}, \\
 V_{R\mathbf{k}_y}^{\Gamma\pm} &= -\frac{k \sin \theta}{m^{\Gamma\pm}} \mp 4 \operatorname{Re} \Sigma_3^{\Gamma} \cos^2 \theta \frac{k \sin \theta}{k^2}, \\
 V_{R\mathbf{k}_x}^{X/Y} &= \frac{k \cos \theta}{m^{X/Y}} \mp 4 \operatorname{Re} \Sigma_3^{X/Y} \sin^2 \theta \frac{k \cos \theta}{k^2}, \\
 V_{R\mathbf{k}_y}^{X/Y} &= \frac{k \sin \theta}{m^{X/Y}} \pm 4 \operatorname{Re} \Sigma_3^{X/Y} \cos^2 \theta \frac{k \sin \theta}{k^2}
 \end{aligned} \tag{D.34}$$

where  $m^{l\pm}$  is the bare mass of the  $l_{\pm}$  pocket whose definition in terms of the Hamiltonian parameters is given by  $m^{\Gamma\pm} = 2(a \mp b)^{-1}$  and  $m^{X/Y} = m^e = 2(a + b)^{-1}$ .

The first term on the right hand side of Eq. D.34, is the  $\alpha$  component of the bare velocity, while the second term  $\mathcal{O}(\operatorname{Re} \Sigma_3^l)$  is an additional contribution due to the orbital mixing induced by the nematic order as expected from the  $(u, v)_R^l$  coherence factors in Eq. D.21.

To compute the  $\mathbf{k}$  integration in Eq. D.25 we will use the delta function and evaluate  $V_{R\mathbf{k}\alpha}^{l\pm}$  at the renormalized Fermi surface. Notice that, in the nematic phase  $k_F^{l\pm}(\theta)$  is no longer constant but gets deformed because of the anisotropic self-energy renormalization. This effect is also of order  $\mathcal{O}(\operatorname{Re} \Sigma_3^l)$  and has to be taken into account.

We estimate the change in the Fermi wave vector at the first order in the self-energy. Replacing the expression of  $k_F^{l\pm}(\theta)$  into Eq. D.34 we find

$$\begin{aligned}
 V_{R\mathbf{k}_x}^{\Gamma\pm} &= V_{0\mathbf{k}_x}^{\Gamma\pm} \left( 1 \pm \cos 2\theta \frac{\operatorname{Re} \Sigma_3^{\Gamma}}{2\epsilon_0^h} \mp 4 \sin^2 \theta \frac{\operatorname{Re} \Sigma_3^{\Gamma}}{2\epsilon_0^h} \right), \\
 V_{R\mathbf{k}_y}^{\Gamma\pm} &= V_{0\mathbf{k}_y}^{\Gamma\pm} \left( 1 \pm \cos 2\theta \frac{\operatorname{Re} \Sigma_3^{\Gamma}}{2\epsilon_0^h} \pm 4 \cos^2 \theta \frac{\operatorname{Re} \Sigma_3^{\Gamma}}{2\epsilon_0^h} \right), \\
 V_{R\mathbf{k}_x}^{X/Y} &= V_{0\mathbf{k}_x}^{X/Y} \left( 1 \pm \cos 2\theta \frac{\operatorname{Re} \Sigma_3^{X/Y}}{2\epsilon_0^{X/Y}} \mp 4 \sin^2 \theta \frac{\operatorname{Re} \Sigma_3^{X/Y}}{2\epsilon_0^{X/Y}} \right), \\
 V_{R\mathbf{k}_y}^{X/Y} &= V_{0\mathbf{k}_y}^{X/Y} \left( 1 \pm \cos 2\theta \frac{\operatorname{Re} \Sigma_3^{X/Y}}{2\epsilon_0^{X/Y}} \pm 4 \cos^2 \theta \frac{\operatorname{Re} \Sigma_3^{X/Y}}{2\epsilon_0^{X/Y}} \right)
 \end{aligned} \tag{D.35}$$

where  $\epsilon_0^h = \epsilon^{\Gamma} + \operatorname{Re} \Sigma_0^{\Gamma}$  and  $\epsilon_0^e = \epsilon^e - \operatorname{Re} \Sigma_0^{X/Y}$  are the Fermi energy in the tetragonal state and  $V_{0\mathbf{k}\alpha}^{\Gamma\pm} = -k_{F\alpha}^{\Gamma\pm}/m^{\Gamma\pm}$  and  $V_{0\mathbf{k}\alpha}^{X/Y} = k_{F\alpha}^e/m^e$  are the  $\alpha$  component of the bare velocity in the tetragonal state with  $k_{F\alpha}^l = \sqrt{\epsilon_0^l/(2m^l)}$ .

From Eq. D.35, one sees that the bare Fermi velocity in the nematic phase has two contributions  $\mathcal{O}(\operatorname{Re} \Sigma_3^l)$  opposite in sign: the first one is due to the change in  $k_F^{l\pm}$ , while the second one comes from the orbital mixing produced by the nematic order.

#### Renormalized scattering rate

The scattering rate is analytically estimated from Eq. D.19 using again the expansion of  $E_R^{l\pm}$  at the first order in  $\Sigma_3^l$

$$\begin{aligned}
 \Gamma_R^{\Gamma\pm} &= \Gamma_0^h \pm \cos 2\theta |\operatorname{Im} \Sigma_3^{\Gamma}|, \\
 \Gamma_R^{X/Y} &= \Gamma_0^e \mp \cos 2\theta |\operatorname{Im} \Sigma_3^{X/Y}|
 \end{aligned} \tag{D.36}$$

where we separate the tetragonal phase scattering rate,  $\Gamma_0^l = \delta\Gamma + |Im\Sigma_0^l|$ , from the angular dependent correction due to the nematic effect  $\sim Im\Sigma_3^l$ .

#### DC conductivity

Last, in order to estimate analytically the conductivity Eq. D.25, we also need to evaluate the norm of the pocket velocity  $|\nabla \epsilon_{R\mathbf{k}}^{l\pm}|$  which is different to the pocket velocity in a given direction  $x/y$  given by Eq. D.35.

By replacing all the analytical expressions found for the velocities, Eq. D.35, and the scattering rate, Eq. D.36 in Eq. D.25 and computing the  $|\nabla \epsilon_{R\mathbf{k}}^{l\pm}|$  term, the pockets dc conductivities read as

$$\begin{aligned}
 \sigma_{x/y}^{\Gamma+} &= \sigma^h \left( \left( \pm \frac{Re\Sigma_3^\Gamma}{2\epsilon_0^h} \mp \frac{Re\Sigma_3^\Gamma}{\epsilon_0^h} \mp \frac{|Im\Sigma_3^\Gamma|}{2\Gamma_0^h} \right), \right. \\
 \sigma_{x/y}^{\Gamma-} &= \sigma^h \left( \left( \mp \frac{Re\Sigma_3^\Gamma}{2\epsilon_0^h} \pm \frac{Re\Sigma_3^\Gamma}{\epsilon_0^h} \pm \frac{|Im\Sigma_3^\Gamma|}{2\Gamma_0^h} \right), \right. \\
 \sigma_{x/y}^X &= \sigma^e \left( \left( \pm \frac{Re\Sigma_3^X}{2\epsilon_0^e} \mp \frac{Re\Sigma_3^X}{\epsilon_0^e} \pm \frac{|Im\Sigma_3^X|}{2\Gamma_0^e} \right), \right. \\
 \sigma_{x/y}^Y &= \sigma^e \left( \left( \mp \frac{Re\Sigma_3^Y}{2\epsilon_0^e} \pm \frac{Re\Sigma_3^Y}{\epsilon_0^e} \mp \frac{|Im\Sigma_3^Y|}{2\Gamma_0^e} \right), \right.
 \end{aligned} \tag{D.37}$$

where  $\sigma^{h/e} = e^2 \epsilon_0^{h/e} / (2\pi\hbar) \Gamma_0^{h/e}$  is the dc conductivity in the tetragonal phase for the hole/electron pocket.

### D.3. Model parameters for FeSe and 122 systems

To perform the numerical analysis discussed in the main text we used the set of band parameters given in and self-energies corrections which reproduce the 122 and FeSe systems. The parameters of the static self-energies ( $\omega = 0$ ) used in the numerical calculation to simulated the FeSe and 122 materials in the tetragonal and nematic phases in Chapter 4 are shown in Table D.1

122		FeSe	
Tetragonal phase			
$\Sigma_{yz}^{\Gamma}$	(-15,-2)	$\Sigma_{yz}^{\Gamma}$	(-55, -4)
$\Sigma_{xz}^{\Gamma}$	(-15,-2)	$\Sigma_{xz}^{\Gamma}$	(-55, -4)
$\Sigma_{yz}^X$	(15,-2)	$\Sigma_{yz}^X$	(30, -3)
$\Sigma_{xz}^Y$	(15,-2)	$\Sigma_{xz}^Y$	(30, -3)
Nematic phase			
$\Sigma_{yz}^{\Gamma}$	(-19, -2.67)	$\Sigma_{yz}^{\Gamma}$	(-70, -4.27)
$\Sigma_{xz}^{\Gamma}$	(-11, -1.73)	$\Sigma_{xz}^{\Gamma}$	(-40, -3.73)
$\Sigma_{yz}^X$	(19, -2.67)	$\Sigma_{yz}^X$	(45, -3.5)
$\Sigma_{xz}^Y$	(11, -1.73)	$\Sigma_{xz}^Y$	(15, -2.50)

**Table D.1:** Self-energies correction parameters for FeSe and 122 system in the tetragonal and nematic phases. All the parameters are in meV.

For the 122 the nematic phase is computed with a symmetric nematic splitting of  $\Phi^h = \Phi^e = 4$  meV. For the FeSe nematic order parameter resulting in  $\Phi^h = \Phi^e = 15$  meV. We fix the background scattering to  $\delta\Gamma = 1$  meV. The scattering rates used in the tetragonal phase for 122 are  $Im\Sigma_{yz/xz}^{\Gamma} = Im\Sigma_{yz/xz}^{X/Y} = -2$  meV, while for the FeSe case we used  $Im\Sigma_{yz/xz}^{\Gamma} = -4$  meV and  $Im\Sigma_{yz/xz}^{X/Y} = -3$  meV. In both cases their variations of the imaginary part of the self-energies in the nematic phase are assumed to be proportional to the variation of their real parts, i.e.  $\Delta\Gamma^h \sim c_h(\Phi^h/Re\Sigma_0^{\Gamma})$  and  $\Delta\Gamma^e \sim c_e(\Phi^e/Re\Sigma_0^{X/Y})$  with  $c_{h/e}$  arbitrary coefficients.

# E

## Appendix Chapter 5

### E.1. Estimation of the quadratic and quartic terms of the effective action for the five-pocket model

In this Appendix we discuss how to compute the quadratic and quartic coefficients of the effective action for the five-pocket model for two cases: one with perfect circular nested Fermi surfaces and other with elliptical electron Fermi surfaces. For that purpose, in Appendix E.1.1 we first introduce the expressions for the Green's functions within the two different cases, and then, in Appendix E.1.2 we evaluate the sum over the Matsubara frequency and momentum for some relevant expressions involving the different pocket Green's functions.

#### E.1.1. Perfect circular nested and elliptical Fermi surfaces

##### *Perfect circular nested Fermi surfaces*

To make a first estimate we consider the simple case where the electron and hole pockets are perfectly nested circular Fermi surfaces. The orbital weights (as we discussed in Section B.2 in Appendix B) simply become

$$\begin{aligned} |u^\Gamma|^2 &= |u^Y|^2 = |v^X|^2 = \cos^2 \theta, \\ |v^\Gamma|^2 &= |v^Y|^2 = |u^X|^2 = \sin^2 \theta \end{aligned} \tag{E.1}$$

with  $\theta = \arctan(k_y/k_x)$ . The pocket Green's function are given by

$$\begin{cases} g_+ = g_- = g_M = g_h = (i\omega_n + \epsilon)^{-1} \\ g_X = g_Y = g_e = (i\omega_n - \epsilon)^{-1} \end{cases} \tag{E.2}$$

where  $\epsilon$  is the parabolic dispersion  $\epsilon = -\epsilon_0 + \mathbf{k}^2/2m$ , with  $\epsilon_0$  is the off-set energy with respect to the chemical potential, put conventionally to zero, and  $m$  the parabolic band mass. Eqs. E.1 and E.2 are Eqs. 5.24 and 5.25 from the main text. For a perfect nested Fermi surface, the Green's function of the system is only differentiate between the hole and electron sector, but inside each sector all the hole/electron pockets have the same energy.

### Elliptical approximation

We account for the deviations from the perfectly nested parabolic band approximation perturbatively. One can describe the ellipticity of the electronic band dispersion as

$$E^{X/Y} \simeq \epsilon \mp \delta_e \cos 2\theta_{\mathbf{k}}, \quad \delta_e = \epsilon_0 m \left( \frac{m_x - m_y}{2m_x m_y} \right), \quad (\text{E.3})$$

where  $\delta_e$  accounts for the ellipticity of the electron pocket via the  $x/y$  anisotropy of the masses with respect the parabolic band mass  $m$ . The expressions in Eqs. E.3 correctly reproduces the opposite ellipticity of the  $X/Y$  pockets. For the sake of completeness we also consider the deviation from perfect nesting due to, such as for example, a mass, offset energy, spin-orbit coupling mismatch of the hole pockets via

$$E^{\Gamma_{\pm}, M} \simeq -\epsilon + \delta_{m_{\pm}, M}, \quad \delta_{m_{\pm}, M} = \epsilon_0 \left( \frac{m_{\pm}/M - m}{m} \right). \quad (\text{E.4})$$

These perturbations can be included in the estimate of the quadratic and quartic terms of the action by expanding the Green functions for small  $\delta_e, \delta_{m_{\pm}, M}$

$$\begin{aligned} g_{\pm, M} &= g_h(1 + \delta_{m_{\pm}, M} g_h) \\ g_{X/Y} &= g_e(1 \mp \delta_e \cos(2\theta_{\mathbf{k}}) g_e). \end{aligned} \quad (\text{E.5})$$

In general we set  $\delta_{m_+} = 0$  because it is only necessary one  $\delta_m$  to differentiate the two gamma pockets, so we choose a finite  $\delta_{m_-}$ . Eqs. E.5 and E.5 are Eqs. 5.41 and 5.41 from the main text.

In principle the perturbations  $\delta_e$  and  $\delta_{m_{\pm}, M}$  affect also the angular orbital factors, which should deviate from the  $\cos \theta / \sin \theta$  expressions of Eq. E.1. However in first approximation we will neglect these modifications and we will retain only the effects of  $\delta_e$  and  $\delta_{m_{\pm}}$  on the Green's functions.

#### E.1.2. Evaluation of the sum over frequency and momenta

To compute the sum over Matsubara frequency and momenta we will use the usual decomposition

$$\sum_{\mathbf{k}} \left( \int_{\text{BZ}} \frac{d^2 \mathbf{k}}{(2\pi)^2} = \int_0^{2\pi} \frac{d\theta}{2\pi} \int d\epsilon N_F \right) \quad (\text{E.6})$$

where  $\epsilon$  is the energy,  $\theta$  the azimuthal angle  $N_F = m/2\pi$  is the density of state per spin at the Fermi level in 2D. In this way the only difference between the various models is in the angular integration of the orbital factors. Let us then discuss briefly the remaining common integrals over energy and the Matsubara sums.

Starting from the Gaussian term within the perfectly nested parabolic band approximation we need to compute the  $\Pi_{eh}$  bubble

$$\Pi_{eh} \equiv T N_F \sum_{i\omega_n} \left( \int d\epsilon g_e g_h \right) \quad (\text{E.7})$$

By performing the energy integration via the calculus of the residua of the Green functions poles we found

$$T \sum_{i\omega_n} \left( \int d\epsilon g_e g_h \right) = -2 \sum_{n \geq 0} \frac{\pi}{\omega_n} = - \sum_{n \geq 0} \frac{1}{(n + 1/2)} \quad (\text{E.8})$$

where we used that  $\omega_n = 2\pi T(n + 1/2)$ . The calculation of the above sum can be carried out in terms of Euler digamma functions

$$\psi^{(N)}(z) = (-1)^{N+1} N! \sum_{n=0}^{\infty} \left( \frac{1}{(n+z)^{N+1}} \right). \quad (\text{E.9})$$

The logarithmic divergence at the upper limit ( $\psi^{(0)}(z \gg 1) \sim \ln(z)$ ) is cut-off by the  $\omega_0$  typical energy scale of the spin mode and one gets

$$\begin{aligned} \Pi_{eh} &= -N_F \left( \psi^{(0)} \left( \frac{1}{2} + \frac{\omega_0}{2\pi T} \right) - \psi^{(0)} \left( \frac{1}{2} \right) \right) \left( \right. \\ &= -N_F \left( \ln(\omega_0/T) + \ln(2/\pi) + C_E \right) \left( \right. \\ &= -N_F \left( \ln(\omega_0/T) + \text{const} \right) \left( \right. \end{aligned} \quad (\text{E.10})$$

where we used that  $\psi^{(0)}(1/2) = -C_E - 2\ln(2)$  with  $C_E$  being the Euler-Mascheroni constant and we called  $\text{const} = \ln(2/\pi) + C_E$ .

In order to compute the quartic terms within the perfectly nested parabolic band approximation we need to compute

$$T \sum_{i\omega_n} \int d\epsilon g_e^2 g_h^2 = T \sum_{n \geq 0} \left( \frac{\pi}{\omega_n^3} \right) \quad (\text{E.11})$$

while beyond such approximation the Green functions expansion lead to:

$$\begin{aligned} T \sum_{i\omega_n} \int d\epsilon g_e^4 g_h^2 &= -T \sum_{n \geq 0} \left( \frac{\pi}{2\omega_n^5} \right) \\ T \sum_{i\omega_n} \int d\epsilon g_e^3 g_h^3 &= -T \sum_{n \geq 0} \left( \frac{3\pi}{4\omega_n^5} \right) \end{aligned} \quad (\text{E.12})$$

and analogously for the  $g_e^2 g_h^4$  case. It is easy to verify that the integrals of combination  $(g_e g_h)^{m_1} g_{e/h}^{2m_2+1}$  with odd unpaired powers of the electron/hole Green's functions vanish, since the contribution coming from Matsubara frequency with positive  $n$  exactly cancels out with the contribution of the negative ones. Using that  $\omega_n = 2\pi T(n + 1/2)$ , one can recognize in Eqs. E.11 - E.12 the Euler digamma functions, Eq. E.9 for  $z = 1/2$  and  $N = 2, 4$ . For  $z = 1/2$  one can express  $\psi^{(N)}(1/2)$  in terms of the Riemann  $\zeta(n)$  functions as

$$\psi^{(N)}(1/2) = (-1)^{N+1} N! (2^{N+1} - 1) \zeta(N+1)$$

Using these definitions in Eqs. E.11 - E.12 we obtain

$$T \sum_{i\omega_n} \left( \int d\epsilon g_e^2 g_h^2 \right) = \frac{7\zeta(3)}{8\pi^2 T^2} \equiv \mathcal{A}(T) \quad (\text{E.13})$$

$$T \sum_{i\omega_n} \left( \int d\epsilon g_e^4 g_h^2 \right) = -\frac{31\zeta(5)}{64\pi^4 T^4} \equiv \mathcal{B}(T) \quad (\text{E.14})$$

$$T \sum_{i\omega_n} \left( \int d\epsilon g_e^3 g_h^3 \right) = -\frac{93\zeta(5)}{128\pi^4 T^4} \equiv \mathcal{C}(T) \quad (\text{E.15})$$

where  $\zeta(3) \sim 1.202$  and  $\zeta(5) \sim 1.037$ .



## E.2. Magnetic and nematic couplings and order parameters: eigenvalues and eigenvectors of the quartic term of the effective action

In the present Appendix we first review in Section E.2.1 the calculation of the magnetic and nematic couplings and order parameters for the three and four-pocket models which correspond to the eigenvalues and eigenvectors of the quartic term of the effective action given in Eq. 2.29. Then, in Section E.2.2 we try to derive the magnetic and nematic order parameters and couplings for the case of the five-pocket model. We show that in this case, even for the perfect circular nested case, the definition of these quantities is not unique and the analytical calculation becomes very complex due to the higher form of the effective action matrix given in Eq. 5.11.

### E.2.1. Three and four-pockets models

#### *Eigenvalues and eigenvectors*

The quartic term matrix (Eq. 2.29) for three and four-pockets models is written as

$$A = \begin{pmatrix} u_{11} & u_{12} \\ u_{12} & u_{11} \end{pmatrix} \quad (\text{E.16})$$

Therefore the eigenvalues are given by

$$\lambda_1 = u_{11} + u_{12} \quad (\text{E.17})$$

$$\lambda_2 = u_{11} - u_{12} \quad (\text{E.18})$$

and the corresponding normalized eigenvectors are:

$$v_1 = \frac{1}{\sqrt{2}}(1, 1) \quad (\text{E.19})$$

$$v_2 = \frac{1}{\sqrt{2}}(1, -1) \quad (\text{E.20})$$

#### *New eigenvectors: magnetic and nematic order parameters*

Now we can related the old eigenvectors with the new one performing a simple change of basis. We want to get a quartic effective action of this form

$$S_{\text{eff}}^{\text{quartic}} = \begin{pmatrix} (M_X)^2 & (M_Y)^2 \end{pmatrix} \begin{pmatrix} u_{11} & u_{12} \\ u_{12} & u_{11} \end{pmatrix} \begin{pmatrix} (M_X)^2 \\ (M_Y)^2 \end{pmatrix} = \quad (\text{E.21})$$

$$= \begin{pmatrix} \psi & \phi \end{pmatrix} \begin{pmatrix} \lambda_\psi & 0 \\ 0 & \lambda_\phi \end{pmatrix} \begin{pmatrix} \psi \\ \phi \end{pmatrix} \quad (\text{E.22})$$

So, we want to get an  $S_{\text{eff}}^{\text{quartic}}$  expressed in terms of the new field  $\psi$  and  $\phi$ . With  $\lambda_\psi = \lambda_1$  and  $\lambda_\phi = \lambda_2$  and the new corresponding eigenvectors  $\psi$  and  $\phi$ . The change of basis matrix will be just the matrix with the normalized old eigenvectors as columns so

$$\begin{pmatrix} \frac{1}{\sqrt{2}} & 1 & 1 \\ & 1 & -1 \end{pmatrix} \begin{pmatrix} (M_X)^2 \\ (M_Y)^2 \end{pmatrix} = \begin{pmatrix} \psi \\ \phi \end{pmatrix} \quad (\text{E.23})$$

So we get the new eigenvectors with is corresponding eigenvalues are:

$$\psi = \frac{1}{\sqrt{2}} \left( (M_X)^2 + (M_Y)^2 \right), \left( \begin{array}{l} \lambda_\psi = u_{11} + u_{12} \end{array} \right. \quad (\text{E.24})$$

$$\phi = \frac{1}{\sqrt{2}} \left( (M_X)^2 - (M_Y)^2 \right), \left( \begin{array}{l} \lambda_\phi = u_{11} - u_{12} \end{array} \right. \quad (\text{E.25})$$

$$(\text{E.26})$$

where we can call  $\psi$  the magnetic and  $\phi$  the nematic order parameters and  $\lambda_\psi$  and  $\lambda_\phi$  the magnetic and nematic couplings.

### E.2.2. Five pockets model

In this Section we try to perform the same procedure than for the three and four-pocket models to obtain the magnetic and nematic order parameters and couplings.

#### *Eigenvalues and eigenvectors*

The quartic term matrix (Eq. 5.11) for the five pocket model is given by

$$A = \begin{pmatrix} u_{11} & u_{12} & 0 & k_{12} \\ u_{12} & u_{11} & k_{12} & 0 \\ 0 & k_{12} & \tilde{u}_{11} & \tilde{u}_{12} \\ k_{12} & 0 & \tilde{u}_{12} & \tilde{u}_{11} \end{pmatrix} \left( \begin{array}{l} \end{array} \right) \quad (\text{E.27})$$

The general form for the eigenvalues for the five pocket case is given by

$$\begin{aligned} \lambda_1 &= \frac{1}{2}(u_{11} + u_{12} + \tilde{u}_{11} + \tilde{u}_{12}) - \\ &\quad - \sqrt{\left( (u_{11} + u_{12} + \tilde{u}_{11} + \tilde{u}_{12})^2 + 4[k_{12}^2 - (u_{11} + u_{12})(\tilde{u}_{11} + \tilde{u}_{12})] \right)} \\ \lambda_2 &= \frac{1}{2}(u_{11} - u_{12} + \tilde{u}_{11} - \tilde{u}_{12}) - \\ &\quad - \sqrt{\left( (u_{11} - u_{12} + \tilde{u}_{11} - \tilde{u}_{12})^2 + 4[k_{12}^2 - (u_{11} - u_{12})(\tilde{u}_{11} - \tilde{u}_{12})] \right)} \\ \lambda_3 &= \frac{1}{2}(u_{11} + u_{12} + \tilde{u}_{11} + \tilde{u}_{12}) + \\ &\quad + \sqrt{\left( (u_{11} + u_{12} + \tilde{u}_{11} + \tilde{u}_{12})^2 + 4[k_{12}^2 - (u_{11} + u_{12})(\tilde{u}_{11} + \tilde{u}_{12})] \right)} \\ \lambda_4 &= \frac{1}{2}(u_{11} - u_{12} + \tilde{u}_{11} - \tilde{u}_{12}) + \\ &\quad + \sqrt{\left( (u_{11} - u_{12} + \tilde{u}_{11} - \tilde{u}_{12})^2 + 4[k_{12}^2 - (u_{11} - u_{12})(\tilde{u}_{11} - \tilde{u}_{12})] \right)} \end{aligned} \quad (\text{E.28})$$

As we can see the definition for the eigenvalues of the quartic term acquires a very complex structure and it is very difficult to define in a proper way the corresponding eigenvectors. To gain insight into the problem we analyse down below a perfect nested case and try to compute the eigenvectors of the five-pocket system.

### Perfect nested parabolic band approximation

For the perfect case we have  $u_{12}^0 = 0$  and  $u_{11} = \tilde{u}_{11}$ ,  $k_{12} = \tilde{u}_{12}$ , so that the eigenvalues given by Eq. E.28 slightly simplify and the computation of the corresponding eigenvectors can be treated analytically.

#### Eigenvalues and eigenvectors

The eigenvalues in Eq. E.28 simplify as

$$\begin{aligned}\lambda_1^0 &= u_{11} + \frac{1}{2}(1 - \sqrt{5})\tilde{u}_{12} = \frac{N_F}{16}c_1 \mathcal{A}(T) \\ \lambda_2^0 &= u_{11} - \frac{1}{2}(1 + \sqrt{5})\tilde{u}_{12} = \frac{N_F}{16}c_2 \mathcal{A}(T) \\ \lambda_3^0 &= u_{11} + \frac{1}{2}(1 + \sqrt{5})\tilde{u}_{12} = \frac{N_F}{16}c_3 \mathcal{A}(T) \\ \lambda_4^0 &= u_{11} - \frac{1}{2}(1 - \sqrt{5})\tilde{u}_{12} = \frac{N_F}{16}c_4 \mathcal{A}(T)\end{aligned}\quad (\text{E.29})$$

with  $\mathcal{A}(T) = \frac{7\zeta(3)}{8\pi^2 T^2}$  defined in Eq. E.13 and  $c_1 = (7 + \sqrt{5})$ ,  $c_2 = (5 + \sqrt{5})$ ,  $c_3 = (7 - \sqrt{5})$ ,  $c_4 = (5 - \sqrt{5})$  where  $c_i > 0$  with  $i = \{1, 2, 3, 4\}$ .

The corresponding normalized eigenvectors are

$$v_1 = \frac{1}{\sqrt{5 - \sqrt{5}}} \left( \frac{1}{2}(\sqrt{5} - 1), \frac{1}{2}(\sqrt{5} - 1), 1, 1 \right) = \frac{1}{A}(a, a, 1, 1) \quad (\text{E.30})$$

$$v_2 = \frac{1}{\sqrt{5 + \sqrt{5}}} \left( \frac{1}{2}(\sqrt{5} + 1), -\frac{1}{2}(\sqrt{5} + 1), -1, 1 \right) = \frac{1}{B}(b, -b, -1, 1) \quad (\text{E.31})$$

$$v_3 = \frac{1}{\sqrt{5 + \sqrt{5}}} \left( -\frac{1}{2}(\sqrt{5} + 1), -\frac{1}{2}(\sqrt{5} + 1), 1, 1 \right) = \frac{1}{B}(-b, b, 1, 1) \quad (\text{E.32})$$

$$v_4 = \frac{1}{\sqrt{5 - \sqrt{5}}} \left( -\frac{1}{2}(\sqrt{5} - 1), \frac{1}{2}(\sqrt{5} - 1), -1, 1 \right) = \frac{1}{A}(-a, a, -1, 1) \quad (\text{E.33})$$

with  $A = \sqrt{5 - \sqrt{5}}$ ,  $a = \frac{1}{2}(\sqrt{5} - 1)$  and  $B = \sqrt{5 + \sqrt{5}}$ ,  $b = \frac{1}{2}(\sqrt{5} + 1)$ . It is very interesting to realize that  $a/A = 1/B$  and  $b/B = 1/A$ , so we will use that fact in the next section.

#### New eigenvectors: magnetic and nematic order parameters

Now we can relate the old eigenvectors with the new one performing a simple change of basis. We want to get a quartic effective action of this form:

$$\begin{aligned}S_{\text{eff}}^{\text{quartic}} &= \begin{pmatrix} (M_X)^2 & (M_Y)^2 & (\tilde{M}_X)^2 & (\tilde{M}_Y)^2 \end{pmatrix} \begin{pmatrix} u_{11} & u_{12} & 0 & k_{12} \\ u_{12} & u_{11} & k_{12} & 0 \\ 0 & k_{12} & \tilde{u}_{11} & \tilde{u}_{12} \\ k_{12} & 0 & \tilde{u}_{12} & \tilde{u}_{11} \end{pmatrix} \begin{pmatrix} (M_X)^2 \\ (M_Y)^2 \\ (\tilde{M}_X)^2 \\ (\tilde{M}_Y)^2 \end{pmatrix} \\ &= \begin{pmatrix} \rho_1 & \rho_2 & \rho_3 & \rho_4 \end{pmatrix} \begin{pmatrix} \lambda_1 & 0 & 0 & 0 \\ 0 & \lambda_2 & 0 & 0 \\ 0 & 0 & \lambda_3 & 0 \\ 0 & 0 & 0 & \lambda_4 \end{pmatrix} \begin{pmatrix} \rho_1 \\ \rho_2 \\ \rho_3 \\ \rho_4 \end{pmatrix} \quad (\text{E.34})\end{aligned}$$

So, we want to get an  $S_{\text{eff}}^{\text{quartic}}$  expressed in terms of the new fields  $\rho_i$  with  $i = \{1, 2, 3, 4\}$ .

The change of basis matrix will be just the matrix with the normalized old eigenvectors as columns so

$$\frac{1}{A} \begin{pmatrix} a & 1 & -1 & -a \\ a & -1 & -1 & a \\ 1 & -a & a & -1 \\ 1 & a & a & 1 \end{pmatrix} \begin{pmatrix} (M_X)^2 \\ (M_Y)^2 \\ (\widetilde{M}_X)^2 \\ (\widetilde{M}_Y)^2 \end{pmatrix} = \begin{pmatrix} \rho_1 \\ \rho_2 \\ \rho_3 \\ \rho_4 \end{pmatrix} \quad (\text{E.35})$$

where we use the relation between the normalization and the coefficients  $a/A = 1/B$  and  $b/B = 1/A$  and with  $A = \sqrt{5 - \sqrt{5}}$  and  $a = \frac{1}{2}(\sqrt{5} - 1)$ .

The new eigenvectors are:

$$\rho_1 = \frac{1}{A} \left[ \left( a(M_X)^2 + (M_Y)^2 \right) - \left( (\widetilde{M}_X)^2 + a(\widetilde{M}_Y)^2 \right) \right] \quad (\text{E.36})$$

$$\rho_2 = \frac{1}{A} \left[ \left( a(M_X)^2 - (M_Y)^2 \right) - \left( (\widetilde{M}_X)^2 - a(\widetilde{M}_Y)^2 \right) \right] \quad (\text{E.37})$$

$$\rho_3 = \frac{1}{A} \left[ \left( (M_X)^2 - a(M_Y)^2 \right) + \left( a(\widetilde{M}_X)^2 - (\widetilde{M}_Y)^2 \right) \right] \quad (\text{E.38})$$

$$\rho_4 = \frac{1}{A} \left[ \left( (M_X)^2 + a(M_Y)^2 \right) + \left( a(\widetilde{M}_X)^2 + (\widetilde{M}_Y)^2 \right) \right] \quad (\text{E.39})$$

As we can see from Eq. E.39 there are many forms to "regroup" the different terms to get a magnetic and nematic vectors. Therefore, even for the perfect circular nested case, the definition of the magnetic and nematic order parameters is not unique. The form to define in a proper way the order parameters and couplings is an open problem that we are going to analyse in depth in the near future.

### E.3. Parameters for the quantitative analysis for the $\Gamma$ -XY and MXY models

We consider the same band-structure parameters than in Ref. [27], which are appropriate for 122 iron-based compounds e.g.  $BaFe_2As_2$ . For the spin fluctuations we refer to [67] and use  $\omega_0 \sim 18meV$ .

To compute the static  $q=0$  magnetic susceptibilities  $\chi^{\Gamma-XY^{-1}}$  and  $\tilde{\chi}^{MXY^{-1}}$ , Eq. 5.53 and 5.59 respectively from the main text, we need first consider the difference in Néel temperatures,  $T_N$ , for the two the three-pocket models,  $\Gamma$ -XY and MXY. To determine the Néel temperature we need the value of the low-energy coupling  $\tilde{U}$ . We choose this value in order to reproduce, within the  $\Gamma$ -XY model, the experimental value  $T_N^{\Gamma-XY} = 110K$  found for weakly doped  $BaFe_2As_2$  compounds [29]. Keeping then all the parameters fixed we can estimate  $N_F \tilde{U}$  and use this value to compute the  $T_N$  for the MXY model. In this way we get that  $T_N^{MXY} = 132K$ .

For the band structure we choose again parameters appropriate for weakly-doped 122 compounds: we set  $\epsilon_0 = 90meV$  and  $1/(2m) \sim 60meV$ , ( $N_F \sim 1.3eV^{-1}$ ) for the perfect parabolic case. With these parameters we have circular Fermi pockets of radius  $k_F^0 \sim 0.31$  in  $\pi/a$  unit, with  $a \sim 3.96A$  the lattice parameter. Then, beyond the parabolic-band approximation we further consider the ellipticity of the electron pockets assuming  $\delta_e = 0.55\epsilon_0$ . This define electronic elliptical Fermi pockets with  $k_F^{x/y} \sim 0.39$  and  $k_F^{y/x} \sim 0.21$  for the X/Y pockets respectively.

# Bibliography

- [1] H. Kamerlingh Onnes. *Comm. Phys.*, 29, 1911.
- [2] W. Meissner and R. Ochsenfeld. Ein neuer effekt bei eintritt der supraleitfähigkeit. *Naturwissenschaften*, 21:787–788, 1933. doi:[10.1007/BF01504252](https://doi.org/10.1007/BF01504252).
- [3] J. Schmalian. Failed theories of superconductivity. *Modern Physics Letters B*, 24:2679–2691, 2010. doi:[10.1142/S0217984910025280](https://doi.org/10.1142/S0217984910025280).
- [4] J. Bardeen, L. N. Cooper, and J. R. Schrieffer. Microscopic theory of superconductivity. *Phys. Rev.*, 106:162–164, 1957. doi:[10.1103/PhysRev.106.162](https://doi.org/10.1103/PhysRev.106.162).
- [5] J. Bardeen, L. N. Cooper, and J. R. Schrieffer. Theory of superconductivity. *Phys. Rev.*, 108:1175–1204, 1957. doi:[10.1103/PhysRev.108.1175](https://doi.org/10.1103/PhysRev.108.1175).
- [6] F. Steglich, J. Aarts, C. D. Bredl, W. Lieke, D. Meschede, W. Franz, and H. Schafer. Superconductivity in the presence of strong pauli paramagnetism:  $CeCu_2Si_2$ . *Phys. Rev. Lett.*, 43:1892–1896, 1979. doi:[10.1103/PhysRevLett.43.1892](https://doi.org/10.1103/PhysRevLett.43.1892).
- [7] J. Georg Bednorz and K. Alex Muller. Possible high  $T_c$  superconductivity in the  $Ba - La - Cu - O$  system. *Z. Physik B - Condensed Matter*, 64:189–193, 1986. doi:[10.1007/BF01303701](https://doi.org/10.1007/BF01303701).
- [8] M. K. Wu, J. R. Ashburn, C. J. Torng, P. H. Hor, R. L. Meng, L. Gao, Z. J. Huang, Y. Q. Wang, and C. W. Chu. Superconductivity at 93 K in a new mixed-phase  $Y - Ba - Cu - O$  compound system at ambient pressure. *Phys. Rev. Lett.*, 58:908–910, 1987. doi:[10.1103/PhysRevLett.58.908](https://doi.org/10.1103/PhysRevLett.58.908).
- [9] Hai-Hu Wen and Shiliang Li. Materials and novel superconductivity in iron pnictide superconductors. *Annual Review of Condensed Matter Physics*, 2(1):121–140, 2011. doi:[10.1146/annurev-conmatphys-062910-140518](https://doi.org/10.1146/annurev-conmatphys-062910-140518).
- [10] G. R. Stewart. Superconductivity in iron compounds. *Rev. Mod. Phys.*, 83:1589–1652, 2011. doi:[10.1103/RevModPhys.83.1589](https://doi.org/10.1103/RevModPhys.83.1589).
- [11] D. C. Johnston. The puzzle of high temperature superconductivity in layered iron pnictides and chalcogenides. *Advances in Physics*, 59:803–1061, 2010. doi:[10.1080/00018732.2010.513480](https://doi.org/10.1080/00018732.2010.513480).
- [12] Y. Kamihara, T. Watanabe, M. Hirano, and H. Hosono. Iron based layered superconductor  $LaO_{1-x}F_xFeAs$   $x = 0.05 - 0.12$  with  $T_c = 26K$ . *Journal of the American Chemical Society*, 130:3296–3297, 2008. doi:[10.1021/ja800073m](https://doi.org/10.1021/ja800073m).
- [13] H. Takahashi, K. Igawa, K. Arii, Y. Kamihara, M. Hirano, and H. Hosono. Superconductivity at 43 K in an iron-based layered compound  $LaO_{1-x}F_xFeAs$ . *Nature*, 430:376–378, 2008. doi:[10.1038/nature06972](https://doi.org/10.1038/nature06972).
- [14] P. J. Ray. Structural investigation of  $La(2 - x)Sr(x)CuO(4 + y)$  - following staging as a function of temperature. 2016. doi:[10.6084/m9.figshare.2075680.v2](https://doi.org/10.6084/m9.figshare.2075680.v2).

- [15] A. Chubukov and P. Hirschfeld. Iron-based superconductors, seven years later. *Physics Today*, 68:46–52, 2015. doi:[10.1063/PT.3.2818](https://doi.org/10.1063/PT.3.2818).
- [16] S. Lebegue. Electronic structure and properties of the fermi surface of the superconductor  $LaOFeP$ . *Phys. Rev. B*, 75:035110, 2007. doi:[10.1103/PhysRevB.75.035110](https://doi.org/10.1103/PhysRevB.75.035110).
- [17] D. J. Singh and M.-H. Du. Density functional study of  $LaFeAsO_{1-x}F_x$ : A low carrier density superconductor near itinerant magnetism. *Phys. Rev. Lett.*, 100:237003, 2008. doi:[10.1103/PhysRevLett.100.237003](https://doi.org/10.1103/PhysRevLett.100.237003).
- [18] C. Cao, P. J. Hirschfeld, and H. P. Cheng. Proximity of antiferromagnetism and superconductivity in  $LaFeAsO_{1-x}F_x$ : Effective hamiltonian from ab initio studies. *Phys. Rev. B*, 77:220506, 2008. doi:[10.1103/PhysRevB.77.220506](https://doi.org/10.1103/PhysRevB.77.220506).
- [19] I. I. Mazin, D. J. Singh, M. D. Johannes, and M. H. Du. Unconventional superconductivity with a sign reversal in the order parameter of  $LaFeAsO_{1-x}F_x$ . *Phys. Rev. Lett.*, 101:057003, 2008. doi:[10.1103/PhysRevLett.101.057003](https://doi.org/10.1103/PhysRevLett.101.057003).
- [20] K. Kuroki, S. Onari, R. Arita, H. Usui, Y. Tanaka, H. Kontani, and H. Aoki. Unconventional pairing originating from the disconnected fermi surfaces of superconducting  $LaFeAsO_{1-x}F_x$ . *Phys. Rev. Lett.*, 101:087004, 2008. doi:[10.1103/PhysRevLett.101.087004](https://doi.org/10.1103/PhysRevLett.101.087004).
- [21] Z.-R. Ye, Y. Zhang, B.-P. Xie, and D.-L. Feng. Angle-resolved photoemission spectroscopy study on iron-based superconductors. *Chinese Physics B*, 22(8), 20013. doi:[10.1088/1674-1056/22/8/087407](https://doi.org/10.1088/1674-1056/22/8/087407).
- [22] E. Bascones, B. Valenzuela, and M. J. Calderón. Magnetic interactions in iron superconductors: A review. *Comptes Rendus Physique*, 17:36–39, 2016. doi:[10.1016/j.crhy.2015.05.004](https://doi.org/10.1016/j.crhy.2015.05.004).
- [23] R. M. Fernandes, A. V. Chubukov, and J. Schmalian. What drives nematic order in iron-based superconductors? *Nature Phys*, 10:97–104, 2014. doi:[10.1038/nphys2877](https://doi.org/10.1038/nphys2877).
- [24] A. Kreisel, P. J. Hirschfeld, and Brian M. Andersen. On the remarkable superconductivity of fese and its close cousins. *Symmetry*, 12, 20020. doi:[10.3390/sym12091402](https://doi.org/10.3390/sym12091402).
- [25] R. M Fernandes and A. V. Chubukov. Low-energy microscopic models for iron-based superconductors: a review. *Reports on Progress in Physics*, 80:014503, 2016. doi:[10.1088/1361-6633/80/1/014503](https://doi.org/10.1088/1361-6633/80/1/014503).
- [26] Laura Fanfarillo, Alberto Cortijo, and Belén Valenzuela. Spin-orbital interplay and topology in the nematic phase of iron pnictides. *Phys. Rev. B*, 91:214515, 2015. doi:[10.1103/PhysRevB.91.214515](https://doi.org/10.1103/PhysRevB.91.214515).
- [27] Laura Fanfarillo, Lara Benfatto, and Belén Valenzuela. Orbital mismatch boosting nematic instability in iron-based superconductors. *Phys. Rev. B*, 97:121109, 2018. doi:[10.1103/PhysRevB.97.121109](https://doi.org/10.1103/PhysRevB.97.121109).

- 
- [28] R. M. Fernandes, A. V. Chubukov, J. Knolle, I. Eremin, and J. Schmalian. Preemptive nematic order, pseudogap, and orbital order in the iron pnictides. *Phys. Rev. B*, 85:024534, 2012. doi:[10.1103/PhysRevB.85.024534](https://doi.org/10.1103/PhysRevB.85.024534).
  - [29] J. Paglione and R. Greene. High-temperature superconductivity in iron-based materials. *Nature Phys*, 6:645–658, 2010. doi:[10.1038/nphys1759](https://doi.org/10.1038/nphys1759).
  - [30] H. Luetkens, H.H. Klauss, M. Kraken, F. J. Litterst, T. Dellmann, R. Klingeler, C. Hess, R. Khasanov, A. Amato, C. Baines, M. Kosmala, O. J. Schumann, M. Braden, J. Hamann-Borrero, N. Leps, A. Kondrat, G. Behr, J. Werner, and B. Buchner. The electronic phase diagram of the  $LaO_{1-x}F_xFeAs$  superconductor. *Nature*, 8:305–309, 2009. doi:[10.1038/nmat2397](https://doi.org/10.1038/nmat2397).
  - [31] S. Kasahara, H. J. Shi, K. Hashimoto, S. Tonegawa, Y. Mizukami, T. Shibauchi, K. Sugimoto, T. Fukuda, T. Terashima, Andriy H. Nevidomskyy, and Y. Matsuda. Electronic nematicity above the structural and superconducting transition in  $BaFe_2(As_{1-x}P_x)_2$ . *Nature*, 486:382–385, 2012. doi:[10.1038/nature11178](https://doi.org/10.1038/nature11178).
  - [32] A. I. Coldea and M. D. Watson. The key ingredients of the electronic structure of  $FeSe$ . *Annual Review of Condensed Matter Physics*, 9:125–146, 2018. doi:[10.1146/annurev-conmatphys-033117-054137](https://doi.org/10.1146/annurev-conmatphys-033117-054137).
  - [33] P. Dai. Antiferromagnetic order and spin dynamics in iron-based superconductors. *Rev. Mod. Phys.*, 87:855–896, 2015. doi:[10.1103/RevModPhys.87.855](https://doi.org/10.1103/RevModPhys.87.855).
  - [34] P J Hirschfeld, M M Korshunov, and I I Mazin. Gap symmetry and structure of fe-based superconductors. *Reports on Progress in Physics*, 74:124508, 2011. doi:[10.1088/0034-4885/74/12/124508](https://doi.org/10.1088/0034-4885/74/12/124508).
  - [35] H. Eschrig and K. Koepernik. Tight-binding models for the iron-based superconductors. *Phys. Rev. B*, 80:104503, 2009. doi:[10.1103/PhysRevB.80.104503](https://doi.org/10.1103/PhysRevB.80.104503).
  - [36] M. H. Christensen, R. M. Fernandes, and A. V. Chubukov. Orbital transmutation and the electronic spectrum of  $FeSe$  in the nematic phase. *Phys. Rev. Research*, 2:013015, 2020. doi:[10.1103/PhysRevResearch.2.013015](https://doi.org/10.1103/PhysRevResearch.2.013015).
  - [37] A. I. Coldea, J. D. Fletcher, A. Carrington, J. G. Analytis, A. F. Bangura, J.-H. Chu, A. S. Erickson, I. R. Fisher, N. E. Hussey, and R. D. McDonald. Fermi surface of superconducting  $LaFePO$  determined from quantum oscillations. *Phys. Rev. Lett.*, 101:216402, 2008. doi:[10.1103/PhysRevLett.101.216402](https://doi.org/10.1103/PhysRevLett.101.216402).
  - [38] S. E. Sebastian, J. Gillett, N. Harrison, P. H. C. Lau, D. J. Singh, C. H. Mielke, and G. G. Lonzarich. Quantum oscillations in the parent magnetic phase of an iron arsenide high temperature superconductor. *Journal of Physics: Condensed Matter*, 20:422203, 2008. doi:[10.1088/0953-8984/20/42/422203](https://doi.org/10.1088/0953-8984/20/42/422203).
  - [39] A. I. Coldea. Quantum oscillations probe the normal electronic states of novel superconductors. *Phil. Trans. R. Soc. A.*, 368:3503–3517, 2010. doi:[10.1098/rsta.2010.0089](https://doi.org/10.1098/rsta.2010.0089).
  - [40] J. G. Analytis, C. M. J. Andrew, A. I. Coldea, A. McCollam, J.-H. Chu, R. D. McDonald, I. R. Fisher, and A. Carrington. Fermi surface of  $SrFe_2P_2$  determined



- by the de Haas – van Alphen effect. *Phys. Rev. Lett.*, 103:076401, 2009. doi:[10.1103/PhysRevLett.103.076401](https://doi.org/10.1103/PhysRevLett.103.076401).
- [41] H. Shishido, A. F. Bangura, A. I. Coldea, S. Tonegawa, K. Hashimoto, S. Kasahara, P. M. C. Rourke, H. Ikeda, T. Terashima, R. Settai, Y. Ōnuki, D. Vignolles, C. Proust, B. Vignolle, A. McCollam, Y. Matsuda, T. Shibauchi, and A. Carrington. Evolution of the fermi surface of  $BaFe_2(As_{1-x}P_x)_2$  on entering the superconducting dome. *Phys. Rev. Lett.*, 104:057008, 2010. doi:[10.1103/PhysRevLett.104.057008](https://doi.org/10.1103/PhysRevLett.104.057008).
- [42] T. Terashima, N. Kurita, M. Tomita, K. Kihou, C. Lee, Y. Tomioka, T. Ito, A. Iyo, H. Eisaki, T. Liang, M. Nakajima, S. Ishida, S. Uchida, H. Harima, and S. Uji. Complete fermi surface in  $BaFe_2As_2$  observed via Shubnikov – de Haas oscillation measurements on detwinned single crystals. *Phys. Rev. Lett.*, 107:176402, 2011. doi:[10.1103/PhysRevLett.107.176402](https://doi.org/10.1103/PhysRevLett.107.176402).
- [43] S. E. Sebastian. Quantum oscillations in iron pnictide superconductors. *Magnetism and Superconductivity: from Cuprates to Iron-Pnictides*, Chapter 4, 2012. doi:[arxiv.org/abs/1208.5862](https://doi.org/10.1103/PhysRevLett.107.176402).
- [44] C. Putzke, A. I. Coldea, I. Guillamon, D. Vignolles, A. McCollam, D. LeBoeuf, M. D. Watson, I. I. Mazin, S. Kasahara, T. Terashima, T. Shibauchi, Y. Matsuda, and A. Carrington. de haas–van alphen study of the fermi surfaces of superconducting lifep and lifeas. *Phys. Rev. Lett.*, 108:047002, 2012. doi:[10.1103/PhysRevLett.108.047002](https://doi.org/10.1103/PhysRevLett.108.047002).
- [45] H. Ding, P. Richard, K. Nakayama, K. Sugawara, T. Arakane, Y. Sekiba, A. Takayama, S. Souma, T. Sato, T. Takahashi, Z. Wang, X. Dai, Z. Fang, G. F. Chen, J. L. Luo, and N. L. Wang. Observation of Fermi-surface-dependent nodeless superconducting gaps in  $Ba_{0.6}K_{0.4}Fe_2As_2$ . *EPL (Europhysics Letters)*, 83:47001, 2008. doi:[10.1209/0295-5075/83/47001](https://doi.org/10.1209/0295-5075/83/47001).
- [46] D. H. Lu, M. Yi, S.-K. Mo, A. S. Erickson, J. Analytis, J.-H. Chu, D. J. Singh, Z. Hussain, T. H. Geballe, I. R. Fisher, and Z. X. Shen. Electronic structure of the iron-based superconductor  $LaOFeP$ . *Nature*, 455:81–84, 2008. doi:[10.1038/nature07263](https://doi.org/10.1038/nature07263).
- [47] L. Wray, D. Qian, D. Hsieh, Y. Xia, L. Li, J. G. Checkelsky, A. Pasupathy, K. K. Gomes, C. V. Parker, A. V. Fedorov, G. F. Chen, J. L. Luo, A. Yazdani, N. P. Ong, N. L. Wang, and M. Z. Hasan. Momentum dependence of superconducting gap, strong-coupling dispersion kink, and tightly bound cooper pairs in the high- $T_c$   $(Sr, Ba)_{1-x}(K, Na)_xFe_2As_2$  superconductors. *Phys. Rev. B*, 78:184508, Nov 2008. doi:[10.1103/PhysRevB.78.184508](https://doi.org/10.1103/PhysRevB.78.184508).
- [48] T. Kondo, A. F. Santander-Syro, O. Copie, C. Liu, M. E. Tillman, E. D. Mun, J. Schmalian, S. L. Bud’ko, M. A. Tanatar, P. C. Canfield, and A. Kaminski. Momentum dependence of the superconducting gap in  $NdFeAsO_{0.9}F_{0.1}$  single crystals measured by angle resolved photoemission spectroscopy. *Phys. Rev. Lett.*, 101:147003, 2008. doi:[10.1103/PhysRevLett.101.147003](https://doi.org/10.1103/PhysRevLett.101.147003).
- [49] L. X. Yang, Y. Zhang, H. W. Ou, J. F. Zhao, D. W. Shen, B. Zhou, J. Wei, F. Chen, M. Xu, C. He, Y. Chen, Z. D. Wang, X. F. Wang, T. Wu, G. Wu, X. H. Chen,



- M. Arita, K. Shimada, M. Taniguchi, Z. Y. Lu, T. Xiang, and D. L. Feng. Electronic structure and unusual exchange splitting in the spin-density-wave state of the  $BaFe_2As_2$  parent compound of iron-based superconductors. *Phys. Rev. Lett.*, 102:107002, 2009. doi:[10.1103/PhysRevLett.102.107002](https://doi.org/10.1103/PhysRevLett.102.107002).
- [50] H Ding, K Nakayama, P Richard, S Souma, T Sato, T Takahashi, M Neupane, Y-M Xu, Z-H Pan, A V Fedorov, Z Wang, X Dai, Z Fang, G F Chen, J L Luo, and N L Wang. Electronic structure of optimally doped pnictide  $Ba_{0.6}K_{0.4}Fe_2As_2$ : a comprehensive angle-resolved photoemission spectroscopy investigation. *Journal of Physics: Condensed Matter*, 23(13):135701, 2011. doi:[10.1088/0953-8984/23/13/135701](https://doi.org/10.1088/0953-8984/23/13/135701).
- [51] V. Brouet, M. Marsi, B. Mansart, A. Nicolaou, A. Taleb-Ibrahimi, P. Le Fèvre, F. Bertran, F. Rullier-Albenque, A. Forget, and D. Colson. Nesting between hole and electron pockets in  $Ba(Fe_{1-x}Co_x)_2As_2$  ( $x = 0 - 0.3$ ) observed with angle-resolved photoemission. *Phys. Rev. B*, 80:165115, 2009. doi:[10.1103/PhysRevB.80.165115](https://doi.org/10.1103/PhysRevB.80.165115).
- [52] M. Sunagawa, T. Ishiga, K. Tsubota, T. Jabuchi, J. Sonoyama, K. Iba, K. Kudo, M. Nohara, K. Ono, H. Kumigashira, T. Matsushita, M. Arita, K. Shimada, H. Namatame, M. Taniguchi, T. Wakita, Y. Muraoka, and T. Yokoya. Characteristic two-dimensional fermi surface topology of high- $T_c$  iron-based superconductors. *Sci Rep*, 4:4381, 2015. doi:[10.1038/srep04381](https://doi.org/10.1038/srep04381).
- [53] K. Terashima, Y. Sekiba, J. H. Bowen, K. Nakayama, T. Kawahara, T. Sato, P. Richard, Y.-M. Xu, L. J. Li, G. H. Cao, Z.-A. Xu, H. Ding, and T. Takahashi. Fermi surface nesting induced strong pairing in iron-based superconductors. *PNAS*, 106:7330–7333, 2009. doi:[10.1073/pnas.0900469106](https://doi.org/10.1073/pnas.0900469106).
- [54] S. V. Borisenko, V. B. Zabolotnyy, D. V. Evtushinsky, T. K. Kim, I. V. Morozov, A. N. Yaresko, A. A. Kordyuk, G. Behr, A. Vasiliev, R. Follath, and B. Buchner. Superconductivity without nesting in lifeas. *Phys. Rev. Lett.*, 105:067002, 2010. doi:[10.1103/PhysRevLett.105.067002](https://doi.org/10.1103/PhysRevLett.105.067002).
- [55] J. Malet, V. B. Zabolotnyy, D. V. Evtushinsky, S. Thirupathaiah, A. U. B. Wolter, L. Harnagea, A. N. Yaresko, A. N. Vasiliev, D. A. Chareev, A. E. Böhmer, F. Hardy, T. Wolf, C. Meingast, E. D. L. Rienks, B. Büchner, and S. V. Borisenko. Unusual band renormalization in the simplest iron-based superconductor  $FeSe_{1-x}$ . *Phys. Rev. B*, 89:220506, 2014. doi:[10.1103/PhysRevB.89.220506](https://doi.org/10.1103/PhysRevB.89.220506).
- [56] A. Tamai, A. Y. Ganin, E. Rozbicki, J. Bacsá, W. Meevasana, P. D. C. King, M. Caffio, R. Schaub, S. Margadonna, K. Prassides, M. J. Rosseinsky, and F. Baumberger. Strong electron correlations in the normal state of the iron-based  $FeSe_{0.42}Te_{0.58}$  superconductor observed by angle-resolved photoemission spectroscopy. *Phys. Rev. Lett.*, 104:097002, 2010. URL: <https://link.aps.org/doi/10.1103/PhysRevLett.104.097002>, doi:[10.1103/PhysRevLett.104.097002](https://doi.org/10.1103/PhysRevLett.104.097002).
- [57] L. de’ Medici. Weak and strong correlations in fe superconductors. *Springer, Cham*, 211, 2015. doi:[10.1007/978-3-319-11254-1\\_11](https://doi.org/10.1007/978-3-319-11254-1_11).
- [58] L. Fanfarillo and E. Bascones. Electronic correlations in hund metals. *Phys. Rev. B*, 92:075136, 2015. doi:[10.1103/PhysRevB.92.075136](https://doi.org/10.1103/PhysRevB.92.075136).

- [59] A.I. Coldea, S.F. Blake, S. Kasahara, Amir A. H., Matthew D. W., William K., Eun S. C., Alix M., Pascal R., Takuya Y., Mara B., Susannah C. S., Yuji M., Thomas W., Takasada S., and Andrew J. S. Evolution of the low-temperature fermi surface of superconducting  $FeSe_{1-x}S_x$  across a nematic phase transition. *npj Quant Mater*, 4, 2019. doi:10.1038/s41535-018-0141-0.
- [60] L. Fanfarillo, J. Mansart, P. Toulemonde, H. Cercellier, P. Le Fèvre, F. Bertran, B. Valenzuela, L. Benfatto, and V. Brouet. Orbital-dependent *Fermi* surface shrinking as a fingerprint of nematicity in  $FeSe$ . *Phys. Rev. B*, 94:155138, 2016. doi:10.1103/PhysRevB.94.155138.
- [61] L. Ortenzi, E. Cappelluti, L. Benfatto, and L. Pietronero. Fermi-surface shrinking and interband coupling in iron-based pnictides. *Phys. Rev. Lett.*, 103:046404, 2009. doi:10.1103/PhysRevLett.103.046404.
- [62] S. Bhattacharyya, K. Bjornson, K. Zantout, D. Steffensen, L. Fanfarillo, A. Kreisel, R. Valent, B. M. Andersen, and P. J. Hirschfeld. Nonlocal correlations in iron pnictides and chalcogenides. *Phys. Rev. B*, 102:035109, 2020. doi:10.1103/PhysRevB.102.035109.
- [63] P. Dai, J. Hu, and E. Dagotto. Magnetism and its microscopic origin in iron-based high-temperature superconductors. *Nature Phys*, 8:709–718, 2012. doi:10.1038/nphys2438.
- [64] G. Li, W. Z. Hu, J. Dong, Z. Li, P. Zheng, G. F. Chen, J. L. Luo, and N. L. Wang. Probing the superconducting energy gap from infrared spectroscopy on a  $Ba_{0.6}K_{0.4}Fe_2As_2$  single crystal with  $T_c = 37K$ . *Phys. Rev. Lett.*, 101:107004, 2008. doi:10.1103/PhysRevLett.101.107004.
- [65] D. V. Evtushinsky, D. S. Inosov, V. B. Zabolotnyy, A. Koitzsch, M. Knupfer, B. Buchner, M. S. Viazovska, G. L. Sun, V. Hinkov, A. V. Boris, C. T. Lin, B. Keimer, A. Varykhalov, A. A. Kordyuk, and S. V. Borisenko. Momentum dependence of the superconducting gap in  $Ba_{1-x}K_xFe_2As_2$ . *Phys. Rev. B*, 79:054517, 2009. doi:10.1103/PhysRevB.79.054517.
- [66] K. Hashimoto, T. Shibauchi, S. Kasahara, K. Ikada, S. Tonegawa, T. Kato, R. Okazaki, C. J. van der Beek, M. Konczykowski, H. Takeya, K. Hirata, T. Terashima, and Y. Matsuda. Microwave surface-impedance measurements of the magnetic penetration depth in single crystal  $Ba_{1-x}K_xFe_2As_2$  superconductors: Evidence for a disorder-dependent superfluid density. *Phys. Rev. Lett.*, 102:207001, 2009. doi:10.1103/PhysRevLett.102.207001.
- [67] P. Bourges D. L. Sun Y. Sidis A. Schneidewind K. Hradil D. Haug C. T. Lin B. Keimer D. S. Inosov, J. T. Park and V. Hinkov. Normal-state spin dynamics and temperature-dependent spin-resonance energy in optimally doped  $BaFe_{1.85}Co_{0.15}As_2$ . *Nature Physics*, 6:178–181, 2010. doi:10.1038/nphys1483.
- [68] H.-J. Grafe, D. Paar, G. Lang, N. J. Curro, G. Behr, J. Werner, J. Hamann-Borrero, C. Hess, N. Leps, R. Klingeler, and B. Buchner.  $As^{75}$  nmr studies of superconducting  $LaFeAsO_{0.9}F_{0.1}$ . *Phys. Rev. Lett.*, 101:047003, 2008. doi:10.1103/PhysRevLett.101.047003.

- 
- [69] Fanlong N., Kanagasingham A., Takashi I., Athena S. S., Ronying J., Michael A. M., Brian C. S., and David M. Spin susceptibility, phase diagram, and quantum criticality in the electron-doped high  $T_c$  superconductor  $Ba(Fe_{1-x}Co_x)_2As_2$ . *J. Phys. Soc. Jpn.*, 78:4, 2009. doi:[10.1143/JPSJ.78.013711](https://doi.org/10.1143/JPSJ.78.013711).
  - [70] I.I. Mazin and J. Schmalian. Pairing symmetry and pairing state in ferropnictides: Theoretical overview. *Physica C: Superconductivity*, 469:614 – 627, 2009. doi:[10.1016/j.physc.2009.03.019](https://doi.org/10.1016/j.physc.2009.03.019).
  - [71] S. Maiti, M. M. Korshunov, T. A. Maier, P. J. Hirschfeld, and A. V. Chubukov. Evolution of the superconducting state of Fe-based compounds with doping. *Phys. Rev. Lett.*, 107:147002, 2011. doi:[10.1103/PhysRevLett.107.147002](https://doi.org/10.1103/PhysRevLett.107.147002).
  - [72] Peter J. Hirschfeld. Using gap symmetry and structure to reveal the pairing mechanism in Fe-based superconductors. *Comptes Rendus Physique*, 17:197–231, 2016. doi:<https://doi.org/10.1016/j.crhy.2015.10.002>.
  - [73] L. Boeri, O. V. Dolgov, and A. A. Golubov. Is  $LaFeAsO_{1-x}F_x$  an electron-phonon superconductor? *Phys. Rev. Lett.*, 101:026403, 2008. doi:[10.1103/PhysRevLett.101.026403](https://doi.org/10.1103/PhysRevLett.101.026403).
  - [74] H. Kontani, T. Saito, and S. Onari. Origin of orthorhombic transition, magnetic transition, and shear-modulus softening in iron pnictide superconductors: Analysis based on the orbital fluctuations theory. *Phys. Rev. B*, 84:024528, 2011. doi:[10.1103/PhysRevB.84.024528](https://doi.org/10.1103/PhysRevB.84.024528).
  - [75] H. Kontani and S. Onari. Orbital-fluctuation-mediated superconductivity in iron pnictides: Analysis of the five-orbital hubbard-holstein model. *Phys. Rev. Lett.*, 104:157001, 2010. doi:[10.1103/PhysRevLett.104.157001](https://doi.org/10.1103/PhysRevLett.104.157001).
  - [76] S. Graser, T. A. Maier, P. J. Hirschfeld, and D. J. Scalapino. Near-degeneracy of several pairing channels in multiorbital models for the Fe pnictides. *New Journal of Physics*, 11:025016, 2009. doi:[10.1088/1367-2630/11/2/025016](https://doi.org/10.1088/1367-2630/11/2/025016).
  - [77] S. Kivelson, E. Fradkin, and V. Emery. Electronic liquid-crystal phases of a doped mott insulator. *Nature*, 396:550–553, 1998. doi:[10.1038/31177](https://doi.org/10.1038/31177).
  - [78] E. Fradkin, S. A. Kivelson, M. J. Lawler, J. P. Eisenstein, and A. P. Mackenzie. Nematic fermi fluids in condensed matter physics. *Annual Review of Condensed Matter Physics*, 1:153–178, 2010. doi:[10.1146/annurev-conmatphys-070909-103925](https://doi.org/10.1146/annurev-conmatphys-070909-103925).
  - [79] R. M. Fernandes and J. Schmalian. Manifestations of nematic degrees of freedom in the magnetic, elastic, and superconducting properties of the iron pnictides. *Superconductor Science and Technology*, 25:084005, 2012. doi:[10.1088/0953-2048/25/8/084005](https://doi.org/10.1088/0953-2048/25/8/084005).
  - [80] M. G. Kim, R. M. Fernandes, A. Kreyssig, J. W. Kim, A. Thaler, S. L. Bud'ko, P. C. Canfield, R. J. McQueeney, J. Schmalian, and A. I. Goldman. Character of the structural and magnetic phase transitions in the parent and electron-doped  $BaFe_2As_2$  compounds. *Phys. Rev. B*, 83:134522, 2011. doi:[10.1103/PhysRevB.83.134522](https://doi.org/10.1103/PhysRevB.83.134522).

- [81] J. H. Chu, J. G. Analytis, D. Press, K. De Greve, T. D. Ladd, Y. Yamamoto, and I. R. Fisher. In-plane electronic anisotropy in underdoped  $Ba(Fe_{1-x}Co_x)_2As_2$  revealed by partial detwinning in a magnetic field. *Phys. Rev. B*, 81:214502, 2010. [doi:10.1103/PhysRevB.81.214502](https://doi.org/10.1103/PhysRevB.81.214502).
- [82] I. R. Fisher, L. Degiorgi, and Z. X. Shen. In-plane electronic anisotropy of underdoped 122 *Fe*-arsenide superconductors revealed by measurements of detwinned single crystals. *Reports on Progress in Physics*, 74(12):124506, 2011. [doi:10.1088/0034-4885/74/12/124506](https://doi.org/10.1088/0034-4885/74/12/124506).
- [83] Y. Gallais and I. Paul. Charge nematicity and electronic raman scattering in iron-based superconductors. *Comptes Rendus Physique*, 17:113–139, 2016. [doi:10.1016/j.crhy.2015.10.001](https://doi.org/10.1016/j.crhy.2015.10.001).
- [84] J. Chu, J. G. Analytis, K. De Greve, P. L. McMahon, Z. Islam, Y. Yamamoto, and I. R. Fisher. In-plane resistivity anisotropy in an underdoped iron arsenide superconductor. *Science*, 329:824–826, 2010. [doi:10.1126/science.1190482](https://doi.org/10.1126/science.1190482).
- [85] Y. Suzuki, T. Shimojima, T. Sonobe, A. Nakamura, M. Sakano, H. Tsuji, J. Omaichi, K. Yoshioka, M. Kuwata-Gonokami, T. Watashige, R. Kobayashi, S. Kasahara, T. Shibauchi, Y. Matsuda, Y. Yamakawa, H. Kontani, and K. Ishizaka. Momentum-dependent sign inversion of orbital order in superconducting *FeSe*. *Phys. Rev. B*, 92:205117, 2015. [doi:10.1103/PhysRevB.92.205117](https://doi.org/10.1103/PhysRevB.92.205117).
- [86] D. Liu, C. Li, J. Huang, B. Lei, L. Wang, X. Wu, B. Shen, Q. Gao, Y. Zhang, X. Liu, Y. Hu, Y. Xu, A. Liang, J. Liu, P. Ai, L. Zhao, S. He, L. Yu, G. Liu, Y. Mao, X. Dong, X. Jia, F. Zhang, S. Zhang, F. Yang, Z. Wang, Q. Peng, Y. Shi, J. Hu, T. Xiang, X. Chen, Z. Xu, C. Chen, and X. J. Zhou. Orbital origin of extremely anisotropic superconducting gap in nematic phase of *FeSe* superconductor. *Phys. Rev. X*, 8:031033, 2018. [doi:10.1103/PhysRevX.8.031033](https://doi.org/10.1103/PhysRevX.8.031033).
- [87] S. H. Baek, D. V. Efremov, J. M. Ok, J. S. Kim, J. van den Brink, and B. Buchner. Orbital-driven nematicity in *FeSe*. *Nature Mater*, 14:210–214, 2015. [doi:10.1038/nmat4138](https://doi.org/10.1038/nmat4138).
- [88] Y. Su, H. Liao, and T. Li. The form and origin of orbital ordering in the electronic nematic phase of iron-based superconductors. *Journal of Physics: Condensed Matter*, 27:105702, 2015. [doi:10.1088/0953-8984/27/10/105702](https://doi.org/10.1088/0953-8984/27/10/105702).
- [89] S. Mukherjee, A. Kreisel, P. J. Hirschfeld, and B. M. Andersen. Model of electronic structure and superconductivity in orbitally ordered *FeSe*. *Phys. Rev. Lett.*, 115:026402, 2015. [doi:10.1103/PhysRevLett.115.026402](https://doi.org/10.1103/PhysRevLett.115.026402).
- [90] M. D. Watson, T. K. Kim, A. A. Haghighirad, N. R. Davies, A. McCollam, A. Narayanan, S. F. Blake, Y. L. Chen, S. Ghannadzadeh, A. J. Schofield, M. Hoesch, C. Meingast, T. Wolf, and A. I. Coldea. Emergence of the nematic electronic state in *FeSe*. *Phys. Rev. B*, 91:155106, 2015. [doi:10.1103/PhysRevB.91.155106](https://doi.org/10.1103/PhysRevB.91.155106).
- [91] K. Jiang, J. Hu, H. Ding, and Z. Wang. Interatomic coulomb interaction and electron nematic bond order in *FeSe*. *Phys. Rev. B*, 93:115138, 2016. [doi:10.1103/PhysRevB.93.115138](https://doi.org/10.1103/PhysRevB.93.115138).

- 
- [92] R. Q. Xing, L. Classen, and A. V. Chubukov. Orbital order in *FeSe*: The case for vertex renormalization. *Phys. Rev. B*, 98:041108, 2018. doi:[10.1103/PhysRevB.98.041108](https://doi.org/10.1103/PhysRevB.98.041108).
  - [93] P. Massat, D. Farina, I. Paul, S. Karlsson, P. Strobel, P. Toulemonde, M. A. Méasson, M. Cazayous, A. Sacuto, S. Kasahara, T. Shibauchi, Y. Matsuda, and Y. Gallais. Charge-induced nematicity in *FeSe*. *Proceedings of the National Academy of Sciences*, 113:9177–9181, 2016. doi:[10.1073/pnas.1606562113](https://doi.org/10.1073/pnas.1606562113).
  - [94] E. C. Blomberg, M. A. Tanatar, R. M. Fernandes, I. I. Mazin, Bing Shen, Hai-Hu Wen, M. D. Johannes, J. Schmalian, and R. Prozorov. Sign-reversal of the in-plane resistivity anisotropy in hole-doped iron pnictides. *Nat Commun*, 4:1914, 2013. doi:[10.1038/ncomms2933](https://doi.org/10.1038/ncomms2933).
  - [95] C. Mirri, A. Dusza, S. Bastelberger, M. Chinotti, L. Degiorgi, J.-H. Chu, H.-H. Kuo, and I. R. Fisher. Origin of the resistive anisotropy in the electronic nematic phase of *BaFe<sub>2</sub>As<sub>2</sub>* revealed by optical spectroscopy. *Phys. Rev. Lett.*, 115:107001, 2015. doi:[10.1103/PhysRevLett.115.107001](https://doi.org/10.1103/PhysRevLett.115.107001).
  - [96] L. Fanfarillo, A. Valli, and M. Capone. Synergy between hund-driven correlations and boson-mediated superconductivity. *Phys. Rev. Lett.*, 125:177001, 2020. doi:[10.1103/PhysRevLett.125.177001](https://doi.org/10.1103/PhysRevLett.125.177001).
  - [97] L. Fanfarillo, G. Giovannetti, M. Capone, and E. Bascones. Nematicity at the hund’s metal crossover in iron superconductors. *Phys. Rev. B*, 95:144511, 2017. doi:[10.1103/PhysRevB.95.144511](https://doi.org/10.1103/PhysRevB.95.144511).
  - [98] A. V. Chubukov, D. V. Efremov, and I. Eremin. Magnetism, superconductivity, and pairing symmetry in iron-based superconductors. *Phys. Rev. B*, 78:134512, 2008. doi:[10.1103/PhysRevB.78.134512](https://doi.org/10.1103/PhysRevB.78.134512).
  - [99] P. M. R. Brydon and C. Timm. Spin excitations in the excitonic spin-density-wave state of the iron pnictides. *Phys. Rev. B*, 80:174401, 2009. doi:[10.1103/PhysRevB.80.174401](https://doi.org/10.1103/PhysRevB.80.174401).
  - [100] A. B. Vorontsov, M. G. Vavilov, and A. V. Chubukov. Superconductivity and spin-density waves in multiband metals. *Phys. Rev. B*, 81:174538, 2010. doi:[10.1103/PhysRevB.81.174538](https://doi.org/10.1103/PhysRevB.81.174538).
  - [101] I. Eremin and A. V. Chubukov. Magnetic degeneracy and hidden metallicity of the spin-density-wave state in ferropnictides. *Phys. Rev. B*, 81:024511, 2010. URL: <https://link.aps.org/doi/10.1103/PhysRevB.81.024511>, doi:[10.1103/PhysRevB.81.024511](https://doi.org/10.1103/PhysRevB.81.024511).
  - [102] T. A. Maier, S. Graser, D. J. Scalapino, and P. J. Hirschfeld. Origin of gap anisotropy in spin fluctuation models of the iron pnictides. *Phys. Rev. B*, 79:224510, 2009. URL: <https://link.aps.org/doi/10.1103/PhysRevB.79.224510>, doi:[10.1103/PhysRevB.79.224510](https://doi.org/10.1103/PhysRevB.79.224510).
  - [103] R. Fernández-Martín, L. Fanfarillo, L. Benfatto, and B. Valenzuela. Anisotropy of the dc conductivity due to orbital-selective spin fluctuations in the nematic phase of iron superconductors. *Phys. Rev. B*, 99:155117, 2019. doi:[10.1103/PhysRevB.99.155117](https://doi.org/10.1103/PhysRevB.99.155117).

- [104] S. Raghu, Xiao-Liang Qi, Chao-Xing Liu, D. J. Scalapino, and Shou-Cheng Zhang. Minimal two-band model of the superconducting iron oxypnictides. *Phys. Rev. B*, 77:220503, 2008. [doi:10.1103/PhysRevB.77.220503](https://doi.org/10.1103/PhysRevB.77.220503).
- [105] Maria Daghofer, Andrew Nicholson, Adriana Moreo, and Elbio Dagotto. Three orbital model for the iron-based superconductors. *Phys. Rev. B*, 81:014511, 2010. [doi:10.1103/PhysRevB.81.014511](https://doi.org/10.1103/PhysRevB.81.014511).
- [106] Patrick A. Lee and Xiao-Gang Wen. Spin-triplet  $p$ -wave pairing in a three-orbital model for iron pnictide superconductors. *Phys. Rev. B*, 78:144517, 2008. [doi:10.1103/PhysRevB.78.144517](https://doi.org/10.1103/PhysRevB.78.144517).
- [107] M. J. Calderón, B. Valenzuela, and E. Bascones. Tight-binding model for iron pnictides. *Phys. Rev. B*, 80:094531, 2009. [doi:10.1103/PhysRevB.80.094531](https://doi.org/10.1103/PhysRevB.80.094531).
- [108] D. J. Scalapino. A common thread: The pairing interaction for unconventional superconductors. *Rev. Mod. Phys.*, 84:1383–1417, 2012. [doi:10.1103/RevModPhys.84.1383](https://doi.org/10.1103/RevModPhys.84.1383).
- [109] Hiroaki Ikeda, Ryotaro Arita, and Jan Kune. Phase diagram and gap anisotropy in iron-pnictide superconductors. *Phys. Rev. B*, 81:054502, 2010. [doi:10.1103/PhysRevB.81.054502](https://doi.org/10.1103/PhysRevB.81.054502).
- [110] A. M. Oles. Antiferromagnetism and correlation of electrons in transition metals. *Phys. Rev. B*, 28:327–339, 1983. [doi:10.1103/PhysRevB.28.327](https://doi.org/10.1103/PhysRevB.28.327).
- [111] Tetsuya Takimoto, Takashi Hotta, and Kazuo Ueda. Strong-coupling theory of superconductivity in a degenerate hubbard model. *Phys. Rev. B*, 69:104504, 2004. [doi:10.1103/PhysRevB.69.104504](https://doi.org/10.1103/PhysRevB.69.104504).
- [112] K. Kubo. Pairing symmetry in a two-orbital hubbard model on a square lattice. *Phys. Rev. B*, 75:224509, 2007. [doi:10.1103/PhysRevB.75.224509](https://doi.org/10.1103/PhysRevB.75.224509).
- [113] C. Castellani, C. R. Natoli, and J. Ranninger. Magnetic structure of  $v_2o_3$  in the insulating phase. *Phys. Rev. B*, 18:4945–4966, 1978. [doi:10.1103/PhysRevB.18.4945](https://doi.org/10.1103/PhysRevB.18.4945).
- [114] S. Graser, A. F. Kemper, T. A. Maier, H.-P. Cheng, P. J. Hirschfeld, and D. J. Scalapino. Spin fluctuations and superconductivity in a three-dimensional tight-binding model for  $\text{bafe}_2\text{as}_2$ . *Phys. Rev. B*, 81:214503, 2010. [doi:10.1103/PhysRevB.81.214503](https://doi.org/10.1103/PhysRevB.81.214503).
- [115] E. Bascones, M. J. Calderón, and B. Valenzuela. Low magnetization and anisotropy in the antiferromagnetic state of undoped iron pnictides. *Phys. Rev. Lett.*, 104:227201, 2010. [doi:10.1103/PhysRevLett.104.227201](https://doi.org/10.1103/PhysRevLett.104.227201).
- [116] N. E. Bickers, D. J. Scalapino, and S. R. White. Conserving approximations for strongly correlated electron systems: Bethe-salpeter equation and dynamics for the two-dimensional hubbard model. *Phys. Rev. Lett.*, 62:961–964, 1989. [doi:10.1103/PhysRevLett.62.961](https://doi.org/10.1103/PhysRevLett.62.961).



- 
- [117] Morten H. Christensen, Jian Kang, Brian M. Andersen, and Rafael M. Fernandes. Spin-driven nematic instability of the multiorbital hubbard model: Application to iron-based superconductors. *Phys. Rev. B*, 93:085136, 2016. doi:[10.1103/PhysRevB.93.085136](https://doi.org/10.1103/PhysRevB.93.085136).
  - [118] V. Cvetkovic and O. Vafek. Space group symmetry, spin-orbit coupling, and the low-energy effective hamiltonian for iron-based superconductors. *Phys. Rev. B*, 88:134510, 2013. doi:[10.1103/PhysRevB.88.134510](https://doi.org/10.1103/PhysRevB.88.134510).
  - [119] J. W. Negele and H. Orland. *Quantum many particle system*. Addison-Wesley, 1988.
  - [120] K. Kuroki, H. Usui, S. Onari, R. Arita, and H. Aoki. Pnictogen height as a possible switch between high- $T_c$  nodeless and low- $T_c$  nodal pairings in the iron-based superconductors. *Phys. Rev. B*, 79:224511, 2009. doi:[10.1103/PhysRevB.79.224511](https://doi.org/10.1103/PhysRevB.79.224511).
  - [121] A. F. Kemper, M. M. Korshunov, T. P. Devereaux, J. N. Fry, H-P. Cheng, and P. J. Hirschfeld. Anisotropic quasiparticle lifetimes in fe-based superconductors. *Phys. Rev. B*, 83:184516, 2011. doi:[10.1103/PhysRevB.83.184516](https://doi.org/10.1103/PhysRevB.83.184516).
  - [122] Ying Ran, Fa Wang, Hui Zhai, Ashvin Vishwanath, and Dung-Hai Lee. Nodal spin density wave and band topology of the feas-based materials. *Phys. Rev. B*, 79:014505, 2009. doi:[10.1103/PhysRevB.79.014505](https://doi.org/10.1103/PhysRevB.79.014505).
  - [123] L. Classen, R.-Q. Xing, M. Khodas, and A. V. Chubukov. Interplay between magnetism, superconductivity, and orbital order in 5-pocket model for iron-based superconductors: Parquet renormalization group study. *Phys. Rev. Lett.*, 118:037001, 2017. doi:[10.1103/PhysRevLett.118.037001](https://doi.org/10.1103/PhysRevLett.118.037001).
  - [124] P. Reiss, M. D. Watson, T. K. Kim, A. A. Haghighirad, D. N. Woodruff, M. Bruma, S. J. Clarke, and A. I. Coldea. Suppression of electronic correlations by chemical pressure from fese to fes. *Phys. Rev. B*, 96:121103, 2017. doi:[10.1103/PhysRevB.96.121103](https://doi.org/10.1103/PhysRevB.96.121103).
  - [125] Youichi Yamakawa and Hiroshi Kontani. Nematicity, magnetism, and superconductivity in *FeSe* under pressure: Unified explanation based on the self-consistent vertex correction theory. *Phys. Rev. B*, 96:144509, 2017. doi:[10.1103/PhysRevB.96.144509](https://doi.org/10.1103/PhysRevB.96.144509).
  - [126] L. Fanfarillo, E. Cappelluti, C. Castellani, and L. Benfatto. Unconventional hall effect in pnictides from interband interactions. *Phys. Rev. Lett.*, 109:096402, 2012. doi:[10.1103/PhysRevLett.109.096402](https://doi.org/10.1103/PhysRevLett.109.096402).
  - [127] G. M. Eliashberg. Interactions between electrons and lattice vibrations in a superconductor. *Sov. Phys. - JETP*, 11, 1960.
  - [128] L. C. Rhodes, M. D. Watson, A. A. Haghighirad, D. V. Evtushinsky, M. Eschrig, and T. K. Kim. Scaling of the superconducting gap with orbital character in *FeSe*. *Phys. Rev. B*, 98:180503, 2018. doi:[10.1103/PhysRevB.98.180503](https://doi.org/10.1103/PhysRevB.98.180503).
  - [129] T. Shimojima, Y. Suzuki, T. Sonobe, A. Nakamura, M. Sakano, J. Omachi, K. Yoshioka, M. Kuwata-Gonokami, K. Ono, H. Kumigashira, A. E. Böhmer, F. Hardy, T. Wolf, C. Meingast, H. v. Löhneysen, H. Ikeda, and K. Ishizaka. Lifting of xz/yz

- orbital degeneracy at the structural transition in detwinned *FeSe*. *Phys. Rev. B*, 90:121111, 2014. doi:10.1103/PhysRevB.90.121111.
- [130] K. Nakayama, Y. Miyata, G. N. Phan, T. Sato, Y. Tanabe, T. Urata, K. Tanigaki, and T. Takahashi. Reconstruction of band structure induced by electronic nematicity in an *FeSe* superconductor. *Phys. Rev. Lett.*, 113:237001, 2014. doi:10.1103/PhysRevLett.113.237001.
- [131] P. Zhang, T. Qian, P. Richard, X. P. Wang, H. Miao, B. Q. Lv, B. B. Fu, T. Wolf, C. Meingast, X. X. Wu, Z. Q. Wang, J. P. Hu, and H. Ding. Observation of two distinct  $d_{xz}/d_{yz}$  band splittings in *FeSe*. *Phys. Rev. B*, 91:214503, 2015. doi:10.1103/PhysRevB.91.214503.
- [132] Y. Zhang, M. Yi, Z.-K. Liu, W. Li, J. J. Lee, R. G. Moore, M. Hashimoto, M. Nakajima, H. Eisaki, S.-K. Mo, Z. Hussain, T. P. Devereaux, Z.-X. Shen, and D. H. Lu. Distinctive orbital anisotropy observed in the nematic state of a *FeSe* thin film. *Phys. Rev. B*, 94:115153, 2016. doi:10.1103/PhysRevB.94.115153.
- [133] B. Valenzuela L. Benfatto and L. Fanfarillo. Nematic pairing from orbital-selective spin fluctuations in *FeSe*. *npj Quant Mater*, 3, 2008. doi:10.1038/s41535-018-0129-9.
- [134] T. Chen, Y. Chen, A. Kreisel, X. Lu, A. Schneidewind, Y. Qiu, J. T. Park, T. G. Perring, J. R. Stewart, H. Cao, R. Zhang, Y. Li, Y. Rong, Y. Wei, P. J. Hirschfeld B. M. Andersen, C. Broholm, and P. Dai. Anisotropic spin fluctuations in detwinned *fese*. *Nature*, 18:709?716, 2019. doi:10.1038/s41563-019-0369-5.
- [135] V. Cvetkovic and Z. Tesanovic. Multiband magnetism and superconductivity in fe-based compounds. *EPL (Europhysics Letters)*, 85:37002, 2009. doi:10.1209/0295-5075/85/37002.
- [136] R. M. Fernandes and J. Schmalian. Competing order and nature of the pairing state in the iron pnictides. *Phys. Rev. B*, 82:014521, 2010. doi:10.1103/PhysRevB.82.014521.
- [137] L. Benfatto, M. Capone, S. Caprara, C. Castellani, and C. Di Castro. Multiple gaps and superfluid density from interband pairing in a four-band model of the iron oxypnictides. *Phys. Rev. B*, 78:140502, 2008. doi:10.1103/PhysRevB.78.140502.
- [138] M. Altmeyer, D. Guterding, P. J. Hirschfeld, T. A. Maier, R. Valentí, and D. J. Scalapino. Role of vertex corrections in the matrix formulation of the random phase approximation for the multiorbital *Hubbard* model. *Phys. Rev. B*, 94:214515, 2016. doi:10.1103/PhysRevB.94.214515.
- [139] A F Kemper, T A Maier, S Graser, H-P Cheng, P J Hirschfeld, and D J Scalapino. Sensitivity of the superconducting state and magnetic susceptibility to key aspects of electronic structure in ferropnictides. *New Journal of Physics*, 12(7):073030, 2010. doi:10.1088/1367-2630/12/7/073030.
- [140] D. J. Scalapino, E. Loh, and J. E. Hirsch.  $d$ -wave pairing near a spin-density-wave instability. *Phys. Rev. B*, 34:8190–8192, 1986. doi:10.1103/PhysRevB.34.8190.



- 
- [141] M. A. Tanatar, E. C. Blomberg, A. Kreyssig, M. G. Kim, N. Ni, A. Thaler, S. L. Bud'ko, P. C. Canfield, A. I. Goldman, I. I. Mazin, and R. Prozorov. Uniaxial-strain mechanical detwinning of  $\text{CaFe}_2\text{As}_2$  and  $\text{BaFe}_2\text{As}_2$  crystals: Optical and transport study. *Phys. Rev. B*, 81:184508, 2010. doi:[10.1103/PhysRevB.81.184508](https://doi.org/10.1103/PhysRevB.81.184508).
  - [142] A. Dusza, A. Lucarelli, F. Pfuner, J.-H. Chu, I. R. Fisher, and L. Degiorgi. Anisotropic charge dynamics in detwinned  $\text{Ba}(\text{Fe}_{1-x}\text{Co}_x)_2\text{As}_2$ . *EPL (Europhysics Letters)*, 93:37002, 2011. doi:[10.1209/0295-5075/93/37002](https://doi.org/10.1209/0295-5075/93/37002).
  - [143] A. Dusza, A. Lucarelli, A. Sanna, S. Massidda, J.-H. Chu, I. R. Fisher, and L. Degiorgi. Anisotropic in-plane optical conductivity in detwinned  $\text{Ba}(\text{Fe}_{1-x}\text{Co}_x)_2\text{As}_2$ . *New Journal of Physics*, 14:023020, 2012. doi:[10.1088/1367-2630/14/2/023020](https://doi.org/10.1088/1367-2630/14/2/023020).
  - [144] C. Mirri, A. Dusza, S. Bastelberger, J.-H. Chu, H.-H. Kuo, I. R. Fisher, and L. Degiorgi. Nematic-driven anisotropic electronic properties of underdoped detwinned  $\text{Ba}(\text{Fe}_{1-x}\text{Co}_x)_2\text{As}_2$  revealed by optical spectroscopy. *Phys. Rev. B*, 90:155125, 2014. doi:[10.1103/PhysRevB.90.155125](https://doi.org/10.1103/PhysRevB.90.155125).
  - [145] T. M. Chuang, M. P. Allan, Jinho Lee, Yang Xie, Ni Ni, S. L. Bud'ko, G. S. Boebinger, P. C. Canfield, and J. C. Davis. Nematic electronic structure in the "parent" state of the iron-based superconductor  $\text{Ca}(\text{Fe}_{1-x}\text{Co}_x)_2\text{As}_2$ . *Science*, 327:181–184, 2010. doi:[10.1126/science.1181083](https://doi.org/10.1126/science.1181083).
  - [146] M. Nakajima, S. Ishida, Y. Tomioka, K. Kihou, C. H. Lee, A. Iyo, T. Ito, T. Kakeshita, H. Eisaki, and S. Uchida. Effect of Co doping on the in-plane anisotropy in the optical spectrum of underdoped  $\text{Ba}(\text{Fe}_{1-x}\text{Co}_x)_2\text{As}_2$ . *Phys. Rev. Lett.*, 109:217003, 2012. doi:[10.1103/PhysRevLett.109.217003](https://doi.org/10.1103/PhysRevLett.109.217003).
  - [147] S. Ishida, M. Nakajima, T. Liang, K. Kihou, C. H. Lee, A. Iyo, H. Eisaki, T. Kakeshita, Y. Tomioka, T. Ito, and S. Uchida. Anisotropy of the in-plane resistivity of underdoped  $\text{Ba}(\text{Fe}_{1-x}\text{Co}_x)_2\text{As}_2$  superconductors induced by impurity scattering in the antiferromagnetic orthorhombic phase. *Phys. Rev. Lett.*, 110:207001, 2013. doi:[10.1103/PhysRevLett.110.207001](https://doi.org/10.1103/PhysRevLett.110.207001).
  - [148] M. P. Allan, T.-M. Chuang, F. Masee, Yang Xie, Ni Ni, S. L. Bud'ko, G. S. Boebinger, Q. Wang, D. S. Dessau, P. C. Canfield, M. S. Golden, and J. C. Davis. Anisotropic impurity states, quasiparticle scattering and nematic transport in underdoped  $\text{Ca}(\text{Fe}_{1-x}\text{Co}_x)_2\text{As}_2$ . *Nat Commun*, 9:220–224, 2013. doi:[10.1038/nphys2544](https://doi.org/10.1038/nphys2544).
  - [149] H.-H. Kuo and I. R. Fisher. Effect of disorder on the resistivity anisotropy near the electronic nematic phase transition in pure and electron-doped  $\text{BaFe}_2\text{As}_2$ . *Phys. Rev. Lett.*, 112:227001, 2014. doi:[10.1103/PhysRevLett.112.227001](https://doi.org/10.1103/PhysRevLett.112.227001).
  - [150] C. Mirri, A. Dusza, S. Bastelberger, M. Chinotti, J.-H. Chu, H.-H. Kuo, I. R. Fisher, and L. Degiorgi. Electrodynamical response in the electronic nematic phase of  $\text{BaFe}_2\text{As}_2$ . *Phys. Rev. B*, 93:085114, 2016. doi:[10.1103/PhysRevB.93.085114](https://doi.org/10.1103/PhysRevB.93.085114).
  - [151] M. Schütt, J. Schmalian, and R. M. Fernandes. Origin of dc and ac conductivity anisotropy in iron-based superconductors: Scattering rate versus spectral weight effects. *Phys. Rev. B*, 94:075111, 2016. doi:[10.1103/PhysRevB.94.075111](https://doi.org/10.1103/PhysRevB.94.075111).

- [152] M. Chinotti, A. Pal, L. Degiorgi, A. E. Böhmer, and P. C. Canfield. Optical anisotropy in the electronic nematic phase of *FeSe*. *Phys. Rev. B*, 96:121112, 2017. [doi:10.1103/PhysRevB.96.121112](https://doi.org/10.1103/PhysRevB.96.121112).
- [153] C. C. Lee, W. G. Yin, and W. Ku. Ferro-orbital order and strong magnetic anisotropy in the parent compounds of iron-pnictide superconductors. *Phys. Rev. Lett.*, 103:267001, 2009. [doi:10.1103/PhysRevLett.103.267001](https://doi.org/10.1103/PhysRevLett.103.267001).
- [154] W. Lv, F. Krüger, and P. Phillips. Orbital ordering and unfrustrated  $(\pi, 0)$  magnetism from degenerate double exchange in the iron pnictides. *Phys. Rev. B*, 82:045125, 2010. [doi:10.1103/PhysRevB.82.045125](https://doi.org/10.1103/PhysRevB.82.045125).
- [155] R. M. Fernandes, L. H. VanBebber, S. Bhattacharya, P. Chandra, V. Keppens, D. Mandrus, M. A. McGuire, B. C. Sales, A. S. Sefat, and J. Schmalian. Effects of nematic fluctuations on the elastic properties of iron arsenide superconductors. *Phys. Rev. Lett.*, 105:157003, 2010. [doi:10.1103/PhysRevLett.105.157003](https://doi.org/10.1103/PhysRevLett.105.157003).
- [156] M. Breitzkreiz, P. M. R. Brydon, and C. Timm. Resistive anisotropy due to spin-fluctuation scattering in the nematic phase of iron pnictides. *Phys. Rev. B*, 90:121104, 2014. [doi:10.1103/PhysRevB.90.121104](https://doi.org/10.1103/PhysRevB.90.121104).
- [157] M. N. Gastiasoro, I. Paul, Y. Wang, P. J. Hirschfeld, and B. M. Andersen. Emergent defect states as a source of resistivity anisotropy in the nematic phase of iron pnictides. *Phys. Rev. Lett.*, 113:127001, 2014. [doi:10.1103/PhysRevLett.113.127001](https://doi.org/10.1103/PhysRevLett.113.127001).
- [158] Y. Wang, M. N. Gastiasoro, B. M. Andersen, M. Tomić, H. O. Jeschke, R. Valentí, I. Paul, and P. J. Hirschfeld. Effects of lifshitz transition on charge transport in magnetic phases of *Fe*-based superconductors. *Phys. Rev. Lett.*, 114:097003, 2015. [doi:10.1103/PhysRevLett.114.097003](https://doi.org/10.1103/PhysRevLett.114.097003).
- [159] S. Liang, G. Alvarez, C. Şen, A. Moreo, and E. Dagotto. Anisotropy of electrical transport in pnictide superconductors studied using *Monte Carlo* simulations of the spin-fermion model. *Phys. Rev. Lett.*, 109:047001, 2012. [doi:10.1103/PhysRevLett.109.047001](https://doi.org/10.1103/PhysRevLett.109.047001).
- [160] B. Valenzuela, E. Bascones, and M. J. Calderón. Conductivity anisotropy in the antiferromagnetic state of iron pnictides. *Phys. Rev. Lett.*, 105:207202, 2010. [doi:10.1103/PhysRevLett.105.207202](https://doi.org/10.1103/PhysRevLett.105.207202).
- [161] K. Sugimoto, P. Prelovšek, E. Kaneshita, and T. Tohyama. Memory function approach to in-plane anisotropic resistivity in the antiferromagnetic phase of iron arsenide superconductors. *Phys. Rev. B*, 90:125157, 2014. [doi:10.1103/PhysRevB.90.125157](https://doi.org/10.1103/PhysRevB.90.125157).
- [162] M. A. Tanatar, A. E. Böhmer, E. I. Timmons, M. Schütt, G. Drachuck, V. Taufour, K. Kothapalli, A. Kreyssig, S. L. Bud'ko, P. C. Canfield, R. M. Fernandes, and R. Prozorov. Origin of the resistivity anisotropy in the nematic phase of *FeSe*. *Phys. Rev. Lett.*, 117:127001, 2016. [doi:10.1103/PhysRevLett.117.127001](https://doi.org/10.1103/PhysRevLett.117.127001).
- [163] L. Fanfarillo. Transport properties in multichannel systems. *University of Rome La Sapienza*, 2012.

- 
- [164] G. Mahan. *Many particle physics*. Springer, 1990.
  - [165] M. J. Calderón, L. de' Medici, B. Valenzuela, and E. Bascones. Correlation, doping, and interband effects on the optical conductivity of iron superconductors. *Phys. Rev. B*, 90:115128, 2014. doi:[10.1103/PhysRevB.90.115128](https://doi.org/10.1103/PhysRevB.90.115128).
  - [166] M. M. Korshunov. Itinerant spin fluctuations in iron-based superconductors. *ArXiv e-prints*, 2017. [arXiv:1710.09888](https://arxiv.org/abs/1710.09888), doi:<https://arxiv.org/abs/1710.09888>.
  - [167] S. Onari and H. Kontani. In-plane anisotropy of transport coefficients in electronic nematic states: Universal origin of nematicity in fe-based superconductors. *Phys. Rev. B*, 96:094527, 2017. doi:[10.1103/PhysRevB.96.094527](https://doi.org/10.1103/PhysRevB.96.094527).
  - [168] M. Chinotti, A. Pal, L. Degiorgi, A. E. Böhrer, and P. C. Canfield. Ingredients for the electronic nematic phase in *FeSe* revealed by its anisotropic optical response. *Phys. Rev. B*, 98:094506, 2018. doi:[10.1103/PhysRevB.98.094506](https://doi.org/10.1103/PhysRevB.98.094506).
  - [169] Y. S. Kushnirenko, A. V. Fedorov, E. Haubold, S. Thirupathaiah, T. Wolf, S. Aswartham, I. Morozov, T. K. Kim, B. Büchner, and S. V. Borisenko. Three-dimensional superconducting gap in *FeSe* from angle-resolved photoemission spectroscopy. *Phys. Rev. B*, 97:180501, 2018. doi:[10.1103/PhysRevB.97.180501](https://doi.org/10.1103/PhysRevB.97.180501).
  - [170] T. Nomura, Y. Inoue, S. Matsuishi, M. Hirano, J. E. Kim, K. Kato, M. Takata, and H. Hosono. Comparison of crystal structures and the effects of co substitution in a new member of the *fe* – 1111 superconductor family *aeFeAsF* (*ae* = *ca* and *sr*): a possible candidate for a higher-*tc* superconductor. *Superconductor Science and Technology*, 22:055016, 2009. doi:[10.1088/0953-2048/22/5/055016](https://doi.org/10.1088/0953-2048/22/5/055016).
  - [171] H. Ogino, Y. Katsura, S. Horii, K. Kishio, and J. Shimoyama. New iron-based arsenide oxides (*Fe<sub>2</sub>As<sub>2</sub>*)(*Sr<sub>4</sub>M<sub>2</sub>O<sub>6</sub>*)(*m* = *sc*, *cr*). *Superconductor Science and Technology*, 22:085001, 2009. doi:[10.1088/0953-2048/22/8/085001](https://doi.org/10.1088/0953-2048/22/8/085001).
  - [172] M. Rotter, M. Tegel, and D. Johrendt. Superconductivity at 38 *K* in the iron arsenide (*Ba<sub>1-x</sub>K<sub>x</sub>*)*Fe<sub>2</sub>As<sub>2</sub>*. *Phys. Rev. Lett.*, 101:107006, 2008. doi:[10.1103/PhysRevLett.101.107006](https://doi.org/10.1103/PhysRevLett.101.107006).
  - [173] J. Zhao, Q. Huang, C. de la Cruz, S. Li, J. W. Lynn, Y. Chen, M. A. Green, G. F. Chen, G. Li, Z. Li, J. L. Luo, N. L. Wang, and P. Dai. Structural and magnetic phase diagram of *CeFeAsO<sub>1-x</sub>F<sub>x</sub>* and its relation to high-temperature superconductivity. *Nature*, 7:953?959, 2008. doi:[doi.org/10.1038/nmat2315](https://doi.org/10.1038/nmat2315).
  - [174] S. A. J. Kimber, A. Kreyssig, Y.-Z. Zhang, H. O. Jeschke, R. Valenti, F. Yokaichiya, E. Colombier, J. Yan, T. C. Hansen, T. Chatterji, R. J. McQueeney, P. C. Canfield, Alan I. Goldman, and D. N. Argyriou. Similarities between structural distortions under pressure and chemical doping in superconducting *BaFe<sub>2</sub>As<sub>2</sub>*. *Nature*, 8:471?475, 2009. doi:[doi.org/10.1038/nmat2443](https://doi.org/10.1038/nmat2443).
  - [175] X. Hong, F. Caglieris, R. Kappenberger, S. Wurmehl, S. Aswartham, F. Scaravaggi, P. Lepucki, A. U. B. Wolter, H.-J. Grafe, B. Büchner, and C. Hess. Evolution of the nematic susceptibility in *LaFe<sub>1-x</sub>Co<sub>x</sub>AsO*. *Phys. Rev. Lett.*, 125:067001, 2020. doi:[10.1103/PhysRevLett.125.067001](https://doi.org/10.1103/PhysRevLett.125.067001).

- [176] F. Scaravaggi, S. Sauerland, L. Wang, R. Kappenberger, P. Lepucki, A. P. Dioguardi, X. Hong, F. Caglieris, C. Wuttke, C. Hess, H.-J. Grafe, S. Aswartham, S. Wurmehl, R. Klingeler, A. U. B. Wolter, and B. Buchner. Revisiting the phase diagram of  $LaFe_{1-x}Co_xAsO$  on single crystals by thermodynamic methods. 2021. [doi:arXiv:2101.05760](#).
- [177] M. Nakahara. *Geometry, topology and physics*. 2003.